

Radiation Hydrodynamics Experiments on Large High-Energy-Density-Physics Facilities that are Relevant to Astrophysics

by

Heath J. LeFevre

A dissertation submitted in partial fulfillment
of the requirements for the degree of
Doctor of Philosophy
(Applied Physics)
in The University of Michigan
2021

Doctoral Committee:

Professor Emeritus R. P. Drake, Chair
Dr. Paul A. Keiter, Los Alamos National Laboratory, Co-Chair
Associate Professor Eric Johnsen
Associate Professor Carolyn C. Kuranz
Associate Professor Ryan D. McBride

Heath J. LeFevre

hjlefe@umich.edu

ORCID iD: 0000-0002-7091-4356

©Heath J. LeFevre 2021

ACKNOWLEDGEMENTS

I want to thank my family and friends for supporting me and listening to my various plans on how I will finish my thesis and when I would graduate. You don't have to hear about my thesis anymore, but you will almost certainly have to suffer through more plans.

I would also like to thank my advisors Paul Drake, Carolyn Kuranz, and Paul Keiter. I appreciate the opportunity you gave me to complete my PhD and the financial support you provided so that I could run around the country blowing things up, with lasers, for five years.

Further thanks are due to my committee members Eric Johnsen and Ryan McBride who are unlucky enough to be the only people who have to read this thesis that did not sign up for the job when I entered grad school.

TABLE OF CONTENTS

ACKNOWLEDGEMENTS	ii
LIST OF FIGURES	vi
LIST OF TABLES	xvi
LIST OF APPENDICES	xvii
LIST OF ABBREVIATIONS	xviii
ABSTRACT	xx
CHAPTER	
I. Introduction	1
1.1 High-Energy-Density-Physics	1
1.2 Radiation Hydrodynamics in Astrophysics and Cosmology	5
1.2.1 Photoionization Fronts	5
1.2.2 Radiative Shocks	8
1.3 HEDP Experiments at Large Facilities	13
1.4 Organization of This Thesis	14
II. Relevant Theory for these Experiments	17
2.1 Hydrodynamics	17
2.1.1 Derivation of the Euler equations	18
2.1.2 Hydrodynamic shocks	20
2.2 Radiation transport	21
2.2.1 Definitions	21
2.2.2 Derivation of the Transport Equation	25
2.2.3 Moments of the Transport Equation	26
2.2.4 Solutions to the Transport Equation	28
2.3 Radiation hydrodynamics	31
2.3.1 Nonlinear Diffusion Waves	33

2.3.2	Photoionization fronts	36
2.3.3	Radiative shocks	48
III.	Photoionization Front Experiments on the Omega Laser Facility	58
3.1	Omega Laser Facility	59
3.2	Primary Diagnostic: Absorption Spectroscopy	60
3.3	Design Simulations	61
3.3.1	Helios-CR Radiation Hydrodynamics Simulations	62
3.4	September 11th 2018 Experiments	64
3.4.1	Experiment Geometry	64
3.4.2	Laser Configuration	67
3.4.3	Diagnostic Choices and Configurations	68
3.4.4	Capsule Anisotropy Characterization	71
3.4.5	Experimental Results and Simulations	74
3.4.6	PrismSPECT Atomic Kinetics Calculations	82
3.5	Conclusions	85
IV.	Photoionization Front Experiment Design for the Z-Machine	87
4.1	The Z-Machine at Sandia National Laboratories	88
4.2	Primary Diagnostic: Streaked Visible Spectroscopy	89
4.3	Description of Problem	90
4.4	Photoionization Front Simulations with the Nominal Physics Model	92
4.4.1	Simulation Setup and PI Front Analysis	92
4.4.2	Parameter space study	98
4.5	Testing the model validity	100
4.5.1	Resolution study	100
4.5.2	Atomic model sophistication	102
4.5.3	Number of angles in the radiation transport	105
4.6	Artificially Attenuated source	106
4.7	Estimated measurements	110
4.8	Conclusions	112
V.	Radiative Shock Experiments on The National Ignition Facility	113
5.1	The National Ignition Facility	114
5.2	Primary Diagnostics	115
5.2.1	X-ray Thomson Scattering	115
5.2.2	Streaked Optical Self-Emission	117
5.3	Target Design	119
5.3.1	First XRTS Shielding and Probe Design	120
5.3.2	Second XRTS Shielding and Probe Design	122

5.4	Laser Configuration	123
5.4.1	Drive Lasers	123
5.4.2	Probe Lasers	123
5.5	Diagnostic Configuration	124
5.5.1	Monoangle Crystal Spectrometer (MACS)	124
5.5.2	VISAR and SOP Cameras	126
5.6	July 17th Shot Day	127
5.6.1	Self-emission Data	127
5.6.2	XRTS Data	133
5.7	February 10th Shot Day	135
5.7.1	Self-emission Data	135
5.7.2	XRTS Data	136
5.8	Conclusions	139
VI. Conclusions		140
6.1	Summary	140
6.2	Conclusions	141
6.3	Future Work	141
APPENDICES		144
A.1	Dante Analysis	145
B.1	Integrated Physics Target - RID 68435	150
B.2	Au Foil Characterization Target - RID 68712	163
B.3	Capsule Characterization Shot - RID 69902	174
C.1	High Drive Shot N190717-001	184
C.2	Low Drive Shot N190717-002	184
D.1	High Drive Shot N200210-001	186
D.2	High Drive Shot N200210-002	186
D.3	Low Drive Shot N200211-001	187
BIBLIOGRAPHY		188

LIST OF FIGURES

Figure

1.1	A parameter space plot that shows the boundary of the HEDP regime and where different physics are relevant in HEDP conditions. This image was taken from Chapter 1 of Reference 1[1].	2
1.2	The x-ray emission from the super-luminous supernova SN2006gy, which shows that it is comparable in brightness and size to the galactic core of the progenitor host galaxy. Supernovae and their remnants produce radiative shocks and can drive photoionization fronts in the surrounding gas, which this work tries to replicate in the laboratory. This image was adapted from NASA/CXC M.Weiss; X-ray: NASA/CXC/UC Berkeley/N.Smith et al.; IR: Lick/UC Berkeley/J.Bloom & C.Hansen.	5
1.3	The timeline of the universe’s evolution with a particular focus on the age of reionization, which is relevant to the physics of PI fronts. This image was taken from the work of Robertson <i>et al.</i> [2].	6
2.1	This describes the geometry for the radiation energy density calculation showing the volume v where the radiation propagates and the encapsulating surface Σ	23
2.2	a) The calculated values of κ_{rad} in N over a range of density and temperature values using PrismSPECT to generate the opacities. b) The calculated values of κ_{rad} in CH over a range of density and temperature values using PrismSPECT to generate the opacities	32
2.3	The density ratio, front Mach number, and flow Mach number for the heat front analysis of a PI front for the four types described in the text with a \hat{Q} of 10 and a γ of $\frac{4}{3}$. This demonstrates the limited density jump for the weak R-type front, which is the focus of the experiments described in this thesis. The abscissa is different between the plots on the left and right hand side, which demonstrates the extent of the region where there is no purely real solution.	41

2.4	A comparison of the PI front propagation with constant-flux, geometrically decaying flux, and geometrically decaying, time-dependent flux to constant flux, nonlinear diffusion wave models. This comparison shows that PI fronts travel faster than nonlinear diffusion waves, even considering the upper bound of velocity for the nonlinear diffusion waves. The inset shows the different distances the constant-flux, nonlinear diffusion waves and PI fronts with real source models travel in more detail.	43
2.5	The 3D and top down projection geometries for the calculations used to determine the average path length of an arbitrary point above a disk of radius R	45
2.6	a) The average path length where the dimensions of the propagation volume is larger than the source radius with contours showing the curvature decreasing with distance. b) The average path length where the dimensions of the propagation volume is smaller than the source radius with contours showing the curvature decreasing with distance. c) The source in the curvature calculations is Lambertian due to the geometric nature of the system. d) The bent Marshak wave results[3] show the increase of front curvature due to losses through the walls of the propagating medium container.	47
2.7	The three layer model that demonstrates the fluxes in an optically-thick, radiative shock structure with a downstream state, an optically thin cooling layer, and a precursor region.	51
2.8	The shock compression and normalized temperature in the cooling layer (a) and precursor (b) using a Q of 10^5 and γ of $\frac{4}{3}$. The precursor is diffusive and shows a transmissive region at the leading edge before the unaffected upstream state.	52
2.9	The three-layer model describing the physical picture of the thick-thin radiative shock. The upstream state has an initial pressure and radiation flux compared to the optically thick case, which sets these values to zero. This figure was adapted from the work of McClarren <i>et al.</i> [4]	54
3.1	The Omega laser facility at the Laboratory for Laser Energetics taken from the image gallery at lle.rochester.edu.	59
3.2	a) The geometry of the Helios-CR simulations used to design the Omega experiments to measure PI fronts with the zoning, the materials, and the physics model. b) The time dependence of the temperature boundary, which use the results of Davis <i>et al.</i> to determine the rise time and maximum temperature [5, 6].	61

3.3	The calculated values of α , a), and β , b), from the Helios-CR simulations with the electron temperature overlaid to give a more physical reference. These figures show a selection of ionization state transitions with the minimum value of α indicating the location of the PI front. The values of α are well below one suggesting the plasma is photoionizing and the values of β at the locations of minimum α are about one, satisfying the conditions for a PI front.	63
3.4	a) A cartoon of the experiment geometry showing the dimensions and measurement geometry. b) An image of the target used in the experiments showing how this connects to the cartoon in a).	65
3.5	The different diagnostic views of the target for these experiments. a) The view of the target from the time-integrated spectrometer in TIM 1. b) The view of the target from the x-ray framing camera in TIM 2. c) The view of the target from the time-integrated spectrometer in TIM 3. d) The view of the target from the soft x-ray framing camera in TIM 5. e) The view of the target from the soft x-ray framing camera in TIM 6. f) The view of the target from the Dante diagnostic.	69
3.6	a) The laser intensity on the surface of the capsule used in the experiments described here from the VisRad view factor code. b) The spherically symmetric case, modeled with the Omega-60 laser geometry, to approximate a uniformly-irradiated capsule using the VisRad view factor code. c) The polar drive case, modeled with the NIF laser geometry, to show a cylindrically symmetric irradiation pattern using the VisRad view factor code. d) The laser intensity pattern used in the capsule implosions from the work of Hansen <i>et al.</i> [7].	71
3.7	a) X-ray emission, > 2 keV, from the stagnated implosion at 1.25 ns after the start of the laser pulses. The image is saturated, but will provide an upper bound of about $125 \mu\text{m}$ for the emitting source size. The red curve is the 50% contour from the maximum pixel value. b) Soft x-ray emission, < 700 eV, from the capsule near stagnation at 0.9 ns from the start of the laser pulses. This image similarly suffers from saturation and provides an upper bound on the soft x-ray emission. The stalk is visible to the bottom right of the image. The red curve is the 50% contour from the highest pixel value.	73
3.8	The mass density from Helios-CR simulations that varied the incident laser power over the range present in the laser irradiation pattern with the 8.52 TW the average over the capsule.	74
3.9	a) A comparison of the spectra recorded on two different spectrometers during the same shot. b) The raw image plate data showing the spectral fiducial from the Saran filter and the line emission from the Ar and S contamination in the capsule target and glue.	76

3.10	a) The simulated net flux out of the surface that is half the maximum density at each time step for the laser power range on the capsule with 8.52 TW the average over the whole capsule. b) The Dante unfold of the capsule implosion. This figure has a shifted time axis so that the peak emission is at 1.25 ns to match the x-ray framing camera results. This is reasonable because the timing of the Dante measurement is not connected to the laser timing. The small signal that occurs before 0 ns is likely the result of inaccuracies in the alignment of the Dante channels in time.	78
3.11	The dashed curve is the channel 11 Dante data, which spans 2-5 keV, deconvolved with a 160 ps width Gaussian to account for the diode temporal response. The dot-dash curve is a Gaussian fit to the Dante data, which has a FWHM of 200 ps. The solid curve is the flux calculated at half of the maximum density at each time step using the capsule-average laser power, which has a width of 50 ps.	79
3.12	The analyzed data from the Dante diagnostic with the dedicated target to observe the emission from the rear surface of the Au foil.	81
3.13	a) The calculated emission spectra along a ray propagated through the profiles from the Helios-CR simulations and integrated over 400 ps centered around the implosion stagnation time. b) The estimated absorption spectrum, using the calculated spectrum in a) integrated over the duration of the simulation.	83
3.14	The capsule emission spectrum measured through the gas cell. The signal cuts off below about 3.4 keV due to the aperture on the target limiting the angular divergence of the capsule emission.	85
4.1	The Z-Machine at Sandia National Laboratories.	88
4.2	a) The general setup for the experiment on Z showing the radial flux from the pinch driving a PI front into a N gas cell with a fiber to couple the self-emission to a streaked, visible spectrometer. b) The geometry used in the HELIOS-CR simulations and the physics models used to describe the mylar front window and the N gas.	89
4.3	The time evolution of the input flux file about the peak emission time of 100 ns.	93

4.4	The values of α and β calculated from the HELIOS-CR simulations while varying the pressure of the N gas. Here, there are only a subset of ionization states shown because preheat affects the NI→NII front and the states above NVI are not desirable for making a measurement. a)-c) and g)-i) show that increasing the pressure reduces the velocity of the front, but does not affect the magnitude of α significantly. The values of β in d)-f) and j)-l) show the same spatial behavior but a gradual decrease in the β value for the NV→NVI transition as the pressure increases while the value increases slightly for the other transitions shown. This suggests that the photoionization rate changes similarly to the recombination rate with increasing particle density, but the electron collisional ionization rate grows more slowly for the NV→NVI transition and faster for the other transitions shown.	94
4.5	These values of α with mylar window thickness of 1.44 μm , 2.16 μm , and 2.88 μm at three different pressures (a)-c) 0.5 atm, d)-f) 0.75 atm, and g)-i) 1.5 atm) show a reduction in velocity when increasing either parameter. All three pressures show slightly lower values of α with increased window thickness, which is likely due to the radiation having to travel through less material to get to the front, reducing the amount of absorption.	95
4.6	The values of β with mylar window thicknesses of 1.44 μm , 2.16 μm , and 2.88 μm at three different pressures (a)-c) 0.5 atm, d)-f) 0.75 atm, and g)-i) 1.5 atm). These figures show β stays relatively constant at the location of the front, but the downstream behavior is more complicated. The downstream values of β decrease with increasing window thickness with a spike, likely due to the shock propagating into the N from the released window material, that can break this trend.	96
4.7	The comparisons, at 100 ns, between plasma parameter values when increasing the resolution from the nominal 100 zones of N show minimal deviation in a) and b) with 200 and 400 zones respectively. However, there are lower electron temperatures of about 5% in the downstream region in c) and d) with 800 and 1000 zones respectively. There is also an increase in upstream electron temperature in d), but this is less than 5% from the nominal model. The large deviation below 0.2 cm are due to the mylar window and are not of concern to the propagation of a PI front.	101

4.8	The comparison of variations in the atomic model to the nominal model, which only excludes autoionizing states, show minimal differences in the plasma parameters and radiation temperature for models with maximum principal quantum number larger than 6 in a)-c). When the maximum principal quantum number is between 3 and 5 in d)-f) there is a decrease of electron temperature in the downstream with small decreases in the mean charge and electron density, then there are increases of these values compared to the nominal model in the upstream. All of these deviations are limited to within 15%. When the maximum principal quantum number is 2 in g) the behavior flips with a relative increase in the plasma parameters in the downstream and a decrease in the upstream with maximum deviations of 20%. The more sophisticated atomic models in h) and i) show less than 10% deviations from the nominal model with increases in plasma parameters in the downstream material and decreases in the upstream.	103
4.9	The comparison between the nominal 5 angle radiation transport calculations and a 2 angle calculation in a) show minimal differences below 5%. The single angle calculations in b) show very large decreases in the plasma parameters in the upstream material compared to the nominal model.	104
4.10	The attenuation of the input flux at the peak emission time using the iterative process described in the text for the first and second iterations.	106
4.11	The calculated values of α and β using the second iteration of the attenuated input file, which shows that this source is sufficient to produce a PI front. a) This shows a slowed front velocity, similar to the effects of increased density and window thickness, but it also shows an order of magnitude decrease in the value of α , which is a result of the reduced radiation flux. b) This shows increased values of β compared to the simulations without consideration of the geometric flux losses in the upstream and downstream material.	107
4.12	Calculations using SPECT3D use the HELIOS-CR results to estimate the expected signal of a one meter streaked, optical spectrometer. Both a) and b), which show the spectra calculations using the nominal model with the input flux file and the second iteration of the geometric attenuation respectively, display line emission early in time and as the plasma heats the thermal emission becomes the dominant signal. Figures c and d show the evolution of the line emission early in time with the nominal and attenuated input flux. These figures have two primary results, one is that there are not significant differences in line structure between the two different sources and the second is the transition from significant NII to NIII populations in the plasma.	109

5.1	The National Ignition Facility at Lawrence Livermore National Laboratory taken from the laser.llnl.gov/media website	114
5.2	A depiction of the geometry in x-ray scattering that shows the scattering vector \mathbf{k} , which determines the electron density modulation scale length, and the screening length in the plasma. To the right there are some useful relations regarding x-ray Thomson scattering, such as the scattering parameter, α , and the doppler broadening contribution to the Compton shift, which introduces the temperature dependence in non-collective scattering.	116
5.3	MCSS calculations that demonstrate the effect of changing temperature on the scattering spectrum. These three synthetic spectra have the same input parameters except for the listed differences in electron temperature and the scaling of the spectra makes the inelastic peak equal to one. It is clear that larger electron temperatures lead to increased broadening of the inelastic scattering peak due to the Doppler effect.	116
5.4	A cartoon of the target physics package, which shows the hohlraum, solid plastic, and CH foam regions.	118
5.5	The CAD model from the July shot day showing the scattering and probe shields to provide an image to go along with the description in the text.	119
5.6	The CAD model from the February shot day pointing out the scattering and probe shields to indicate where the changes are in the second iteration of shielding.	121
5.7	The drive laser pulse shape showing the power for each of the sixty beams.	123
5.8	The probe x-ray pulse shape showing the power for each of the eight beams.	124
5.9	The physics package with labels indicating the shock propagation direction and the relative locations of the self-emission measurement to the XRTS measurement.	125
5.10	a) The SOP camera data with a six pixel average over the time and space axes with labels to indicate the location of the Ta shield and the line out in c). b) The combined shock location data from all three cameras as well as the power law fit to the trajectory. The right axis shows the calculated velocity, which is the derivative of the power law fit, and provides an average velocity in the measurement window of $130 \mu\text{m ns}^{-1}$. c) A line out from a) that shows the presence of upstream heating due to the shock, which indicates this is a radiative shock.	127

5.11	The decay parameter from fitting the upstream heating in the SOP data. Other than one outlier, this indicates that the upstream has an electron heating length scale of about 1 mm, which should correspond to a similar value for the photon mean free path, and indicates that there is a significant amount of radiation that can escape through the end of the shock tube.	128
5.12	a) The final state compression from the thick-thin radiative shock model as a function of the upstream ionization with a dashed line indicating the value used in the analysis. b) The final state temperature from the thick-thin radiative shock model as a function of upstream ionization with a dashed line showing the value used in the analysis.	129
5.13	The scaling of the emission in the bandwidth of the SOP optical path under the assumption of a Planckian emitter. This suggests that the response is linear with temperature and that a mapping is possible if one has a measured value for the temperature in one pixel.	131
5.14	a) The SOP camera data with the temperature mapping from the thick-thin model analysis. This shows a peak post-shock temperature of about 60 eV. b) The line out at 25 ns shown in Figure 5.10 c scaled to temperature. c) The post-shock temperature as a function of time in the measurement window with a power law fit to the data and the calculated derivative from the fit. This shows that the time derivative is decreasing with time.	133
5.15	a) The top down view of the scattering geometry, which shows the 113° scattering angle and the shielding. b) The view from the MACS crystal of the actual target, indicating the scattering window dimensions and the shock propagation direction.	134
5.16	a) The raw MACS data showing the Au L-shell lines that dominate the signal and the strip timing for the camera. The vertical offset of the line data suggests that these features originate at the hohlraum. b) A spatially integrated spectrum from strip 1 at 17.3 ns showing the lines have no redshifted portion of the spectrum, which would indicate scattering signal.	134
5.17	a) The SOP data from the February shot day showing a very fast feature that does not make sense for the physics in the experiment. If this is a shock, its average velocity would be about $350 \mu\text{m ns}^{-1}$ with the same drive energy for the lasers. b) A line out at 16 ns showing the absence of a precursor, which is not consistent with the large average velocity, further suggesting that this signal is not the shock propagating in the foam.	136

5.18	a) The raw XRTS data from the MACS for the February shot day that shows the reduced signal from the Au L-shell lines from the July shot day and the presence of inelastic scattering in the center of the strips. b) The spatially averaged data from strip 1 clearly showing the inelastic scattering feature extending to about 8.2 keV. c) A comparison of the data between strip one and strip two after the background subtraction described in the text. The second strip (in red) clearly has a narrower inelastic scattering feature, which indicates that the volume averaged temperature is lower later in time after the shock has cooled and the entrained flow moves into the scattering window.	137
5.19	a) A comparison of the scattering data at 18.3 ns with MCSS calculations indicating a volume-averaged, electron temperature of around 80 eV. b) The same as in a), but for the scattering data at 20.5 ns, which indicates a volume-averaged, electron temperature of around 40 eV. This is in reasonable agreement with the 49 eV final state temperature from the analysis of the self-emission data in the July shot.	138
A.1	a) The synthetic Dante data using Planckian input at each time step. b) The synthetic Dante data using a Planckian with a constant Gaussian component. The channels show larger values than with only a Planckian component input. c) The synthetic Dante date with a Planckian plus a random Gaussian component. The randomness of Gaussian component introduces fluctuations in time that appear as “noisy” signal on the channel output.	146
A.2	a) The unfold output from Planckian input compared to the temperature profile values and the brightness temperature. The brightness and profile temperatures are the same for this case as the spectrum is Planckian b) The unfold output with a Planckian plus a constant Gaussian as input compared to the brightness temperature and the Planckian temperature. This shows that the brightness temperature is larger than the Planckian temperature, as one would expect, and the Dante unfold temperature is larger than the Brightness temperature. c) The unfold output with a Planckian plus a random Gaussian as input compared to the brightness temperature and the Planckian temperature. The signal is noisy due to the random nature of the Gaussian component, but the three temperatures follow the same trends as the other two cases.	146

- A.3 a) A comparison between the ratios of the Planckian, brightness, and Dante temperatures with a Planckian input. This shows that the unfolded temperature is no more than 17% greater than the input Planckian temperature. b) A comparison between the ratios of the Planckian, brightness, and Dante unfolded temperatures with a Planckian plus a constant Gaussian as input. This shows under about 20% difference between the unfolded temperature and the Planckian temperature, then it shows a less than 10% difference between the unfolded temperature and the brightness temperature. c) The comparison of the temperature ratios for a Planckian plus a random Gaussian as input, which shows the same trends as the constant Gaussian case, but with significant noise due to the randomness of the Gaussian component. The scale of this figure is larger than figures a and b. 147

LIST OF TABLES

Table

3.1	The diagnostic configuration on the Omega laser facility for the experiments to measure PI fronts.	68
C.1	The diagnostic configuration from the high drive shot during the July 2019 NIF shot day.	184
C.2	The diagnostic configuration for the low drive shot during the July 2019 NIF shot day.	185
D.1	The diagnostic configuration for the first high drive shot during the February NIF shot day.	186
D.2	The diagnostic configuration for the second high drive shot during the February NIF shot day.	187
D.3	The diagnostic configuration for the low drive shot during the February NIF shot day.	187

LIST OF APPENDICES

Appendix

A. Dante Analysis Technique 145

B. September 11th 2018 Omega Shot Day SRFs 149

C. July 17th 2019 NIF Shot Day 184

D. February 10th 2020 NIF Shot Day 186

LIST OF ABBREVIATIONS

HEDP	High-energy-density physics
ICF	Inertial confinement fusion
D	Deuterium
T	Tritium
EOS	Equations of state
PI	Photoionization
SN	Supernova
CSM	Circumstellar medium
IGM	Intergalactic medium
NIF	National Ignition Facility
LTE	Local thermodynamic equilibrium
TIM	Ten inch manipulator
DCA	Detailed configuration accounting
TCC	Target chamber center
ADP	Ammonium dihydrogen phosphate
XRFC	X-ray framing camera
MCP	Microchannel plate
PFM	Pulse forming module
IP	Image plate
FWHM	Full-width half-maximum

NLTE Non-local thermodynamic equilibrium
ZAPP Z astrophysical properties platform
CR Collisional radiative
XRTS X-ray Thomson scattering
MACS Mono-angle crystal spectrometer
HOPG Highly oriented pyrolytic graphite
CCD Charge coupled device
VISAR Velocity interferometry system from any reflector
SOP Streaked optical pyrometry
ND Neutral density
MCSS Multi-component scattering simulation
W Tungsten

ABSTRACT

This thesis presents the design of three radiation hydrodynamics experiments at the largest high-energy-density-physics facilities in the United States. Two of these experiments explore the first measurements of photoionization fronts, in the laboratory on two independent facilities. The third is a radiative shock experiment at the National Ignition Facility, which is novel in its use of temperature measurements of shocks in foam targets. The results also use a novel analysis of streaked self-emission data and x-ray Thomson scattering measurements to understand the post-shock electron temperature.

The design and execution of a photoionization front experiment at the Omega laser facility resulted in the characterization of a platform to perform measurements of photoionization fronts using absorption spectroscopy as the primary diagnostic. These experiments use laser to produce ionizing radiation that drives a photoionization front into a gas cell that contains a mixture of nitrogen with argon as a spectroscopic dopant. The data allows for a characterization of the flux emitted from the rear surface of the gold drive source, the capsule implosion backlighter, and the geometry of the absorption measurement. An analysis of the capsule implosions introduces a new metric for comparing the implosion performance based on the initial laser irradiation pattern.

A computational study to design a photoionization front experiment at the Z-Machine provides a complementary experiment to those at Omega also using nitro-

gen gas but utilizing optical emission spectroscopy as the primary diagnostic. This design provides a comparison between the laser-driven foil source on Omega and the wire array z-pinch source to produce a photoionization front. The simulation study explores the parameter space for the experiment, suggests experimental conditions that should create a photoionization front and varies the physics detail in the model to validate the approximations used in the design. Estimates of the streaked visible spectroscopy show evolution of the line structure as the front passes the diagnostic viewing window before continuum emission dominates the signal.

Radiative shock experiments at the National Ignition Facility use a hohlraum to launch a shock into 20 mg cm^{-2} plastic foam. These experiments use x-ray Thomson scattering and streaked, self-emission measurements to observe the shock velocity and electron temperature as a function of time. The analysis of the self-emission data uses the thick-thin model of a radiative shock to extract the temperature using the measured velocity and making some assumptions about the upstream conditions. The scattering measurements largely agree with the self-emission results providing further confidence in the analysis.

The work presented in this thesis introduces and characterizes a new experimental design for the Omega laser facility to measure photoionization fronts in the laboratory, which has never been done before. An additional design for a new photoionization front experiment on the Z-machine shows that a complementary experiment is possible on this facility. The differences between the velocity of a photoionization front and Marshak-like waves are explored in greater detail and an analysis of the curvature of each type of heat front shows this could be a measurable feature to distinguish a photoionization front from a Marshak wave. Finally, radiative shock experiments on the National Ignition Facility use x-ray Thomson scattering and self-emission data with a novel data analysis technique to make multiple electron temperature measurements for the first time.

CHAPTER I

Introduction

1.1 High-Energy-Density-Physics

High-energy-density-physics (HEDP) is typically defined as the science of matter at pressures greater than one million atmospheres[1]. These types of conditions can also lead to very high temperatures, typically from thousands to tens of million Kelvin. To put these numbers in perspective, the pressure of a full-grown elephant sitting on a human's chest is about two atmospheres, which surprisingly one should survive fairly easily if the elephant sits slowly, and the temperature of a hot stove is about 530 Kelvin. These HEDP systems are in very extreme conditions and are commonly in a plasma state. However, at the same time, they are able to exist in a wide range of physics regimes, from low density, hot plasmas to dense, strongly-coupled and electron degenerate plasmas as well as everywhere in between, as seen in Figure 1.1. This makes these systems quite complicated and interesting to study because they require considerations of many different areas of physics including electrodynamics, quantum mechanics, fluid mechanics, thermodynamics, and the list goes on.

It is very rare to directly interact with HED objects in everyday life, but HED conditions exist throughout the universe, including the interiors of massive planets [8]. There are many examples of astrophysical objects that are in HED conditions. For example, the interiors of stars, supernovae, supernova remnants, black hole accretion

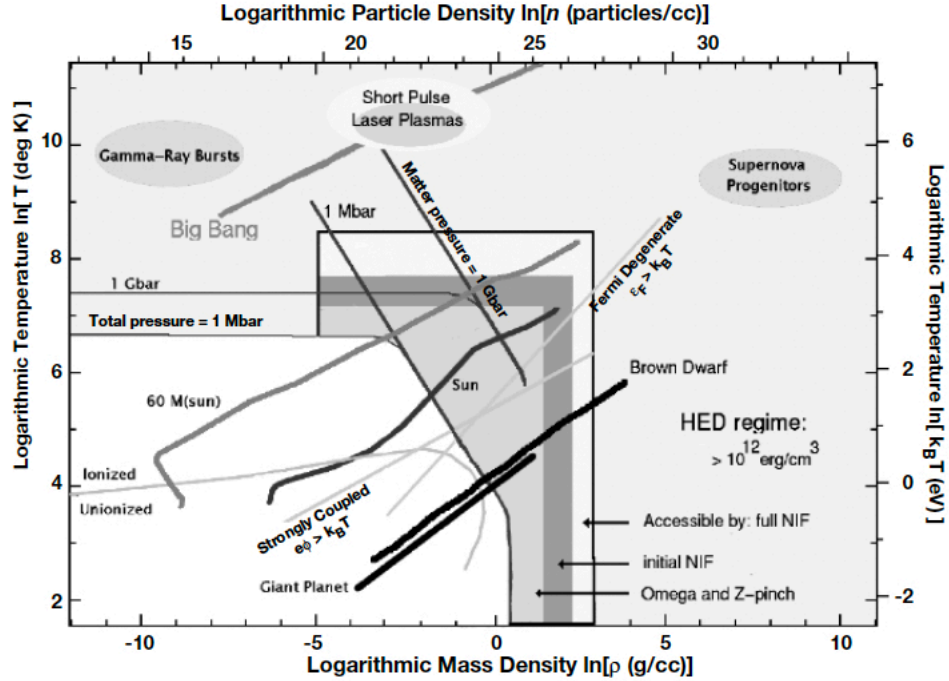


Fig. 1.1. Regimes of high-energy-density physics. Adapted from the NRC Report: *High Energy Density Physics: The X-Games of Contemporary Science*

Figure 1.1: A parameter space plot that shows the boundary of the HEDP regime and where different physics are relevant in HEDP conditions. This image was taken from Chapter 1 of Reference 1[1].

disks, white dwarf stars, neutron stars, gas giant planets, and the cores of rocky planets[9, 10, 11, 12, 13, 14]. There are also efforts to create these conditions in the laboratory as a way to harness nuclear fusion energy in inertial confinement fusion (ICF) schemes[15, 16, 17, 18, 19]. These ICF approaches to fusion energy use some mechanism, typically lasers or current, to compress a shell of material that confines heavy isotopes of hydrogen, deuterium (D) and tritium (T), to heat and confine the DT fuel, creating a runaway fusion reaction that releases more energy as neutrons than the input energy. There are many approaches to ICF and increasing the amount of DT fuel that burns to a point of ignition is an active area of research in HEDP. This thesis will not present ICF in any further detail, but it is perhaps the most visible research effort in HEDP and required mentioning.

HED spans many different research areas, including material science, nuclear

physics, hydrodynamic instabilities, magnetized plasmas, and radiation hydrodynamics. The experiments to study these sub-disciplines use shock and ramp compression to study the equations of state (EOS) of different materials, radiative heating to study opacity, and proton radiography to study magnetic field generation in plasmas[10, 11, 12, 20, 21, 22]. These experiments use lasers or current to drive compression, produce radiation sources, probe sources, and magnetic fields[5, 6, 21, 22, 23, 24, 25]. Focusing on the radiation hydrodynamics experiments, there are two main categories of experiments that explore the effects of radiation plasmas. The first is where the radiation field develops in the plasma due to interacting flows or shocks, and the second uses an external radiation source to influence the gas or plasma where the physics of interest takes place. The first type appears in radiative shock and in flows that are radiatively cooling[9, 26]. The second type of experiment is typical of heat front experiments where the external radiation source can be a laser-driven hohlraum or foil, or a z-pinch[10, 27, 28, 29, 30, 31, 32, 33, 34]. These experiments use a wide variety of diagnostics to measure the temperature and density profiles of these plasmas with significant radiation effects, as well as the flow parameters.

The objects of interest here are all astrophysically motivated and rely on the large temperatures possible in HEDP systems, such that radiation is significant in their evolution. These systems include the x-rays from young stars heating the surrounding gas, the x-rays from the first stars and galaxies in the universe heating the intergalactic medium, and shocks from supernovae sufficiently heating the compressed, stellar plasma that it begins to emit x-rays that affect the circumstellar material. When there is significant radiation in the plasma, it is necessary to use the radiation hydrodynamics equations to describe the system and this is where one can find observables to measure in an experiment. The radiation can enter the equations in two ways, through the radiation energy flux or the radiation pressure and energy density. The former affects the energy conservation in the system, while the later has contributions

in the energy and momentum conservation equations[35, 36]. Marshak was the first to derive the Rankine-Hugoniot jump conditions for the radiation hydrodynamics equations in 1958 and went on to evaluate supersonic heat front problems considering only the radiation energy flux in the fluid[37]. About five years later, Zel'Dovich and Raizer expanded that understanding to the structure of radiative acoustic waves and shocks with a focus on optically thick media[35]. They also, briefly, considered the effects of the radiation energy density and pressure on the structure of radiative shocks[35]. In the mid 1980s Mihalas and Weibel-Mihalas further developed the knowledge of radiation hydrodynamics by deriving the relativistically consistent set of equations. They then went on to explore non-relativistic, radiating flows including steady and propagating radiative shocks, including systems with an optically thin upstream and ionization fronts[36]. Mihalas and Weibel-Mihalas cover applications that include the radiation energy density and radiation pressure, but they do not explore any relativistic, radiating plasmas. This is a clear next step in the history of radiation hydrodynamics, but since none of the work in this thesis is relativistic, the discussion of this history will stop here.

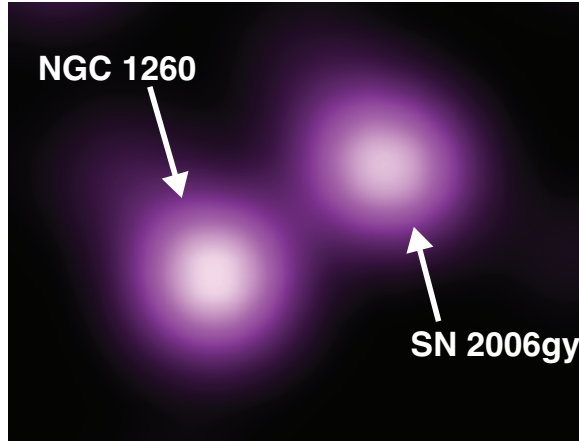


Figure 1.2: The x-ray emission from the super-luminous supernova SN2006gy, which shows that it is comparable in brightness and size to the galactic core of the progenitor host galaxy. Supernovae and their remnants produce radiative shocks and can drive photoionization fronts in the surrounding gas, which this work tries to replicate in the laboratory. This image was adapted from NASA/CXC M.Weiss; X-ray: NASA/CXC/UC Berkeley/N.Smith et al.; IR: Lick/UC Berkeley/J.Bloom & C.Hansen.

1.2 Radiation Hydrodynamics in Astrophysics and Cosmology

The specific objects this thesis will explore are photoionization (PI) fronts and radiative shocks. Chapter II will give detailed descriptions of the physics of these objects.

1.2.1 Photoionization Fronts

In present-day astrophysics, radiation from the forward shock of supernovae (SN) heats the relatively stationary, circumstellar medium (CSM) through photoionization (PI) fronts[38, 39, 40, 41, 42, 43]. Specifically, type IIn SN have narrow lines in their observed spectra that correspond to the recombination of the photoionized CSM[38], but a variety of other SN show interactions with the CSM during their evolution, such as type IIP, super-luminous SN, and type Ia-CSM SN[42, 44, 45, 46, 47, 48]. Figure 1.2 shows an x-ray image of a super-luminous SN that is about the same brightness and

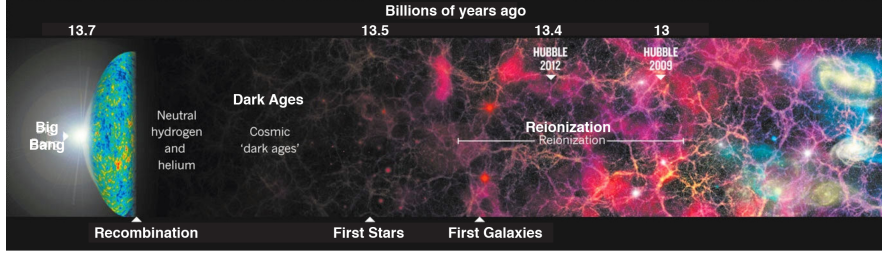


Figure 1.3: The timeline of the universe’s evolution with a particular focus on the age of reionization, which is relevant to the physics of PI fronts. This image was taken from the work of Robertson *et al.*[2].

size as the galactic core of the galaxy that hosted the progenitor star. The ionization states present in these narrow lines are higher than one would expect from ionization due to electron collisions, which indicates photoionization is the mechanism behind this heating. There are few places in the SN literature that discuss the physics occurring in the photoionizing CSM[38, 42], let alone discuss the properties of the resulting heat front. This is likely due to insufficient angular resolution in the current observatories to discern this behavior and the need to understand the wind structure for each SN discovered[44].

In the setting of early universe cosmology, the first galaxies produced very large, zero-age main sequence stars having masses greater than $100M_{\odot}$, where M_{\odot} is the mass of the sun. These massive stars ionized the surrounding nebula and are thought to have led to the reionization of the intergalactic medium (IGM) through photoionization fronts[2, 49, 50]. Knowledge of the fraction of ionizing radiation that escapes these galaxies is important for determining the cause of reionization at the end of the cosmic dark ages[2], but current, space-based measurement techniques can have large uncertainties [51], which provides a role for laboratory experiments. Figure 1.3 shows the evolution of the universe from the big bang to the current epoch. The region of Figure 1.3 that is most relevant to this work is from about 13.5 to 13 billion years ago during the age of reionization.

The typical method for identifying high redshift galaxies involves observing changes

in emission across images using different filtration in the infrared called the Lyman or Balmer break technique, depending on the energy range of the filters[2, 52]. This measurement exploits the change in the escaping galactic emission across the K or L edge in H for the Lyman and Balmer break galaxies respectively. Lyman-break galaxies have more active star formation and Balmer-break galaxies are less actively forming stars[52, 53, 54, 55]. However, the redshifted line and continuum emission from the heated nebula can affect the magnitude of this change in signal across the filtered images, which changes the model fits, significantly, and the stellar ages[52, 53, 54, 55]. Specifically, the inferred ages of these galaxies depend on the inclusion of the nebular emission in the model fitting[52, 53, 54, 55]. Measurements of high redshift galaxies are difficult due to the limited number of photons that arrive at earth from these distant galaxies. This also makes spectroscopic measurements very difficult and means the emission spectra used to fit the observational data are exclusively dependent on models. The difficulty of making highly precise measurements of these early galaxies suggests that laboratory experiments can play a useful role in understanding their evolution, in which PI fronts play a role.

There has been much work to understand the theory of PI fronts starting in the 1930s with the work of Strömgren[56]. Following this, the work of Kahn explores the effects of varying intensity of the driving source and develops the theory of the subsonic and supersonic cases for PI fronts[57]. This also introduces the idea of the M-type front which develops a shock when the radiation is not strong enough to drive a supersonic front but is still larger than the critical value for a subsonic front. Goldsworthy further explored self-similar solutions to the PI front problem in cylindrical and spherical geometries with details about the different types of fronts, which the next chapter will explain in more detail, and Axford published a follow-up paper providing additional computational results plus some mathematical properties of the equations in this problem[58, 59, 60]. Mihalas and Weibel-Mihalas provide

an overview of the physics of the problem and the resulting structure for the different types of fronts in their book on radiation hydrodynamics[36]. The next major advance, relevant to the work presented here, are the papers of Drake *et al.* and Gray *et al.*[61, 62, 63]. These papers describe the design of experiments to observe PI fronts in the laboratory using purely analytic techniques, the CRASH radiation hydrodynamics code, and the Helios-CR radiation hydrodynamics code[64, 65].

There have been numerous HEDP experiments that explore heat fronts with many different energy sources to drive the experiments and resulting x-ray sources to support the front[27, 28, 29, 30, 31, 66]. These experiments vary from investigating diffusive, radiative heating to a more optically thin environment where the diffusive approximation does not hold as well. However, to the Author’s knowledge, all previous heat front experiments have had non-negligible electron heating and therefore did not produce PI fronts[61].

This thesis introduces experiments to specifically measure PI fronts and demonstrates, through the use of simulation tools, that photoionization dominates the energy deposition at the heat front. Simple physics models and arguments introduce observables for PI fronts that can be diagnosable features in an experiment to prove the existence of a PI front. Additionally, this thesis presents the development of an experimental platform for the Omega laser facility as well as a design study for an experiment on the Z-Machine, which will provide independent measurements of the same physics at different conditions and using different diagnostics.

1.2.2 Radiative Shocks

Radiative shocks are a fundamental problem in radiation hydrodynamics and they are prevalent throughout astrophysics. The forward shock in a supernova, while it is inside the star, as well as the ejecta-driven shock in supernova remnants can be radiative[9, 38]. Thermonuclear explosions or the collapse of an iron core drive the

shock inside the star, while the ejected material from the supernova explosion impacts the circumstellar material, which drives the shock in the supernova remnant[9, 38]. There is also the possibility of a radiative shock in the accretion column onto a star or compact object[36]. This occurs when the material from an accretion disk is able to transport away its angular momentum and can fall onto the compact object or star. The interaction of the infalling material with the atmosphere of the compact object or star produces the shock, which has the potential to be radiative[36].

Section 1.1 has a brief overview of the history of radiation hydrodynamics and radiative shocks, which follows the development of radiative shocks fairly well. The work of Zel'Dovich and Raizer develops the structure of radiative shocks for the case where only radiation energy flux influences the hydrodynamics, for an optically thick medium[35]. Mihalas and Weibel-Mihalas then extended this work to include the effects of optically thin upstream materials and goes into detail on the effects of radiation energy density and pressure[36]. Both of these developments of radiative shock physics describe, in detail, the effects of strong radiation on shock structure, where they discuss the ability of radiation to smooth out the typical discontinuous jump in density and temperature across a shock until it is a continuous transition, when radiation energy density and pressure dominate the dynamics[35, 36]. This happens even without the considering viscous effects and electron heat transport that can create a continuous shock transition in hydrodynamic systems[35, 36]. Bouquet *et al.* developed the theory with the total energy density and pressure to analytically solve for the shock structure under local thermodynamic equilibrium (LTE) conditions relevant to astrophysical phenomena[67]. The theory continued to develop through work at the Omega laser facility and the LULI laser in France[4, 68, 69, 70, 71, 72]. This work considered the four different combinations of the optical depth in the upstream and downstream regions with a focus on the optically thick radiative shock and the case with an optically thick downstream and an optically thin upstream that

are most achievable in laboratory experiments[4, 70]. The work at LULI proceeded in parallel to the Omega experiments and developed an analytic approach to finding the temperature of laboratory radiative shock measurements[71, 72, 73]. These later advances in the theory of radiative shocks are the result of interpreting and analyzing the data from experiments at laser and pulsed-power facilities, which the following paragraphs describe.

Some early laser-driven radiative shock experiments set out to measure the upstream heating due to the radiative precursor that the emission from the shock front supports[74, 75]. These experiments used SiO₂ foam on the Omega laser facility and Xe gas at the LULI laser in France. The Omega experiments used absorption spectroscopy to observe the increasing ionization states due to the radiative heating of the upstream material and the LULI experiments use interferometry to observe the increase in electron density due to the precursor heating the upstream material. Both then compare the experimental results with the output from available radiation hydrodynamics codes.

Further radiative shock experiments at the Omega laser facility have made measurements in Xe and Ar using a variety of different diagnostics, with x-ray radiography being the primary observation tool[76, 77, 78, 79, 80]. The general geometry of these experiments used a Be disk coupled to a polyimide shock tube that is gas tight to allow for a nominally one dimensional, planar system. The first result of these experiments was the observation of radiative collapse in the cooling layer of a radiative shock in Xe gas where post-shock compression was much larger than the limit of four in monatomic ideal gases[76, 81, 82]. These experiments exploit the high atomic weight of Xe, which causes increased radiative effects compared to those seen in shocks involving lower-atomic-weight nuclei at the same conditions. This work continued with more detailed analysis of the shock layer thickness to better understand the magnitude of the radiative collapse by measuring the angle of the shock front relative to

the axis of the experimental platform, which used statistical methods to extract the true compression from the collected data[83]. Doss *et al.* explored the interaction of the radiative shock with the walls of the shock tubes to determine the behavior of oblique radiative shocks and to develop the structure of the interaction region as a diagnostic for the shock Mach number[84, 85]. There is another push in the work at the Omega laser to understand repeatability and perform uncertainty quantification of these radiative shock experiments to provide a best comparison for benchmarking the results of the CRASH radiation hydrodynamics code[79, 86]. There were additional experiments that used Ar with x-ray Thomson scattering to measure the electron temperature of the radiative shock, to understand the early time evolution of radiative shocks, and experiments to observe radiative reverse shocks to that mimic accretion flows onto stars[77, 82, 87, 88, 89].

The experiments at the LULI laser have happened in parallel to the Omega experiments in the previous paragraph. These experiments all use Xe in a shock tube setup, but instead of Be the laser irradiates a plastic foil with a buried layer of Ti to prevent x-rays from the laser interacting with the plastic from preheating the gas[71]. The work used interferometry and velocity interferometry to identify the radiative precursor and shock velocity. They also used absolute photon counting measurements to understand the brightness temperature of the shock heated region. This work continued to diagnose the nature of radiative shocks with a gated optical imager to observe the shock front curvature and the precursor, as well as the interferometry and emission measurements of the previous study[72].

There are a variety of experiments conducted at other laser facilities exploring the physics of radiative shocks. Experiments at the GEKKO XII laser used interferometry, streaked shadowgraphy, and streaked self-emission to understand the electron density and the shock velocity in Xe gas with comparisons to one and two dimensional simulation results[90]. Using the PALS laser system in the Czech Republic, Busquet

et al. used interferometry and the absorption of a probe laser to understand the extent of the precursor from radiative shocks in Xe gas and compared these results to two and three dimensional simulations with non-diffusive radiation transport to understand the lateral radiation losses and the wall albedo[91]. The work of Hoarty *et al.* using the VULCAN laser system used spatially resolved absorption spectroscopy of the Cl K-shell to observe the temperature and density profiles of a radiative shock in chlorinated triacrylate foam through comparisons with an atomic kinetics code[92]. It is important to note that those experiments directly irradiate the foam propagating medium with the laser rather than using a some kind of solid density piston to shock the foam. Experiments using Xe on the Orion laser observed the interaction of counter-propagating radiative shocks using interferometry and x-ray radiography to observe the electron densities and the features due to the interaction of the shocks and the interaction region[93]. These experiments also compared the measurements with simulations to understand the expected temperatures of the forward shocks as well as the temperature and compression of the reverse shocks that form after the interaction[93]. Additional experiments at the Orion laser created a plasma flow that strikes a solid obstacle to emulate the accretion flow in binary star systems with streaked, self-emission measurements to observe the dynamics of the system and x-ray radiography to visualize the structures formed during the interaction[94]. Experiments at the National Ignition Facility used a hohlraum to drive a radiative shock in SiO₂ foam to observe the effects of the strong radiation field on the development of the Rayleigh-Taylor instability of a perturbed interface with the radiation providing a mitigating effect to the instability growth rate[9, 95]. There have also been radiative shock experiments using pulsed power devices, such as the Z-Machine at Sandia National Laboratories, where Rochau *et al.* measured very fast radiative shocks in CH₂ foam using a wire array implosion to drive the converging shock in the foam, which sits on the pinch axis[96].

The radiative shock experiments presented in this thesis use low density plastic foams with a hohlraum to drive the shock and x-ray Thomson scattering and streaked, self-emission measurements to observe the electron temperature and shock velocity. First, these experiments are one of the few that use x-ray Thomson scattering to make measurements of radiative shocks, with the work of Reigard *et al.* and Visco *et al.* the only other examples the author identified[77, 82]. This is also the first time that a single target has combined x-ray Thomson scattering and streaked, self-emission measurements. The data analysis uses the temperature measurement from the scattering data and compares that with an analytically extracted temperature from the self emission, which is the first radiative shock experiment to make two temperature measurements. Additionally, the self-emission data allowed for a measurement of the time derivative of the shock temperature, which previous work has only deduced from simulation[91].

1.3 HEDP Experiments at Large Facilities

The bridge between HEDP and space-based astrophysics and cosmology measurements is the field of laboratory astrophysics[1]. The work in this field designs experiments, using the experimental infrastructure of HEDP, to capture the physics of a small portion of an astrophysical object or problem. These experiments are often scaled to the astrophysics or cosmology of interest[9, 94, 97], but can also be at the same density and temperature conditions as the objects they imitate[10, 11, 24]. These types of experiments can provide more detail about a system, especially the dynamics, than the space-based observations because of the ability to tune the plasma parameters and initial conditions, which is obviously not possible in astrophysical objects. Laboratory experiments also provide a means for producing repeat measurements with the well-constrained initial conditions that are possible in HEDP.

There are a number of HEDP facilities in the United States and abroad that

are capable of driving these sorts of experiments. Here, the focus will be on the three largest facilities in the United States: The Omega laser facility, The National Ignition Facility (NIF), and The Z-Machine. These are all Department of Energy funded facilities that users can submit proposals for access to experiment time. The chapters that use the facilities will provide more detail about the capabilities of these research tools.

1.4 Organization of This Thesis

The approach taken here is to introduce most everything the reader needs to understand this work in the next chapter, which covers much of the theory that drives the experiments. Then, each of the chapters addressing the experiments or experimental design are fairly self-contained. So, each of those chapters will motivate the experiments, discuss the facility and the primary measurement techniques used, and present the results to give a complete story within the chapter. This should, hopefully, reduce the need to search through the document to understand what is in any one section.

Chapter I provides the context for the thesis and sets the scope of the work within the broader field of HEDP. It provides examples of PI fronts and radiative shocks in astrophysics and cosmology, that still contain open questions where laboratory experiments can assist in furthering the understanding. It follows this with historical perspectives on the development of the theory for PI fronts and radiative shocks as well as the results from laboratory experiments relevant to the topics.

Chapter II introduces the current theoretical understanding of PI fronts and radiative shocks to provide a foundation for analyzing and motivating the experimental approaches and results presented in later chapters. It starts with the derivation of the Euler equations then presents the non-relativistic, semi-classical treatment of radiation in a plasma as a starting point for understanding the radiation hydrodynamics

problems that follow. It then focuses on the theory of heat fronts to introduce the theory of PI fronts as Drake *et al.* and Gray *et al.* derived and distinguish this physics from that of nonlinear diffusion waves, which are commonly studied [61, 62, 63]. It concludes with the development of radiative shock theory in the opacity regimes that are potentially relevant to a laboratory experiment. The author’s original contributions are the further analytical developments of PI front velocity and the distinction between the curvature of PI fronts and Marshak waves as a function of time.

Chapter III shows the results of experiments using the Omega laser facility at the Laboratory for Laser Energetics demonstrating a platform to make measurements of PI fronts. This discusses the results of simulations to design the experiment, the capabilities of the primary measurement, and the outcomes of characterizing the platform. The experiments used absorption spectroscopy as the primary diagnostic and the analysis of the backlighter for that measurement contains excerpts from a recently submitted paper to *Review of Scientific Instruments* titled, “Effectiveness of capsule backlighters with an anisotropic irradiation pattern”. The author’s original contributions to this work include radiation hydrodynamics simulations to design the experiment, modeling of the gas cell target, simulations of the capsule backlighter, running the Omega experiments, and analysis of the experimental data to characterize the platform.

Chapter IV designs an experiment to observe PI fronts using the Z-Machine at Sandia National Laboratory, which would provide a complementary experiment to the ones at Omega. This shows a simulation study and demonstrates that the atomic model used to design the experiment contains sufficient detail for the available computational tool. It also presents estimated measurements using the simulations output. Much of this analysis is taken from a paper submitted to *Physics of Plasmas* titled “The design of a photoionization front experiment using the Z-machine as a driving source and estimated measurements”. The author’s original contributions to this

work include running and post-processing radiation hydrodynamics simulations to design the experiment, running further simulations to validate the physics model approximations, and using a radiation transport code to estimate the streaked visible spectroscopy measurement.

Chapter V presents the experimental results of radiative shock measurements conducted on the National Ignition Facility using x-ray Thomson scattering and streaked, self-emission diagnostics. This shows the target design that was published in *Review of Scientific Instruments* and the analysis of the shock physics showing agreement between the two diagnostics [98]. Kevin Ma provided simulation work that aided in the target design and measurement timing and Tilo Döppner and Mike MacDonald provided support in making the scattering measurement and configuring the laser. These results present novel measurements of radiative shocks and a publication is in preparation to report these findings. The author's original contributions to this work include developing the target shielding, running the experiments at the NIF, analyzing the x-ray Thomson scattering data, and performing a novel analysis of the streaked self-emission data to extract the electron temperature.

Chapter VI summarizes the work presented in this thesis, then discusses the conclusions from the preceding chapters. It concludes with an outlook of the future directions each of these experiments can take and some potential pitfalls or failure modes that one should pay particular attention to when attempting to advance this work.

CHAPTER II

Relevant Theory for these Experiments

The previous chapter described the astrophysics and cosmology motivations for studying radiation hydrodynamic systems. It also presented the historical development of the theory and experiments relating to PI fronts and radiative shocks. This chapter will introduce the theory of these objects in a quantitative way, such that it can assist in the development and analysis of the experiments presented below. The derivations will start by developing the Euler equations and the radiation transport equation followed by the radiation hydrodynamics equations, which describe the physics of fluids with significant contributions from a radiation field. Following this, a description of the physics of radiation-driven heat fronts indicated the difference between nonlinear diffusion waves and PI fronts with suggested observables that can distinguish between the two. Finally, the theory of radiative shocks, as it pertains to experimental studies, shows the results that are useful in connected measurable quantities to the shock structure. This treatment will limit the results to the non-relativistic regime, as that matches the physics of the experimental work.

2.1 Hydrodynamics

In many nanosecond timescale HEDP problems, it is reasonable to use a fluid approximation, at least to describe the bulk behavior. This is clearly not the case

in short-pulse laser experiments or work that focuses on interactions of lasers with matter. However, for all of the problems discussed here, it is reasonable to consider a fluid approximation solution, at least as a first approach for designing an experiment. This section will arrive at the Euler equations describing a continuum approximation to plasma dynamics by deriving an equation governing the evolution of the velocity distribution of an ensemble of particles and taking the velocity moments of that equation assuming a Maxwellian distribution. This will also lay the foundation of the basic shock physics that a later section will expand upon by including the effects of radiation to describe the resulting modifications to the shock structure.

2.1.1 Derivation of the Euler equations

Starting from a general distribution function in a six dimensional position-momentum phase space with an independent time dependence, one can derive the Boltzmann equation. The derivation here will not include any collision or interaction term resulting in a derivation of the Vlasov equation as the details of particle interactions is outside the scope of this work. The distribution function $f = f(\vec{x}, \vec{p}; t)$ represents the velocity distribution as a function of position, momentum, and time within a volume. Displacing this volume leads to a new distribution $f' = f(\vec{x} + \Delta\vec{x}, \vec{p} + \Delta\vec{p}; t + \Delta t)$. This makes $\Delta f = f' - f$ the displacement of the velocity distribution for this collection of plasma particles. The particle species is intentionally not specified because this derivation is the same for any single species plasma. Adding multiple species would result in interaction terms, which are not considered here, as mentioned above. Taylor expanding f' and taking only the first order terms results in the following expression for the displacement,

$$\Delta f = f + \left. \frac{\partial f}{\partial \vec{x}} \right|_{\vec{x}_o} \cdot \Delta\vec{x} + \left. \frac{\partial f}{\partial \vec{p}} \right|_{\vec{p}_o} \cdot \Delta\vec{p} + \left. \frac{\partial f}{\partial t} \right|_{t_o} \Delta t - f, \quad (2.1)$$

where the subscript o represents the initial values of the variables in the non-displaced distribution. The values of f cancel, then dividing by Δt and taking the limit as the displacement goes to zero results in,

$$\frac{df}{dt} = \vec{v} \cdot \nabla_{\vec{x}} f + \vec{F} \cdot \nabla_{\vec{v}} f + \frac{\partial f}{\partial t} = 0, \quad (2.2)$$

where \vec{v} is the velocity, \vec{F} is the force on the particles, and ∇i represents the gradient in the subscript vector space.

To construct the fluid equations out of the Vlasov equation requires taking the velocity moments of equation 2.2 with a Maxwellian velocity distribution, $f(\vec{v}) = \left(\frac{m}{2\pi k_B T}\right)^{3/2} e^{-\frac{m|\vec{v}|^2}{2\pi k_B T}}$ with mass m , Boltzmann constant k_B , and temperature T . In these integrals, the macroscopic quantities of interest such as the density, momentum density, energy density, and pressure are the zeroth, first, second scalar, and second tensor velocity moments of f . The results of these integrals are,

$$\frac{\partial \rho}{\partial t} + \nabla \cdot (\rho \vec{u}) = 0, \quad (2.3a)$$

$$\frac{\partial \rho \vec{u}}{\partial t} + \nabla \cdot \rho \vec{u} \vec{u} = -\nabla p, \quad (2.3b)$$

$$\frac{\partial}{\partial t} \left(\frac{\rho u^2}{2} + \rho \epsilon \right) + \nabla \cdot \left[\rho \vec{u} \left(\epsilon + \frac{u^2}{2} \right) + p \vec{u} \right], \quad (2.3c)$$

where ρ is the material density, \vec{u} is the fluid velocity, ϵ is the specific internal energy density, and p is the pressure. These equations assume an isotropic pressure and no body forces or viscous effects as this is sufficient for the desired outcome of this section.

2.1.2 Hydrodynamic shocks

To evaluate the change in conditions across a shock, it is useful to derive the so called jump conditions. One finds these conditions by integrating across the shock along the direction normal to the shock surface, which results in the time derivative terms reducing to zero, but the flux terms maintain finite values mathematically by the divergence theorem. The physical reason for this is that the change in conditions must converse the fluxes across the boundary, which makes the following equations the mass, momentum, and energy conservation conditions for the formation of a shock[99],

$$\rho_1 u_1 = \rho_2 u_2, \quad (2.4a)$$

$$\rho_1 u_1^2 + p_1 = \rho_2 u_2^2 + p_2, \quad (2.4b)$$

$$\rho_1 u_1 \left(\epsilon_1 + \frac{u_1^2}{2} \right) + p_1 u_1 = \rho_2 u_2 \left(\epsilon_2 + \frac{u_2^2}{2} \right) + p_2 u_2, \quad (2.4c)$$

where the subscripts indicate the upstream (1) and downstream (2) material. The above fluid equations and therefore jump conditions are not a closed system. The fluid equations are five equations in, at least, six variables, so in order to close this system a minimum of one more equation is necessary. These closure equations are called equations of state and these are an active area of research on their own. However, there are some common assumptions used to make analytic work tractable and the polytropic equation of state is probably the most prevalent. This relates the specific internal energy density to the pressure by,

$$\rho \epsilon = \frac{p}{\gamma - 1}, \quad (2.5)$$

where $\gamma = \frac{c_P}{c_V}$ is the polytropic index, c_V is the specific heat at constant volume, and c_P is the specific heat at constant pressure. The polytropic index is a function of the degrees of freedom in a system with γ being approximately $\frac{5}{3}$ in an ideal gas and $\frac{4}{3}$ in a radiation-dominated or ionizing system. In the small amount of space this document dedicates to shock physics, it would be impossible to cover even a fraction of the accumulated work on the subject and clearly this is not a complete treatment of the topic, but it should be enough to motivate the radiation hydrodynamics material below.

The next section will discuss the nature of radiation using a classical description that is applicable to the experiments presented later on. The remainder of this chapter presents the application of this radiation to fluid problems by developing the radiation hydrodynamics equations from the Euler equations and the relevant solutions.

2.2 Radiation transport

2.2.1 Definitions

In plasmas where the radiation field acts to transport significant energy within and out of the system, a mathematical framework is necessary to describe the evolution of this radiation field. Following the derivation in Chandrasekhar[100], the change in radiation energy, in a frequency range $\nu + d\nu$, in a region with solid angle $d\Omega$, with a duration dt , due to an emitter with area dA at an angle θ is,

$$dE_\nu = I_\nu \cos\theta dA d\Omega dt d\nu, \quad (2.6)$$

where dE_ν is the change in energy. The above expression uses a particular direction, θ , for a pencil of radiation, one can generalize this to an arbitrary angular distribution using $\cos\theta dA \rightarrow \hat{n} \cdot d\vec{A}$, where \hat{n} is the unit vector representing the angle of incidence for the radiation field and $d\vec{A}$ is the normal vector describing the infinitesimal area dA .

To calculate the net flux from a surface due to a pencil of radiation, defined as parallel rays of radiation with some spatial extent, one integrates the radiation intensity, in equation 2.6, over the solid angle of the surface through which the radiation passes. This results in the expression,

$$\pi F_\nu = \int I_\nu \cos\theta d\Omega, \quad (2.7)$$

where F_ν is the net flux. Further results require knowledge of the system geometry, an example using spherical symmetry allows for a tractable solution. In a system with spherical symmetry, one can use spherical polar coordinates, which results in $d\Omega = \sin\theta d\theta d\phi$ as the expression for the differential of solid angle and the net flux is then,

$$\pi F_\nu = \int I_\nu(\theta, \phi) \cos\theta \sin\theta d\theta d\phi. \quad (2.8)$$

For an isotropic radiation field, the radiation intensity has no dependence on viewing angle, therefore the integrand is $\cos\theta \sin\theta d\theta d\phi$. Integrating this over the sphere results in 0 net flux, as expected.

Another quantity of interest is the radiation energy density, as this is relevant to the energy balance in the radiation hydrodynamic equations. To calculate this quantity, which is the amount of radiation energy per unit volume local to some point, P , it is necessary to construct an infinitesimal volume, v , bounded by a surface σ . Then, have v exist inside a much larger volume bounded by a surface Σ . Figure 2.1 shows the detail of this geometry. To calculate the radiation emitted from a patch, $d\sigma$, one must consider the solid angle, $d\Omega'$, that Σ can observe from an infinitesimal patch, $d\Sigma$, in the frequency range ν to $\nu + d\nu$. The radiation intensity from $d\sigma$ to $d\Sigma$ is then,

$$Q_{\sigma \rightarrow \Sigma} = I_\nu \cos\Theta d\Sigma d\Omega' d\nu, \quad (2.9)$$

where $Q_{\sigma \rightarrow \Sigma}$ is the radiation energy per second per area, Θ is the incidence angle

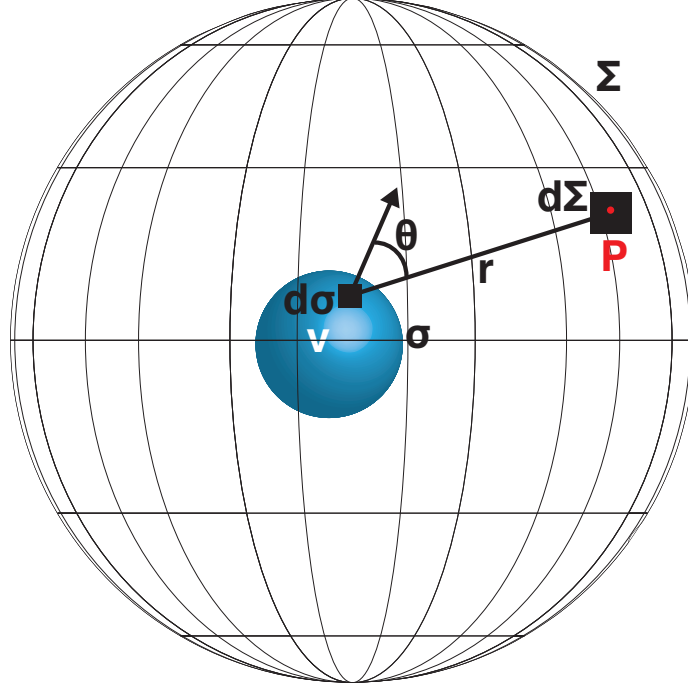


Figure 2.1: This describes the geometry for the radiation energy density calculation showing the volume v where the radiation propagates and the encapsulating surface Σ .

between the radiation and $d\Sigma$. One then writes the solid angle, $d\Omega'$, as $d\Omega' = \frac{\cos\theta d\sigma}{r^2}$, where θ is the viewing angle between $d\Sigma$ and $d\sigma$, and r is the distance between $d\sigma$ and $d\Sigma$. Combining the solid angle with the expression for $Q_{\sigma \rightarrow \Sigma}$,

$$Q_{\sigma \rightarrow \Sigma} = I_\nu \frac{\cos\theta}{r^2} \cos\Theta d\Sigma d\sigma d\nu, \quad (2.10)$$

Taking l as the path length of the radiation through the volume, v , and using c as the speed of light, $\frac{l}{c}$ is the time it takes for radiation to travel through v . One can then multiply equation 2.10 by $\frac{l}{c}$ to get the energy passing through the volume v and using the expressions $d\Omega = \frac{\cos\Theta}{r^2} d\Sigma$ and $dv = l \cos\theta d\sigma$ as the differentials of solid angle for $d\Sigma$ and the intercepted volume provides a simple expression for the energy density in terms of the spectral intensity. Integrating over the solid angle and volume, then

dividing through by the integrated volume gives the radiation energy density,

$$u_\nu = \frac{1}{c} \int d\Omega I_\nu, \quad (2.11)$$

where u_ν is the, frequency-resolved, radiation energy density. One can then integrate over the radiation frequency to get the frequency-averaged radiation energy density,

$$u_R = \frac{1}{c} \int d\Omega \int d\nu I_\nu. \quad (2.12)$$

An additional useful quantity is the average intensity over a sphere, which has the definition,

$$J_\nu = \frac{1}{4\pi} \int d\Omega I_\nu. \quad (2.13)$$

Inserting equation 2.13 into the equation 2.11 provides an expression relating the average intensity to the radiation energy density,

$$u_\nu = \frac{4\pi}{c} J_\nu. \quad (2.14)$$

The above material dealt with the definitions of the radiation field and relevant derived quantities. It is now necessary to characterize the ways the propagating medium can interact with the radiation field. Principally, there are three ways the radiation field interacts with the propagating medium, which are absorption, emission, and scattering. Absorption is when the propagation medium converts of radiation energy of a particular frequency into another form and the specific material opacity, κ_ν , in units $\text{cm}^2 \text{g}^{-1} \text{eV}^{-1}$, describes this interaction. An example of this is photoionization where the medium absorbs one, or more, quanta of radiation energy and converts it to electron kinetic energy. Emission extracts energy from the medium, which it then emits as radiation energy, with spontaneous emission of a photon from an excited

atomic state serving as one example. The emissivity, η_ν , in units $\text{erg s}^{-1} \text{cm}^{-3} \text{sr}^{-1} \text{eV}^{-1}$, describes the emission properties of a medium. Scattering of radiation energy by a medium results in the randomization of the propagation direction according to a process dependent distribution. The scattered radiation can also deposit or extract energy from the medium through inelastic scattering processes. The scattering opacity, $\kappa_{\nu,sc}$, where the *sc* subscript indicates scattering, accounts for the effects of total scattering, elastic and inelastic processes, in analyzing radiation transport problems, any more detail requires knowledge of a specific scattering process or phenomenon.

2.2.2 Derivation of the Transport Equation

The above definitions and derived relations are useful for describing the radiation field. It is now necessary to use the opacity and emissivity, which are material dependent terms, to formulate an equation that captures the evolution of the spectral intensity with the spatial and temporal dynamics of the plasma. Following the treatment in Drake[1], there is some $I_\nu = I_\nu(\vec{x}, t, \hat{n}, \nu)$, where \vec{x} is the position vector for the volume element of plasma, t is the time, \hat{n} is the normal vector parallel to the direction of transport, and ν is the frequency of the radiation. It is also useful to define an infinitesimal path length, ds , to transport the radiation along. This radiation field changes when moving to the next fluid element to $I'_\nu(\vec{x} + ds\hat{n}, t + \frac{ds}{c}, \hat{n}, \nu)$. Taking the difference between the spectral intensities in the two different volume elements and multiplying by the differentials for area, solid angle, and frequency provides the change in energy with time,

$$\Delta I_\nu dAd\Omega d\nu = \left[I'_\nu \left(\vec{x} + ds\hat{n}, t + \frac{ds}{c}, \hat{n}, \nu \right) - I_\nu(\vec{x}, t, \hat{n}, \nu) \right] dAd\Omega d\nu. \quad (2.15)$$

Dividing the expression for ΔI_ν by ds and taking the limit as ds goes to zero is the definition of a derivative and leads to the following left-hand-side of a differential

equation,

$$\left[\frac{d}{ds} + \frac{1}{c} \frac{d}{dt} \right] I_\nu dA d\Omega d\nu ds = \frac{\text{Energy}}{\text{Time}}. \quad (2.16)$$

The right hand side of equation 2.16, is the difference between the emission and absorption over a length s through the plasma, which the emissivity and opacity, defined above, describe. The right-hand-side of equation 2.16, is then,

$$\left[\frac{d}{ds} + \frac{1}{c} \frac{d}{dt} \right] I_\nu = \eta_\nu - [\chi_\nu + \sigma_\nu] I_\nu, \quad (2.17)$$

where here $\chi_\nu = \rho\kappa_\nu$ is the absorption with units of length^{-1} , σ_ν is the scattering with units of length^{-1} , and η_ν is the emissivity with the subscript ν indicating frequency-resolved quantities, as above. The scattering is not typically relevant for HEDP plasmas because the absorption dominates the opacity in the regions of the spectrum containing the majority of the energy. Equation 2.17 is a generalization of the well known Beer's law for transmission through cold material. Rewriting equation 2.17 to move all of the spectral intensity terms to the left side and dividing through by the absorption results in the following,

$$\frac{1}{\chi_\nu} \left[\frac{1}{c} \frac{d}{dt} + \frac{d}{ds} \right] I_\nu + I_\nu = \frac{\eta_\nu}{\chi_\nu} = S_\nu, \quad (2.18)$$

where S_ν is the source function, which characterizes the emission from the plasma and has the same units as the spectral intensity. It is relevant to note that the time derivative term in the transport equation is only necessary for relativistic plasmas and that it will be negligible for the physics discussed below.

2.2.3 Moments of the Transport Equation

HEDP plasmas can often have significant radiation fields, and it can be useful to take the solid angle moments of the radiation transport equation to facilitate com-

binning radiation physics with the fluid equations. Section 2.3 will cover the resulting radiation hydrodynamic equations in more detail. The most useful is the zeroth moment in solid angle, which rewrites the transport equation in terms of the net flux, F_ν . Taking the integral of equation 2.17 over the solid angle,

$$\frac{1}{c} \frac{d}{dt} \vec{F}_\nu + \frac{d}{ds} \vec{F}_\nu = \int (\eta_\nu - \chi_\nu I_\nu) \hat{n} d\Omega. \quad (2.19)$$

To simplify the derivative along the path length, s , the directional derivative reduces to the divergence of the net flux, in a planar geometry. It is also reasonable to set the time derivative to zero for non-relativistic plasmas treated here, therefore, the moment of the transport equation is,

$$\nabla \cdot \vec{F}_\nu = \int (\eta_\nu - \chi_\nu I_\nu) \hat{n} d\Omega. \quad (2.20)$$

Integrating this over frequency, because this will be most useful in the radiation hydrodynamics equations later, gives the following expression,

$$\nabla \cdot \vec{F}_R = 4\pi \int \chi_\nu (S_\nu - J_\nu) d\nu, \quad (2.21)$$

where F_R is the frequency integrated net flux. The first moment, in solid angle, of the transport equation will be useful in describing systems with diffusive transport and is,

$$\frac{1}{c^2} \frac{d}{dt} \vec{F}_\nu + \nabla \cdot \bar{P} = \frac{1}{c} \int_{4\pi} (\eta_\nu \chi_\nu I_\nu) \hat{n} d\Omega, \quad (2.22)$$

where \bar{P} is the radiation pressure tensor and the bar above the P represents the fact that this is a rank two tensor.

2.2.4 Solutions to the Transport Equation

It is useful to demonstrate some solutions, or at least simplifications, of the transport equation that are analytically accessible as a first step to understanding the effects of radiation in a particular problem. Starting with the assumption that the time derivative in equation 2.18 is negligible, and changing variables to the frequency-resolved optical depth, τ_ν ,

$$\mu \frac{d}{d\tau_\nu} I_\nu + I_\nu = S_\nu(\tau_\nu), \quad (2.23)$$

where $d\tau_\nu = \chi_\nu \mu ds$, with $\mu = \cos\theta$, and θ is the angle a ray makes with the surface normal. This equation has an analytic solution using the integrating factor $e^{-\frac{|\tau_s - \tau_o|}{\mu}}$,

$$I_\nu(\tau_\nu) = I_{\nu,o} e^{-\frac{|\tau_{\nu,s} - \tau_{\nu,o}|}{\mu}} + \int_{\tau_{\nu,o}}^{\tau_{\nu,s}} e^{-\frac{|\tau'_{\nu,s} - \tau_{\nu,o}|}{\mu}} S_\nu d\tau'_\nu, \quad (2.24)$$

where the subscripts o represent values at the boundary and s values at some distance away in the plasma. It is then possible to evaluate the integral on the right hand side using atomic codes to evaluate the source function for a particular set of plasma parameters and materials. To proceed from this point analytically, it is necessary to make further assumptions about the source function. This document will limit the analysis to two cases, one where the source function is a linear combination of the thermal emission and coherent scattering and a diffusion approximation for the flux in systems extending over a large number of photon mean free paths, which are common in HEDP problems and the next two sections describe. There are more details about solutions to the transport equation under a variety of conditions in the books by Drake, Mihalas and Weibel-Mihalas, and Chandrasekhar[1, 36, 100].

2.2.4.1 Transport Regime

In the first case, it is reasonable to describe the emissivity of the medium as the linear combination of thermal self emission and isotropic, coherent scattering, as described above. This takes the form,

$$\eta_\nu = \chi_\nu B_\nu(T) + \sigma_{\nu,sc} J_\nu, \quad (2.25)$$

where $B_\nu(T)$ is the thermal spectral intensity, $\sigma_{\nu,sc}$ is the coherent scattering absorption, and $I_\nu = J_\nu$ because the scattering is isotropic. The thermal spectral intensity is the emission from a material in equilibrium, or local-thermodynamic equilibrium, which has temperature as the only parameter and follows a Planckian distribution,

$$B_\nu(E, T) dE = \frac{E^3}{c^2 \hbar^3} \frac{1}{e^{\frac{E}{kT}} - 1} dE, \quad (2.26)$$

where c is the speed of light in vacuum in units of cm s^{-1} , \hbar is the reduced Planck's constant in units of erg s , E is the photon energy in erg , k is the Boltzmann constant in units of erg eV^{-1} and T is the plasma temperature in eV . The total absorption is then the sum of χ_ν and $\sigma_{\nu,sc}$, which makes the source function,

$$S_\nu = \frac{\kappa_\nu B_\nu(T) + \sigma_\nu J_\nu}{\kappa_\nu + \sigma_\nu}. \quad (2.27)$$

Inserting these values for the emissivity and absorption,

$$\frac{d}{ds} I_\nu = \kappa_\nu (B_\nu - I_\nu) + \sigma_\nu (J_\nu - I_\nu), \quad (2.28)$$

and since $J_\nu = I_\nu$ in the isotropic, coherent scattering regime the second term in equation 2.28 is zero. Integrating the result over frequency and solid angle produces

an expression for the net flux,

$$\nabla \cdot \vec{F}_R = 4\pi\kappa [B(T) - J_R], \quad (2.29)$$

where $B(T) = \frac{\sigma_{SB}T^4}{2\pi}$ is the thermal radiation flux, σ_{SB} is the Stefan-Boltzmann constant, and κ is a weighted average of the continuum absorption term κ_ν .

2.2.4.2 Radiation Diffusion Regime

The limit where the system scale length is a large number of mean free paths, it is possible to simplify the transfer equation into a diffusion equation. Using equation 2.22 and making the same assumptions of the time derivative term being negligible and isotropic radiation as before, leading to a relationship between the divergence of the radiation pressure tensor and the radiation flux,

$$\nabla \cdot \bar{P} = -\frac{\chi_\nu}{c} \vec{F}_\nu. \quad (2.30)$$

Under the further assumptions of a planar system and the Eddington approximation, which says that the radiation pressure is proportional to the radiation energy density, $P_\nu = f_E u_\nu$, reduces the divergence of the pressure tensor to the gradient of a scalar pressure, due to the systems isotropy, Near equilibrium the proportionality factor, $f_\nu \rightarrow \frac{1}{3}$ and the radiation energy density, $u_\nu \rightarrow \frac{4\pi}{c} B_\nu(T)$. Since the temperature only varies in space, one can rewrite the flux as the gradient of the temperature. The frequency-integrated flux is most useful in the radiation hydrodynamics equations, and will be useful in the discussions of heat waves and radiative shocks below,

$$\vec{F}_R = -\frac{4\pi}{3\chi_R} \frac{\partial B}{\partial T} \nabla T, \quad (2.31)$$

where $\frac{1}{\chi_R}$ is the Rosseland mean opacity, which has a functional form,

$$\frac{1}{\chi_R} = \frac{\int_0^\infty \frac{1}{\chi_\nu} \frac{\partial B_\nu}{\partial T} d\nu}{\int_0^\infty \frac{\partial B}{\partial T} d\nu}. \quad (2.32)$$

Since B is a known function of T , one can evaluate $\frac{\partial B}{\partial T}$, which results in $\vec{F}_R = -\frac{16\sigma_{SB}T^3}{3\chi_R}\nabla T$. Defining the coefficient to the temperature gradient as κ_{rad} , with units energy length⁻¹ time⁻¹ temperature⁻¹ improves the aesthetics of the resulting equations and is the diffusion coefficient for the divergence of the radiation flux,

$$\nabla \cdot \vec{F}_R = -\nabla \cdot (\kappa_{rad}\nabla T). \quad (2.33)$$

2.3 Radiation hydrodynamics

After deriving some relations for radiation transport that are relevant for HED systems above, the next logical step is to combine these results with the Euler equations discussed in section 2.1. This addresses the physical systems where a fluid approximation is appropriate and the radiation field is significant for the fluid evolution. The experiments discussed below are all in this radiation hydrodynamics regime, and this section will broadly discuss the underlying physics of Marshak-like nonlinear diffusion heat fronts, photoionization fronts, and radiative shocks, which the experimental results in later chapters will explore in greater detail.

The derivation of these equations in a way that is consistent in relativistic frames of reference and between inertial and co-moving frames is very involved and this document will not cover it in any detail. The derivation in full is in the book by Mihalas and Weibel-Mihalas[36], which starts from the transport equation and relativistic fluid equations then ends with a set of equations handling the momentum and energy in the radiation and material. For the equations in the co-moving reference frame, it is possible to assume the material parameters as isotropic. This frame also makes the

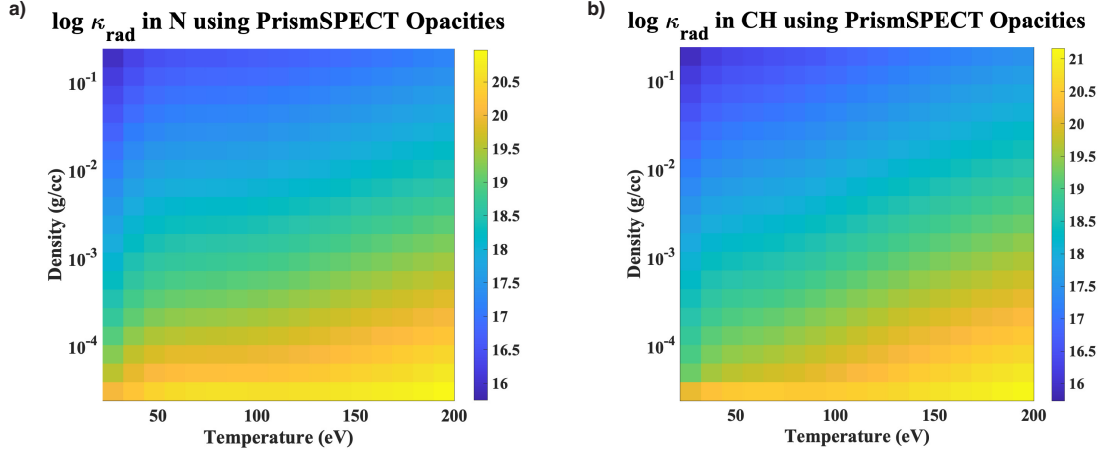


Figure 2.2: a) The calculated values of κ_{rad} in N over a range of density and temperature values using PrismSPECT to generate the opacities. b) The calculated values of κ_{rad} in CH over a range of density and temperature values using PrismSPECT to generate the opacities

bulk fluid velocity zero, which cancels out any velocity dependent terms that arise in the derivation. Keeping terms to order $\frac{v}{c}$, where v is the fluid velocity and c is the speed of light, results in the total energy and momentum being equal to the sum of radiation and fluid components,

$$p_T = p + p_R, \quad (2.34)$$

and

$$\rho\epsilon_T = \rho\epsilon + u_R, \quad (2.35)$$

where the subscript R indicates the contribution from the radiation pressure and energy density in equations 2.34 and 2.35 respectively and the subscript T indicates the total quantity. Since the plasmas discussed here are firmly in the non-relativistic regime, the material variables are constant between reference frames and no specification is necessary. This leaves the mass conservation equation unchanged from

equation 2.3a. Therefore, the radiation hydrodynamic equations are,

$$\rho \frac{D}{Dt} \vec{v} = -\nabla p_T, \quad (2.36)$$

$$\rho \frac{D}{Dt} \frac{v^2}{2} = -\vec{v} \cdot \nabla p_T, \quad (2.37)$$

$$\frac{\partial}{\partial t} \left(\frac{\rho v^2}{2} + \rho \epsilon_T \right) + \nabla \cdot \left[\rho \vec{v} \left(\frac{u^2}{2} + \gamma_T \epsilon_T \right) \right] = -\nabla \cdot \vec{F}_R, \quad (2.38)$$

where γ_T is the appropriate index for the EOS when radiation is significant. Equation 2.36 is the total momentum equation, equation 2.36 is the mechanical momentum equation, and equation 2.38 is the total energy equation. The radiation energy and momentum equations are 2.21 and 2.22, which one uses to derive a radiation transport model to close the system of equations.. These equations exclude the terms for gravity and thermonuclear interactions from the Mihalas and Weibel-Mihalas[36] derivation as they are not relevant to the experiments presented below.

2.3.1 Nonlinear Diffusion Waves

To begin an investigation into supersonic heat fronts, it makes sense to start with the diffusion approximation of equation 2.33 where the propagation medium extends for many photon mean-free-paths. This results in a nonlinear diffusion wave in the fluid temperature, which allows for self-similar solutions under certain assumptions. The simplest form of this is the Marshak wave, from the 1958 Marshak paper [37], which has the base assumptions of a planar geometry and negligible radiation energy density and pressure. However, the radiation flux has significant energy, otherwise the radiation hydrodynamics equations converge to the Euler equations. These assumptions, along with a radiation diffusive conductivity that is a power law in temperature,

$$\kappa_{rad} = (\kappa_{rad})_{T_0} T^n,$$

where $(\kappa_{rad})_{T_o}$ is a temperature independent constant and n is a number that has a value of 4 to 5 in HEDP plasmas, while it is 6 to 7 in astrophysical plasmas[1, 36, 37]. Figure 2.2 shows the values of κ_{rad} for N over a range of temperatures and densities relevant to the experiments described below using the atomic physics code PrismSPECT[101] to calculate the Rosseland mean opacity. Additional assumptions of constant density and supersonic propagation of the heat front, combined with the previous assumptions, allows one to simplify the energy equation to,

$$\frac{\partial \epsilon}{\partial t} = -\frac{(\kappa_{rad})_{T_o}}{n+1} \nabla^2 T^{n+1}, \quad (2.39)$$

where ϵ is the material specific internal energy. Additionally, assuming that the material internal energy be written as $\epsilon = \rho c_V T$, with a constant specific heat, allows one to write a diffusion equation in temperature.

Defining a value $W = \frac{(\kappa_{rad})_{T_o}}{\rho c_V (n+1)}$ to simplify the notation, the similarity variable is then, $\xi = \frac{x}{\sqrt{Wt}}$, rewriting things in terms of ξ reduces the equation to the second order ordinary differential equation (ODE),

$$\frac{d^2 f^{n+1}}{d\xi^2} = -\frac{\xi}{2} \frac{df}{dt}, \quad (2.40)$$

where f is the boundary-normalized temperature profile. One is able to solve equation 2.40 numerically, but assuming a constant flux in equation 2.31 allows for an analytic solution for f ,

$$f = \left(1 - \frac{\xi}{\xi_o}\right)^{1/(n+1)}, \quad (2.41)$$

where ξ_o is the location of the front in the similarity variable. The increase in wave energy as a function of time then allows for the evaluation of ξ_o from which one can

find the front location and velocity in real space coordinates,

$$x_o = \frac{\sqrt{n+2}}{n+1} \sqrt{\frac{(\kappa_{rad})_{T_o}}{\rho c_V}} \sqrt{2t}, \quad (2.42)$$

$$u_o = \frac{\sqrt{n+2}}{n+1} \sqrt{\frac{(\kappa_{rad})_{T_o}}{\rho c_V}} \frac{1}{\sqrt{2t}}. \quad (2.43)$$

The above solution to the radiation hydrodynamic equations has many assumptions, but the one that is most glaringly incorrect for HEDP systems is the assumption of constant c_V because the heating in these kinds of experiments typically results in significant ionization. This will change the effective charge per ion through the factor Z , using a simple Hydrogenic model of the atom, Drake[1] provides this approximate model for the specific heat at constant volume in an ionizing medium as,

$$c_V = \left(\frac{3}{2}\right) \frac{[1 + (\frac{3}{2})Z] k_B}{Am_p} + \frac{k_B E_H Z + 6Z^2 + 12Z^3}{12T Am_p}, \quad (2.44)$$

where k_B is the Boltzmann constant, A is the number of nucleons in an atom, m_p is the mass of a proton, E_H is the binding energy of the Hydrogen atom at 13.6 eV, and Z is the ionization of an atom. Z is a function of temperature and approximating the relationship as $Z \propto \sqrt{T}$, while limiting c_V to the highest order terms in Z allows for a self-similar solution to an ionization wave. The self-similar ordinary differential equation is then,

$$\frac{1}{\sqrt{f}} \frac{d^2 f}{d\xi^2} = -\frac{\xi}{2} \frac{df}{dt}. \quad (2.45)$$

Following the same analysis as in the Marshak wave, and assuming a constant radiation flux, results in expressions for the position and velocity of the ionizing heat front.

$$x_o = \frac{2\sqrt{2n+6}}{2n+3} \sqrt{\frac{(\kappa_{rad})_{T_o}}{\rho c_{V_o}}} \sqrt{t}, \quad (2.46)$$

$$u_o = \frac{\sqrt{2n+6}}{2n+3} \sqrt{\frac{(\kappa_{rad})_{T_o}}{\rho c_{V_o}}} \frac{1}{\sqrt{t}}, \quad (2.47)$$

where c_{V_o} is the constant value of the specific heat used in the Marshak wave derivation above.

2.3.2 Photoionization fronts

Photoionization (PI) fronts are heat fronts where photoionization is the dominant mechanism for depositing energy at the front, which Strömgren first explored in the 1930s[56]. This section will explore atomic kinetics and radiation hydrodynamics of PI fronts developing useful dimensionless parameters along the way, in addition, there will be a comparison to the nonlinear diffusion waves of the previous section. This will demonstrate the measurable differences that an experiment could use to distinguish the different transport mechanisms. The small number of downstream photon mean free paths in a PI front disallows the assumption of diffusive radiation transport, as the radiation streams to the interface, and $\nabla \cdot \vec{F}$ does not have a simple relationship to the plasma parameters.

The physics of a PI front has an external radiation source driving the heating, at the front. This means that the flux term in the previous paragraph only includes the flux from the external source, there are no significant contributions from the self emission of the heated plasma or from the electron energy flux transported along the temperature gradient. To calculate the minimum external flux needed to sustain a PI front, one starts with interaction rate for photoionization, $\nu_{PI}(E) = n_a \sigma(E) c$, where $\nu_{PI}(E)$ is the interaction rate, n_a is the atomic number density, $\sigma(E)$ is the interaction cross section, and c is the speed of light. Multiplying $\nu_{PI}(E)$ with the photon energy spectrum, $f(E) dE$, and then integrating over energy provides the source power delivered to an atom or ion. This results in an expression in the average photon energy and cross section, $w = E_{av} n_a \sigma_{av} c$, where w is the delivered power,

E_{av} is the average photon energy, and the subscript av represents an averaged value. Normalizing this expression to the area of an atom or ion provides the required flux to photoionize a population of n_a atoms or ions,

$$F = \frac{E_{av}c}{\sigma_{av}\lambda_{av}}, \quad (2.48)$$

where $\lambda_{av} = \frac{1}{n_a\sigma_{av}}$ is the average photon mean free path.

2.3.2.1 Atomic kinetics

The atomic kinetics, at the front, will dictate the microphysics processes that contribute most to the heating of the medium. As it is necessary to have photoionization dominate the energy deposition in a PI front, it is necessary to find conditions where that is the dominant microphysical process. Following the descriptions in Drake and Gray[61, 62, 63], the two or three level atom model has sufficient detail to give some insight into the scale length over which the ionization state changes as the front passes by, while still being tractable with pencil and paper calculations. However, to utilize the full detail of the atomic structure calculations currently available, one must use computational tools, such as PrismSPECT or FLYCHK[101, 102], to solve the large matrix equations incorporating thousands of atomic levels.

To find the ionizations state populations, one needs to solve the system of rate equations, which compare the processes that increase or decrease the state population densities. In LTE systems, the Saha equation is sufficient for describing the relationship between the different ionization state densities. This generalizes to the collisional-radiative equations in systems that are not collisional enough for LTE physics[103]. The collisional-radiative rate equations for a three-level system are then,

$$\frac{dn_1}{dt} = -\langle\sigma v\rangle_{1,2}n_en_1 - \Gamma_{i,i+1}n_i + R_{2,1}n_en_2, \quad (2.49)$$

$$\frac{dn_2}{dt} = - \left(\frac{dn_1}{dt} + \frac{dn_3}{dt} \right), \quad (2.50)$$

$$\frac{dn_3}{dt} = \langle \sigma v \rangle_{2,3} n_e n_2 - \Gamma_{2,3} n_2 + R_{3,2} n_e n_3, \quad (2.51)$$

where n_i is the population number density of the i th ionization state, $\langle \sigma v \rangle_{i,i+1}$ is the electron collisional ionization rate in units of $\text{cm}^3 \text{s}^{-1}$, $\Gamma_{i,i+1}$ is the photoionization rate in units of s^{-1} , and $R_{i+1,i}$ is the recombination rate coefficient in units of $\text{cm}^3 \text{s}^{-1}$. The recombination rate considers radiative recombination, dielectronic recombination, and three-body recombination using the fits of Verner and Ferland and the Lotz formula[104, 105]. Equations conserving the total number of particles closes the set of equations,

$$n_e = Z_1 n_1 + Z_2 n_2 + Z_3 n_3, \quad (2.52)$$

$$n_T = n_1 + n_2 + n_3, \quad (2.53)$$

where Z_i is the ionization of the i th ionization state, and n_T is the total ion number density. This system allows for the number of optical depths, τ from the source to act as an additional independent variable due to the dependence of the photoionization rate on the photon flux. The photoionization rate is the cross section-weighted integral over the incident photon flux,

$$\Gamma_{i,i+1} = \int_0^\infty \sigma_{PI,\nu} F_{R,l} dE, \quad (2.54)$$

where $\sigma_{PI,\nu}$ is the frequency-dependent photoionization cross section that is a function of photon energy, ionization state, and electron bound state. Here the photoionization cross section uses the Verner and Ferland[106, 107] fits and assumes a blackbody radiation source to calculate the integral. Assuming the flux has the form, $F_{R,l} =$

$F_{R,0}g[\tau]$ and the dependence on changing optical depth goes as follows,

$$\frac{dg[\tau]}{dt} = -\frac{(f_1\sigma_{PI,1} + f_2\sigma_{PI,2})g[\tau]}{\sqrt{\sigma_{PI,1}^2 + \sigma_{PI,2}^2}}, \quad (2.55)$$

where f_i is the ionization fraction of the i th state, and $\sigma_{PI,i}$ is the average photoionization cross section of the i th state. In addition, the analysis identifies two dimensionless parameters that identify the physics regime of the atomic kinetics,

$$\alpha = \frac{n_{i+1}}{n_i} \frac{R_{i+1,i}n_e}{\Gamma_{i,i+1}}, \quad (2.56)$$

$$\beta = 1 + \frac{n_i}{n_{i+1}} \frac{\langle\sigma v\rangle_{i,i+1}}{R_{i+1,i}}, \quad (2.57)$$

where α shows if photoionization occurs more frequently than recombination at the front and β determines the importance of electron impact ionization. In order to have a PI front, an experiment needs an α value less than unity and a value of β that is approximately unity. If this is not the case, the system may have significant photoionization with non-negligible contributions from electron heat transport if the value of β is larger than one, or one may have a system with insufficient flux to sustain a PI front if α is greater than one.

2.3.2.2 Heat front analysis

Since the previous paragraphs explored the microphysics of the PI front, it makes sense to now look at the macrophysics using the radiation hydrodynamics equations described above. With the assumption of a steady-state front, the jump conditions across the interface are,

$$\rho_1 u_1 = \rho_2 u_2, \quad (2.58)$$

$$\rho_1 u_1^2 + p_1 = \rho_2 u_2^2 + p_2, \quad (2.59)$$

$$\left(\frac{\rho_1 u_1^2}{2} + \frac{\gamma p_1}{\gamma - 1}\right) u_1 - F_R = \left(\frac{\rho_1 u_1^2}{2} + \frac{\gamma p_1}{\gamma - 1}\right) u_1, \quad (2.60)$$

where γ is the polytropic index from the assumption of an adiabatic EOS, and the remaining variables correspond to their usual values. It is important to note that F_R in the above equation comes from the flux term in equation 2.38 without an assumed functional form for the flux and that, similarly to nonlinear diffusion waves, this problem considers the radiation momentum and energy density as negligible. This breaks the assumption of diffusive radiation transport, as one can no longer simply relate the flux to the temperature gradient.

One can rearrange equation 2.48 to solve for the velocity, $c = \frac{F_\gamma}{n_a}$, where F_γ is the photon number flux. Here the velocity is c because the calculation considered interactions with individual atoms or ions, in a PI front c goes to the front velocity u_1 . This results in the following expression for the flux,

$$F_R = -\frac{E_{av}\zeta}{\bar{M}}\rho_1 u_1 = -Q^2 \rho_1 u_1, \quad (2.61)$$

where ζ is the average number of electrons removed from the ion, \bar{M} is the average ion mass, and Q has units of velocity. Following the normalization in the Drake paper[61], the variables are then, $\frac{\rho_2}{\rho_1} = \mu$, $a_2 = \hat{a}_2 a_1$, $u_1 = \hat{u}_1 a_1$, $u_2 = \hat{u}_1 \frac{a_1}{\mu}$, and $Q = \hat{Q} a_1$, where $a^2 = \frac{p}{\rho}$ is the isothermal sound speed. Substituting these values into the jump conditions provides a set of normalized equations for PI fronts,

$$\mu + \hat{u}_1^2 (\mu - 1) - \hat{a}_2^2 \mu^2 = 0, \quad (2.62)$$

$$\mu^2 \left[\left(2\hat{Q}^2 + \hat{u}_1^2 \right) (\gamma - 1) + 2\gamma \right] - \mu 2\gamma (\hat{u}_1^2 + 1) + \hat{u}_1^2 (\gamma + 1) = 0. \quad (2.63)$$

Solving those equations for \hat{a}_2 and μ gives,

$$\hat{a}_2 = \frac{\sqrt{\mu + \hat{u}_1^2 (\mu - 1)}}{\mu}, \quad (2.64)$$

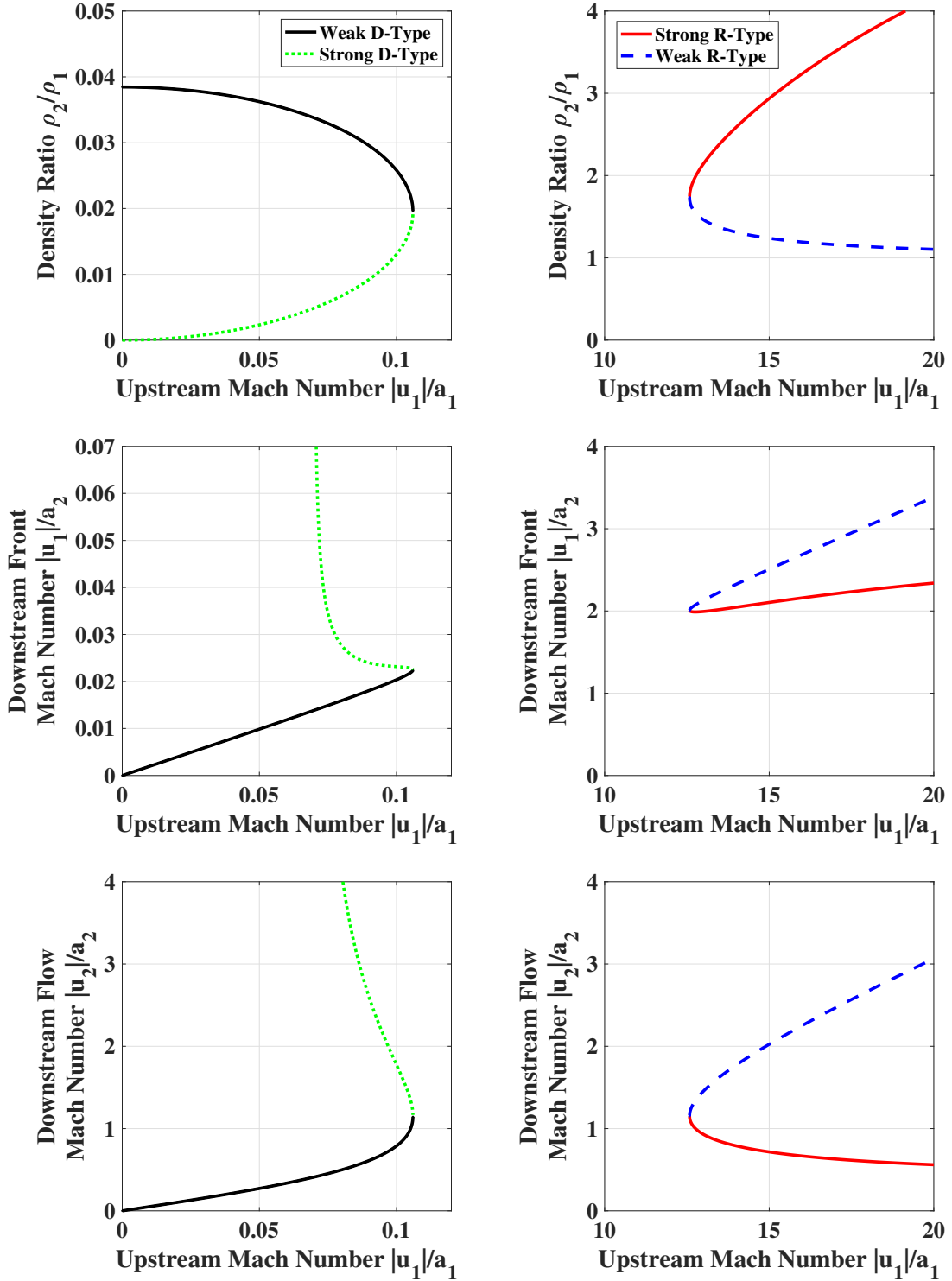


Figure 2.3: The density ratio, front Mach number, and flow Mach number for the heat front analysis of a PI front for the four types described in the text with a \hat{Q} of 10 and a γ of $\frac{4}{3}$. This demonstrates the limited density jump for the weak R-type front, which is the focus of the experiments described in this thesis. The abscissa is different between the plots on the left and right hand side, which demonstrates the extent of the region where there is no purely real solution.

$$\mu = \frac{\gamma(\hat{u}_1^2 + 1) \pm \sqrt{(\hat{u}_1^2 - \gamma)^2 - 2\hat{Q}^2\hat{u}_1^2(\gamma^2 - 1)}}{2\hat{Q}^2(\gamma - 1) + \hat{u}_1^2(\gamma - 1)2\gamma}. \quad (2.65)$$

In the above equations, \hat{u}_1 and \hat{Q} are the independent variables. This leads to four different regions of solutions to these equations, which the literature call the strong D-type, weak D-type, strong R-type, and weak R-type[57, 58, 59, 60]. The weak R-type front is a supersonic heat front that has no density jump across the interface, which results in a low opacity region that radiation streams through until the upstream material rapidly absorbs it. The strong R-type front is a modified shock where the radiation acts to reduce the compression. The weak D-type front is a subsonic expansion wave with moderate heating. The strong D-type front is a supersonic rarefaction where the density drops behind the interface. For the experiments discussed below, the most relevant types are the weak-R and strong-D type fronts. This is because the experiments intend to produce weak-R type fronts, as the radiation decreases the pressure creates a shock, which allows for the development of a strong D-type front. The Strong R-type front is not possible as there is no incoming flow to support the modified shock and the boundary conditions will not support a weak D-type front.

2.3.2.3 Propagation and curvature

All of the heat front analysis to this point has been in one dimension to keep the calculations simple. However, it is very difficult to create a 1D heat front experimentally because the geometric falloff of the source alone causes changes in the flux transverse to the source axis. This introduces two dimensional, at least, effects in the system through the curvature of the heat front and can also affect the velocity of a PI front through a medium. This section will present the differences in the curvature and velocity of between nonlinear diffusion waves and PI fronts as a means of experimentally distinguishing the two systems.

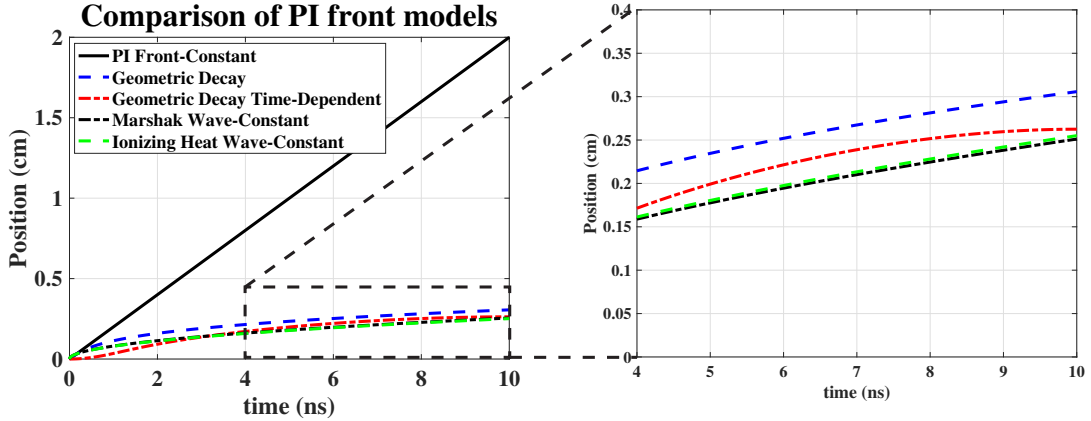


Figure 2.4: A comparison of the PI front propagation with constant-flux, geometrically decaying flux, and geometrically decaying, time-dependent flux to constant flux, nonlinear diffusion wave models. This comparison shows that PI fronts travel faster than nonlinear diffusion waves, even considering the upper bound of velocity for the nonlinear diffusion waves. The inset shows the different distances the constant-flux, nonlinear diffusion waves and PI fronts with real source models travel in more detail.

2.3.2.4 PI front Propagation Compared to Nonlinear Diffusion Waves

Under constant flux models, the propagation velocity of nonlinear diffusion waves and PI fronts are quite different. The fastest nonlinear diffusion wave propagation is proportional to $\frac{1}{\sqrt{t}}$, while a PI front propagates linearly with time. However, the constant flux model isn't accurate for the characteristics of a real source that one would find in an experiment. To account for this, one needs to add spatial and temporal dependence to the flux, which makes the velocity a function of time. This allows for the simple equation for the PI front velocity, $v_f = \frac{F_{R,\gamma}}{n_o}$, mentioned above to be written as a differential equation, $\frac{dX_{PI}(x,t)}{dt} = \frac{F(x,t)}{n_o}$, where X_{PI} is the PI front location, x is the spatial axis, and t is the time. Using different flux models in this equation will let various real source effects, such as geometric decay and source pulse shape, alter the location of the front. Comparing the results of these models with the constant flux models of nonlinear diffusion waves will show how useful location measurements are for distinguishing between different types of heat fronts.

Here, the analysis will use three flux models, one with a spatial dependence, one

with temporal dependence, and one with both spatial and temporal dependence. None of the solutions will use normalized coordinates to facilitate a comparison with the nonlinear diffusion wave solutions discussed above. The general form of the flux for these models is,

$$F(t) = F_o a(t) b(t), \quad (2.66)$$

where F_o is the initial flux, $a(t)$ is the temporal dependence, and $b(X_{PI}(t))$ is the spatial dependence. The temporal dependence of the source will be quadratic in time,

$$a(t) = c_1 (t - t_o)^2 + c_0, \quad (2.67)$$

where c_1 and c_0 are constants. The spatial dependence is the on-axis geometric decay profile for a finite source,

$$b(X_{PI}) = \frac{\left(\frac{R}{X_{PI}}\right)^2}{1 + \left(\frac{R}{X_{PI}}\right)^2}, \quad (2.68)$$

where R is the source radius. For the model where $F = aF_o$ the resulting solution for $X_{PI}(t)$ is,

$$X_{PI}(t) = \frac{-F_o}{n_o} c_1 \left[\frac{1}{3} \left(t - \sqrt{\frac{c_0}{c_1}} \right)^3 + \left(\frac{c_0}{c_1} \right)^{\frac{3}{2}} \right] + c_0 t. \quad (2.69)$$

The solutions to the equations $\frac{\partial X_{PI}}{\partial t} = b(t) \frac{F_o}{n_a}$ and $\frac{\partial X_{PI}}{\partial t} = a(t) b(t) \frac{F_o}{n_a}$ are found numerically with the solutions shown in figure 2.4. The nonlinear diffusion wave propagation uses $4 * 10^{17} \text{ erg s}^{-1} \text{ cm}^{-1} \text{ eV}^{-1}$ for $(\kappa_{rad})_{T_o}$ and the PI front models use $-4 * 10^{16}$ and 1 for c_1 and c_0 respectively. These results show that a PI front with real source features is faster or similar to multiple constant flux, nonlinear diffusion wave models under the same material conditions. A nonlinear diffusion wave under the constant flux model will have the maximum velocity shown and adding features of a real source will only act to slow down the nonlinear diffusion wave. Since a PI front is already faster than the constant flux, nonlinear diffusion waves after a couple

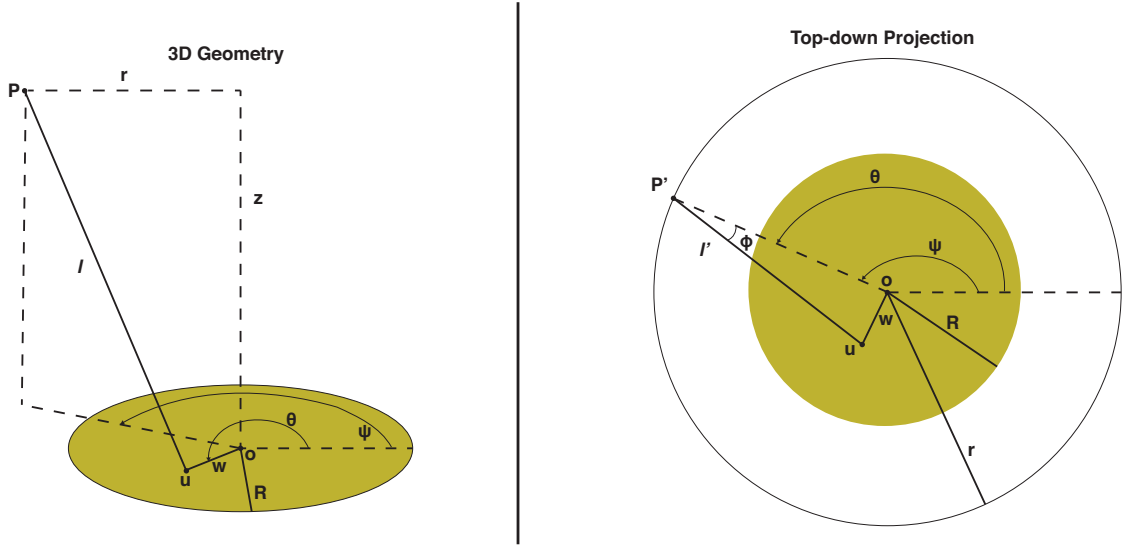


Figure 2.5: The 3D and top down projection geometries for the calculations used to determine the average path length of an arbitrary point above a disk of radius R .

hundred picoseconds, real source effects will make them substantially slower than PI fronts later in time. This means that the PI front velocity is a powerful tool for distinguishing between different types of heat fronts and can act as a metric for an experiment as well as a testable parameter for computer simulations.

2.3.2.5 PI Front Curvature Compared to Marshak Waves

The radiation in a PI front streams through the optically-thin, downstream region to an interface where the cold upstream rapidly absorbs it. This means that the front properties should be equivalent at locations of the same average path length from the source; suggesting geometry provides a decent estimate of the curvature. To calculate the average path length, it is necessary to calculate the distance from a point to an arbitrary location on the source. Figure 2.5 shows the details of this geometry. Here the source is a disk and the average path length is the integral over the radial and polar dimensions of the source. It is important to point out that there are two regimes of solution to the geometry, one for a point inside and outside the radius of the source.

To solve the geometry, the length, l' , between the points u and P' combined with

the height, z , above the source plane provides the distance between the observation point and an arbitrary location on the source disk, $L = \sqrt{z^2 + l'^2}$. For $r > R$, the length from u to l is, in number of source radii,

$$\frac{L}{R} = \frac{1}{R} \sqrt{\left[\frac{w^2 \sin^2 \beta}{r - w \cos \beta} + r - w \cos \beta \right]^2 + z^2}, \quad (2.70)$$

where $\beta = |\psi - \theta|$. For the case where $r < R$, the length to an arbitrary point on the source disk is,

$$\frac{L}{R} = \frac{1}{R} \sqrt{\left[\frac{w - r \cos \phi}{\sin \left[\text{atan} \left(\frac{w - r \cos \phi}{r \sin \phi} \right) \right]} \right]^2 + z^2}, \quad (2.71)$$

where ϕ is the angle $uP'o$ in the projection of P to the source plane. This geometry makes the length from a point on the source disk to the point P a function of r , z , w , and either β or ϕ depending on where P is. Integrating over w and the angle variable provides an average distance to the point P from the source,

$$\left\langle \frac{L}{R} \right\rangle = \begin{cases} \int_0^R \int_0^{2\pi} d\phi dw \frac{L}{R} & r < R \\ \int_0^R \int_0^\pi d\beta dw \frac{L}{R} & r > R. \end{cases} \quad (2.72)$$

Figures 2.6 a and b show the average path length with sources smaller than and similar to the dimensions of the propagating medium. This analysis shows that the radius of curvature for a PI front should increase as it moves away from the source, which makes intuitive sense because as one moves farther away from a point source, the resulting spherical wavefronts approach a plane wave. Additionally, figure 2.6 b shows that, for a one dimensional system, the curvature of a PI front changes very little as it propagates away from the source.

In order for this to be useful information for diagnosing the presence of a PI front, there needs to be differences between the evolution of curvature in different types of heat fronts. Back's experiments in the early 2000's [27, 28] show a curvature that

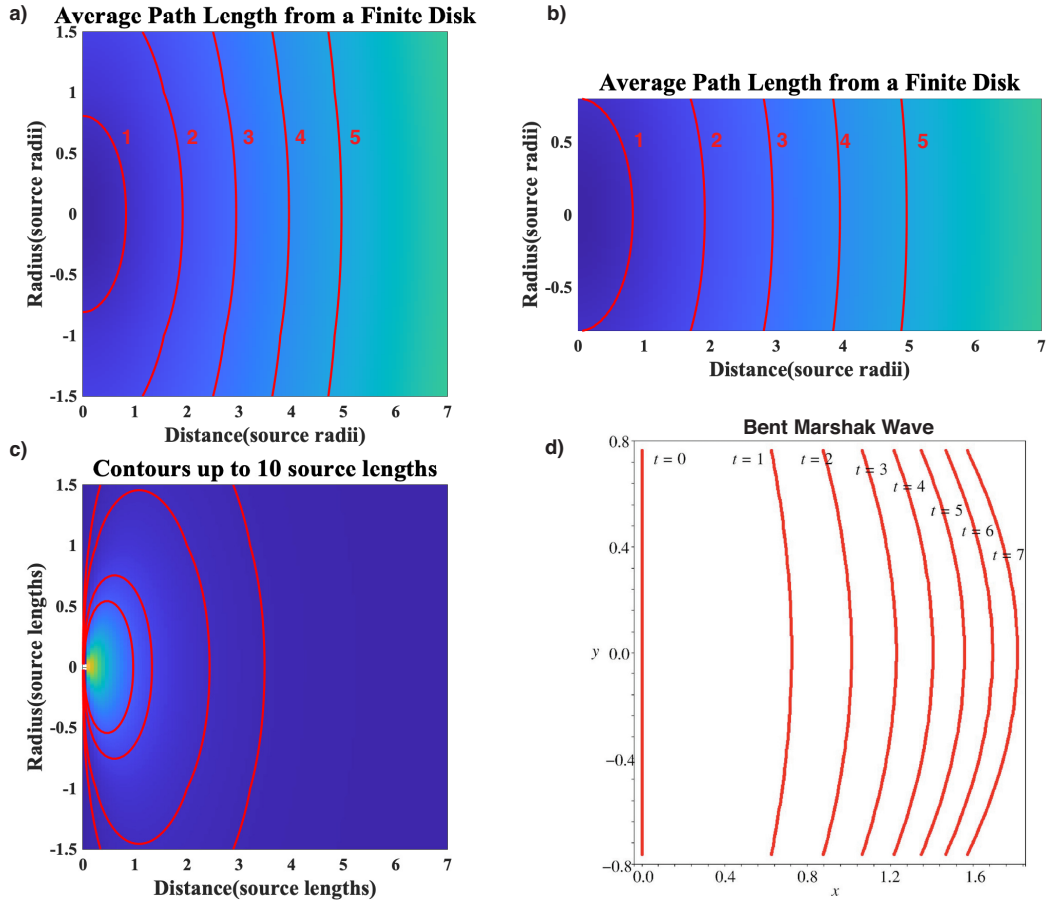


Figure 2.6: a) The average path length where the dimensions of the propagation volume is larger than the source radius with contours showing the curvature decreasing with distance. b) The average path length where the dimensions of the propagation volume is smaller than the source radius with contours showing the curvature decreasing with distance. c) The source in the curvature calculations is Lambertian due to the geometric nature of the system. d) The bent Marshak wave results[3] show the increase of front curvature due to losses through the walls of the propagating medium container.

increases with propagation distance in the measured diffusive heat fronts and theory confirmed these results[3], shown in 2.6 d. This is due to heat leaving through the walls in these diffusive heat fronts. As the heat front propagates through the medium, the radiation energy diffuses along the axis, but if the walls are not perfectly insulating, which is never the case in experiment, there is additional lateral heat loss that acts to cool the edges of the propagating medium. There should not be as significant wall losses in PI fronts because the radiation from the source is non-diffusive meaning there are only conductive losses through the walls and geometric losses of the source flux. This means that the curvature of nonlinear diffusion waves evolves in the opposite way to a PI front, making this a diagnostic tool for heat front experiments.

2.3.3 Radiative shocks

The previous paragraphs discussed the inclusion of radiation in the Euler equations to produce the radiation hydrodynamics equations, then showed solutions to these equations for heat fronts in static media. To continue this discussion, the following will discuss the effects of radiation on fluid motion and the development of radiative shocks. The opacity in the upstream and downstream material dictates the behavior and structure of the shock[1, 68] depending on the number of optical depths. Laboratory systems using foams as the propagating medium typically have an optically thick downstream and optically thick or thin upstream[4, 70]. This section will focus on the behavior of optically thick and thick-thin shocks, then will calculate some relevant quantities.

Starting from the radiation hydrodynamics equations and assuming a γ law equation of state, the following shock frame jump conditions result,

$$\rho u = -\rho_o u_s \tag{2.73a}$$

$$p + \rho u^2 = p_o + \rho_o u_s^2 \quad (2.73b)$$

$$\frac{\gamma}{\gamma - 1} p u + \frac{\rho u^3}{2} + F_R = -\frac{\rho_o u_s^3}{2} - \frac{\gamma}{\gamma - 1} p_o u_s + F_{R,o} \quad (2.73c)$$

where u_s is the shock velocity with positive velocity in the upstream direction, and the remainder of the variables have the usual definition. The variables with subscript o represent upstream material quantities and variables without subscripts are downstream materials. This analysis will use a three region model, shown in figure 2.7, with a final state downstream, a radiative precursor upstream, and an optically thin cooling layer just after the density jump that allows the radiation to affect the upstream material. There are actually five regions with adaptation zones on either side of the cooling layer that transition between the upstream and downstream conditions and the cooling layer[70], but this analysis will not include those regions. Setting the boundary conditions allows one to solve energy conservation equations across the boundaries and generate shock profiles.

It is useful to define normalizations of typical radiation hydrodynamic variables that will be utilized in the analysis below, starting with the inverse compression, $\eta = \frac{\rho_o}{\rho}$. The normalized pressure is then, from equation 2.73b $p_n = \frac{p}{\rho_o u_s^2}$ and, assuming an ideal gas equation of state $p = \rho RT$, the normalized temperature is $RT_n = \frac{RT}{u_s^2}$, where $R = \frac{k_B(1+Z)}{Am_p}$ is the gas constant. Using the jump condition above, it is possible to write the normalized pressure and temperature as functions of only the inverse compression independent of the boundary conditions in the upstream and downstream media. Combining equations 2.73a and 2.73b, the expression for the normalized pressure is

$$p_n = 1 - \eta + p_{o,n}. \quad (2.74)$$

Then from equation 2.73b and the ideal gas equation of state, one can derive the

following expression for normalized temperature as a function of inverse compression,

$$RT_n = \eta(1 - \eta + p_{o,n}) \quad (2.75)$$

2.3.3.1 Thick-Thick Shocks

For the optically thick shock, the upstream and downstream states are optically thick, naturally, this means that far enough upstream there is no radiation flux and downstream there is no net flux. The upstream pressure p_o is negligible compared to the shock generated pressures and the analysis will take it to be zero from here on. Considering equation 2.73c with $p_{n,o} = 0$ and $F_{n,o} = 0$ because the upstream is optically thick and cold, one can write an expression for the normalized flux as a function of the inverse compression

$$F_{R,n} = -1 + \frac{2\gamma}{\gamma - 1}\eta - \eta^2 \left(\frac{\gamma + 1}{\gamma - 1} \right), \quad (2.76)$$

where $F_{R,n} = \frac{F_R}{\rho_o u_s^3}$. The next step is to use the energy equation at the two boundaries in the three layer model to find the optical depth and upstream temperature of the cooling layer by assuming the strong shock limit.

In the three-layer model, shown in figure 2.7, the optically thick downstream material has a temperature T_f and an isotropic thermal radiation field $B(T_f)$. The cooling layer, as stated above, is optically thin with an optical depth τ_{cl} , which is necessary to accurately account for the energy balance across the boundaries. The thermal radiation field in the cooling layer is a function of the optical depth, $B_d(\tau)$, where the optical depth in the cooling layer increases monotonically from the upstream edge to the beginning of the downstream state, and, therefore, the intensity decreases towards the downstream state. The temperatures just upstream and downstream of the density jump have the subscripts us and ds respectively. This analysis assumes

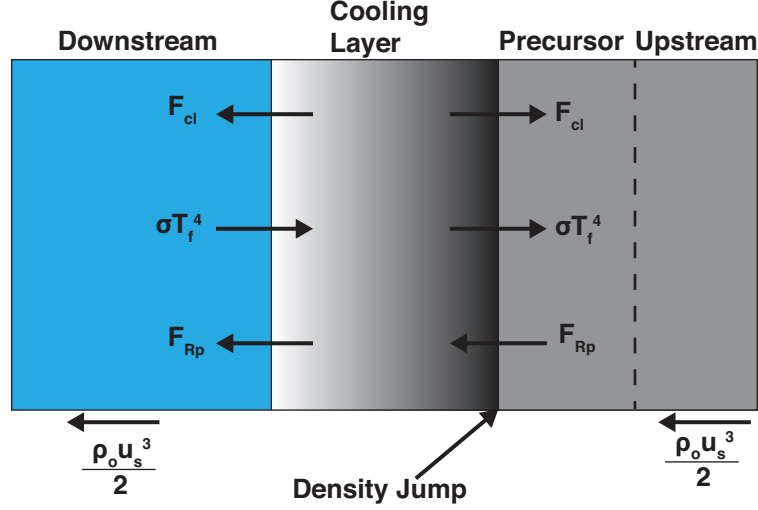


Figure 2.7: The three layer model that demonstrates the fluxes in an optically-thick, radiative shock structure with a downstream state, an optically thin cooling layer, and a precursor region.

a very optically thick precursor region and that the upstream temperature can be written as proportional to the final temperature, $T_{us} = f_s T_f$. Across the downstream cooling layer boundary, the energy balance is the result of the flux from the edge of final state, the cooling layer, and the precursor. The flux from the downstream is σT_f^4 , from the cooling layer is $-1.2\tau_{cl}\sigma T_{ds}^4$, and from the precursor is $f_s^4\sigma T_f^4(1 - \tau_{cl})$. The factor of 1.2 in the cooling layer flux term comes from the integral of the solution to the transport equation over solid angle. The precursor flux term propagates, at temperature T_{us} to the downstream boundary, where $(1 - \tau_{cl})$ is the exponential decay of the source under the approximation of small τ_{cl} . The sum of these fluxes is zero because there is no flux in the downstream final state. The energy conservation at the boundary between the cooling layer and the precursor uses the same fluxes just described, but with the inclusion of the material energy flux from upstream, which results in the expression,

$$(1 - \tau_{cl})\sigma T_f^4 + 1.2\tau_{cl}\sigma T_{ds}^4 - f_s^4\sigma T_f^4 = \left(-1 + \frac{2\gamma}{\gamma - 1}\eta - \frac{\gamma + 1}{\gamma - 1}\eta^2\right) \frac{\rho_o u_s^3}{2}. \quad (2.77)$$

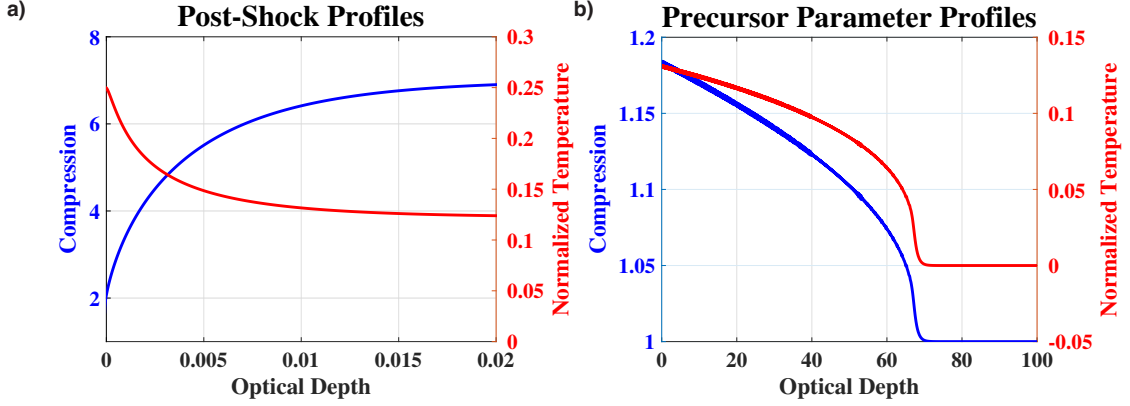


Figure 2.8: The shock compression and normalized temperature in the cooling layer (a) and precursor (b) using a Q of 10^5 and γ of $\frac{4}{3}$. The precursor is diffusive and shows a transmissive region at the leading edge before the unaffected upstream state.

On the left hand side of the above equation, the first term is the emission from the downstream state with the decay from the opacity in the cooling layer, the second term is the emission from the cooling layer, the third term is the emission from the precursor. The right hand side of the equation is the normalized photon flux times the material energy flux from upstream. Solving these two equations under the strong shock conditions, $T_{ds} = (3 - \gamma) T_f$ and $\eta_{ds} = \frac{2(\gamma-1)}{\gamma+1}$, results in values for τ_{cl} and f_s . It is useful to simplify these equations with the shock strength parameter $Q = \frac{2\sigma u_s^5}{\rho_o R^4}$ and the shock γ as the free parameters. When numerically solving these equations using $\gamma = \frac{4}{3}$ and $Q = 10^5$, the values of τ_{cl} and f_s are 0.0019 and 0.996 respectively.

Evaluating the radiation transport in the three-layer model allows one to solve for the inverse compression profile. Since the optical depth of the cooling layer is small and considering the flux must be continuous across boundaries, it is reasonable to assume that J_R is constant in the cooling layer. This also implies that the flux in the cooling layer equals the final state flux, $J_R = \frac{\sigma T_f^4}{\pi}$. Taking the derivative with respect to the propagation direction z of equation 2.76 is,

$$\frac{\partial F_{R,n}}{\partial z} = \left[\frac{-2\gamma + 2\eta(\gamma + 1)}{\gamma - 1} \right] \frac{\partial \eta}{\partial z}. \quad (2.78)$$

Using the transport model, described above, for the radiation and the assumptions for J_R in the cooling layer described above, one is left with the following equation for η in the cooling layer,

$$\left[\frac{-2\gamma + 2\eta(\gamma + 1)}{\gamma - 1} \right] \frac{\partial \eta}{\partial z} + 4Q\eta^4(1 - \eta)^4 = 4Q \left(\frac{\gamma + 1}{\gamma - 1} \right)^4 \left(1 - \frac{\gamma + 1}{\gamma - 1} \right)^4. \quad (2.79)$$

Numerically solving equation 2.79 with $\gamma = \frac{4}{3}$ and $Q = 10^5$ results in the compression and temperature profiles shown in figure 2.8 a.

Assuming diffusive radiation transport for the precursor region, which is reasonable for the system with many photon mean free paths described here, one finds two coupled equations for η as a function of optical depth. Using equation 2.76 for the flux as a function of η and combining this with an Eddington diffusion model results in an expression relating the average intensity to η ,

$$1 - \frac{2\gamma}{\gamma - 1}\eta + \frac{\gamma + 1}{\gamma - 1}\eta^2 - \frac{4\pi\kappa_P f_E}{\bar{\chi}} \frac{\partial J_{R,n}}{\partial \tau} = 0, \quad (2.80)$$

where $f_E = \frac{1}{3}$ is the Eddington factor, $J_{R,n}$ is the normalized average intensity, κ_P is the Planck mean opacity, $\bar{\chi}$ is the Rosseland mean opacity, and $\tau = \kappa_P \partial z$ is the optical depth. The second equation comes results from an approach similar to the derivation of the cooling layer equation above. The result is,

$$\pi \left[J_{R,n} - \frac{Q}{\pi} \eta^4 (1 - \eta)^4 \right] = \left[\frac{\eta(\gamma + 1) - \gamma}{\gamma - 1} \right] \frac{\partial \eta}{\partial \tau}. \quad (2.81)$$

Simultaneously solving equations 2.80 and 2.81 with the same γ and Q values as above results in the precursor compression and temperature profiles shown in figure 2.8 b. The temperature profile in figure 2.8 b shows a diffusive precursor, which is reasonable based on the assumptions of the radiation transport, and the required transmissive region at the leading edge[1].

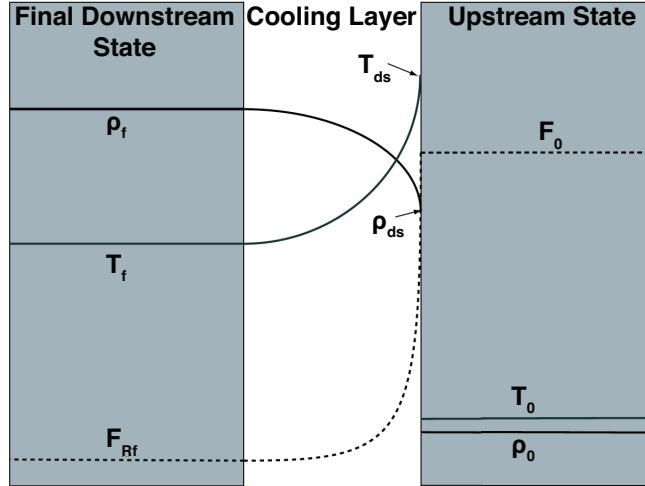


Figure 2.9: The three-layer model describing the physical picture of the thick-thin radiative shock. The upstream state has an initial pressure and radiation flux compared to the optically thick case, which sets these values to zero. This figure was adapted from the work of McClarren *et al.* [4]

In laboratory experiments, the upstream material is finite in extent and therefore, if it starts optically thick, always becomes optically thin. This further implies there is a point where the upstream medium is several mean free paths in length and neither an optically thick or thin treatment is applicable. In this situation, it is necessary to evaluate the precursor flux in the transport regime described above and evaluate the integral for J_R explicitly in order to correctly satisfy the energy balance. This is not treated further here, but the author points this out to acknowledge the limits of the theory in the analysis of experimental results.

2.3.3.2 Thick-Thin Shocks

As previously stated, when the upstream is optically thin, whether by the nature of the medium or due to its finite extent, there are changes to the physical picture of the shock structure. This section will discuss the differences in the guiding equations and the results of the analysis that will be useful for comparing to experimental results later.

The thick-thin shock uses a three-layer model, similar to the optically thick shock,

but here the upstream region has a constant value for the flux because the radiation is streaming through this region and is not readily absorbed. This model also uses $p_0 \neq 0$ and $F_{R,0} \neq 0$ due to the radiation present in the upstream material. The results presented below follow the approach McClarren *et al.* take in deriving the final state and immediate downstream conditions in a thick-thin radiative shock [4]. Progressing in the same way as for the optically thick shock, combining the three jump condition equations, equations 2.73a, 2.73a, and 2.73a, into a single expression results in the equation,

$$F_{Rn} - F_{Rn0} = -1 + \frac{2\gamma}{\gamma - 1} [\eta - p_{0n} (1 - \eta)] - \frac{\gamma + 1}{\gamma - 1} \eta^2, \quad (2.82)$$

where the subscript n indicates the normalized values and the 0 represents the upstream values. The variable names have the same definitions as in the optically thick shock case. This equation allows one to come up with fairly simple expressions for the final state temperature and inverse compression.

One can find the final state inverse compression from equation 2.82 with the realization that the net flux is zero in the final state due to the fact that it is optically thick. This allows for the solution of equation 2.82 as a function of the upstream pressure and radiation flux. The solution of this quadratic equation is,

$$\eta_f = \frac{\gamma(1 + p_{0n}) - \sqrt{(p_{0n}\gamma - 1)^2 + F_{Rn0}(\gamma^2 - 1)}}{\gamma + 1}. \quad (2.83)$$

Using the normalized temperature, described above, and inserting the final value of the inverse compression provides an expression for the final temperature,

$$RT_{nf} = \frac{1}{(\gamma + 1)^2} \left[p_{0n}\gamma + \gamma - \sqrt{(p_{0n}\gamma - 1)^2 + F_{Rn0}(\gamma^2 - 1)} \right] \left[p_{0n} + 1 + \sqrt{(p_{0n}\gamma - 1)^2 + F_{Rn0}(\gamma^2 - 1)} \right], \quad (2.84)$$

which has a dependence on the upstream pressure and radiation flux. Under the assumption of a small optical depth of the cooling layer, the cooling layer flux is, to accuracy of order τ_{cl}^2 ,

$$F_{Rn0} = 2Q [\eta_f (1 + p_{0n} - \eta_f)]^4, \quad (2.85)$$

where τ_{cl} is the optical depth of the cooling layer, as in the optically thick shock. This expression for the upstream flux allows one to solve for the final inverse compression, and consequently the final state temperature [4]. This results in an eighth order polynomial where the numerical solution typically has one real root, that is less than one and physical.

The immediate post-shock state describes the conditions on the post-shock side of the density jump and the fact that the flux at that point must be the same as the upstream flux allows for simple analysis understand this state. Solving equation 2.82 for η under this condition results in the following expression for the initial downstream inverse compression,

$$\eta_{ds} = \frac{\gamma - 1}{\gamma + 1} + \frac{2\gamma}{\gamma + 1} p_{0n}, \quad (2.86)$$

where η_{ds} is the initial downstream inverse compression, and is only a function of the upstream pressure. The normalized temperature is then the result of substituting the above result in equation 2.75,

$$RT_{dsn} = \frac{[2 - (\gamma - 1) p_{0n}] [2\gamma p_{0n} + \gamma - 1]}{(\gamma + 1)^2}. \quad (2.87)$$

The last feature of thick-thin shocks that this document will discuss is the optical depth of the cooling layer. This is a relevant value for understanding the volume of the region providing the greatest cooling effect to the post-shock material and will verify the assumption used to determine the final state conditions. The radiation leaving the final must balance the cooling layer flux, as the upstream does not contribute a flux traveling towards the downstream state, an expression for the cooling layer

flux is necessary to determine the cooling layer optical depth [4]. Leaving the details to the work of McClarren *et al.*, the cooling layer optical depth, to a second order approximation is,

$$\tau_{cl} = \frac{T_f^4}{2T_{ds}^4}. \quad (2.88)$$

This means that in order for the earlier assumption to hold, T_{ds} must be larger than the final state temperature, T_f . For a reference point, a factor of 2 difference between the final and downstream temperatures results in a cooling layer optical depth of about 0.03. These conditions can occur in a shock with Q of a few thousand, with the exact threshold depending on the upstream pressure, which is very achievable in the laboratory.

CHAPTER III

Photoionization Front Experiments on the Omega Laser Facility

Heat fronts have been a topic of experimental studies in HEDP for at least the last three decades [27, 28, 29, 30, 31, 66]. None of these experiments have definitively shown that they produced photoionization (PI) fronts as described in the previous chapters [61]. To fully understand the evolution and behavior of PI fronts, it is necessary to design an experiment that has the correct conditions and set of measurements to distinguish between the physics regime of the atomic kinetics. This means that one needs to measure enough of the plasma parameters to determine α and β . The following sections will describe the Omega Laser Facility at the Laboratory for Laser Energetics located on the University of Rochester campus, which is the energy source used to create the x-ray drive for the heat front. It will continue with a discussion of x-ray absorption spectroscopy as the primary diagnostic technique, the setup of the experiment, design simulations, and the analysis of the data from a day of experiments in September of 2018.

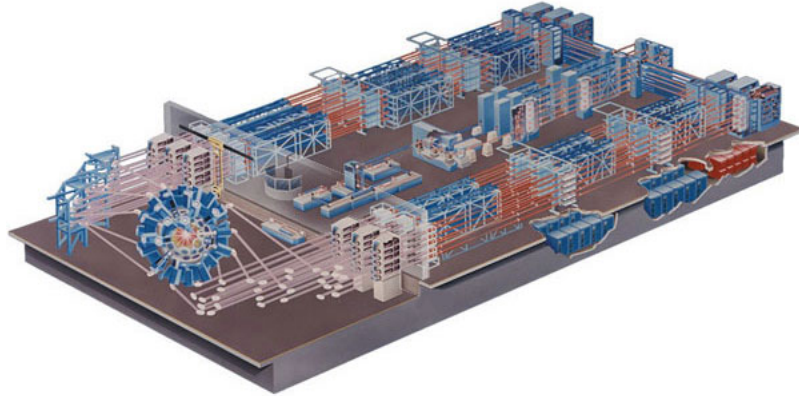


Figure 3.1: The Omega laser facility at the Laboratory for Laser Energetics taken from the image gallery at lle.rochester.edu.

3.1 Omega Laser Facility

The Omega Laser Facility, called Omega from here on, is a 60 beam ND:glass laser that produces pulses on the order of 1 ns with up to 500 J per beam for a total available energy of 30 kJ. It uses three seed pulses, which are then split into a total of 60 beams, arranged in a sphere, that can have independent pointing within the 3 m diameter target chamber [108]. A variety of phase plates are available to users to smooth the spatial profile of the beams and smoothing by spectral dispersion to change the speckle pattern in time. Each of the 60 beams has the capability for an independent time delay of about -7 ns to 9 ns, depending on the particular beam. The benefits of a user facility like the Omega laser facility is the large number of diagnostics available to perform the measurements desired for a particular experiment. There are six diagnostic ports on the target chamber that are able to house a wide array of instruments based on a standard interface called the ten-inch manipulator (TIM).

3.2 Primary Diagnostic: Absorption Spectroscopy

The primary measurement in these experiments on PI fronts conducted on Omega is K-shell absorption spectroscopy. This means that the collected spectra will show line features corresponding to the electronic transitions from the $n = 1$ state to the $n = m$ state where n is the principal quantum number and m is an integer greater than 1. This measurement probes the ground states of the ions and allows one to determine a wealth of information about the plasma conditions including the ionization state distribution, the temperature, and the density under various assumptions [34, 109]. The bound-bound electron transitions in an atom or ion introduce sharp line features in the opacity, with the exact details captured in the line shape functions that are very dependent on the particular transition of interest.[103, 109] The appearance of the absorption features depends on the shape of the input spectrum and the material opacity with the dependence $I_{abs,\nu} = I_{0,\nu}e^{-\rho\kappa_\nu z}$ where $I_{abs,\nu}$ is the absorbed spectrum, $I_{0,\nu}$ is the initial spectrum, ρ is the mass density in g cm^{-3} , κ_ν is the frequency-resolved opacity in $\text{cm}^2 \text{g}^{-1}$, and z is the propagation distance. Each ionization state of a particular element has a different set of energy levels due to the increase of effective nuclear charge that an electron sees. This leads to a change in the line structure due to the differing number of electrons and effective nuclear charge in addition to a general blue shift in the bound-bound transitions and the bound-free continuum.

The practical application of this measurement technique requires an external radiation source that is spectrally featureless. Typically, experiments accomplish this using unresolved transition arrays from high-Z elements, capsule implosions, or foil emission above the K-edge [13, 110, 111, 112, 113, 114, 115]. In order to make absorption measurements, the external source flux must exceed the self-emission from the plasma. This corresponds to the first term in equation 2.24 dominating over the second, integral term and therefore the detector only sees contributions from the

plasma opacity in the exponent.

3.3 Design Simulations

In order to make informed decisions on measurement timing, diagnostic window locations, and data estimates, this work conducted a simulation study that should reasonably approximate the experiment. This is an important step in any experimental work as it provides all of the information about a system, which is not the case in an experiment, and can help one develop a physical intuition for the processes at play. This comes with the tradeoff that simulations always require assumptions to make it possible for a computer to reach a stable answer. This has the secondary benefit of requiring the scientist to think critically about the simulation output to determine if the results are physical or an artifact of the numerical methods and computational errors at play.

Here, there are two simulation tools used in the design of photoionization front experiments: Radiation hydrodynamics simulations and atomic kinetics calculations. The radiation hydrodynamics simulations provide a view of the macrophysics that occurs due to the heat front passing through the gas cell, such as changes in temperature, density, and velocity. The atomic kinetics calculations investigate the microphysics of

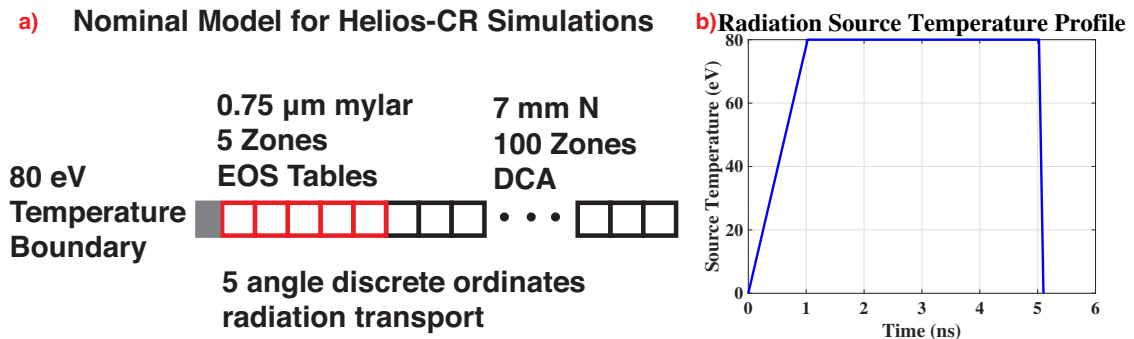


Figure 3.2: a) The geometry of the Helios-CR simulations used to design the Omega experiments to measure PI fronts with the zoning, the materials, and the physics model. b) The time dependence of the temperature boundary, which use the results of Davis *et al.* to determine the rise time and maximum temperature [5, 6].

the plasma by evaluating the rate coefficients to determine the ionization state distribution and resulting opacities and emissivities at different temperature and density conditions. As section 2.3.2 described above, it is necessary to have both pictures of the PI front to fully understand what is happening.

3.3.1 Helios-CR Radiation Hydrodynamics Simulations

The Helios-CR from Prism Computational Sciences code is one dimensional, radiation hydrodynamics code that uses Lagrangian spatial coordinate and allows for non-diffusive radiation transport and in-line atomic kinetics calculations [65]. The non-diffusive radiation transport model evaluates the general solution to the radiation transport equation with 1, 2, or 5 angles and uses absorption and scattering opacities. The atomic kinetics calculations solve the collisional radiative equations using the following atomic processes: Radiative recombination, stimulated recombination, photoionization, three-body recombination, electron collisional ionization, electron collisional deexcitation, electron collision excitation, spontaneous emission, stimulated emission, photoexcitation, dielectronic recombination, and autoionization. The code calculates the rate coefficients for these processes using a subset of the electron energy levels in the ATBASE atomic structure database on a highly resolved frequency grid and solves the matrix equation to produce an ionization state distribution. The work of Gray *et al.* showed the differences between multi-group diffusion with tabular opacities and the physics model available in Helios-CR for the PI front problem [62, 63].

3.3.1.1 PI Front Simulations

The simulations used a temperature boundary to act as the ionizing radiation source driving the PI front, using the time profile in Figure 3.2 b with a maximum temperature of 80 eV [5, 6]. The gas cell model uses a 0.75 μm mylar window followed

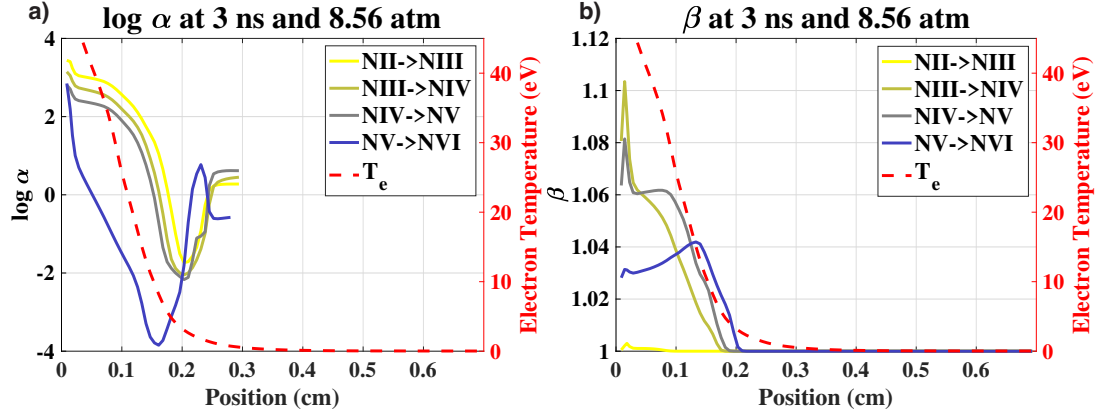


Figure 3.3: The calculated values of α , a), and β , b), from the Helios-CR simulations with the electron temperature overlaid to give a more physical reference. These figures show a selection of ionization state transitions with the minimum value of α indicating the location of the PI front. The values of α are well below one suggesting the plasma is photoionizing and the values of β at the locations of minimum α are about one, satisfying the conditions for a PI front.

by 7000 μm of N gas, as follows the experimental parameters. There are 5 zones of mylar using LTE physics due to the fact that it is at solid density, tabular EOS and opacity tables with a quotidian EOS model, and multi-angle radiation transport. The N uses a pressure of 8.5 atm in 100 zones to provide adequate mass matching to the mylar and uses detailed configuration accounting (DCA) in-line atomic kinetics calculations to generate opacity values for the radiation transport and the radiation hydrodynamics uses tabular EOS values.

As discussed in section 2.3.2, the atomic kinetics determine the physics regime of the PI front through the dimensionless parameters α and β . To do this, a post-processing script takes the plasma parameters and calculates the atomic rate coefficients to determine the dimensionless parameters for each ionization state using the Verner and Ferland rates and the Lotz formula [104, 105]. The photoionization rate, $\Gamma_{i,i+1}$, defined in equation 2.54, needs to account for the changes in radiation flux between zones due to absorption. To accomplish this, the post-processing follows the treatment in Gray *et al.* and uses the fourth power of the ratio between the local

radiation temperature to the source temperature to scale the source flux,

$$F_l = \left(\frac{T_{R,l}}{T_{R,s}} \right)^4 F_s, \quad (3.1)$$

where T is the temperature and F is the flux with s and l indicating the source and local values respectively.

Evaluating the rate coefficients for spatial grid points in the N, the calculated values of α and β in figures 3.3 a and b suggest that this experimental design will produce a PI front out to over 1 mm from the source about halfway through the x-ray drive. This is because in the locations where α is much lower than unity, β is about one. These simulations additionally show that the evolution of the dominant ionization state happens over a fairly small region up until the NV state when the opacity is at a low enough value that the photon mean free path is significant, relative to the experimental length scales. Further investigation of the α profiles provides the insight that the minimum α value coincides with the location of the PI front in that ionization state.

3.4 September 11th 2018 Experiments

Experiments at Omega in September of 2018 were the first to use a gas cell platform with absorption spectroscopy using a capsule implosion as the probe source to characterize PI fronts. As this is the first experiment with this platform, the desired outcome was to characterize the absorption spectroscopy platform and acquire data on all of the diagnostics.

3.4.1 Experiment Geometry

This experiment requires a gas cell to hold the propagating medium, an x-ray source to drive the PI front, and a probe source. Figure 3.4 a shows a cartoon version

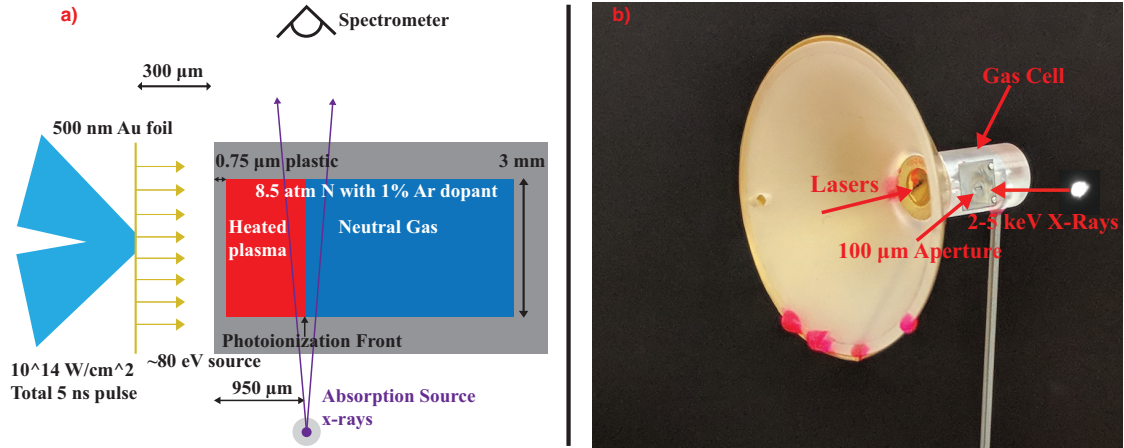


Figure 3.4: a) A cartoon of the experiment geometry showing the dimensions and measurement geometry. b) An image of the target used in the experiments showing how this connects to the cartoon in a).

of the geometry used here. The gas cell is a single, machined structure made of acrylic that has all of the features needed to stalk, fill, and shield the target. The gas cell is mostly cylindrical with a 7 mm long interior dimension and an inner diameter of 3.2 mm, but along the measurement axis there are flat walls with a 3 mm separation to simplify the measurement geometry and to set the window thickness. There is a cone at the front end of the gas cell that extends out 11.75 mm from the front at a 45° angle to support 100 μm Au shielding. There are two 1 mm diameter diagnostic windows, positioned over the flat inner surfaces of the gas cell, which are blind holes leaving 50 μm of acrylic to support the gas but allow the probe x-rays through. In order to limit the spatial integration of the measurement and to limit background, a piece of 100 μm thick Au shielding sits over the diagnostic window towards the TIM 3 spectrometer that limits the detection window to 600 μm along the propagation direction and 1 mm in the transverse direction. There is a well at the front of the gas cell to fit a window that allows the drive x-rays to interact with the gas, which is a 750 nm thick LUXfilm foil from the LUXEL corporation with a 100 μm thick stainless steel hexagonal grid support. The hexagonal grid has a 4 mm OD and a 3 mm ID with 610 μm pitch hexagons and 50 μm thick support bars. The x-ray

source is a $0.5 \mu\text{m}$ thick Au foil irradiated with $10^{14} \text{ W cm}^{-2}$ for 5 ns, which the work of Davis *et al.* showed produces a quasi-blackbody of approximately 80 eV on the surface opposite the laser incidence with a 0.5 ns rise time [5, 6]. The Au foil sits on a $100 \mu\text{m}$ thick Au washer with a 5 mm OD and a 3 mm ID. There is an additional well at the front of the gas cell to seat the Au foil, which places the front surface of the Au foil $1250 \mu\text{m}$ from the center of the probe windows. The stalk is made of a hollow Tungsten Carbide with an $800 \mu\text{m}$ OD and sits at the rear of the target using a blind hole drilled along the axis of the gas cell to allow gas to flow into the target. Figure 3.4 b shows an image of the target and identifies the drive foil, gas cell, and stalk.

The probe source is a CH capsule from General Atomics, described in more detail below, with an about $860 \mu\text{m}$ OD, an $8.7 \mu\text{m}$ wall thickness and an interior volume held at vacuum. The interior volume is initially held at vacuum, but it is almost certain that air leeches into the capsule through the wall before the experiments occur. The Silicon Carbide stalk is $130 \mu\text{m}$ thick and attached using glue to secure the capsule in place. The capsule positioning in the target chamber places it 10 mm from the gas cell axis $1250 \mu\text{m}$ from the front surface of the Au drive foil and $25 \mu\text{m}$ below the center of the measurement windows. In order to limit the source size of the capsule emission, there were two Al posts that attach to a W foil containing a $600 \mu\text{m}$ by $125 \mu\text{m}$ slit that the design fixes over the center of the diagnostic window in the axial direction, but is $20 \mu\text{m}$ below the center of the window in the transverse direction. This shift off of center is to adjust the spectrometer energy range to include the Ar k-shell within the limitations of the target. The W aperture foil sits 5 mm away from the gas cell axis towards the capsule target and figure 3.4 b shows the aperture foil attached to the gas cell.

3.4.2 Laser Configuration

This experiment uses thirty of the available sixty beams on Omega with ten directed towards the Au foil for creating the drive source and 20 towards the CH capsule to produce the probe source. All of these beams use smoothing by spectral dispersion to prevent laser “hot spots” from sitting in the same place through the duration of the pulse.

This experiment uses ten beams to create the x-ray drive, called the drive beams from here on, using SG-5 phase plate that have the effect of smoothing the spatial profiles and limiting the spot size to an ellipse with $850\ \mu\text{m}$ major axis and $630\ \mu\text{m}$ minor axis [116]. These drive beams point $1250\ \mu\text{m}$ off of TCC towards the Au foil and each uses a 1 ns square pulse with 450 J in each beam. To drive the foil for 5 ns, the beams are incident in pairs of two beams with delays of 0, 1, 2, 3, and 4 ns to produce a 5 ns long laser pulse. The angle of incidence determines the beam pairing with the largest angles paired to the smallest angle, and so on, to keep the irradiated area similar throughout the duration of the drive. This results in a laser intensity of about $10^{14}\ \text{W cm}^{-2}$ for each pair of beams.

Due to the size of the gas cell target, only twenty beams are available to drive the capsule implosion that probes the conditions at the PI front, from here on called the probe beams. These beams do not use phase plates, as they point too far away from the center of the target chamber. Each of the beams uses a 1 ns square pulse and nineteen have an $800\ \mu\text{m}$ spot diameter with one having a $400\ \mu\text{m}$ spot diameter to compensate for the lack of available beams due to the large gas cell target acting as an obstacle. The probe beam pointing is 10 mm off of the center of the target chamber along the diagnostic window axis at the CH capsule. By the nature of the beams available, the laser irradiation pattern is not uniform across the capsule surface, section 3.4.4 quantifies this anisotropy, and so the figure of merit is the average intensity, which is about $4 * 10^{14}\ \text{W cm}^{-2}$. The range of the intensities over

Diagnostic Port	Diagnostic	Pointing
TIM 1	ADP Time-Integrated Spectrometer	Capsule
TIM 2	X-Ray Framing Camera	Capsule
TIM 3	ADP Time-Integrated Spectrometer	Gas Cell
TIM 4	TIM Target Positioner	Gas Cell
TIM 5	Soft X-Ray Framing Camera	Au Foil
TIM 6	Soft X-Ray Framing Camera	Capsule
Dante	Dante Diode Array	Capsule

Table 3.1: The diagnostic configuration on the Omega laser facility for the experiments to measure PI fronts.

the capsule surface spans 10^{14} to $7 * 10^{14}$ W cm⁻².

3.4.3 Diagnostic Choices and Configurations

This experiment uses a variety of diagnostics to measure the properties of PI fronts and to characterize the drive and probe sources. This approach is especially necessary in spectroscopic measurements where numerous processes contribute to the total spectrum and it is necessary to extract any background sources or features inherent to the source to produce an accurate analysis. Before going into the details, it is important to define the geometry of the diagnostic ports on Omega. There are six ports that support TIM-based diagnostics, which are arranged in such a way that TIMs 2 and 3 and TIMs 4 and 6 are opposite each other, called the TIM 23 and TIM 46 axes from here on. In addition, the angle between the TIM 23 and TIM 46 axes is 79.8° making them nearly orthogonal. TIMs 1 and 5 view the plane made by the TIM 23 and TIM 46 axes at oblique angles. The gas cell target positioning aligns the diagnostic window axis with the TIM 23 axis having the capsule sit on the TIM 2 side and the Au foil parallel with the TIM 23 and TIM 46 plane.

Table 3.1 provides an overview of the diagnostic selection and relative positions for these experiments. Both of the time-integrated spectrometers, in TIMs 1 and 3, use Ammonium Dihydrogen Phosphate (ADP) crystals at an angle of 19° , which is steeper than the standard 15.56° for the diagnostic housing to shift the spectral

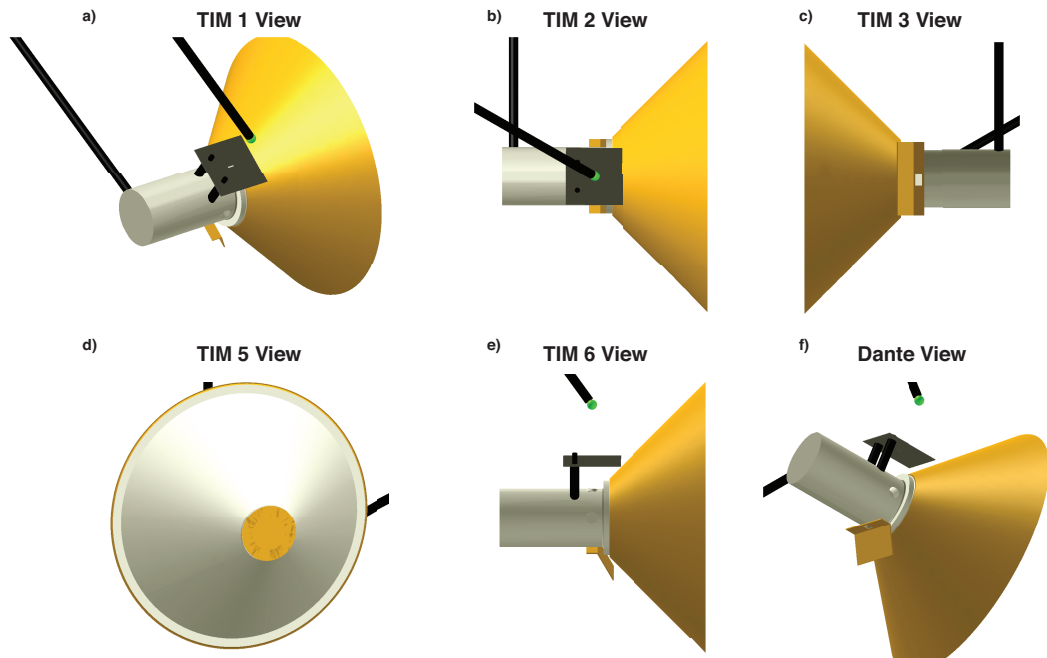


Figure 3.5: The different diagnostic views of the target for these experiments. a) The view of the target from the time-integrated spectrometer in TIM 1. b) The view of the target from the x-ray framing camera in TIM 2. c) The view of the target from the time-integrated spectrometer in TIM 3. d) The view of the target from the soft x-ray framing camera in TIM 5. e) The view of the target from the soft x-ray framing camera in TIM 6. f) The view of the target from the Dante diagnostic.

range from 2-3.25 keV to 2.25-4 keV to accommodate the target geometry for the Ar k-shell lines. These spectrometers use image plates to record data and use a Saran foil over half of the entrance slit to use the Cl K-Edge at 2.82 keV as a spectral fiducial [117, 118, 119].

The TIM 1 spectrometer has a direct line of sight to the capsule emission, which provides a reference spectrum to compare the absorption data to and to remove source features. The TIM 3 spectrometer observes the transmission of the capsule emission through the gas cell. Figures 3.5 a and c show the views of the TIM 1 and TIM 3 spectrometers respectively.

The x-ray framing camera (XRFC) in TIM 2 provides a measure of the source size with four independently timed multichannel plate (MCP) using a 50 ps pulse forming network (PFM) on each strip. An array of sixteen, 15 μm pinholes arranged in a 4x4 grid allows for four images per strip with a magnification of 4.6. There was a 300 V bias applied to each strip to reduce the gain and prevent the images from saturating. Figure 3.5 b shows the view of the experimental target from the TIM 2 camera.

It is possible to use a TIM as a target positioner to add more targets if that is what an experiment calls for. Here, the experiment uses TIM 4 to position the gas cell, which means that in order to correctly align the diagnostic windows with the TIM 23 axis the stalk angle must be 10.8° .

TIMs 5 and 6 have a soft x-ray framing cameras that use two grazing incidence mirrors to select x-rays with energies below about 750 eV along with a center channel that contains higher energy photons. The TIM 5 camera views the front surface of the Au foil with a 200 ps PFM and a four strip MCP that each have a 200 V bias. The TIM 6 camera views the implosion capsule using a 200 ps PFM and a 0 V bias on all four MCP strips with a magnification of 3. There are three channels in each camera with the input channel having a 25 μm pinhole and a 3° Al mirror with a 5 μm thick parylene-N filter, the center, harder x-ray channel has a 10 μm pinhole with

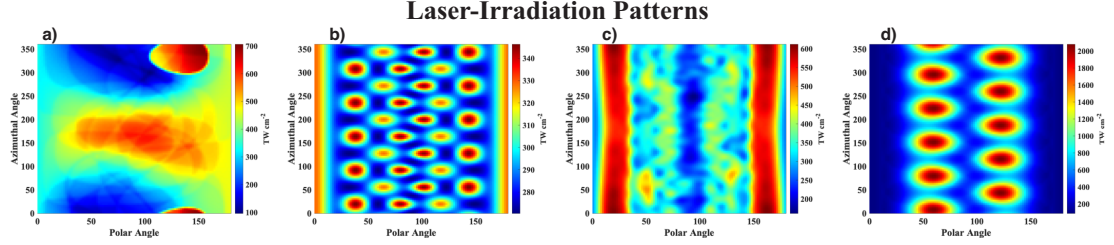


Figure 3.6: a) The laser intensity on the surface of the capsule used in the experiments described here from the VisRad view factor code. b) The spherically symmetric case, modeled with the Omega-60 laser geometry, to approximate a uniformly-irradiated capsule using the VisRad view factor code. c) The polar drive case, modeled with the NIF laser geometry, to show a cylindrically symmetric irradiation pattern using the VisRad view factor code. d) The laser intensity pattern used in the capsule implosions from the work of Hansen *et al.* [7].

a 25.4 μm Be filter, and the output channel has a 25 μm pinhole and a 3° Al mirror with a 1 μm V filter. Figures 3.5 d and e show the target views from TIMs 5 and 6.

The Dante diagnostic is an array of absolutely calibrated, filtered diodes, using either metal foils grazing incidence mirrors, that provides a time resolved flux measurement. There are 18 channels on the Omega Dante that span from 50 to 20000 eV with bandwidths from tens to thousands of eV. These diodes provide information on the time evolution of the capsule implosion and can provide an effective temperature from unfolding the flux measurements with calibrated response functions for each channel [6, 120, 121]. Figure 3.5 f shows the view of the target from the Dante diagnostic.

3.4.4 Capsule Anisotropy Characterization

In the ideal case for capsule implosions, the laser intensity would be the same, or within a small percentage of the average, over the whole surface of the capsule. When this is not possible, it is useful to quantify the anisotropy in the irradiation pattern, in at least a relative way. To develop an anisotropy parameter, one needs a model of the initial laser intensity on the surface of the capsule. These calculations will use the VisRad view factor code to generate a spatial grid on a sphere to perform

this analysis [122]. These laser patterns, created in VisRad, capture the initial laser pattern at zero time, but they will change shortly after irradiation when the capsule surface forms a plasma. The average laser intensity, \bar{I} in TW cm⁻², on the capsule, is the sum of the intensity in each grid divided by the number of gridded regions,

$$\bar{I} = \frac{1}{N} \sum_i^N I_i,$$

where N is the number of regions in the grid and I_i is the intensity in the i th grid region. Since any line-of-sight to the capsule sees a hemisphere, it can never capture the entire surface and the anisotropy should compare how different the capsule appears from various observation directions, making the intensity for a particular line-of-sight important,

$$I_{LoS,j} = \sqrt{\frac{1}{n} \sum_j^n I_j^2},$$

where $I_{LoS,j}$ is the laser intensity from the j th line-of-sight and n is the number of grid regions in a single line-of-sight. I_{LoS} is the root-mean-square value of the intensity, which will capture the range of values in a particular line-of-sight. With these definitions it is possible to construct an anisotropy parameter, ϕ , that characterizes the difference between the line-of-sight values and the total capsule average,

$$\phi = \frac{1}{N_{LoS}} \sum_i^{N_{LoS}} e^{-\left|1 - \frac{I_{LoS,i}}{\bar{I}}\right|},$$

where N_{LoS} is the number of lines-of-sight in the VisRad model.

The anisotropy parameter, ϕ therefore takes into account the variation over the surface by comparing any one view of the sphere to the average, with a uniform irradiation pattern having $\phi = 1$. This allows for the parameter to observe symmetries in the irradiation pattern because symmetric lines of sight will have the same averages, which will increase ϕ overall. Due to the exponential nature of the parameter, the

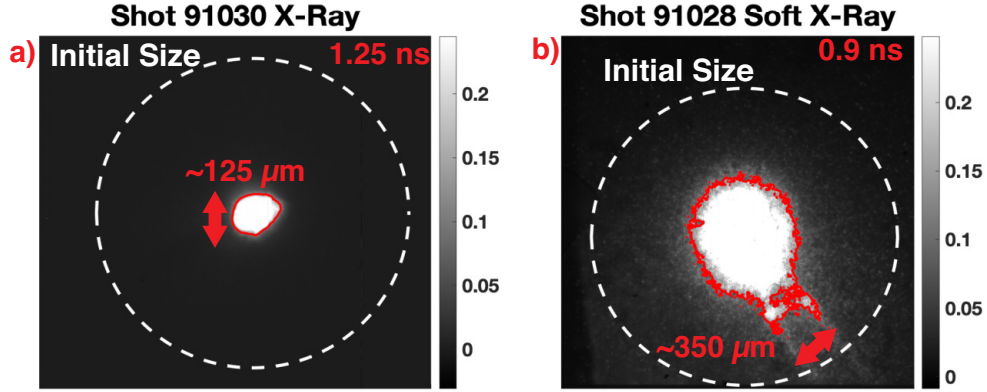


Figure 3.7: a) X-ray emission, > 2 keV, from the stagnated implosion at 1.25 ns after the start of the laser pulses. The image is saturated, but will provide an upper bound of about $125 \mu\text{m}$ for the emitting source size. The red curve is the 50% contour from the maximum pixel value. b) Soft x-ray emission, < 700 eV, from the capsule near stagnation at 0.9 ns from the start of the laser pulses. This image similarly suffers from saturation and provides an upper bound on the soft x-ray emission. The stalk is visible to the bottom right of the image. The red curve is the 50% contour from the highest pixel value.

minimum value of ϕ is zero. This occurs in a situation where the laser energy exists in two opposing grid points as the number of grid points goes to infinity. There may be other laser patterns that produce the minimum value of ϕ , but they will not be explored here. This is a very contrived scenario that is not practical on laser facilities capable of driving a capsule implosion. Since the intensity is an area-normalized quantity and the calculation normalizes ϕ to the average intensity, the scale of the facility or capsule should not affect the interpretation described above.

As stated above, it is possible to compare laser-irradiation patterns using ϕ . Figs. 3.6 a-d show the laser irradiation patterns for four different configurations: irradiated as in the experiment described here, in a spherical geometry at Omega, in a polar geometry at NIF, and in the 10 beam pattern from the work of Hansen *et al* [7]. The Omega capsules have an $850 \mu\text{m}$ diameter and the NIF capsule uses a 1.6 mm diameter [114]. To calculate the asymmetry parameter for each of these cases, VisRad view factor models were created for the capsules using 100 azimuthal and 100

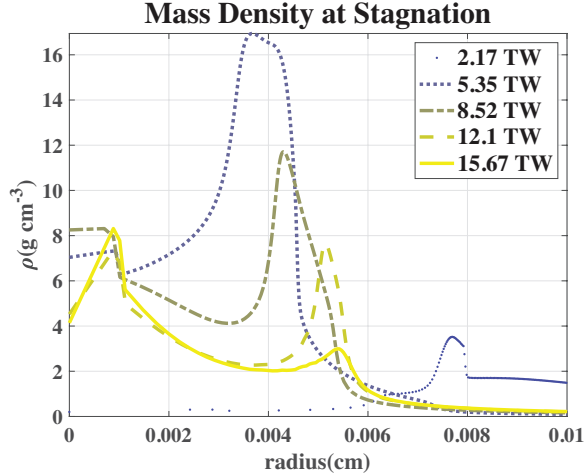


Figure 3.8: The mass density from Helios-CR simulations that varied the incident laser power over the range present in the laser irradiation pattern with the 8.52 TW the average over the capsule.

polar grid points then applying 60 Omega beams to the uniformly irradiated capsule, 64 NIF beams to the polar irradiated capsule, 20 Omega beams for the current work, and 10 Omega beams for the Hansen capsule design. This results in a ϕ of 0.9424 for the experiment presented here, 0.9983 for the spherically symmetric model, 0.9648 for the cylindrically symmetric model, and 0.7664 for the model in the work of Hansen *et al* [7]. From the interpretation stated above, this means the spherically symmetric model is the least anisotropic, followed by the cylindrically symmetric, then the current experiment, followed by the Hansen capsule. This analysis captures the range of intensity values in a particular line of sight, due to the use of the root-mean-square value. This explains why the pattern in the 10 beam pattern from Hansen *et al.* in Fig. 3.6 d is so much lower than the other three patterns with 20 or more beams.

3.4.5 Experimental Results and Simulations

This Omega shot day resulted in nine laser shots to execute the experiment. The experimental plan for this shot day was to take a series of calibration and null shots before moving into integrated physics targets while varying the probe source delay to

measure the evolution of the PI front. Appendix A provides more details on the exact experimental configuration for each shot. This approach provides the background and noise levels from the Au foil and the heated gas, which allows for better understanding of the data that results from the conditions inside the gas cell. The results of the background and null shots showed that there is sufficient shielding on the target and the Au foil and self emission from the gas cell contribute little to no signal to the measurements.

The experimental data, collected as described above, shows the parameters of the capsule implosion compare reasonably well with the data collected in previous experiments [123, 124, 125]. In addition, 1D simulations using the Helios-CR code, which is a Lagrangian radiation magnetohydrodynamics code that has diffusive and non-diffusive radiation transport models, detailed atomic physics, and a ray-tracing laser package, can provide information for designing a laser irradiation pattern [65]. Here, simulations using LTE conditions and diffusive radiation transport with 50 radiation groups varied the laser power on a CH capsule. The simulation used a spherical geometry, with 3 zones of “vacuum”, which is actually 0.2 atm of air for mass matching purposes, that is 420.9 μm thick followed by CH region of 500 zones that is 8.7 μm thick. The simulations vary the laser power using the values 2.17, 5.34, 8.52, 12.1, and 15.67 TW where the first and last values are the minimum and maximum values from the VisRad model and the middle value is the capsule averaged laser power. The other two values are the averages between the minimum and maximum values with the capsule average power.

3.4.5.1 Source Size and Timing Measurements

Characterizing the size of the stagnated implosion determines the dimensions of the source, which is important for calculating the line broadening in spectroscopic measurements. The views of the cameras are nearly orthogonal to each other, which

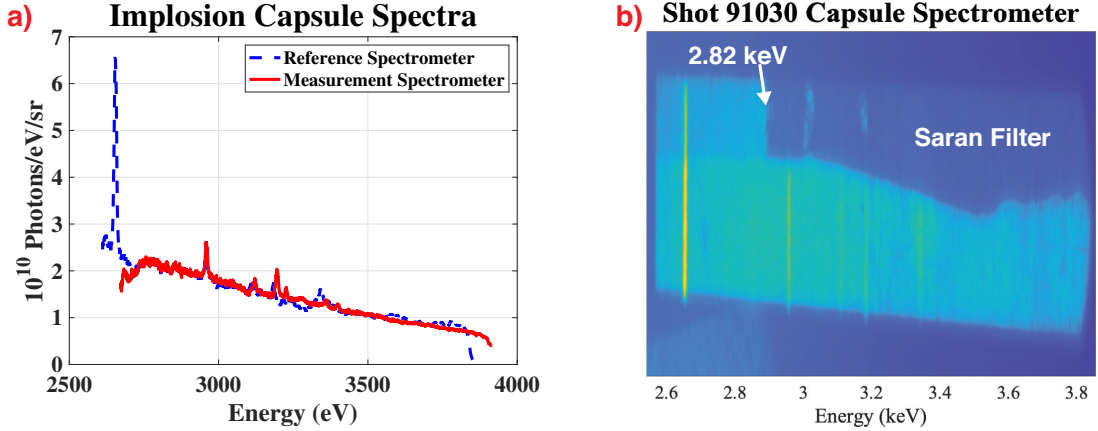


Figure 3.9: a) A comparison of the spectra recorded on two different spectrometers during the same shot. b) The raw image plate data showing the spectral fiducial from the Saran filter and the line emission from the Ar and S contamination in the capsule target and glue.

shows a reasonably uniform implosion at stagnation, to within the measurement resolution. Figs. 3.7a and b show the x-ray and soft x-ray camera data near stagnation with the red contours representing 50% of the maximum signal in the image. The signal from the capsule saturated the camera so the data gives an upper limit for the source radius of about $62.5 \mu\text{m}$, and Fig. 3.8 shows the source radius in the simulations, which is about $50 \mu\text{m}$ for the average laser power on the capsule and defining the boundary as half the maximum density. The measured value is about 20% greater than the simulated value, which is reasonable agreement for 1D simulations to this 3D system. This framing camera data also provides the timing of the x-ray flash, which occurred at about 1.25 ns in the experiments. The capsule-average laser power simulations show an x-ray flash timing of 1.13 ns, which is within about 10% of the measured value.

3.4.5.2 Spectral Measurements

Two flat crystal spectrometers measured the spectral content of the x-ray flash from the capsule implosion using a MS type image plate (IP) as the detector [117, 118]. To identify the spectrometers, the discussion will call one the “measurement”

spectrometer and the other will be the “reference” spectrometer as this language lends itself to a measurement with a probe source. Each had an ADP (101) crystal at an angle of 19.5° relative to the spectrometer axis, which gave a spectral range of about 2500-4000 eV, and a different line-of-sight to the capsule with a 142.6° rotation between the two views.. A Saran filter covered half of the spectrometer aperture to act as a spectral fiducial at the Cl k-edge (2.82 keV), shown in Fig. 3.9 a. The signal on the IP gets recorded in photostimulated luminescence (PSL), but it is possible to convert this into units of photons $\text{eV}^{-1} \text{sr}^{-1}$. Following a treatment used in analysis of capsule spectra elsewhere in the literature, the photon number spectrum, $S(E)$, is,

$$S(E) = \frac{PSL}{S_{IP}(E) \frac{d\Omega}{dA} \frac{dE}{d\theta} R(E) T(E)}, \quad (3.2)$$

where PSL is the signal in PSL, $S_{IP}(E)$ is the IP sensitivity in mPSL γ^{-1} , $\frac{d\Omega}{dA}$ is the solid angle per $25 \mu\text{m}^2$, $\frac{dE}{d\theta}$ is the crystal dispersion, $R(E)$ is the crystal integrated reflectivity, and $T(E)$ is the transmission through the spectrometer blast shield and the IP protective layer [113, 114, 119]. The integrated reflectivity calculations used the Xoh tool on Sergey Stepanov’s X-Ray Server [126, 127]. Fig. 3.9 b compares the spectra recorded on the measurement and reference spectrometers during a single shot and shows very comparable signal of around $3 \cdot 10^{10}$ photons $\text{eV}^{-1} \text{sr}^{-1}$, however, there is no cross calibration of the crystals. This is sufficient to produce a signal of about 1 to 2 PSL after characterizing and subtracting high energy background from a portion of the IP not visible to the crystal. The minimum signal on the IP is about 0.01 PSL with the scanner used in this study, which is two orders of magnitude lower than the collected signal. There were contaminants in the capsules, which are the cause of the observed line emission in the spectra. Analysis of the line emission shows that these contaminants were Ar and S that are likely from storing the capsules in air and the glue that fixes the capsule to a stalk respectively.

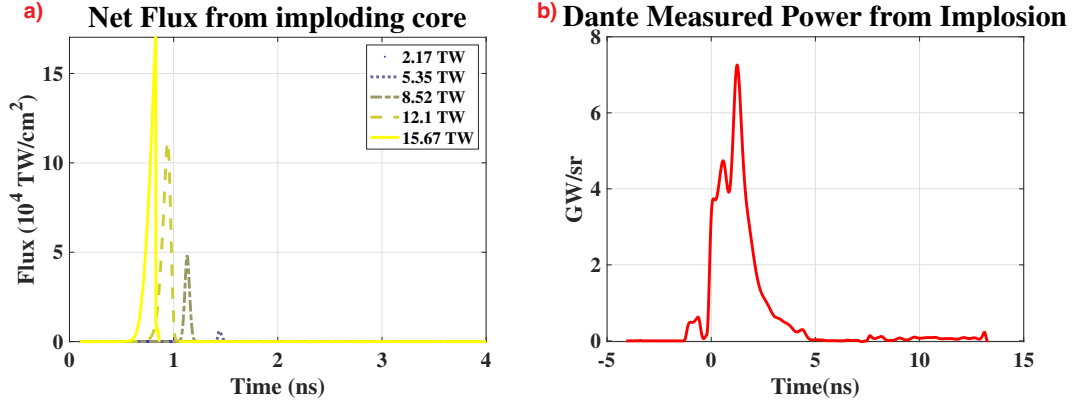


Figure 3.10: a) The simulated net flux out of the surface that is half the maximum density at each time step for the laser power range on the capsule with 8.52 TW the average over the whole capsule. b) The Dante unfold of the capsule implosion. This figure has a shifted time axis so that the peak emission is at 1.25 ns to match the x-ray framing camera results. This is reasonable because the timing of the Dante measurement is not connected to the laser timing. The small signal that occurs before 0 ns is likely the result of inaccuracies in the alignment of the Dante channels in time.

3.4.5.3 Flux Measurements

The Dante diode array, described above, records absolutely calibrated, time-resolved flux from the capsule. Because these measurements are absolutely calibrated, one can extract the power per steradian as a function of time. This can be difficult to accomplish because the oscilloscope timing is separate from the laser timing and the cables for each channel are not calibrated to co-time the data. Here the x-ray flash at stagnation acts as a timing fiducial to align the Dante channels. Fig. 3.10 b shows the measured power per steradian from the capsule using the matrix unfold method and Gaussians as input functions with an 1.2° angle of incidence [120]. To correct for the diode temporal response, the analysis deconvolves the Dante channels with a 160 ps Gaussian using a Lucy-Richardson algorithm [128, 129]. The time dependence in Fig. 3.10 b show some signal at times earlier than zero, which is likely a result of the difficulties in co-timing the channels accurately.

One can use the Helios-CR simulations mentioned above to estimate the flux leaving the capsule that the Dante diagnostic measures. An accurate calculation of

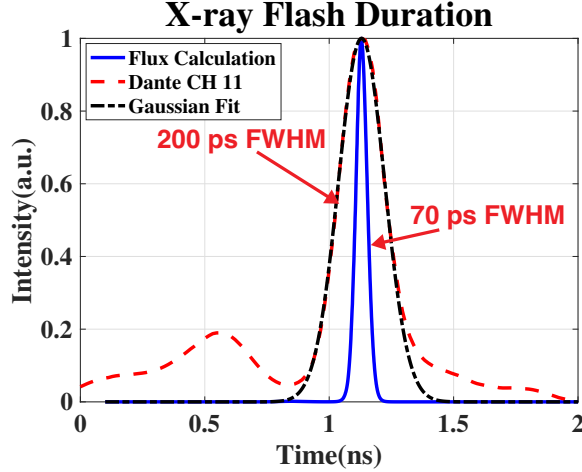


Figure 3.11: The dashed curve is the channel 11 Dante data, which spans 2-5 keV, deconvolved with a 160 ps width Gaussian to account for the diode temporal response. The dot-dash curve is a Gaussian fit to the Dante data, which has a FWHM of 200 ps. The solid curve is the flux calculated at half of the maximum density at each time step using the capsule-average laser power, which has a width of 50 ps.

this flux would be quite involved. For each photon energy one would have to find the ray intensity in each direction for a point on the capsule surface, using the radiation transfer equation. Then one would need to integrate in angle to find the flux at that energy and to sum over energies to find the net flux. However, because of the asymmetric implosion there seems little point in doing this using a 1D simulation. Instead, we did the simpler estimate described next.

Since the simulations use a diffusive radiation transport model and LTE physics, it is reasonable to make the same assumptions in this estimate. In a diffusion model, the radiation energy density is only a function of temperature and is proportional to the radiation pressure.[1] Using an Eddington factor of $\frac{1}{3}$ and assuming spherical symmetry results in a frequency integrated radiation flux of,

$$\vec{F}_R = -\frac{4 * \pi}{3\chi_R} \frac{\partial B}{\partial T} \frac{\partial T}{\partial r} \hat{r} = -\frac{16\sigma_{SB}T^3}{3\chi_R} \frac{\partial T}{\partial r} \hat{r}, \quad (3.3)$$

where χ_R is the Rosseland mean opacity in units of length^{-1} , B is the blackbody energy flux, and \hat{r} is the radial unit vector.

Our estimate amounts to assuming that each computational zone acts as an independent emitter, whose radiation is then attenuated out to the edge of the imploded capsule. Since the total emitted flux is dominated by those hot zones that are close enough to the surface that their emission is not strongly attenuated, this is a plausible approach to use. In detail, the calculation defines the capsule boundary as the location with half of the maximum density in the $+\hat{r}$ direction. It evaluates Equation 3.3 to find the radiation flux at each zone boundary for each time step. It calculates the attenuation of the flux from each zone out to the capsule boundary, and sums the product of the fluxes and attenuations to estimate the total emitted flux at each time step. Fig. 3.10 a shows the result of this calculation. One sees that the x-ray pulse magnitude decreases with lower laser power. For the 2.17 TW simulation, this calculation results in no obvious peak in emission. Comparing the calculated flux for the average laser power case in Fig. 3.10 a with the Dante analysis in Fig. 3.10 b shows that the former is a factor of about 100 greater than the latter. This is likely the result of a number of factors. The simulations are in 1D and the experiment is very much a 3D system, which will act to reduce the radiation output. Additionally, the x-ray flux from the simulations cover a much larger spectral range than the Dante measurements, which only spans from about 50 to 5000 eV due to the active channels for these experiments.

The duration of the x-ray pulse defines the integration time of the measurement. Fig. 3.11 shows a broadband Dante channel, which covers the spectral range of interest from 2000-5000 eV, deconvolved with a 160 ps width Gaussian to account for the temporal response of the diode, a Gaussian fit to the data, and the simulation output [130]. The Gaussian fit suggests an about 200 ps full-width at half-maximum (FWHM) duration of the x-ray flash while the simulation suggests about a 50 ps x-ray flash. This could be a result of not including the ablated plasma in the flux calculation, the three dimensional effects in the implosion, or the line emission from

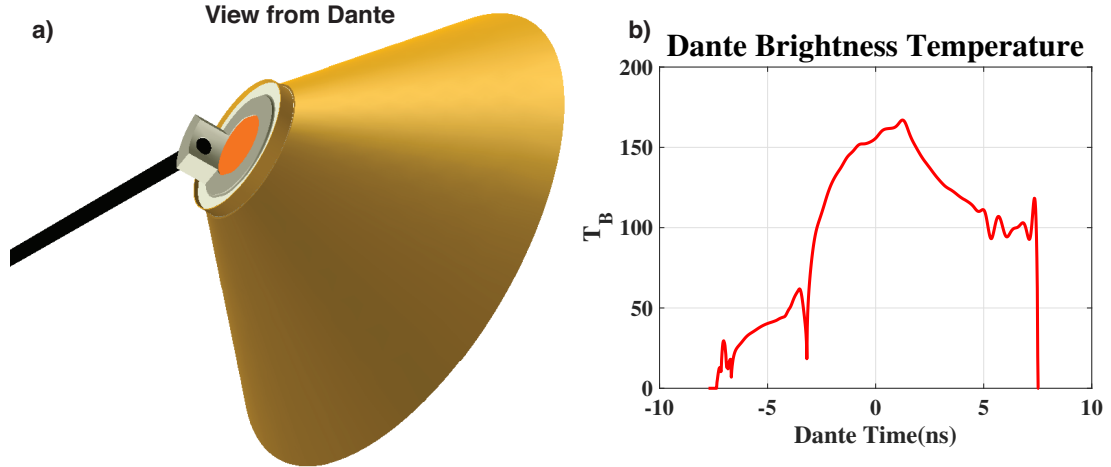


Figure 3.12: The analyzed data from the Dante diagnostic with the dedicated target to observe the emission from the rear surface of the Au foil.

the capsule. In addition, the deconvolution scheme used on this data was a Lucy-Richardson algorithm, which tends to over estimate the width of the initial data and could lead to an overestimate of the x-ray pulse duration [128, 129].

3.4.5.4 Characterization shots

In order to understand the sources of noise present in the absorption spectroscopy measurements, there were four shots dedicated to understanding the different portions of the experiments. One uses only a capsule to observe the unobstructed signal from the probe on all of the relevant diagnostics, another uses a dedicated target, shown in Figure 3.12 a, to observe the output of the Au foil source through the gas cell front window using the Dante diode array to measure the flux. The second two characterization shots determine the effects of the gas cell on the measurements where one drives the gas cell target without the probe to observe any signal from the Au foil that makes it to the detectors and the second uses the probe without the drive to determine how the gas cell itself affects the measurements. The above sections detail the results of the capsule only shots, the Au foil shot provides the time-resolved x-ray flux that reaches the N and Figure 3.12 b shows these calculations. The peak

brightness temperature is around 160 eV, but this calculation does not account for the increasing source size, which means the actual temperature is lower than this. The driven gas cell characterization shot shows almost zero signal on all of the diagnostics. The only measured value is some very dim, broad emission on the time-integrated spectrometer, which is due to the heated Ar in the gas cell. The probe only shot shows bright signal through the gas cell, but the aperture collimates the source and truncates the spectral range. The next section will discuss the effects of this in more detail.

3.4.6 PrismSPECT Atomic Kinetics Calculations

As mentioned above, it is important to understand the spectral content of the probe source when performing absorption spectroscopy measurements. The 50 group approach taken in the radiation hydrodynamics simulations is too coarse for comparison to spectroscopic measurements. Atomic kinetics calculations can bridge this gap with more sophisticated atomic models and finer frequency grids than are reasonable in the hydrodynamic simulations. The PrismSPECT code by Prism Computational Science solves the collisional-radiative equations or Saha equation, in non Local Thermodynamic Equilibrium (NLTE) or LTE conditions respectively, for a set of temperature with a flexible level of detail in the atomic model and the ability to include external radiation sources and non-Maxwellian electron distributions [101]. These calculations will allow for the estimation of the emission spectrum from the capsule implosion and the absorption spectrum from the PI front using the Helios-CR output to set the plasma parameters in the calculations.

3.4.6.1 Calculated Capsule Emission Spectrum

Understanding the probe source is critical in absorption spectroscopy experiments because there are many experimental contributions to features in the measured spec-

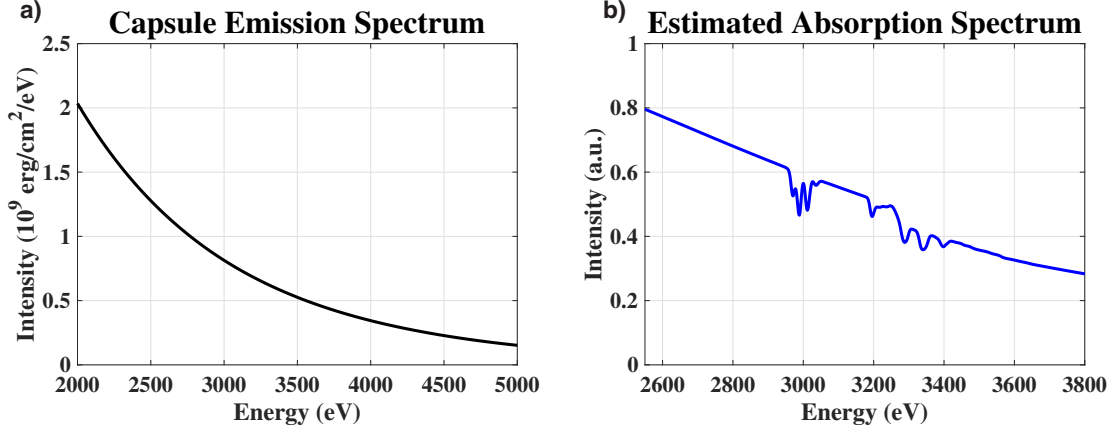


Figure 3.13: a) The calculated emission spectra along a ray propagated through the profiles from the Helios-CR simulations and integrated over 400 ps centered around the implosion stagnation time. b) The estimated absorption spectrum, using the calculated spectrum in a) integrated over the duration of the simulation.

tra and extracting the effects of the sample requires knowledge of each component. For example, the crystal can produce features due to defects, absorption, and geometry in addition to the effects of contaminants, multiple emitters, and the sample itself. Estimating the expected spectrum from simulation, combined with characterization of the contributions from instruments and noise, allows one to extract the features that result from the probe beam passing through the sample plasma, which is a PI front here.

Here, the calculations to estimate the emission spectrum from the capsule use the temperature and density profiles from the Helios-CR simulations and a single ray. Then, using equation 2.24 and a table of frequency-resolved emissivities and opacities from PrismSPECT calculations, one can treat each zone of the simulation as a slab of plasma and calculate the transmission and self-emission through the system. These calculations only propagate radiation in the $+\hat{r}$ direction because that is all that a spectrometer will see. The opacity and emissivity tables use a ten-by-ten temperature and density grid and finds the grid location closest to the plasma parameters in the current zone for the transport calculations. The estimated spectrum in Figure 3.13 a shows the output of the calculation integrated over 400 ps, centered on the time

that the implosion stagnates and Figure 3.13 b shows the time integrated absorption spectrum from the PI front simulations.

3.4.6.2 Estimations of the Absorption Spectrum

Atomic kinetics calculations using the conditions from the PI front simulation output with 99% N and 1% Ar, used as a spectroscopic dopant detailed below, allow for calculating the absorption inside the gas cell. These calculations, combined with the capsule emission spectrum, supply the opacity of the PI front heated, which allows the attenuation of the capsule probe spectrum and an estimation of the absorption measurement. Using the capsule emission spectrum at stagnation, along with the opacity and emissivity values from the PI front simulations from 1 to 3 ns, calculations of the radiation propagation through the x-ray heated material with equation 2.24 integrated over time show the expected absorption spectrum. Figure 3.13 b shows the results of these calculations and the presence of numerous lines from $n=1$ to $n=2$ and the $n=1$ to $n=3$ transitions. Since the electron temperature is about 10 eV or less at the PI front, the ionization from the electron collisions alone is significantly less than the ionization from photoionization.

3.4.6.3 Absorption Spectroscopy Measurements

There were four integrated physics shots where lasers drove the Au foil and the capsule backlighter to probe the N plasma. However, the aperture on the gas cell acts as a collimator and limits the angular divergence of the probe x-rays, which reduces the spectral range of the measurement. This results in the small region of signal on the image plate data in Figure 3.14. The second observation is that the signal starts at about 3.4 keV, which is slightly above the expected energy for the $1\rightarrow3$ transitions in Ar. This issue is easily correctable in future experiments by removing the aperture and increasing the dimension of the windows transverse to the PI front propagation.

Shot 91028 Gas Cell Spectrometer

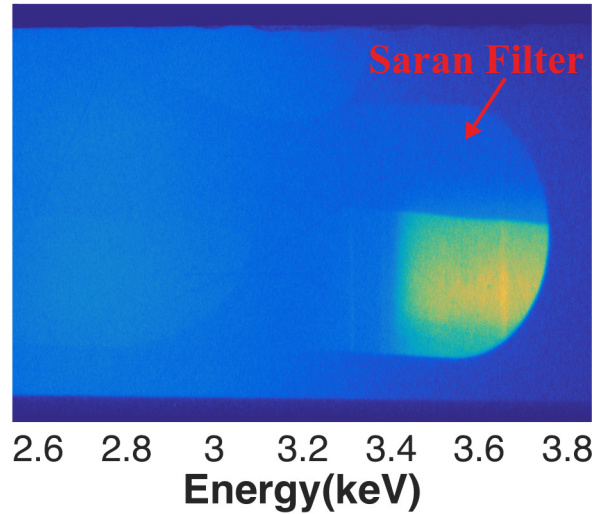


Figure 3.14: The capsule emission spectrum measured through the gas cell. The signal cuts off below about 3.4 keV due to the aperture on the target limiting the angular divergence of the capsule emission.

These are reasonable changes because the measured upper limit on the capsule source size is approximately $125 \mu\text{m}$, which should result in acceptable broadening, and a larger window will allow for more angular divergence of the probe x-rays.

3.5 Conclusions

Photoionization front experiments present numerous challenges in the computational design, the target construction, and the diagnostic selection. This work used the post-processing of one-dimensional radiation hydrodynamics simulations to suggest that it is possible to drive a PI front using the Omega-60 laser facility and to determine a useful location and timing for experimental measurements. Additional simulations similarly characterized the expected conditions and timing of the capsule backlighter for an absorption spectroscopy measurement. An estimate of the absorption spectroscopy measurement that uses the output of both of these radiation hydrodynamics simulations and atomic kinetics calculations shows a reasonable signal level for the designed experiment. Experiments conducted at the Omega-60

laser facility characterized the drive source, probe source, and the spectroscopic diagnostic geometry. Although, these experiments were unable to collect absorption spectra due to a restricted spectral range from a limiting aperture on the target, the characterization data collected will be invaluable to improving the target design in future experiments. Of particular use is the connection between the laser irradiation pattern on the capsule backlighter and the probe timing. This will allow for adjustments to the beam selection and pointing to accommodate changes to the gas cell target without concerns about significantly changing the performance of the probe source.

CHAPTER IV

Photoionization Front Experiment Design for the Z-Machine

When conducting experiments, especially when they require large user facilities, the question of systematic uncertainties is always present and can be difficult to resolve. One way of testing the effects of the experiment on the measurements is to repeat them on an independent platform. Sandia National Laboratories' Z-Machine produces a significant soft x-ray flux, with the appropriate load, and should be capable of driving a PI front. Experiments on Z would serve two purposes, one is to provide an independent measurement of PI front physics for comparison with the ones conducted at Omega, and the second is to use a different source geometry, which will provide a different response from the material while producing the same physics. The later is due to the different distances of the source to the gas cell and the size of the source relative to the gas cell at the two facilities. This is related to the analysis of PI front curvature found in section 2.3.2.5 with the Omega and Z experiments having the source size smaller and larger than the propagating medium respectively.

This chapter will describe the design of a PI front experiment using Sandia National Laboratories' Z-Machine as an x-ray source. It will discuss the capabilities of the Z-Machine for these measurements, a simulation study to design the gas cell, and conclude with estimates of the measurements that these experiments could produce.

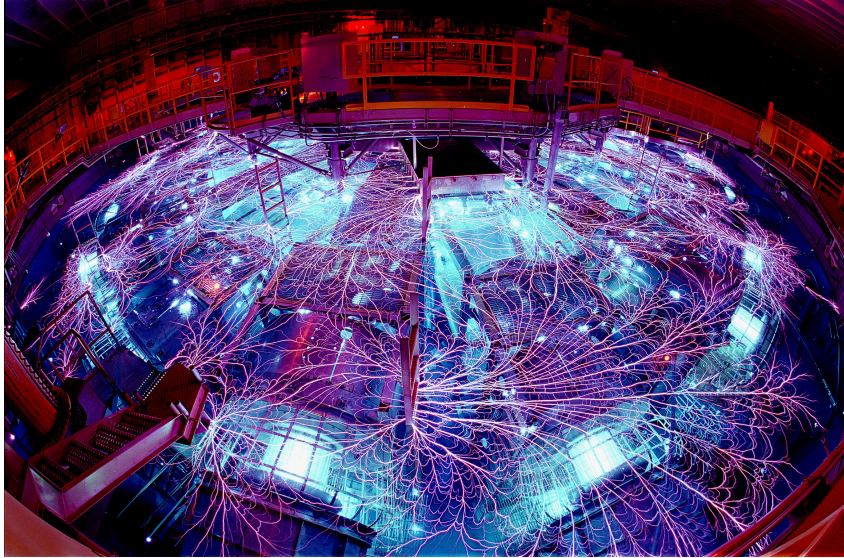


Figure 4.1: The Z-Machine at Sandia National Laboratories.

4.1 The Z-Machine at Sandia National Laboratories

The Z-Machine is a 26 MA pulsed-power facility that uses current to produce and manipulate plasma into an HED state. For the purposes of a PI front experiment, the nested wire array used in the Z Astrophysical Properties Platform (ZAPP) produces about 2 MJ of soft x-rays [24, 96]. The 12 mm tall wire array has a 20 mm inner diameter with 120 tungsten (W) wires and a 40 mm outer diameter with 240 W wires [24]. The W wires are $11.4 \mu\text{m}$ in diameter and there is a 14.5 mg cm^{-2} , CH_2 foam on the axis of the wire array that has a diameter of 6 mm.

In an experiment, the current ablates the wires, and the resulting $\vec{J} \times \vec{B}$ force and magnetic pressure move the resulting plasma towards the axis. When the W plasma reaches the plastic foam, the impact launches a cylindrically converging shock that is strong enough to produce significant amounts of radiation. This radiation launches a heat wave into the W and the resulting emission when the pinch stagnates on axis is the result of the released radiation behind the heat wave and the thermal emission from the hot, dense pinch plasma. Figure 4.1 shows the Z-Machine during a discharge of the current.

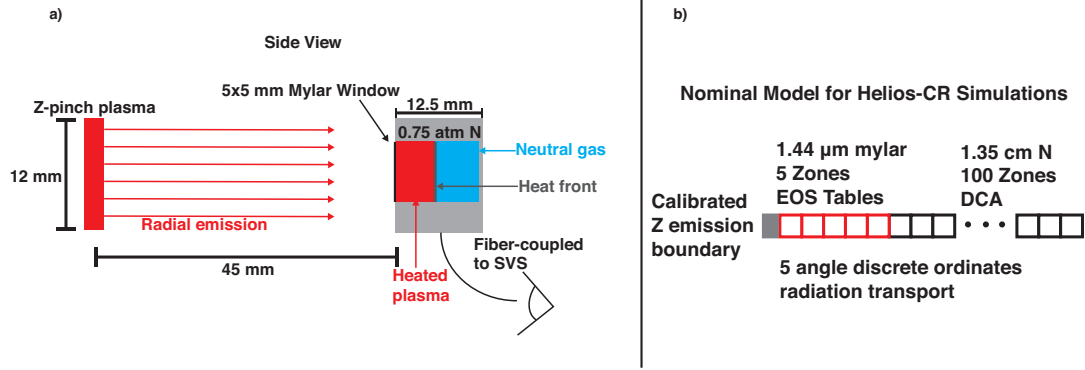


Figure 4.2: a) The general setup for the experiment on Z showing the radial flux from the pinch driving a PI front into a N gas cell with a fiber to couple the self-emission to a streaked, visible spectrometer. b) The geometry used in the HELIOS-CR simulations and the physics models used to describe the mylar front window and the N gas.

4.2 Primary Diagnostic: Streaked Visible Spectroscopy

To measure a PI front with the Z-Machine as a driving radiation source, the best available diagnostic is streaked visible spectroscopy. This will provide a time-resolved measurement of the ionization states present in the plasma. The end of this chapter presents the expected outcome of these measurements, but here it will be useful to describe what they are capable of observing.

Since this is an emission spectroscopy measurement, it captures the excited states of the plasma and since it is in the optical band the transitions are typically among the higher principal quantum numbers, n . It is possible to observe transitions at lower principal quantum numbers, if they are within a single value of n , but the dipole selection rules forbid these transitions, so they will be less frequent. Identifying lines from different ionization states will indicate the relative populations and which state is dominant. Fitting the spectrum can potentially provide information on the temperature, but these photoionized plasmas can make this measurement difficult due to the larger ionization than one would expect from the electron temperature [34].

4.3 Description of Problem

As mentioned in the previous chapter, an experiment observing PI fronts requires a bright, ionizing radiation source and a medium for it to propagate through, with Figure 4.2 showing what that may look like for an experiment at a z-pinch. The source must be bright enough that the photoionization at the heat front that separates the hot and cold material is the dominant process of energy transfer to the plasma. There is the additional requirement that the radiation streams through the heated downstream before being rapidly absorbed over a few mean free paths at the heat front, making the transport non-diffusive for a significant portion of the propagating medium. The implication of these features in PI fronts is that any modeling will need to consider the radiation hydrodynamics, radiation transport, and atomic kinetics in order to best treat the problem with the tools available. Additionally, this places a requirement on the experiment to evaluate the system in a way that provides adequate information about the regimes of radiation transport and dominant atomic processes to ensure the simulations and experiments are observing approximately the same physics.

Many authors have considered the radiation hydrodynamics of this problem, which chapter II presents the relevant portions of, and this chapter will not reproduce these results as they are well documented [57, 58, 59, 60, 61, 62, 63]. To provide context, using the nomenclature and results of Drake *et al.* and Gray *et al.*, the simulations shown here will explore a weak-R type front, which is one of four solutions to the steady-state jump conditions of the radiation hydrodynamics equations under the assumption that the radiation pressure and energy density are negligible, but the radiation flux is not [61, 62, 63]. A weak-R type front is a supersonic heat front that has no density change across the front and limited hydrodynamic motion associated with its passage across a region of material [61].

As mentioned above, the analysis of this problem can not neglect the atomic kinet-

ics because this problem has the requirement that photoionization dominate without significant contributions from electron collisional ionization and the hydrodynamics alone can not determine this. Drake *et al.* and Gray *et al.* address this with two and three level atomic models respectively in an analytic solution of the steady-state rate equations and the simulations in Gray *et al.* uses an atomic model that is averaged over many of the available states [61, 62, 63]. The relevant results from the analytic solutions are two dimensionless parameters comparing the ratios of atomic rates. The first is,

$$\alpha = \frac{n_{i+1} n_e R_{i+1,i}}{n_i \Gamma_{i,i+1}}, \quad (4.1)$$

where n_i is the ion number density of the i th ionization state in cm^{-3} , n_e is the electron number density in cm^{-3} , $R_{i+1,i}$ is the recombination rate from the $i + 1$ th to the i th ionization state in $\text{cm}^3 \text{ s}^{-1}$, and $\Gamma_{i,i+1} = \int \frac{F_l \sigma_{PI}}{E} dE$ is the photoionization rate from the i th to $i + 1$ th ionization state in units of s^{-1} with F_l the local radiation flux, σ_{PI} the photoionization cross section, and E the energy. The recombination rate, $R_{i+1,I}$ is the sum of three-body recombination using the Lotz formula and detailed balance, dielectronic recombination using the fits described in Salzmann, and radiative recombination using the Verner and Ferland fits [103, 104, 105]. The dimensionless number α is the ratio of recombination to photoionization and determines if the plasma is actively photoionizing. For a PI front, it is necessary to have $\alpha \ll 1$, which indicates that the photoionization is occurring more rapidly than recombination. The second dimensionless number is,

$$\beta = 1 + \frac{n_i \langle \sigma v \rangle_{i,i+1}}{n_{i+1} R_{i+1,i}}, \quad (4.2)$$

where $\langle \sigma v \rangle_{i,i+1}$ is the electron collisional ionization rate using the Lotz formula in $\text{cm}^3 \text{ s}^{-1}$ and the remaining variables are as defined in Equation 4.1 [105]. β is one plus the ratio of the electron collisional ionization to the recombination and should be about

unity in the case of a PI front. This is equivalent to saying that the ionizations due to electron collisions occur less frequently than recombinations, which are already much less frequent than photoionizations under the condition $\alpha \ll 1$. These dimensionless numbers take the place of the photoionization parameter, $\xi = \frac{L}{n_e r^2}$, where L is the luminosity, n_e is the electron density, and r is the radius from the source, which is common in the astrophysics literature of photoionized plasmas [131, 132].

4.4 Photoionization Front Simulations with the Nominal Physics Model

4.4.1 Simulation Setup and PI Front Analysis

The simulation study to design a PI front experiment on Z used the Helios-CR code by Prism Computational Sciences [65]. This is a 1D Lagrangian radiation-magnetohydrodynamics code that has the ability to use tabular equations-of-state, tabular or inline detailed atomic calculations for the opacities, and multi-group diffusion or discrete ordinates radiation transport. The inline, frequency-resolved, and non-equilibrium atomic physics calculations generate population distributions, which the code uses to generate opacities and emissivities. The code uses these material properties in the solution of the radiation transport equation using the method of short characteristics for the angle-resolved radiation transport. The radiation flux used in each zone is the angle-averaged value of the specific intensities calculated using the short characteristics method with the selected number of rays. As Gray showed, a more detailed physics model using inline atomic calculations for opacities and multi-angle radiation transport produces significant changes in the propagation of the front compared to a tabular opacity values on a coarse frequency grid and diffusive radiation transport [63]. Additionally, Helios-CR allows for user-input flux boundaries and previous work using the Z radiative properties platform produced a

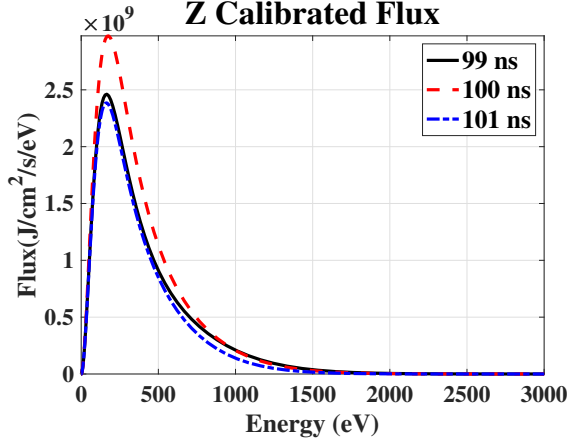


Figure 4.3: The time evolution of the input flux file about the peak emission time of 100 ns.

spectrally-resolved input file of the Z emission, in units of $\text{J cm}^{-2} \text{s}^{-1} \text{eV}^{-1}$, at a radial location 45 mm from the source [24, 96]. The source has a color temperature of 63 eV and its spectral content is best fit by the sum of three geometrically diluted Planckians due to emission from the pinch plasma and the heated, surrounding load hardware. Figure 4.3 shows the calibrated input file at three times over the peak emission and figure 1 in reference 38 shows the contributions of the three Planckians to the total flux.

The nominal setup of the simulations uses 5 zones of mylar with a thickness of $1.44 \mu\text{m}$ that uses quotidian equations-of-state tables and local thermodynamic equilibrium, tabular opacities from the Prism Computational Sciences code Propaceos. Following the mylar, there are 100 zones of N with a thickness of 1.35 cm, which utilizes the non-equilibrium atomic physics, inline detailed configuration accounting opacity calculations on a fine frequency grid that uses more resolution around line features. The radiation transport uses the angle-resolved, short characteristics method for the entire simulation domain. The nominal atomic model for N excludes all autoionizing states from the calculated energy levels in the ATBASE database. The radiation transport uses a S_n model with 5 angles. Figure 4.2 b shows an overview of the physics model and the zoning configuration.

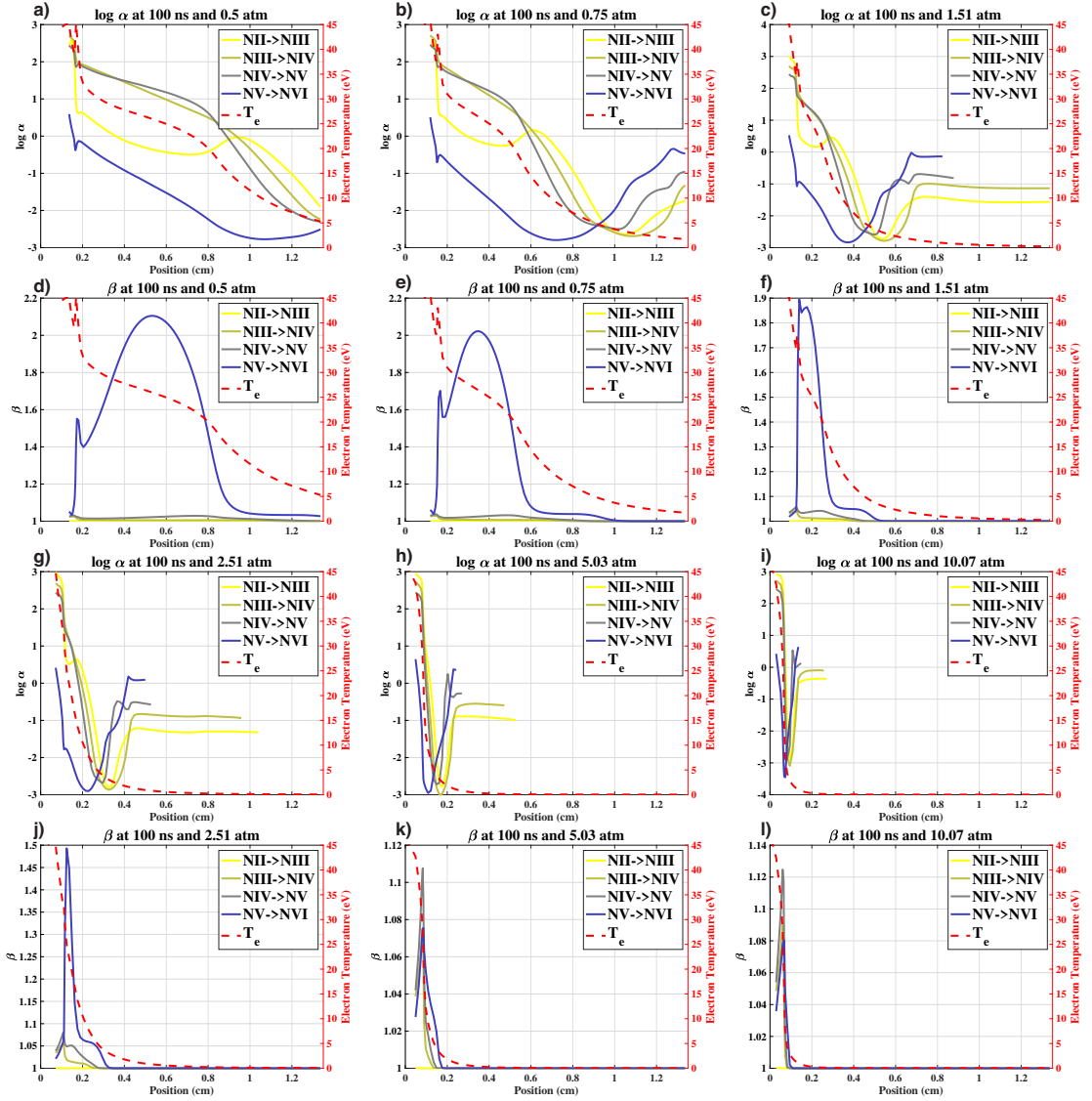


Figure 4.4: The values of α and β calculated from the HELIOS-CR simulations while varying the pressure of the N gas. Here, there are only a subset of ionization states shown because preheat affects the $\text{NI} \rightarrow \text{NII}$ front and the states above NVI are not desirable for making a measurement. a)-c) and g)-i) show that increasing the pressure reduces the velocity of the front, but does not affect the magnitude of α significantly. The values of β in d)-f) and j)-l) show the same spatial behavior but a gradual decrease in the β value for the $\text{NV} \rightarrow \text{NVI}$ transition as the pressure increases while the value increases slightly for the other transitions shown. This suggests that the photoionization rate changes similarly to the recombination rate with increasing particle density, but the electron collisional ionization rate grows more slowly for the $\text{NV} \rightarrow \text{NVI}$ transition and faster for the other transitions shown.

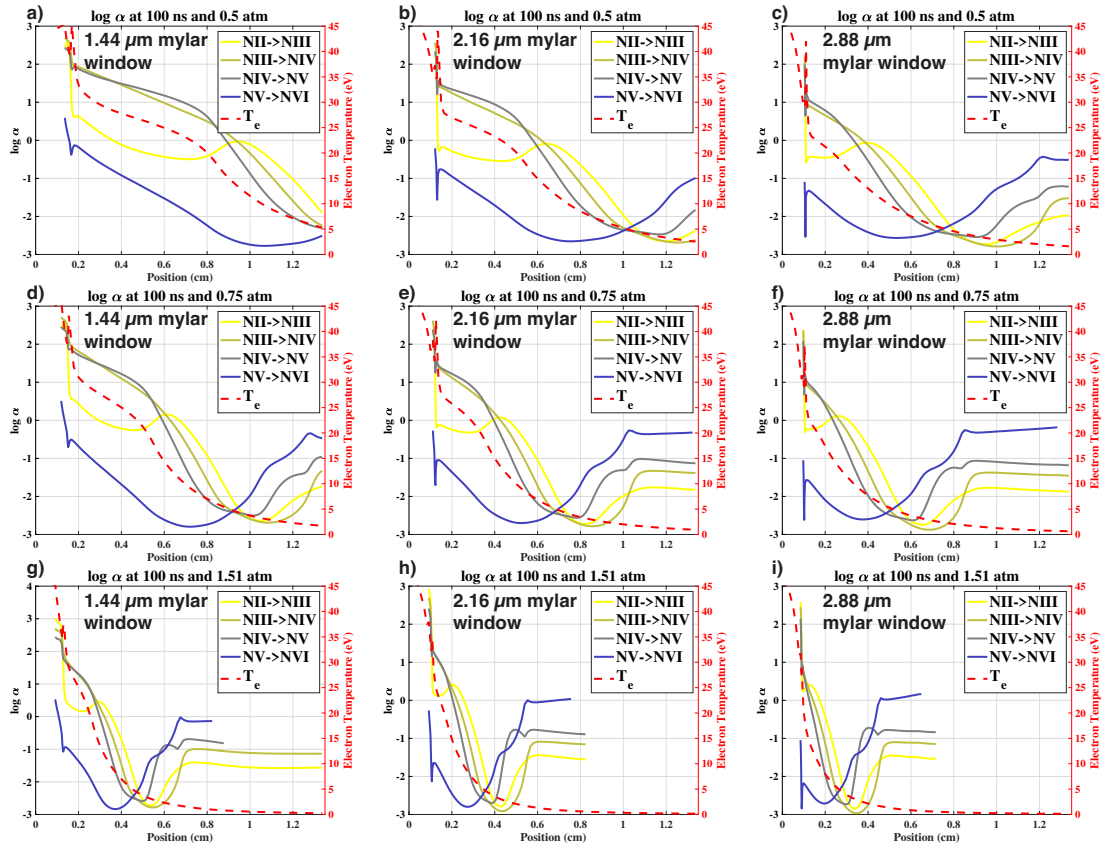


Figure 4.5: These values of α with mylar window thickness of $1.44 \mu\text{m}$, $2.16 \mu\text{m}$, and $2.88 \mu\text{m}$ at three different pressures (a)-c) 0.5 atm , d)-f) 0.75 atm , and g)-i) 1.5 atm) show a reduction in velocity when increasing either parameter. All three pressures show slightly lower values of α with increased window thickness, which is likely due to the radiation having to travel through less material to get to the front, reducing the amount of absorption.

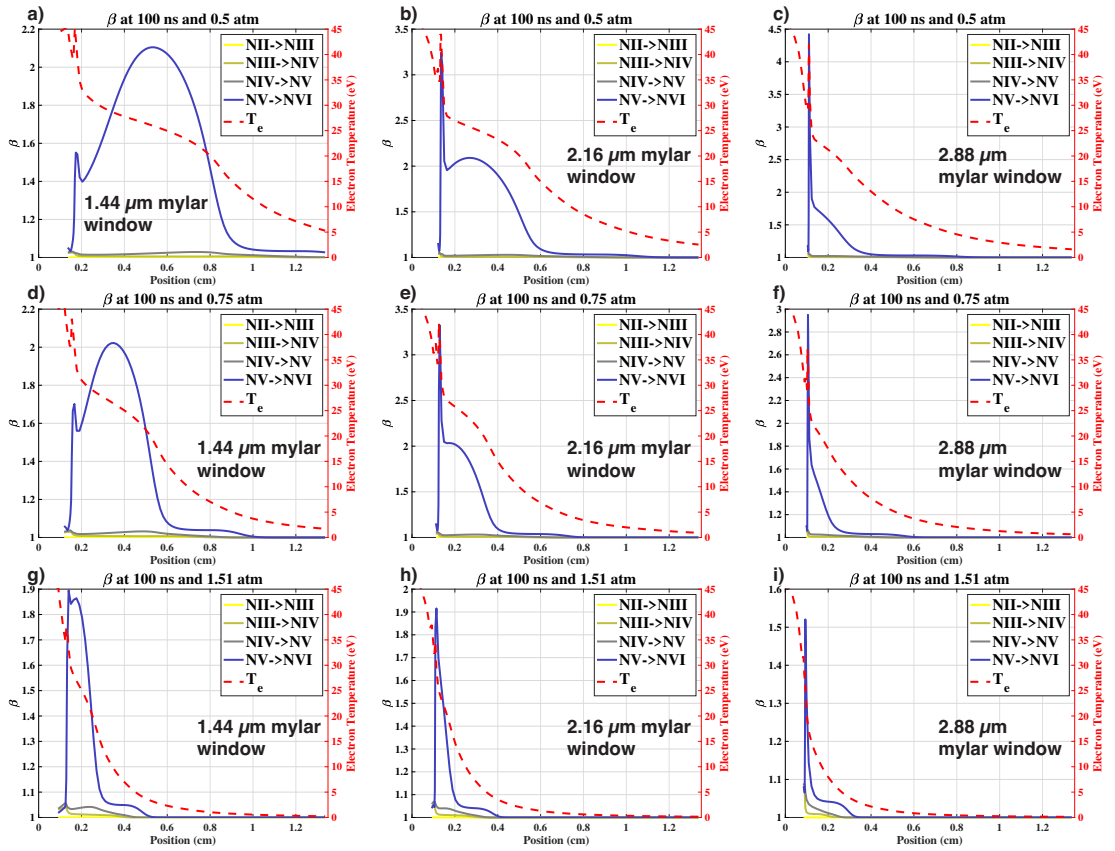


Figure 4.6: The values of β with mylar window thicknesses of $1.44 \mu\text{m}$, $2.16 \mu\text{m}$, and $2.88 \mu\text{m}$ at three different pressures (a)-c) 0.5 atm , d)-f) 0.75 atm , and g)-i) 1.51 atm). These figures show β stays relatively constant at the location of the front, but the downstream behavior is more complicated. The downstream values of β decrease with increasing window thickness with a spike, likely due to the shock propagating into the N from the released window material, that can break this trend.

Helios-CR does not output the atomic rate coefficients needed to calculate the values of α and β , therefore it is necessary to post-process the simulation output. To calculate the rate coefficients, this analysis uses fits to the radiative and dielectronic recombination rate coefficients and the Lotz formula for the electron collisional ionization rate, which combined with detailed balance and the Saha equation provides the three-body recombination rate coefficient [103, 104, 105]. The photoionization rate is slightly more complicated. Gray *et al.* derived a scheme for approximating the photoionization rate from the discrete ordinates radiation transport in Helios-CR as,

$$\Gamma_{i,i+1} = \int 4\pi \left(\frac{T_{R,l}}{T_{R,s}} \right)^4 B_\nu(T_{R,s}) \frac{\sigma_{PI,\nu}}{h\nu} d\nu, \quad (4.3)$$

where $T_{R,l}$ is the local radiation temperature from Helios-CR, $T_{R,s}$ is the radiation temperature of the source, B_ν is a Planckian at the source temperature, $\sigma_{PI,\nu}$ is the photoionization cross section using the fits of Verner *et al.*, h is the Planck constant, and ν is the photon frequency [63, 106, 107]. This was reasonable due to the use of a temperature boundary in that simulation study, but, here, there is not one temperature to prescribe to the input flux file, as mentioned above. The analysis below modifies Equation 4.3 using the brightness temperature, $T_{R,B}$, of the input flux file,

$$T_{B,s} = \left[\frac{1}{\sigma_{SB}} \int F_{s,\nu} d\nu \right]^{\frac{1}{4}}, \quad (4.4)$$

where σ_{SB} is the Stefan-Boltzmann constant and $F_{s,\nu}$ is the frequency-resolved flux from the input file. Using Equation 4.4, the resulting photoionization rate is,

$$\Gamma_{i,i+1} = \int 4\pi \left(\frac{T_{R,l}}{T_{B,s}} \right)^4 F_{s,\nu} \frac{\sigma_{PI,\nu}}{h\nu} d\nu. \quad (4.5)$$

This calculation neglects the thermal, self-emission from the plasma as Gray *et al.* showed that it is not a significant contribution to the radiation field [63].

4.4.2 Parameter space study

The parameter space for the experiment design spans the thickness of the mylar window and the pressure of the N gas. There is also the freedom to change the gas species, but this study does not explore that aspect of the problem. The decision to use N gas allows the atomic physics to be reasonably simple while having the photoionization opacity significantly overlap with the peak of the source spectrum. This deviates from the astrophysical case where the tail of the photon distribution provides the energy to drive the PI front, but it is necessary to change this in the experiment to generate a large enough photoionization rate. The window thickness has a limited role in the PI front physics, other than altering the incident radiation flux on the N, but it is necessary to determine the effects of thicker material for constructing a gas cell in a real experiment. The ablation pressure on the front window does launch a shock into the N, indicated by the peak in temperature around 0.175 cm in Figures 4.4 a-f, but this should not significantly impact the measurements as it is several millimeters behind the PI front.

Using two images as an example, the interpretation of these figures is as follows, Figure 4.4 b shows the log of the parameter α , from equation 4.1, for a selection of N ionization states calculated at each of the 100 spatial zones of N in a single time step. Figure 4.4 e shows the calculation of β , from equation 4.2, under the same conditions as Figure 4.4 b. These figures allow for one to observe where the dimensionless parameters satisfy the conditions for a PI front. To relate this to Figures 4.4 b and e, the former shows values of $\log\alpha$, for this time step, are at a minimum much less than 1 for the NII and NIII states around 1.1 cm with the higher ionization states having minima closer towards the source. The corresponding locations in Figure 4.4 e, which shows the calculated values of β , shows that this parameter is unity at the location of minimum α for each ionization state. The decision to use transitions starting with the NII state and ending with the transition into the NVI state is due

to the preheating of the N from the rise time of the pinch and the decrease in opacity once the N reaches the He-like state. In order to assist the reader in understanding the structure of the heat front, the figures overlay the electron temperature in red, dashed lines over the calculated dimensionless parameters. Figures like this allow for comparisons of the ability to generate PI fronts with different gas pressures and front window thicknesses.

The mylar window thicknesses in this study are 1.44 μm , 2.16 μm , and 2.88 μm with gas pressures of 0.5 atm, 0.75 atm, 1.5 atm, 2.5 atm, 5 atm, and 10 atm. The design parameters of interest are the propagation length of the PI front, which should propagate about the length of the N in the 3 ns of peak emission, and the dimensionless numbers α and β .

The simulations at 2.5, 5, and 10 atm suggest that these densities are too high for the radiation to penetrate a significant distance into the gas and this thesis does not include them in further discussion. The 0.5 atm simulations show the heat front propagating through the gas cell before the peak flux arrives, which is also not a useful design as this will not take advantage of the largest possible photoionization rate. Comparing the electron temperature profiles in addition to the α and β values for the remaining pressures in figures 4.4 a through f show that while all seem to produce PI fronts, 0.75 atm does so in the most convincing fashion. It also seems that the PI front reaches the end of the gas cell during the peak emission, while having sufficient spatial extent between the different ionization states to differentiate them in measurement.

Changing the window thickness reduces the temperature and penetration of the PI front, which makes sense as more of the source energy goes into heating and expanding the window when there is more material. Figures 4.5 and 4.6 show the results for the α and β calculations, respectively, over the range of window thicknesses and a small sample of gas pressures. These have the same interpretation as the values in

Figure 4.4. Increasing the window thickness acts to reduce the radiation flux that is available to support the PI front. This results in lower PI front velocities and therefore smaller propagation distances into the gas cell. Viewing the rows of Figure 4.5 (a-c, d-f, g-i), one sees a similar trend of the minima of $\log\alpha$ shifting to positions closer to the source as the window thickness increases at this simulation time step. Additionally, these values of $\log\alpha$ are sufficiently less than one indicating a photoionizing plasma. The corresponding values of β in Figure 4.6, similarly arranged in rows (a-c, d-f, g-i), show that at the locations of minimum α , the values of β are unity, which shows that all of these window thicknesses allow for sufficient radiation fluxes to support PI fronts without generating significant electron heating.

4.5 Testing the model validity

Gray *et al.* justifies the physics included in the simulations by comparing different models, and this study goes further by probing the effects of changing the resolution on the results. A resolution study, atomic model study, and angular grid for radiation transport study show that the nominal model reasonably captures the physics of interest. The following sections describe these investigations in more detail. The studies compare values from two different simulations using the following metric,

$$\delta = \frac{\epsilon_d - \epsilon_n}{\epsilon_d},$$

where δ is the percent difference between the deviated model and the nominal model, ϵ_d is the value from the deviated model, and ϵ_n is the value from the nominal model.

4.5.1 Resolution study

The nominal spatial resolution, in the N, is $135 \mu\text{m}$. Since the inline atomic calculations produce a fine frequency grid, there is a significant amount of line structure

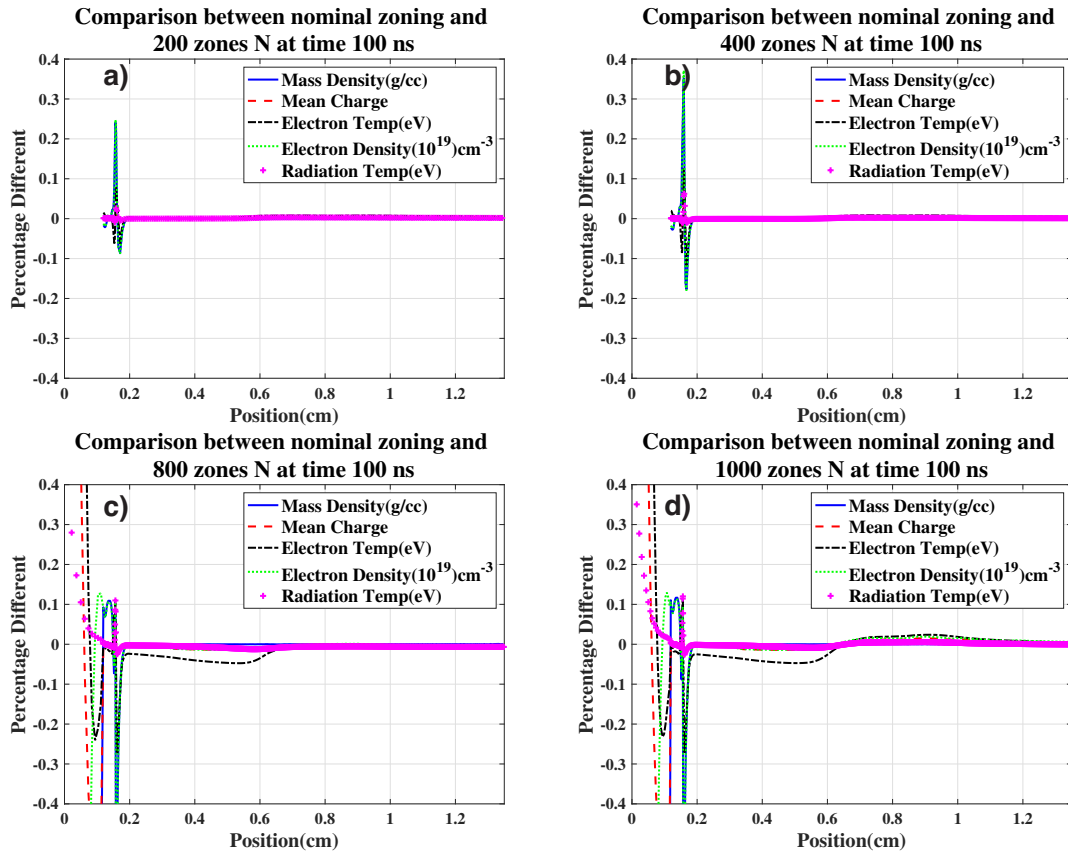


Figure 4.7: The comparisons, at 100 ns, between plasma parameter values when increasing the resolution from the nominal 100 zones of N show minimal deviation in a) and b) with 200 and 400 zones respectively. However, there are lower electron temperatures of about 5% in the downstream region in c) and d) with 800 and 1000 zones respectively. There is also an increase in upstream electron temperature in d), but this is less than 5% from the nominal model. The large deviation below 0.2 cm are due to the mylar window and are not of concern to the propagation of a PI front.

captured by the model that would have large opacity values, which could then have photon mean free paths that are less than the grid spacing of the simulation. To try and capture the possible effects of this, a systematic increase in the number of zones from 100 zones to 200, 400, 800 and 1000 zones, decreased the minimum spatial element to $13.5 \mu\text{m}$. Since Helios-CR is a Lagrangian code, the zone boundaries are able to change with each time step, which would change the spatial resolution. However, there are no significant changes in the zone boundaries as a function of time in the N. This makes sense because the PI front is supersonic and results in little to no change in mass density in the propagating medium. Examining the difference plots in Figures 4.7 a-d show that there is less than 10% differences between the deviated model and the nominal model for any possible number of zones. This suggests that to spatial scales of $13.5 \mu\text{m}$ the nominal model captures all of the relevant physics reasonably well. To improve the mass matching, the simulations with 800 and 1000 zones of N used 20 and 40 zones of mylar respectively instead of the 5 mylar zones in the nominal model. These simulations also used a simplified atomic physics model with a maximum principal quantum number of $n = 4$ to reduce the computation time, which the next section justifies.

4.5.2 Atomic model sophistication

Helios-CR allows the user to vary the number of energy levels in the atomic model used when solving the collisional radiative (CR) equations for the inline opacity calculations. The nominal model excludes only the autoionizing states for each ionization state. To test if the assumption that the autoionizing states contribute little to the radiative heating, a series of simulations systematically increased and decreased the number of levels in the atomic model leaving the rest of the nominal model unchanged.

The process used to decrease the number of atomic levels was to eliminate levels by principal quantum number between simulations until the percent difference exceeded

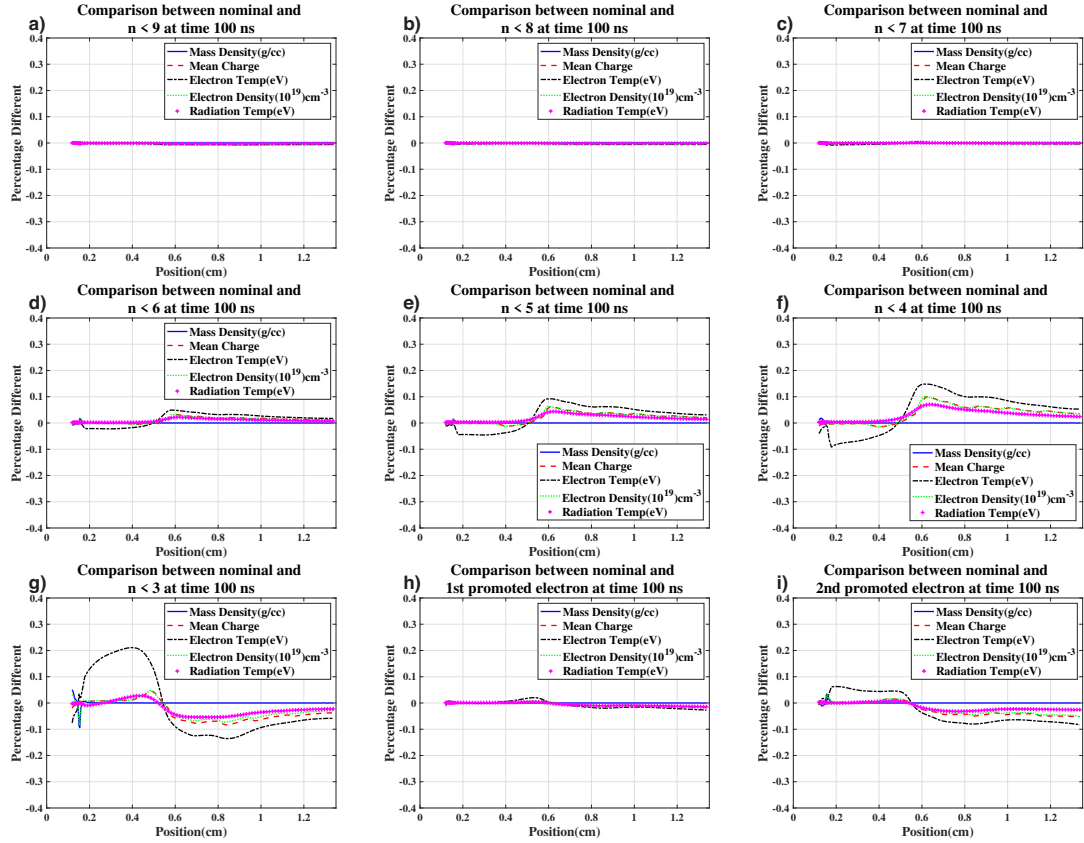


Figure 4.8: The comparison of variations in the atomic model to the nominal model, which only excludes autoionizing states, show minimal differences in the plasma parameters and radiation temperature for models with maximum principal quantum number larger than 6 in a)-c). When the maximum principal quantum number is between 3 and 5 in d)-f) there is a decrease of electron temperature in the downstream with small decreases in the mean charge and electron density, then there are increases of these values compared to the nominal model in the upstream. All of these deviations are limited to within 15%. When the maximum principal quantum number is 2 in g) the behavior flips with a relative increase in the plasma parameters in the downstream and a decrease in the upstream with maximum deviations of 20%. The more sophisticated atomic models in h) and i) show less than 10% deviations from the nominal model with increases in plasma parameters in the downstream material and decreases in the upstream.

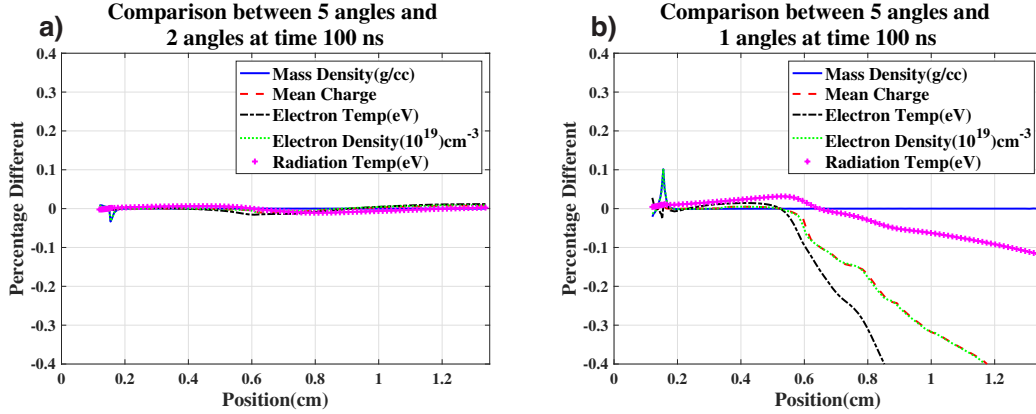


Figure 4.9: The comparison between the nominal 5 angle radiation transport calculations and a 2 angle calculation in a) show minimal differences below 5%. The single angle calculations in b) show very large decreases in the plasma parameters in the upstream material compared to the nominal model.

20%. For example, if a model had $n = 5$ as the highest principal quantum number, the next simplified model would have $n = 4$ as the highest principal quantum number for the available states. The largest principal quantum number used here was $n = 10$ and the smallest was $n = 2$. Figure 4.8 a-g show that these changes in the atomic model produce parameter variations that stay under 10% in the N during the peak emission time of the Z radiation flux for a maximum principal quantum number of 4 or greater and generally under 20% over longer periods. This has the physical interpretation that most of the interaction comes from the photoionization of inner shell electrons. It is interesting to note that for the figures 4.8 a-f there is a reduction of the plasma parameters before about 0.5 cm and an increase after, but that changes in figure 4.8 i where the maximum principal quantum number is 2 and the opposite behavior occurs. It is not clear why this is, but it may be due to the calculated opacity values when the atomic model is so drastically simplified.

To increase the complexity of the atomic model, states were added to the model until an electron gets promoted to the next principal quantum number. Here, this analysis used two iterations of this process before the computation time was exceptionally long. Figures 4.8 h and i show there are no variations beyond about 10% from

the nominal model suggesting that this level of atomic complexity capture the physics a reasonable degree at least in line with the assumptions of 1D planar geometry.

4.5.3 Number of angles in the radiation transport

The multi-angle model of radiation transport in Helios-CR solves the transport equation along a ray through a slab of material on a frequency-resolved optical depth grid. In a planar geometry, this model allows for 1-angle, 2-angle, or 5-angle for solving the transport equation. Comparing the results of simulations using the different angles and an atomic model that has $n = 4$ as the maximum principal quantum number, which has less than 10% deviation from the nominal atomic model, with a window 1.44 μm thick and 0.75 atm N shows minimal difference between the 5-angle and 2-angle calculations. Using the same model configuration in a simulation except with 1-angle for radiation transport shows a drastic difference with the 5-angle calculation. Figures 4.9 a and b compare the differences between the 1-angle and 2-angle calculations and the 5-angle model with the percent difference parameter described above. This study shows that the 1-angle calculation results in a much different distribution of the radiation energy over the spatial grid and that at least 2-angle calculations are necessary.

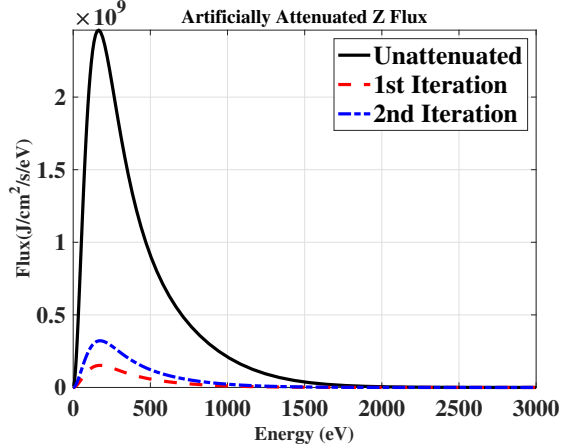


Figure 4.10: The attenuation of the input flux at the peak emission time using the iterative process described in the text for the first and second iterations.

4.6 Artificially Attenuated source

The results of the parameter space scan in section 4.4.2 are useful for initial design, but to gain an understanding of the real effects present in an experiment, multi-dimensional simulation tools are necessary. Unfortunately, at the time of this writing, there aren't any tools that provide the detailed atomic model and non-diffusive radiation transport desired for a PI front with multi-dimensional spatial grids easily accessible to university users. However, there are ways of emulating 3D geometric effects to the source flux, which is of the most importance here, within the constraints of a 1D code. Since the radiation streams up to the heat front interface, the location of the front from the gas cell window is the the relevant distance for geometric dilution. Using a geometric decay model of the on axis dilution of a finite extent source, the resulting attenuation factor is,

$$f = \frac{\left(\frac{R}{D}\right)^2}{1 + \left(\frac{R}{D}\right)^2}, \quad (4.6)$$

where R is the radius of the source and D is the distance from the source. To apply this to the simulation, consider D to be a function of time equal to the position of the

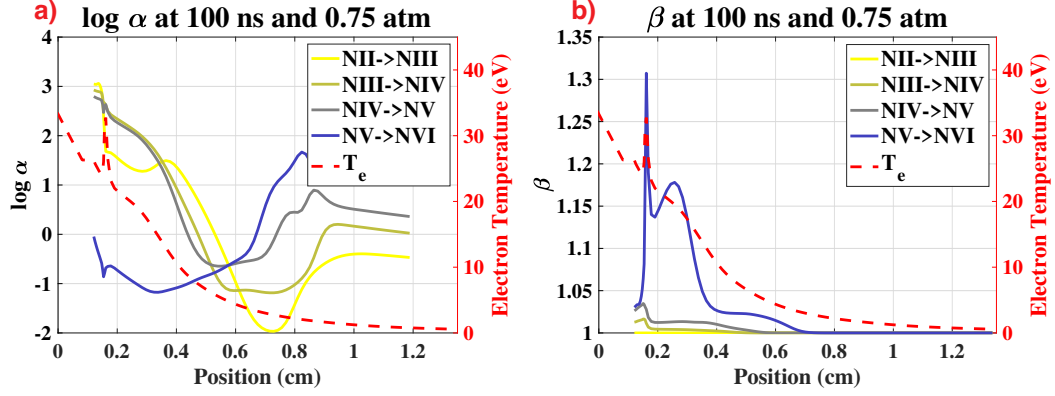


Figure 4.11: The calculated values of α and β using the second iteration of the attenuated input file, which shows that this source is sufficient to produce a PI front. a) This shows a slowed front velocity, similar to the effects of increased density and window thickness, but it also shows an order of magnitude decrease in the value of α , which is a result of the reduced radiation flux. b) This shows increased values of β compared to the simulations without consideration of the geometric flux losses in the upstream and downstream material.

PI front. Then, using an iterative method, one can calculate the front locations to get $D(t)$, use $D(t)$ to calculate $f(t)$, and apply $f(t)$ to the input flux file at the appropriate times to get a geometrically attenuated flux. Figure 4.10 shows the attenuation of the source for two iterations at the peak emission time using this method. Applying this technique over two iterations in a simulation using 0.75 atm of N and a $1.44 \mu\text{m}$ window shows that the second iteration produces a PI front using a source radius of 2.82 mm, which is the radius of a circle with the same area as a 5 mm x 5 mm square as this is the smallest window an experiment would use.

This provides a lower limit on the flux in an experiment because the attenuation factor assumes the source is at the front of the mylar window when in reality it is 45 mm away, which makes the real source much more collimated than in this attenuation method assumes. Figures 4.11 a-f show the calculated values of α and β for the iterations of the artificially attenuated input flux. These simulations suggest that even under very conservative estimates of the flux there is still a PI front with the value of β still unity and α about an order of magnitude larger, which still makes

it less than one. There is a reduction in velocity as one sees with increasing gas pressure and window thickness, but here there is also a significant increase in α due to the reduction in photon flux.

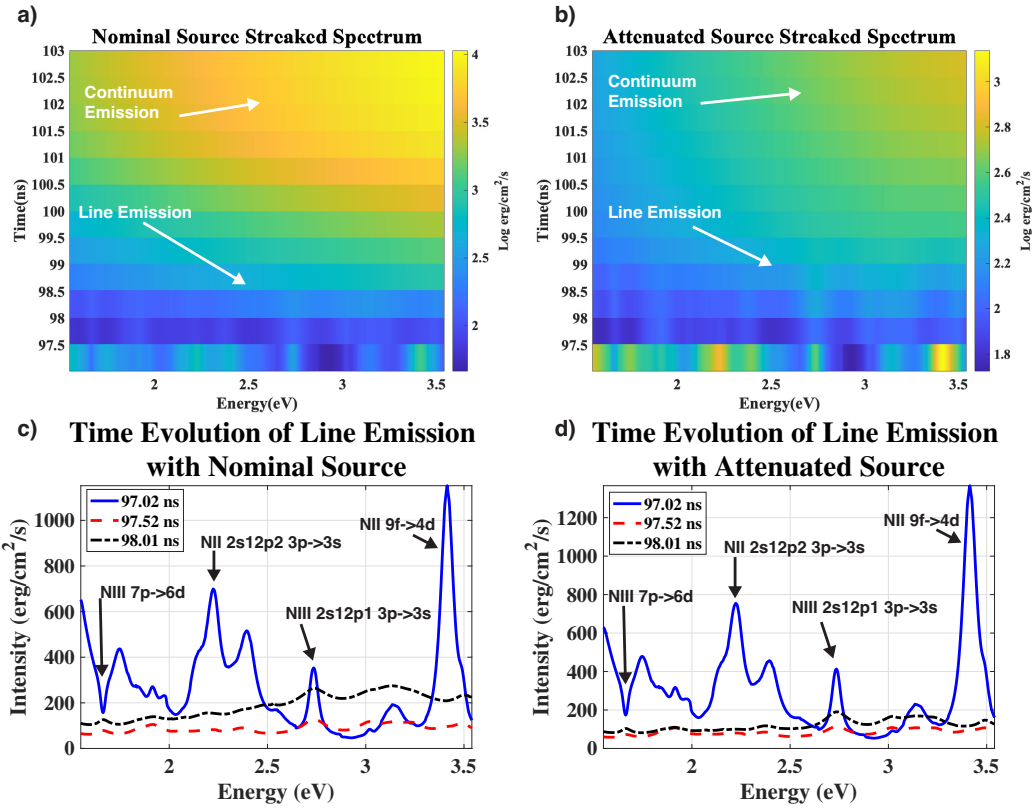


Figure 4.12: Calculations using SPECT3D use the HELIOS-CR results to estimate the expected signal of a one meter streaked, optical spectrometer. Both a) and b), which show the spectra calculations using the nominal model with the input flux file and the second iteration of the geometric attenuation respectively, display line emission early in time and as the plasma heats the thermal emission becomes the dominant signal. Figures c and d show the evolution of the line emission early in time with the nominal and attenuated input flux. These figures have two primary results, one is that there are not significant differences in line structure between the two different sources and the second is the transition from significant NII to NIII populations in the plasma.

4.7 Estimated measurements

While the simulations suggest that it is possible to generate a PI front with the Z flux, an experiment has to use the measurement tools available to observe the front. Since α and β are not directly observable values, it is necessary to measure the plasma parameters that these quantities depend on, which in this case are electron temperature, density, and ionization, in addition to knowledge of the source flux. Additionally, the propagation velocity is a useful parameter to measure for characterizing the PI front behavior. To make this measurement, the most relevant diagnostic technique available on Z is temporally-resolved visible light spectroscopy using a streak camera coupled to a grating spectrometer. This provides spectral information from 1.56 eV to 3.5 eV over timescales of 30-100 ns depending on the streak camera settings. A fiber optic cable couples the emission from the heated N plasma to the grating, which provides spectral information about one location in space as a function of time. The line emission will provide information about the ionization states present in the N at the location of the fiber and fitting this line emission provides information about the electron temperature and density. If thermal emission dominates the plasma, it is still possible to collect a temperature measurement by fitting the spectrum to a blackbody. To measure the velocity, it is necessary to have spectral information from at least two different locations because of an about 3 ns jitter in the peak current on Z.

To estimate the measured self emission from the plasma, the SPECT3D code takes the output from Helios-CR and places it on a 3D spatial grid to calculate the emission and radiation transport in the desired geometry [133]. SPECT3D calculations using the output from the nominal model described above using the unattenuated and second iteration attenuated input flux file coupled to a 1 m spectrometer show the anticipated spectra over the peak emission times. Figure 4.12 a and b show the two spectra with line emission early in time that decays to thermal emission after the

front passes the location of the fiber. As stated above, this allows for measurements based on line emission early in time and thermal emission later in time.

Figures 4.12 c and d show the line structure early in time before the transition to thermal emission as the PI front heats the location observed with the spectrometer in the nominal and attenuated input flux, respectively. There are limited differences in the line structure between the brightness of the sources, which is a good indication that photoionization is driving this behavior as it seems more dependent on the spectral content of the source than the brightness, with the caveat that the source must be bright enough to sustain the state of the plasma. The strongest lines in Figures 4.12 c and d come from the NII and NIII states, with four transitions identified that inform the evolution of the system. The lines identified here satisfy the dipole selection rules and the labels that show $n = 2$ orbitals have a second excited electron. The selected transitions all have a $\Delta l = \pm 1$ and the atomic physics model in SPECT3D averages over the different magnetic and spin quantum numbers, which means these features meet the $\Delta m = 0, \pm 1$ and $\Delta s = 0$ conditions. The earlier time spectra show bright NII transitions from the 9f to 4d orbital at 3.42 eV and the 3p to the 3s with an additional electron in the 2p orbital at 2.23 eV that decrease in relative intensity over the nanosecond time interval shown. At the same time, the two, identified NIII lines, one at 1.67 eV showing the 7p to 6d transition and the other at 2.74 eV showing the 3p to 3S transition, which increase in relative intensity over the one nanosecond time interval. This indicates that the plasma is evolving to a condition where the NIII ionization state is more prevalent than the NII state. It is important to note that there are other lines and ionization states than those identified here, but these show the decrease of the NII and increase of the NIII populations.

4.8 Conclusions

An experiment to observe PI fronts is relevant to the to the understanding of astrophysics, cosmology, and HED physics. The simulation study shown here suggests that the emission from Z is sufficient to produce the correct conditions for a PI front, even with consideration of 3D source effects. The front window and distance of the gas cell from the pinch plasma produces a reasonably collimated source to drive the PI front. This allows for a system that more closely resembles the 1D simulations than a smaller emitter that has to be closer to the gas cell. Estimates of streaked visible spectroscopy measurements show that there is line structure that one can use to find transitions between the NII and NIII states. Then, a temperature measurement is possible after thermal emission dominates the line emission.

CHAPTER V

Radiative Shock Experiments on The National Ignition Facility

The previous two chapters dealt with radiation-driven heat fronts and the properties of those systems. However, in astrophysics, there has to be a source with its own dynamics that drives the heat front or whatever other radiation-driven object is under investigation. Radiative shocks appear in many places in astrophysics including supernova and accretion columns, which are effective at converting energy to radiation energy fluxes. Chapter II discusses some of the theory involved with radiative shocks and the energy available at the NIF allows for large systems and higher densities than smaller drivers. The experiments presented below use a half hohlraum to produce an x-ray drive to launch a shock into a 20 mg cm^{-3} CH foam with the goal of making measurements of the post-shock temperature. This is of interest because while there has been much experimental work performed on radiative shocks, most of the existing measurements are sensitive to the density of the system [9, 81, 84, 93, 94]. The experiment of Visco *et al.* does use x-ray Thomson scattering to extract a temperature from a radiative shock in Ar gas, and the measurements presented here provide additional information that allows for detailed results without the explicit need for simulations [77].

This chapter will present recent experiments at the NIF making temperature mea-

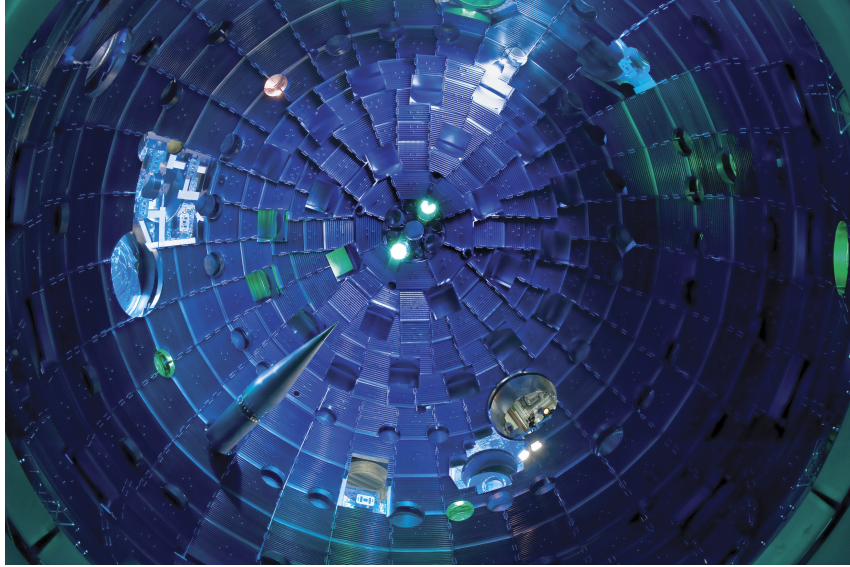


Figure 5.1: The National Ignition Facility at Lawrence Livermore National Laboratory taken from the laser.llnl.gov/media website

surements of radiative shocks. It will start by describing the NIF and the primary diagnostics used in these experiments. Then, it will discuss the targets and experimental configuration before concluding with the results from two shots days producing radiative shocks.

5.1 The National Ignition Facility

The NIF is a ND:glass laser that has 192 beams capable of producing 1.8 MJ of energy in the UV. Each beam is independent and produces about 2 TW of UV laser power to irradiate a target [134, 135]. The NIF target chamber is cut into four cones with the axis oriented normal to the ground. The cones have angles of 23.5° , 30° , 44.5° , and 50° from the cone axis. The beams are arranged in groups of four called quads and each quad lies on one of the cones, which indicates the direction of the beams relative to the target. All of the beams can use continuous phase plates and smoothing by spectral dispersion to keep the spatial profile of the laser reasonably smooth, similar to the Omega laser facility. As with the Omega laser facility, there

are a number of established diagnostics that are available for the NIF and it is not up to the experimenter to develop their own measurement devices.

5.2 Primary Diagnostics

These experiments made a velocity and two temperature measurements, which will constrain the measurement and allow for connections to the other work in the field of radiative shocks. To make these measurements, this experiment observed the time-resolved self-emission of the plasma and the scattering of an x-ray probe to measure the plasma electron temperature. The rest of this section will detail how these measurements can provide the desired information about the radiative shock.

5.2.1 X-ray Thomson Scattering

X-ray Thomson scattering (XRTS) in the non-collective regime provides a measurement of the electron temperature [136]. The non-collective scattering regime requires that the electron screening length is larger than the electron density modulation scale length. This amounts to the ratio,

$$\alpha = \frac{1}{k\lambda_s}, \quad (5.1)$$

where $k = 4\pi \frac{E_0}{hc} \sin(\theta/2)$ is the wavenumber of the density modulations that the probe interacts with and E_0 is the probe photon energy, h is the Planck constant, c is the speed of light, and θ is the scattering angle, being less than one. λ_s is the screening length, which is the Debye length in the non-degenerate case that is relevant here. In the non-collective regime the relatively large screening length means that the scattering is from interactions between photons and individual electrons. Figure 5.2 shows the geometry of the scattering problem that leads to the scattering parameter, α .

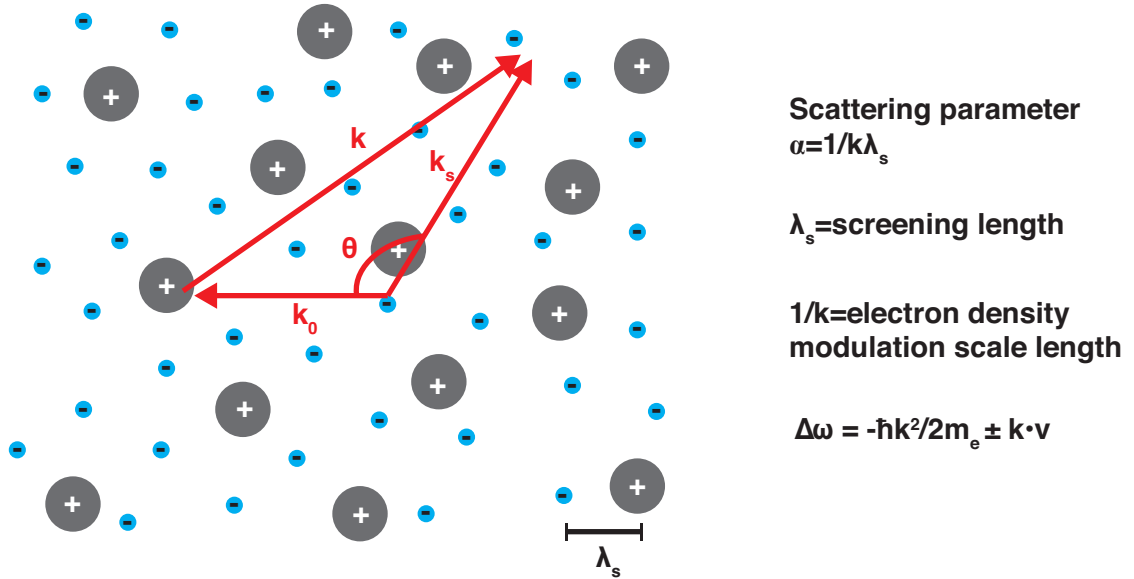


Figure 5.2: A depiction of the geometry in x-ray scattering that shows the scattering vector \mathbf{k} , which determines the electron density modulation scale length, and the screening length in the plasma. To the right there are some useful relations regarding x-ray Thomson scattering, such as the scattering parameter, α , and the doppler broadening contribution to the Compton shift, which introduces the temperature dependence in non-collective scattering.

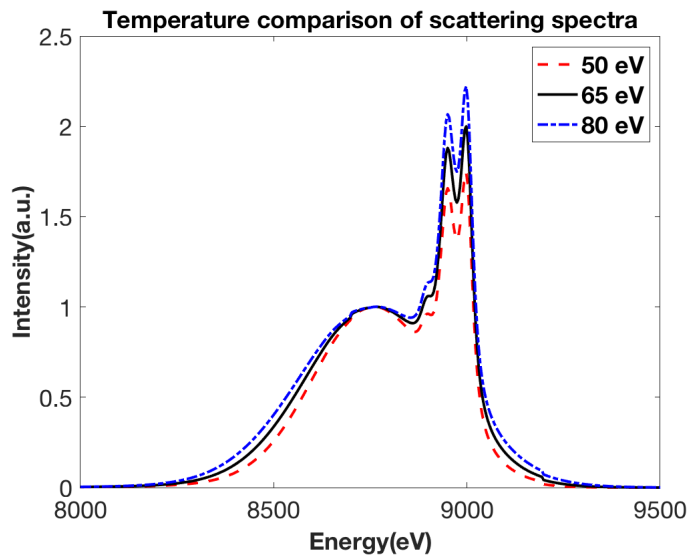


Figure 5.3: MCSS calculations that demonstrate the effect of changing temperature on the scattering spectrum. These three synthetic spectra have the same input parameters except for the listed differences in electron temperature and the scaling of the spectra makes the inelastic peak equal to one. It is clear that larger electron temperatures lead to increased broadening of the inelastic scattering peak due to the Doppler effect.

The literature details the different components of the scattering spectrum, and this overview will only give a qualitative discussion of these features to describe how they are dependent on the electron temperature [136, 137, 138]. The non-collective scattering spectrum in a non-degenerate plasma has an elastic scattering peak due to the bound electrons and an inelastic scattering peak due to the free-free scattering, and the bound-free scattering. The Compton energy determines the shift of the inelastic scattering peak, with the shift in frequency being $\Delta\omega = -\frac{\hbar k^2}{2m_e} \pm \vec{k} \cdot \vec{v}$, where \hbar is the reduced Planck constant, m_e is the electron mass, and \vec{v} is the velocity distribution. The second term in the inelastic frequency shift is due to Doppler broadening. If one assumes a Maxwellian velocity distribution, then the Doppler broadening depends on the electron temperature through the width of the peak. The three synthetic scattering spectra in Figure 5.3 show the dependence of the inelastic scattering peak on temperature with the larger temperature having a broader inelastic feature. If the data is high enough quality, and the components of the plasma well-known, then the ratio of the elastic to inelastic scattering peak can be a measure of the ionization in the plasma [139, 140].

It is necessary to have a probe source with a reasonably narrow line width, at most about 100 eV, to make scattering measurements. To make the probe source, most experiments use a laser irradiated foil to produce He- α emission [77, 137, 139, 140]. These experiments use a Zn foil to generate the Zn He- α doublet with the resonance line at 8999 eV and the intercombination line at 8950 eV. In these experiments, the scattering volume is large enough in the dispersion direction of the crystal that it is not possible to distinguish the two lines in the doublet.

5.2.2 Streaked Optical Self-Emission

Since the shock velocity provides a large amount of information about the conditions in the plasma, as described in section 2.3.3, it is a useful measurement to make

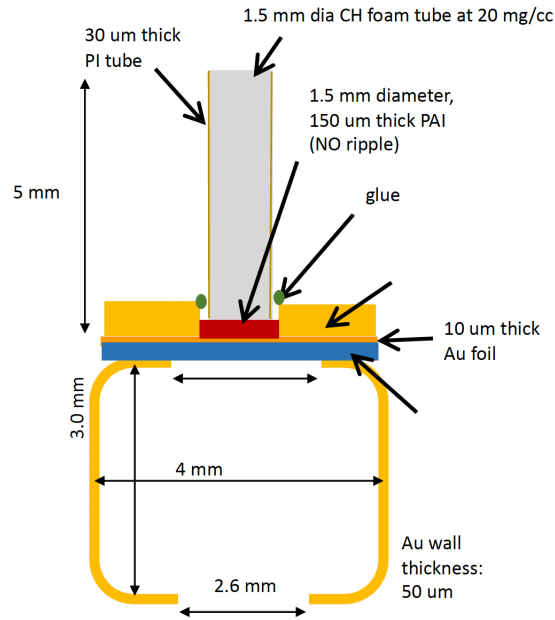


Figure 5.4: A cartoon of the target physics package, which shows the hohlraum, solid plastic, and CH foam regions.

and provides a connection to the radiative shock literature. An axial imaging system will allow for a measurement of the location of the shock because the brightest emission will correspond with the density jump. Streaking the line-imaged measurement will produce a shock location for each time resolution unit in the camera, which will allow for a measurement of the velocity. This will also be useful for the XRTS, as it provides the location of the shock during the x-ray probe.

The second use of this measurement is to convert the signal level to a radiation flux, which can then be used to find a temperature with the assumption of a blackbody emitter. This requires that the detector is absolutely calibrated, which the NIF diagnostic is not. However, it is also possible to find alternative calibrations of the temperature scale based on the observed physics, which is the approach used here.

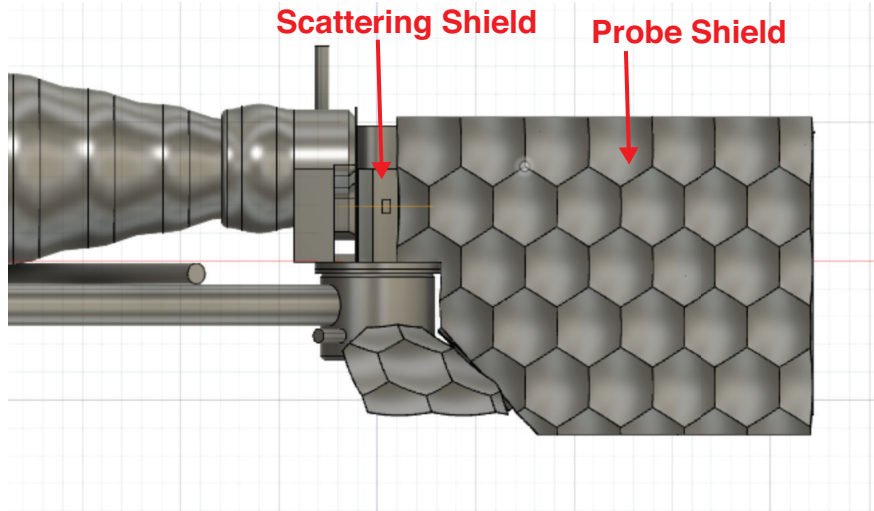


Figure 5.5: The CAD model from the July shot day showing the scattering and probe shields to provide an image to go along with the description in the text.

5.3 Target Design

These experiments use an x-ray drive to ablate a plastic foil, launching a pressure wave into the solid plastic. After propagating through the plastic foil, the shock breaks out the rear surface and launches a shock into a low density foam tube. This lower density material allows for a much faster shock, which is the radiative shock of interest. The remainder of the target supports the shock tube and provides shielding for the two primary diagnostics.

The x-ray drive comes from a Au half hohlraum with a diameter of 4 mm, a height of 3 mm, and a wall thickness of $50\ \mu\text{m}$, which the NIF lasers irradiate to produce the radiation bath that creates the pressure wave in the plastic. The $150\ \mu\text{m}$ plastic foil sits on top of the hohlraum, then there is a $10\ \mu\text{m}$ thick Au foil to absorb the M-band emission from the hohlraum. On top of the Au foil is a plastic disk $150\ \mu\text{m}$ thick and 1.5 mm in diameter with a flat surface, which the foam shock tube sits on top of. The shock tube is a $20\ \text{mg cm}^{-3}$ CH foam cast in a $30\ \mu\text{m}$ thick polyimide tube with a 1.51 mm diameter. There is a $175\ \mu\text{m}$ slit in the shock tube that extends 2 mm from the top towards the hohlraum for the self-emission measurement. This results

in a foam diameter of 1.45 mm and the shock tube is 5 mm long. There is a 250 μm thick Au washer with a 4.1 mm outer diameter and a 1.55 mm inner diameter that sits on top of the Au foil and supports the base of the shock tube against the extreme pressure of the shock breaking out into the CH foam. Figure 5.4 shows these features in the target construction. There is a large cone with support structures that shields the slit in the shock tube for the self emission diagnostic. A Ta shield, with a similar slit laser cut into it, covers the remaining opening of the cone shield and sets the measurement region of the self-emission diagnostic. The remaining features on the target are two alignment features, one on the side of the hohlraum and a second that stands up from the top of the hohlraum parallel to the shock tube. The remainder of this section will discuss the details of the XRTS shielding and probe foil in the different target builds. There was a need to improve the shielding between the shot days to fix an issue with background that section 5.6 will discuss.

5.3.1 First XRTS Shielding and Probe Design

The XRTS shielding in this target has two components, the first is a Au foil on the shock tube that set the scattering volume and prevents scattered light from other portions of the target from reaching the spectrometer, and the other is a large structure that attenuates the x-rays from the expanding plume of plasma from the foil probe. The document will call the Au foil shield the scattering shielding and the large shielding structure the probe shielding from here on.

The scattering shielding is 25 μm thick Au foil that has a 300 μm by 500 μm with the longer side aligned along the shock tube axis. The center of the window is 2.1 mm from the bottom of the shock tube and 2.41 mm above the drive surface of the plastic foil. It extends from the Au washer 3.45 mm up the shock tube, which is approximately the maximum height the the probe x-rays should reach. The scattering shielding then extends to cover the portion rest of the target that the probe x-rays

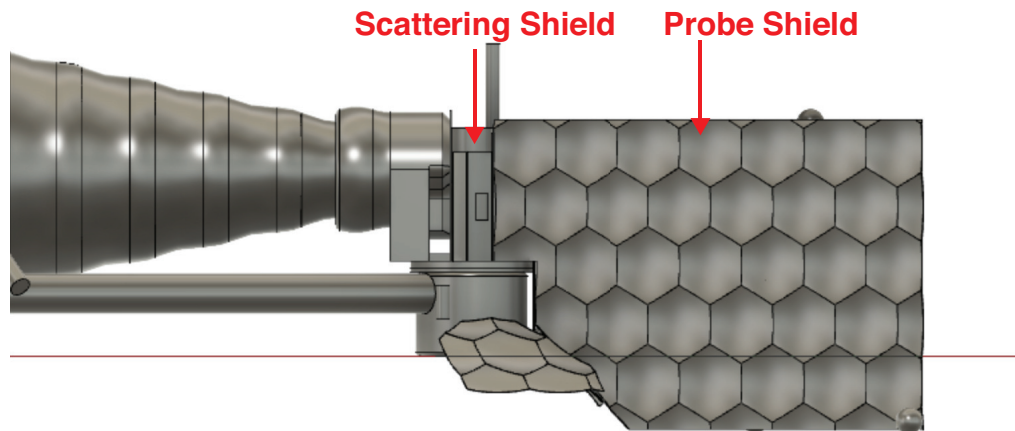


Figure 5.6: The CAD model from the February shot day pointing out the scattering and probe shields to indicate where the changes are in the second iteration of shielding.

could reach, which is the angled portion of the foil. Figure 5.5 shows the scattering shielding in the center of the figure and the large probe shielding to the right.

The probe shielding contains the collimator to limit the scattering geometry, the Zn foil that generates the probe x-rays, and the shielding to keep the Zn plasma from dominating the signal. The collimator is built in to the front of the shielding structure and consists of two $50\ \mu\text{m}$ thick Au foils with $500\ \mu\text{m}$ diameter apertures and a separation of 1 mm from the front of the inner foil to the rear of the outer foil. This limits the range of scattering angles to approximately $\pm 20^\circ$. The Zn foil sits at a 21.6° angle relative to the shock tube axis and the front surface tilts towards the hohlraum to allow the lasers to be closer to normal incidence. The center of the beam spot on the Zn foil is about 1.5 mm from the inner collimator foil. Below the Zn foil there is more Au shielding to prevent x-rays from reaching the outside surface of the hohlraum facing that faces the spectrometer. The large shielding structure extends out 11 mm in the spectrometer object plane, which is a design that has been successful in other XRTS measurements on NIF [137, 139, 140].

5.3.2 Second XRTS Shielding and Probe Design

The components of the XRTS shielding stay the same in this second iteration, but there are some adjustments that improve the ability to collect scattering data and make the shielding structure more x-ray tight. Figure 5.6 shows how the changes would appear to the spectrometer.

The scattering shielding increased in height from 3.35 mm to 4 mm to ensure that all of the probe beam is inside the bounds of the shielding. Additionally, the scattering window increased in size to 1 mm by 0.4 mm with the long side again along the shock tube axis. This is to increase the scattering volume and provide more signal to the spectrometer, which is necessary due to the low signal nature of this measurement.

The probe shielding has some minor changes to decrease the area of the gaps between the different foils, which is especially necessary due to the dimpled shielding on the NIF. These changes include increasing the size of the outer collimator foil to better overlap with the large shielding structure. There was a similar increase in the dimensions of the shielding that sits below the Zn foil. There was a 125 μm plastic foil added to the rear surface of the Zn foil to prevent any plasma from traveling down the collimator and interacting with the shock tube. Finally, the second design increased the length of the probe shielding structure in the object plane of the spectrometer by almost 1 mm to ensure that none of the Zn plasma plume is visible in the measurement.

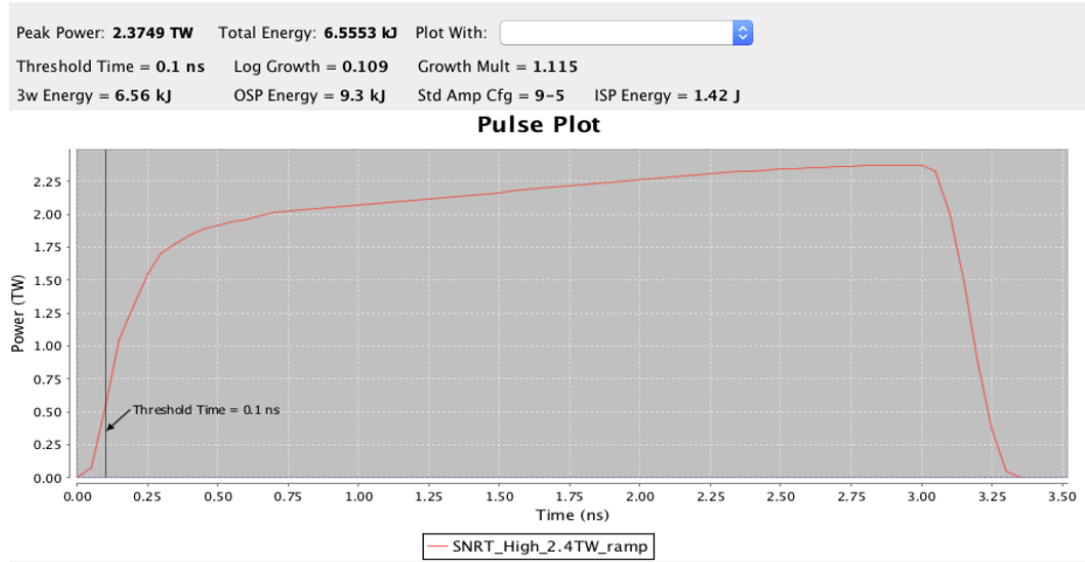


Figure 5.7: The drive laser pulse shape showing the power for each of the sixty beams.

5.4 Laser Configuration

There are two pointing locations on the target described above, one is the laser entrance hole of the hohlraum and the other is the center of the probe foil. All of the beams come from the bottom half of the NIF, which was a decision to protect the upper half of the facility from debris.

5.4.1 Drive Lasers

The experiment used 60 beams to drive the hohlraum with the laser pulse shape used in Figure 5.7 a. This resulted in about 400 kJ of laser energy incident on the Au to create the radiation bath that drives the shock into the plastic foil.

5.4.2 Probe Lasers

There were two quads used to drive the probe foil with a total of about 50 kJ, one of which came from the outer cone and the other from the inner cone. The inner cone beams are the reason for the tilted probe foil as they have a large incidence angle that would cause most of the energy to be reflected away. The pulse shape uses

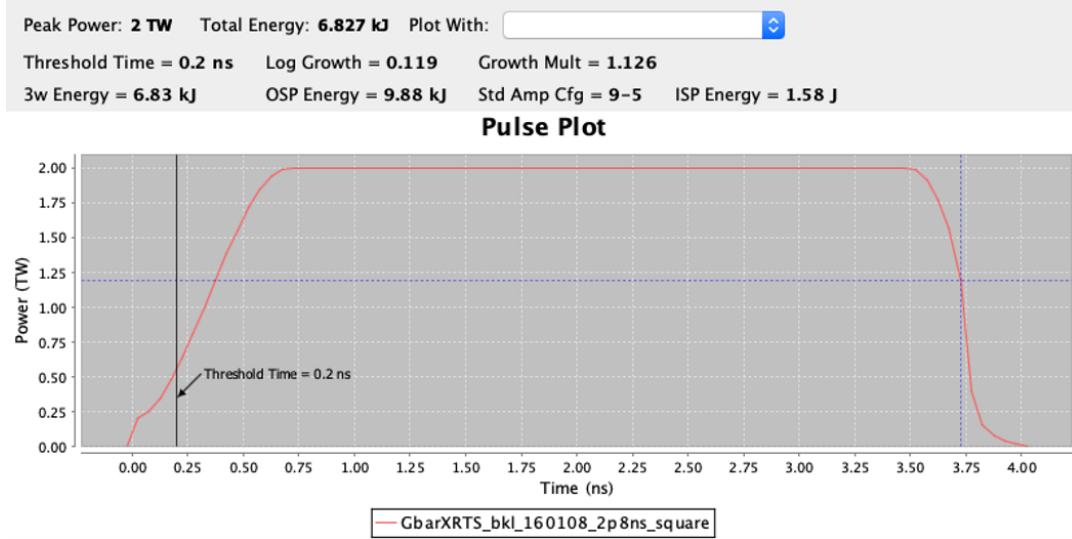


Figure 5.8: The probe x-ray pulse shape showing the power for each of the eight beams.

a ramp followed by a 3 ns duration of peak power with a final intensity of 10^{15} W cm^{-2} because work to develop backlighter foils on the NIF found that a pre-plasma enhances the laser coupling [141, 142]. The work of Barrios *et al.* also found that 10^{15} W cm^{-2} produces the optimal conversion efficiency to K-shell line emission in Zn of about 1% [141, 142]. Figure 5.8 shows the pulse shape used to drive the probe foil.

5.5 Diagnostic Configuration

Section 5.2 presents an overview of the primary measurements used in these experiments. This section will provide more detail about the instruments used to make those measurements and the limitations of the diagnostics.

5.5.1 Monoangle Crystal Spectrometer (MACS)

The Monoangle Crystal Spectrometer (MACS) is an established spectrometer on the NIF that, when paired with a highly oriented pyrolytic graphite (HOPG) crystal, is typically used in XRTS measurements [143, 144]. The crystal is at a 12.4° angle to

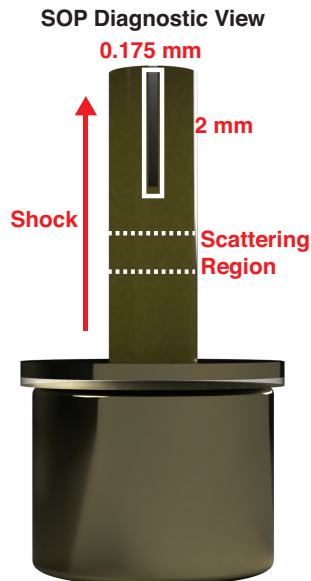


Figure 5.9: The physics package with labels indicating the shock propagation direction and the relative locations of the self-emission measurement to the XRTS measurement.

set a spectral range of 7.4 to 10 keV, which makes this spectrometer well suited to observe the scattering of the Zn He- α around 9 keV. A charge-coupled device (CCD) with a four-strip MCP coupled to the spectrometer records the signal from the experiment. The MCP uses a 230 ps PFM and a 150 V bias, which provides a time gate of about 200 ps [145, 146, 147]. These experiments use a spectrometer configuration with two cylindrically curved HOPG crystals where the geometry focuses each crystal to one MCP strip. Each strip has a 125 μm polyimide filter and there is a 50 μm Al-coated polyimide blast shield on the front of the spectrometer. The spectrometer uses a Von Hamos geometry and satisfies the mosaic focussing condition, which specifies that the source-to-crystal distance equals the crystal-to-detector distance, to focus the x-rays in the non-dispersive direction and provide spatial resolution of about 1 mm [143, 144]. This is not good enough spatial resolution to discern features in the shock tube, but is helpful in locating sources away from the scattering window. The timing of the different strips changed between shot days and later sections will

present the specific values used for different shots.

5.5.2 VISAR and SOP Cameras

The self-emission diagnostic uses the line-imaging velocity interferometry system from any reflector (VISAR) and streaked optical pyrometry (SOP) system on NIF to collect this signal [148, 149]. There are three streak cameras in this system that this document will refer to as VISAR A, VISAR B, and SOP from here on. The VISAR A camera has a 31 ns sweep and a 1 mm field-of-view with a 2 nm bandwidth centered at 660 nm. The VISAR B camera has a 21 ns sweep and 1 mm field-of-view with a 2 nm bandwidth centered at 660 nm. The SOP camera has a 45 ns sweep and a 2 mm field-of-view with a 105 nm bandwidth centered at 580 nm. The spatial resolution of the cameras are $2.5 \mu \pm 4\%$, $1.19 \pm 2.5\%$, and $1.12 \pm 2.8\%$ for the SOP, VISAR A, and VISAR B cameras, respectively. The time resolution of the cameras are about 32 ps, 25 ps, and 16 ps for the SOP, VISAR A, and VISAR B cameras, respectively. The VISAR cameras will not use any fringes, as these experiments are not trying to observe interferometry, however, the probe laser is on for these experiments because it reflects off of the Ta shield and provides a reference location in the VISAR A and VISAR B data. The probe laser does not appear in the SOP data because the optics that lead to the camera front end filter out the probe wavelength. Each of the cameras had neutral density (ND) filtering, which varied between shot days and the following sections will present the values used in different experiments.

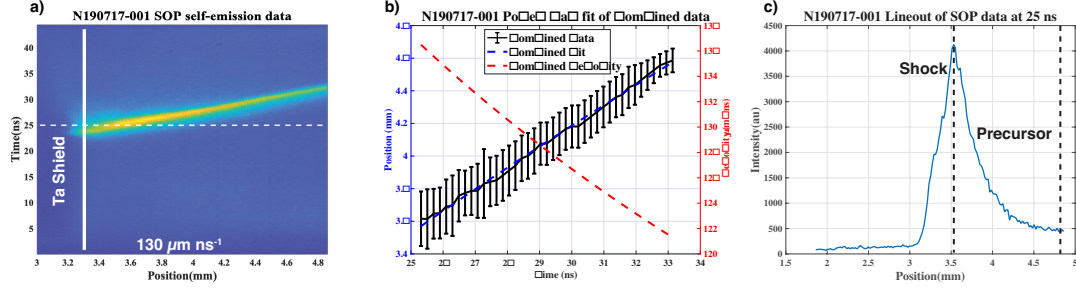


Figure 5.10: a) The SOP camera data with a six pixel average over the time and space axes with labels to indicate the location of the Ta shield and the line out in c). b) The combined shock location data from all three cameras as well as the power law fit to the trajectory. The right axis shows the calculated velocity, which is the derivative of the power law fit, and provides an average velocity in the measurement window of $130 \mu\text{m ns}^{-1}$. c) A line out from a) that shows the presence of upstream heating due to the shock, which indicates this is a radiative shock.

5.6 July 17th Shot Day

A shot day on July 17th 2019 drove a radiative shock into one target using the diagnostics described above. The MCP strip timing on the MACS spectrometer was 17.3 and 18.5 ns and the probe beams turned on 16.24 ns after the hohlraum drive beams. The VISAR A and VISAR B cameras used ND 1 filters and the sweeps started 2 ns and 12 ns after the hohlraum drive lasers, respectively. The SOP camera used a ND 2 filter and the sweep started -0.5 ns from the start of the hohlraum drive lasers.

5.6.1 Self-emission Data

It is important to note that since the measurement uses optical emission, the plasma is above the critical density and therefore the signal is coming from the edge of the plasma. This is not too much of an issue because previous work with this geometry on the NIF measured a very flat shock front using x-ray radiography [9]. The self-emission diagnostic collected good signal with a clear interpretation of a shock propagating through the foam, as seen in Figure 5.10 a. The ND filtering on the VISAR cameras was too strongly attenuating and this made tracking the shock slightly more difficult than on the SOP camera.

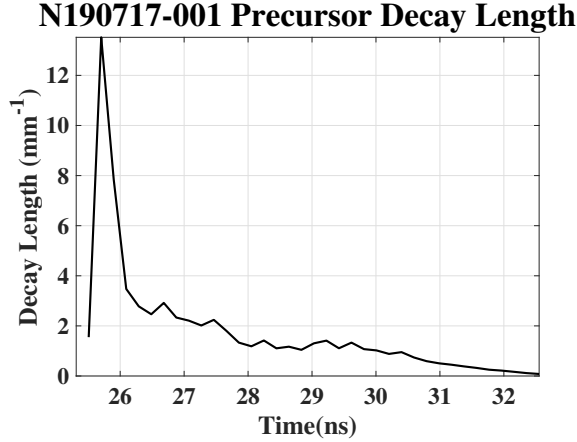


Figure 5.11: The decay parameter from fitting the upstream heating in the SOP data. Other than one outlier, this indicates that the upstream has an electron heating length scale of about 1 mm, which should correspond to a similar value for the photon mean free path, and indicates that there is a significant amount of radiation that can escape through the end of the shock tube.

The analysis averages the self-emission data over six pixels in the time and spatial axes to remove noise. It then tracks the shock location by finding the largest value at each time because the shock transition should produce the largest temperature. Figure 5.10 b shows the combined data from all three cameras where the analysis interpolates the trajectories onto the same spatial grid and then the plot shows the average of those values. The error bars in Figure 5.10 b are from fitting a Gaussian to the peak in signal and taking the width of that fit to be the uncertainty in the location. This results in fairly conservative estimates of the uncertainty in shock location. Fitting the combined data with a power law provides a trajectory of the shock earlier in time, which is useful for the XRTS measurements, and allows for a calculation of the shock velocity. Here the shock velocity in the measurement window is, on average, $130 \mu\text{m ns}^{-1}$. Figure 5.10 c shows a line out of the data at 25 ns and demonstrates heating in the upstream, which this analysis attributes to the radiative precursor from the shock front emission.

The exponentially decaying precursor region suggests a transmissive precursor and the analysis fits this feature at each time step, which gives a decay parameter as a

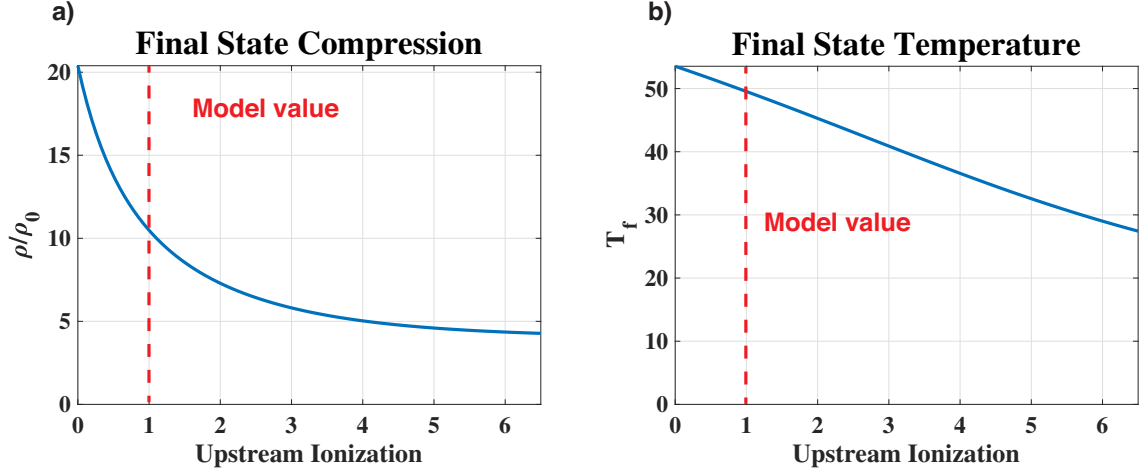


Figure 5.12: a) The final state compression from the thick-thin radiative shock model as a function of the upstream ionization with a dashed line indicating the value used in the analysis. b) The final state temperature from the thick-thin radiative shock model as a function of upstream ionization with a dashed line showing the value used in the analysis.

function of time. Figure 5.11 shows that this value is about 1 mm, except for a single outlier early in the measurement window. These cameras actually measure the electron temperature, not the radiation flux, because the optical emission will come from the electrons. This means that this decay parameter is an electron heating rate instead of an opacity. However, the radiation from the shock goes into heating the electrons, so this decay parameter should be indicative of the absorption length of the radiation. This suggests that the upstream is at most a small number of mean free paths in extent and there is radiation energy leaving the end of the shock tube. The shock has an optically thick downstream and an optically thin upstream.

Since this is a thick-thin shock, it is possible to extract more information from this self-emission data with a fairly simple analytic model, where the following material will remind the reader of the results from section 2.3.3.2. Using the three layer model of McClarren *et al.*, which is analogous to the thick-thick model discussed in chapter II, one can find the final state temperature and compression as well as the initial downstream temperature at the density jump [4]. The expression for the final

inverse compression in the thick-thin model is,

$$(\gamma + 1)\eta_f - \gamma(1 + P_0) = -\sqrt{(P_0\gamma - 1)^2 + 2Q[\eta_f(1 + P_0 - \eta_f)]^4(\gamma^2 - 1)}, \quad (5.2)$$

where γ is the polytropic index, η_f is the final inverse compression, P_0 is the initial normalized upstream pressure, and Q is the shock strength parameter defined in chapter II. A numerical solution to this equation will give eight values for η_f , but the imaginary, negative, and greater than one values can be thrown out as not physical, which typically leaves a single root. The final state temperature is,

$$T_f = \frac{u_s^2}{R(\gamma + 1)^2} \left[\gamma P_0 + \gamma - \sqrt{(\gamma P_0 - 1)^2 + F_{r0}(\gamma^2 - 1)} \right] \left[1 + P_0 + \sqrt{(\gamma P_0 - 1)^2 + F_{r0}(\gamma^2 - 1)} \right], \quad (5.3)$$

where T_f is the final temperature, u_s is the shock velocity in units of cm s^{-1} , R is the gas constant in units of $\text{erg g}^{-1} \text{eV}^{-1}$, and F_{r0} is the normalized upstream radiation flux with all of the other values the same as in equation 5.2. Under the assumption of a thin cooling layer, the expression for F_{r0} is,

$$F_{r0} = 2Q[\eta_f(1 + P_0 - \eta_f)]^4. \quad (5.4)$$

This system of equations depends on the shock velocity, upstream temperature, and upstream ionization. Making the further assumption that the upstream pressure follows the ideal gas law and using the measured velocity of $130 \mu\text{m ns}^{-1}$ with a γ of $5/3$, the system of equations only has the upstream temperature and ionization as free parameters. The rest of this analysis will assume that the upstream ionization is 1 and that the upstream temperature is 1 eV. Figures 5.12 a and b show the results for the final compression and temperature, respectively, as functions of the upstream ionization. It turns out that for upstream temperatures up to 10 eV there are no real

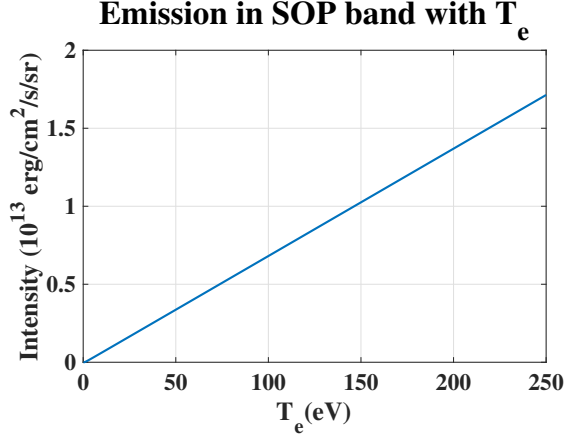


Figure 5.13: The scaling of the emission in the bandwidth of the SOP optical path under the assumption of a Planckian emitter. This suggests that the response is linear with temperature and that a mapping is possible if one has a measured value for the temperature in one pixel.

changes to the final compression or temperature, so that portion of the parameter space is not considered any further here.

The initial downstream temperature is important as well because it provides the the quantity that is useful for calculating the radiative energy flux. The expression for the initial downstream temperature is,

$$T_{ds} = \frac{u_s^2}{R(\gamma + 1)^2} [2 - (\gamma - 1) P_0] [2\gamma P_0 + \gamma - 1], \quad (5.5)$$

where all of the values are as defined above.

The results of these calculations are a final compression of 10.2, a final temperature of 49.3 eV, a Q of 4500, and a T_{ds} of 109 eV. The reason that Q is relatively low for the HEDP conditions is due to the upstream ionization affecting the value of the gas constant. If the upstream ionization is taken to be zero, then Q is about 8×10^4 , which is a typical value for laboratory generated radiative shocks [1]. A last calculation from this model is the ratio of the blackbody energy flux at T_{ds} to the incoming material energy flux, $R_F = \frac{2\sigma_{SB}T_{ds}^4}{\rho u_s^3}$ with σ_{SB} the Stefan-Boltzmann constant in units of erg cm⁻² eV⁴, T_{ds} the initial downstream temperature in units of eV, ρ the mass density in

units of g cm^{-3} , and u_s the shock velocity in units of cm s^{-1} . The model output using the measured velocity, an upstream ionization of 1, and an upstream temperature of 1 eV gives $R_F = 6.6$, which indicates the radiative energy fluxes are significantly larger than the material energy fluxes and further confirms that the shock is radiative.

Having a value of the shock temperature is useful, but it doesn't take full advantage of the self-emission data. To make this temperature value more useful it is necessary to consider the response of the detector as a function of temperature of the emitting plasma. A rough approximation is possible if one assumes a Planckian spectrum from any portion of the plasma, which is fairly reasonable because the downstream is optically thick and while the cooling layer would allow for a more complicated spectrum, it is a very physically small region, to the point of not being resolvable, and will not constitute a significant portion of the image. This makes the measured quantity the post-shock material downstream of the cooling layer. As a comparison, the immediate post-shock temperature for a $130 \mu \text{ns}^{-1}$ shock in the plastic foam used in these experiments is 109 eV and the measured electron temperatures are several tens of eV. Figure 5.13 shows the Planckian emission, integrated over the bandwidth of the SOP camera, as a function of temperature, where it is also assumed that the electron temperature is equal to the radiation temperature. Since this is a linear relationship, it is reasonable to assume there is a linear mapping from the digitized counts of the streak camera to temperature. This relies on the camera and digitizer also having a linear response, which is not necessarily true, but is typically corrected for in the processing of streak camera data.

Using the final state temperature calculated using the thick-thin model of a radiative shock, and the assumed linear mapping justified above, it is possible to put the SOP camera data onto a temperature scale. Figure 5.14 a and b show the SOP data from Figure 5.10 a and b, but with the scaling to temperature. This shows that the peak electron temperature of the post-shock region in the measurement window

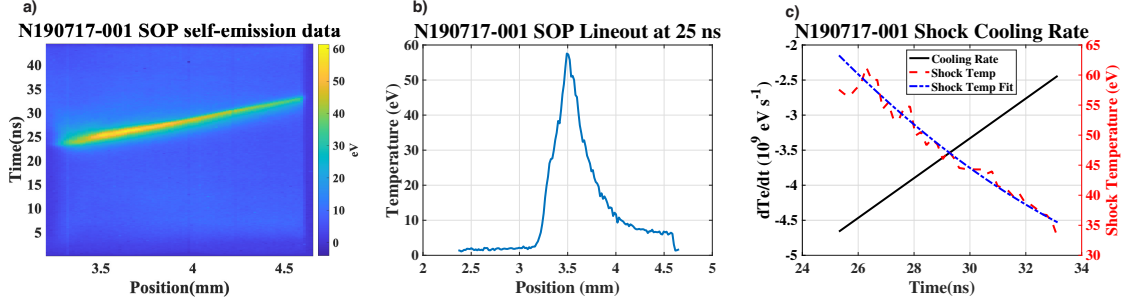


Figure 5.14: a) The SOP camera data with the temperature mapping from the thick-thin model analysis. This shows a peak post-shock temperature of about 60 eV. b) The line out at 25 ns shown in Figure 5.10 c scaled to temperature. c) The post-shock temperature as a function of time in the measurement window with a power law fit to the data and the calculated derivative from the fit. This shows that the time derivative is decreasing with time.

is about 60 eV.

From Figure 5.14 a, the shock temperature decreases with time as it radiates away energy that escapes either through the upstream or radially. With the temperature mapping, it is possible to find the time derivative of the shock temperature, which Figure 5.14 c shows and will be useful in future work to find the radiative cooling rate.

5.6.2 XRTS Data

The fact that there is a second iteration of the XRTS shielding suggests that the design used on the first shot day was not sufficient and that is the case. This section will discuss the collected data and the expected cause for the lack of signal. Figure 5.15 shows the top down geometry of the scattering measurement with a Zn He- α probe and a 113° scattering angle. The data in Figure 5.16 a shows all four strips of the MACS with the timing of the two that are collecting data from a crystal indicated. This shows two bright line features on both strips, one at about 9 keV and the other at about 9.6 keV. These lines are spatially shifted towards the hohlraum indicating that is the likely source for the emission. These are Au L-shell lines with the feature at 9 keV likely combined with elastic scattering of the Zn He- α doublet

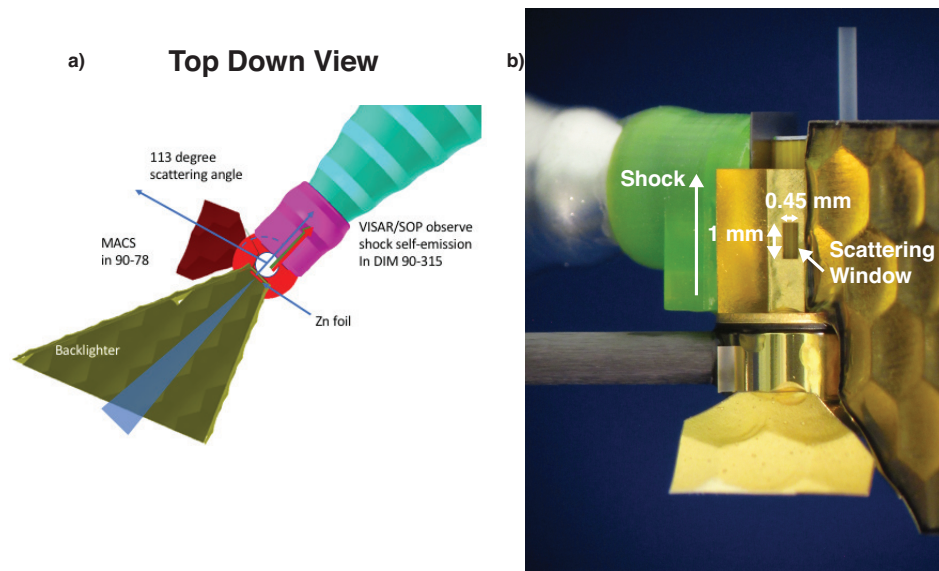


Figure 5.15: a) The top down view of the scattering geometry, which shows the 113° scattering angle and the shielding. b) The view from the MACS crystal of the actual target, indicating the scattering window dimensions and the shock propagation direction.

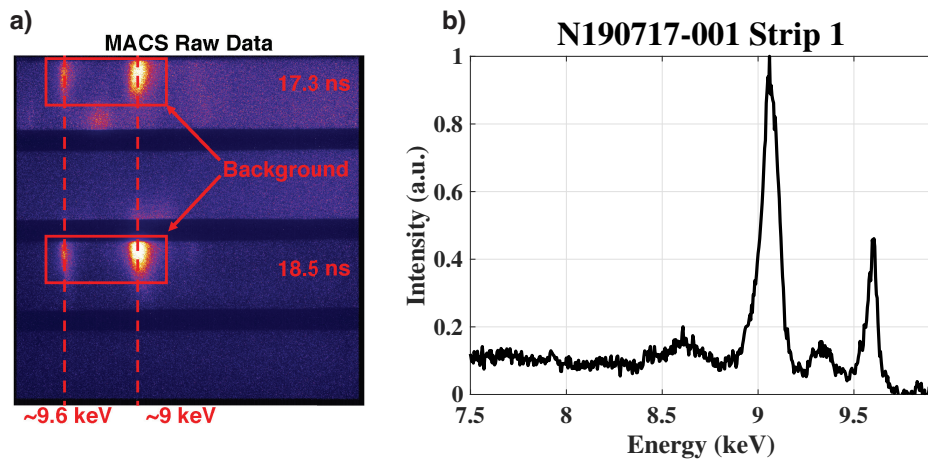


Figure 5.16: a) The raw MACS data showing the Au L-shell lines that dominate the signal and the strip timing for the camera. The vertical offset of the line data suggests that these features originate at the hohlraum. b) A spatially integrated spectrum from strip 1 at 17.3 ns showing the lines have no redshifted portion of the spectrum, which would indicate scattering signal.

[150]. This interaction was possible because the shielding structure used glue to make it gas tight, but there were gaps in the Au that were transparent to the 9 keV probe x-rays, which had lines-of-sight to the hohlraum. Figure 5.16 b shows a line out that indicates there is no elastic scattering peak in this data. The reason for this lack of observed scattering is most likely because background is too bright and dominates the signal, even though predictions suggested the scattering signal would be observable [98]. The way to correct this is to expand the scattering volume to increase the signal and to seal the transparent gaps in the shielding to reduce the background.

5.7 February 10th Shot Day

This shot day used the improved XRTS shielding described above and changed the strip timing to 18.3 ns and 20.5 ns with a probe laser timing of 17.5 ns relative to the start of the drive lasers. The self-emission cameras still use the same sweep speeds and the SOP camera still uses the 2 ND filtering, but the VISAR A and VISAR B cameras have 0 ND filtering for this shot day to improve the signal to noise ratio.

5.7.1 Self-emission Data

The self-emission data in this experiment very clearly shows something propagating through the measurement window, however, it is not clear that it is the shock propagating through the foam like it was for the previous shot day. The reasoning for this is due to multiple inconsistencies in comparing the data with the expected physics. In Figure 5.17 a, the SOP camera shows a feature that appears around 15 ns and exits the field-of-view around 20 ns. This indicates a much faster shock than the previous shot day, about $350 \mu\text{m ns}^{-1}$ compared to $130 \mu\text{ ns}^{-1}$. However, the drive energy is not significantly different and the components are all within 20% between the shot days, which would not be enough to create this difference. Additionally, Figure 5.17 b shows no radiative precursor, which would be unusual on its own be-

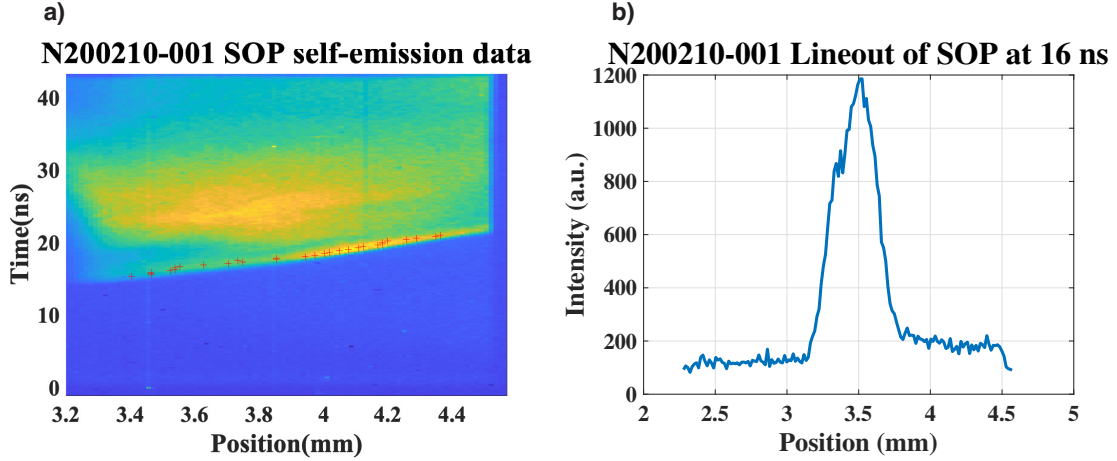


Figure 5.17: a) The SOP data from the February shot day showing a very fast feature that does not make sense for the physics in the experiment. If this is a shock, its average velocity would be about $350 \mu\text{m ns}^{-1}$ with the same drive energy for the lasers. b) A line out at 16 ns showing the absence of a precursor, which is not consistent with the large average velocity, further suggesting that this signal is not the shock propagating in the foam.

cause the drive is similar, but the fact that the shock is supposedly over two and a half times faster than the previous data would suggest a much stronger radiation field from the shock front and therefore a hotter precursor.

This indicates several discrepancies between the data and a reasonable expectation of the physics occurring in the shock tube. The best guess as to what is happening here is, during the foam casting process, the drying foam shrinks and pulls away from the wall of the shock tube. This allows the released material from the plastic foil to freely propagate in this gap and reach the window before the shock, traveling rapidly, and without any precursor because there is no upstream material. This means that this data is not reliable for the shock timing of these experiments and the timing from the previous shots is more relevant because of the consistent drive laser energy.

5.7.2 XRTS Data

To start, the fact that the self-emission diagnostic was not effective on this shot day does not indicate that the XRTS data is not useful. As mentioned before, the

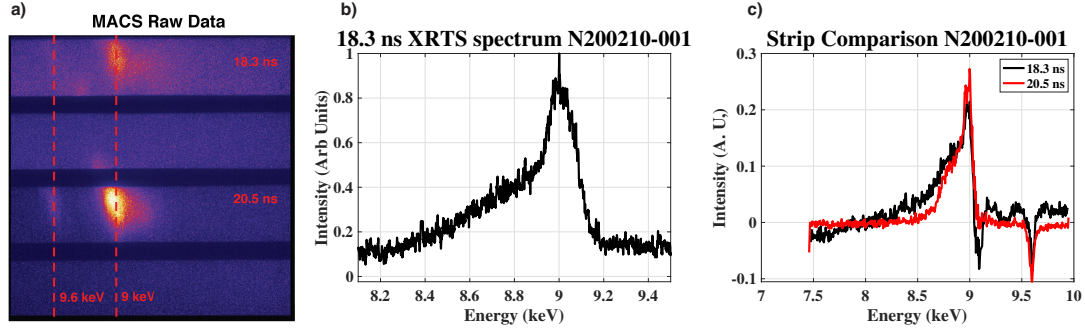


Figure 5.18: a) The raw XRTS data from the MACS for the February shot day that shows the reduced signal from the Au L-shell lines from the July shot day and the presence of inelastic scattering in the center of the strips. b) The spatially averaged data from strip 1 clearly showing the inelastic scattering feature extending to about 8.2 keV. c) A comparison of the data between strip one and strip two after the background subtraction described in the text. The second strip (in red) clearly has a narrower inelastic scattering feature, which indicates that the volume averaged temperature is lower later in time after the shock has cooled and the entrained flow moves into the scattering window.

self-emission data sees the edge of the plasma, but the XRTS data measures the center of the shock tube and the gap at the edges of the foam should not affect the scattering measurement.

With the increased scattering volume and the improved shielding, this experiment was able to collect scattering signal on both strips of the MCP. There is clearly redshifted signal in Figure 5.18 a and Figure 5.18 b shows this more definitively when compared to the July shot day data. However, there is still some of that background from the interaction of the probe with the hohlraum. To correct for this, the data analysis puts the data from the July shot day on the same energy scale, then scales and subtracts it from this data to remove the effects of these lines.

As a starting point in this analysis, it is important to make sure the data makes sense with the physics occurring inside the shock tube. Figure 5.18 c accomplishes this check with a comparison of the scattering signal on the two strips. This shows that the scattering signal at 18.3 ns has an inelastic scattering peak with a larger width than the 20.5 ns data, which indicates that the integrated volume has a lower averaged

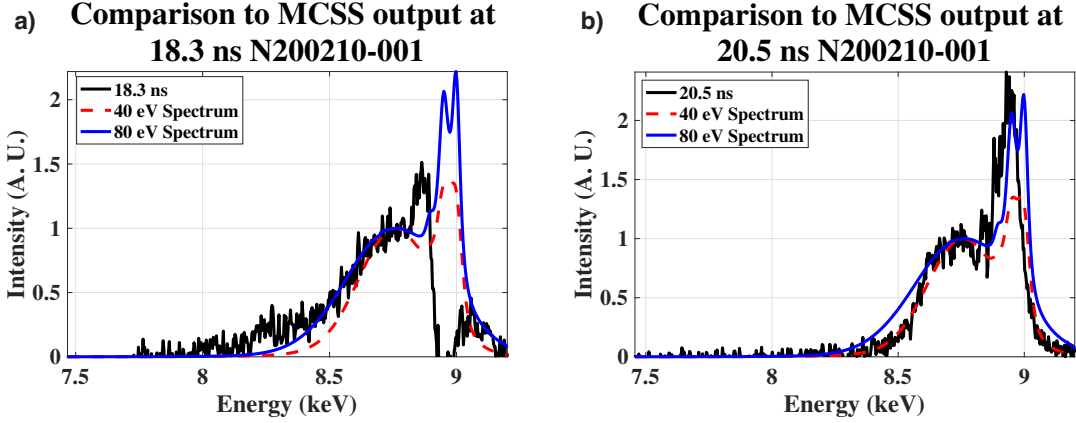


Figure 5.19: a) A comparison of the scattering data at 18.3 ns with MCSS calculations indicating a volume-averaged, electron temperature of around 80 eV. b) The same as in a), but for the scattering data at 20.5 ns, which indicates a volume-averaged, electron temperature of around 40 eV. This is in reasonable agreement with the 49 eV final state temperature from the analysis of the self-emission data in the July shot.

temperature later in time. This makes sense because Figure 5.14 c showed that the shock itself is cooling and the scattering volume is now large enough to capture the entrained flow from the plastic foil, which is dense and cold, in the integration volume.

The final step in understanding this data is to compare with calculated scattering spectra. Here, these calculations will use the multi-component scattering simulation (MCSS) software that Dave Chapman developed at the Atomic Weapons Establishment in the United Kingdom. Using the random phase approximation and Debye-Hückel models for the plasma physics along with a model of the instrument function for the MACS (provided by Tilo Döppner) are all reasonable assumptions due to the weakly coupled, non-degenerate nature of the plasma in this experiment. The plasma parameters used in the input deck are: $Z_C = 4.3$, $Z_H = 1$, $\rho = 0.1265 \text{ g cm}^{-3}$, and $n_e = 3 \times 10^{22} \text{ cm}^{-3}$. The results for the measurement at 18.3 ns in Figure 5.19 a suggest an average electron temperature of about 80 eV. The measurement at 20.5 ns in Figure 5.19 b suggests an averaged electron temperature of about 40 eV. This compares reasonably well with the measurement from the self-emission data on the previous shot day, which is an additional confirmation that these results make sense.

A relevant consideration is the fact that the scattering volume occurs closer to the hohlraum than the self-emission measurement and the shock will be colder in the self-emission measurement. It is relevant to note that this analysis focuses on fitting the inelastic scattering peak and is not as concerned with the elastic scattering peak due to the background subtraction. The background subtraction is necessary to eliminate a distorting signal, but it does tend to affect the elastic scattering peak, which unfortunately means this data is not able to provide any information about the ionization of the shocked foam. However, the consistent temperature measurements between the two independent diagnostics is a powerful result.

5.8 Conclusions

This chapter presents the design process of a target for radiative shock experiments at the NIF and the analysis of the results from two experiment days at the facility. The primary measurements were x-ray Thomson scattering and time-resolved optical self-emission. It describes the changes made to the XRTS shielding between the first and second shot day to improve the performance of the diagnostic and the successful outcome of the modifications. The self-emission measurements provided the shock velocity and the electron temperature when combined with an analytic model of thick-thin radiative shocks. With the electron temperature as a function of time, it was possible to calculate the time derivative of the final state shock electron temperature, which is a novel result. The XRTS data collected on the second shot day demonstrates the volume-integrated electron temperatures are comparable to the self-emission measurements.

CHAPTER VI

Conclusions

6.1 Summary

The goal of this work was to present the underlying physics of photoionization fronts and radiative shocks, show the experimental capabilities of studying these objects in the lab, and demonstrate the work of the author to produce interesting results in the laboratory. The large, HEDP facilities make it possible to achieve these feats experimentally, which is of great use to academia and the astrophysics communities. This work was successful in producing results that are useful in gaining deeper understanding of the physics occurring in radiation hydrodynamics systems and developing experimental approaches to measure complex HEDP plasma systems in the laboratory.

This work introduced an experimental platform for producing and measuring PI fronts on the Omega laser facility, which made a good step towards producing data on the physics of PI fronts. It also developed the geometry and probe source for the absorption spectroscopy of a gas cell, which could have additional applications. At the same time, a PI front experiment for the Z-Machine should be possible with the design presented here, which will allow for independent tests of the physics results and can identify any systematic errors in the measurements.

6.2 Conclusions

The theory presented here allowed for identifying measurable features in these experiments and for improved analysis of the data through the application of relatively simple analytic models. The curvature and velocity of PI fronts should allow for one to distinguish between PI fronts and non-linear diffusion driven heat waves. The model of a thick-thin shock extended the analysis of the radiative shocks produced on the NIF and compensated for the facility's lack of an absolute calibration of the SOP detector, which is incredibly powerful.

As mentioned previously, radiative shocks have been an active area of research for many years, and the experiments on NIF presented here add a useful contribution in the ability to combine two temperature measurements with a single target. Additionally, this experiment presented these measurements in a foam target, which is not typical of radiative shock experiments as most use gases.

6.3 Future Work

The work to create a PI front in the laboratory characterized a platform for making absorption spectroscopy measurements. The clear path for continuing this work is to further adjust the experiments so that they produce the desired spectroscopic data on the primary diagnostic. This also opens up the possibility of streaked absorption measurements, which would be able to capture the changing ionization state of the Ar dopant as the PI front propagates through the gas cell. All of this results in a solid foundation for a set of experiments that provide an understanding of PI front physics and a starting point for feeding these results into the outstanding questions in cosmology and astrophysics.

When running PI front experiments at the Omega-60 laser in the future, the most likely failure mode will be the measurement geometry with specific considerations to

the spectrometers available at the Omega-60 laser facility. A possible pitfall is the dopant percentage being too low for the desired measurement. Estimates of the measurement suggest this will not be the case, but there are many assumptions in those estimates. A target filled with only Ar would ensure that the line opacity is large enough for sufficiently strong signal. Due to the integrated nature of this experiment, it is also critical to consider the effects of the changes made to one component on the other components. For example, if there is a change made to the gas cell outer diameter, this could affect the beams available to drive the capsule backlighter without clipping the gas cell. For this reason, it will be important to continue the practice of using diagnostics to monitor the performance of each component of this experiment, so that the data analysis can account for any changes that may occur between experiments. Another consideration, is to possibly change the primary diagnostic to an imaging measurement to more easily exploit the front curvature and velocity results presented in this thesis.

The designed experiments to observe PI fronts at the Z-machine do a nice job of demonstrating that it is reasonable to produce an experiment that should reach the desired physics regime and the obvious next step is to acquire facility time to conduct an experiment. However, these simulations are not capable of including many of the additional physics that occur in real experiments that could have a significant affect on the measurements. For example, since the simulations are one-dimensional, there is no consideration of the heating of the gas cell walls and its contribution to the estimated spectroscopic measurement. There is an additional concern about the interaction of the emission from the pinch interacting with the fiber used to couple the emission from the gas cell to the spectrometer, which could cause loss of signal and is difficult to simulate. Due to their being a jitter of a few nanoseconds in the arrival time of the peak current on Z, it will be necessary to have at least two spectrometers to record a PI front velocity measurement.

There are only a small number of gases that researchers use for radiative shock experiments in the relevant literature, but it is possible to make foams out of a wide variety of materials and to dope low Z foams with higher Z elements. This allows for experiments that tune the upstream and downstream opacities while having temperature and velocity measurements, which would be a novel study. A shot that places the self-emission window in the same location as the XRTS measurement would provide a useful comparison of the temperature measurements from both diagnostics. However, in order to prevent noise from the probe beam, XRTS would not run on this shot.

To best conduct additional experiments with this platform, it would be useful to make a third iteration of the XRTS shielding that is still more aggressive than the second iteration. This would hopefully remove all of the background observed in the data and allow for a more detailed analysis of the XRTS spectra that could provide additional information about the shock conditions. Additionally, it will be necessary to ensure that the foam adequately fills the shock tube after the casting process. This may not be as much of a problem with silicon dioxide or carbon foams, but it is still worth considering to ensure a quality self-emission measurement. A final useful adjustment would be to include a piece of connecting material at the top of the self-emission slit in the shock tube. This would provide additional stability and consistency between targets and could help improve the ability of the foam to fill the tube volume.

APPENDICES

APPENDIX A

Dante Analysis Technique

A.1 Dante Analysis

The Dante analysis described above provides a brightness temperature measurement using the matrix unfold algorithm to extract a best fit of the spectral content [5, 6, 120]. This method assumes the spectral intensity is a linear combination of basis functions and then solves for the amplitudes, this analysis uses Gaussians for the basis functions. Since independent measurements can provide detector solid angle, emitter size, incidence angle, and response functions to the algorithm, the only unknown quantity is the input spectrum. Therefore, it is important to understand how changing the input spectrum alters the resulting brightness temperature calculation from the Dante data if one intends to use this as a means of describing a source. The literature details that the matrix unfold method does not accurately recreate a spectrum, but does produce a reasonable value for the flux [120, 121]. This will be especially true for capsule emission presented above due to the line emission in the spectrum, as one will see below.

To analyze the code output, a MATLAB script generated a synthetic temperature profile in time. These temperatures were then used to create Blackbody spectra at

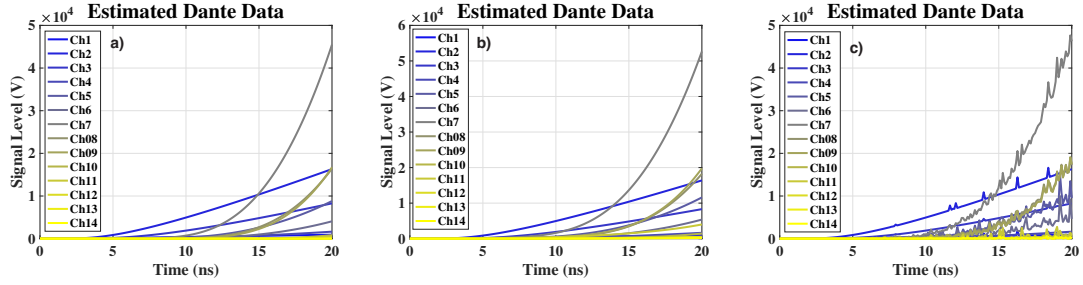


Figure A.1: a) The synthetic Dante data using Planckian input at each time step. b) The synthetic Dante data using a Planckian with a constant Gaussian component. The channels show larger values than with only a Planckian component input. c) The synthetic Dante data with a Planckian plus a random Gaussian component. The randomness of Gaussian component introduces fluctuations in time that appear as “noisy” signal on the channel output.

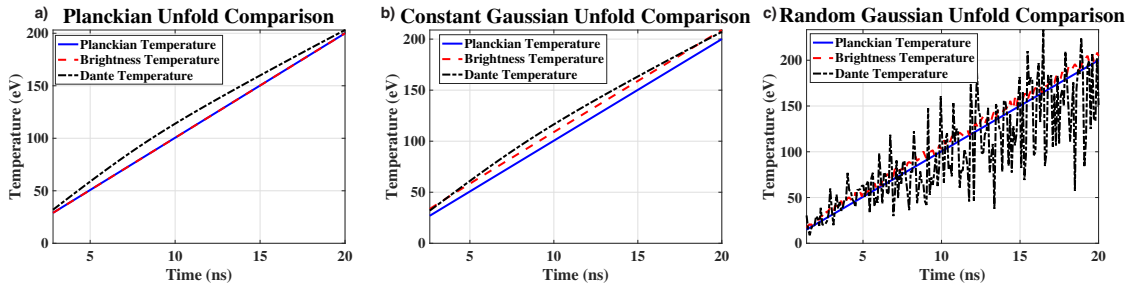


Figure A.2: a) The unfold output from Planckian input compared to the temperature profile values and the brightness temperature. The brightness and profile temperatures are the same for this case as the spectrum is Planckian b) The unfold output with a Planckian plus a constant Gaussian as input compared to the brightness temperature and the Planckian temperature. This shows that the brightness temperature is larger than the Planckian temperature, as one would expect, and the Dante unfold temperature is larger than the Brightness temperature. c) The unfold output with a Planckian plus a random Gaussian as input compared to the brightness temperature and the Planckian temperature. The signal is noisy due to the random nature of the Gaussian component, but the three temperatures follow the same trends as the other two cases.

each point in time and construct the Dante output by applying response functions from August 4th 2016 to these spectra. The response functions only contained data from channels 1 through 14 and 18, and this analysis didn’t use channel 18 because of some difficulties it caused in the analysis. The temperature profile is a line with a slope of 9.95×10^9 and intercept of 1 to create temperatures from 1 to 200 eV over 20 ns.

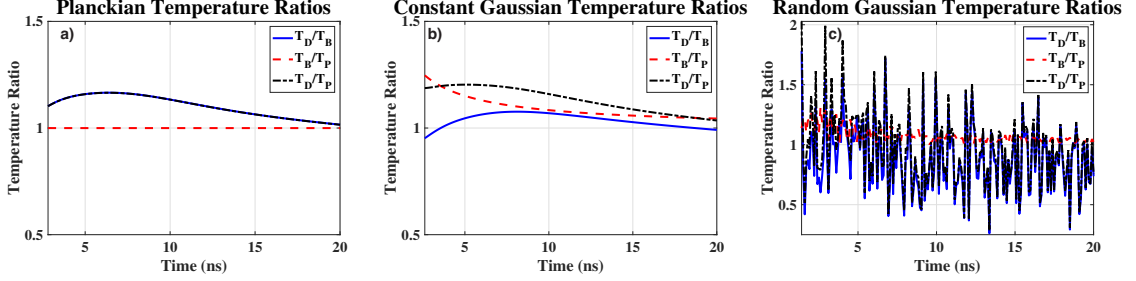


Figure A.3: a) A comparison between the ratios of the Planckian, brightness, and Dante temperatures with a Planckian input. This shows that the unfolded temperature is no more than 17% greater than the input Planckian temperature. b) A comparison between the ratios of the Planckian, brightness, and Dante unfolded temperatures with a Planckian plus a constant Gaussian as input. This shows under about 20% difference between the unfolded temperature and the Planckian temperature, then it shows a less than 10% difference between the unfolded temperature and the brightness temperature. c) The comparison of the temperature ratios for a Planckian plus a random Gaussian as input, which shows the same trends as the constant Gaussian case, but with significant noise due to the randomness of the Gaussian component. The scale of this figure is larger than figures a and b.

This analysis used three models to test how this unfold algorithm responds to different spectral input: Pure Planckians using the linear temperature profile, the Planckians plus a constant Gaussian component, and the Planckian plus a random Gaussian component. The Gaussian components all had heights of one-tenth the maximum Planckian value at each time step. The constant Gaussian had a width of 700 eV and center value of 2200 eV, while the random Gaussian had widths from 1-1000 eV and center values from 0.1-20000 eV at each time step. The resulting synthetic Figs. A.1a, b, and c show the synthetic Dante output for each of these models using the linear temperature profile mentioned above.


To make comparisons between these different models, the analysis uses the Planckian, brightness, and Dante unfold temperatures. Here, the definition of the brightness temperature is $T_B = \left(\frac{\pi F}{\sigma_{SB}} \right)^{\frac{1}{4}}$, where πF is the radiation flux in W cm^{-2} , and σ_{SB} is the Stefan-Boltzmann constant in units of $\text{W cm}^{-2} \text{eV}^{-4}$. Figs. A.2a, b, and c show these temperatures for the three different spectral models for times from the time when the Dante unfold reaches 30 eV to 20 ns. This shows that for pure Planckian

inputs the matrix unfold algorithm is able to replicate the brightness and thermal temperature of the source to within 30%, as seen in Fig. A.3a. For the two models with Gaussian components, the brightness temperature is greater than the Planckian temperature, as expected, and Figs. A.3b and c show that the brightness temperature converges with the Dante temperature at lower input flux values. The brightness temperature in the constant Gaussian model is within 10% of the brightness temperature at all calculated values of the unfold. The random Gaussian model seems to follow this same trend, but the noise in that calculation makes it difficult to draw further conclusions. It seems that spectrally narrow structures lead to very strong deviations from the input spectral parameters in the calculated temperature. This suggests that narrow line structures in the spectrum can significantly skew the results of a Dante measurement when using the matrix unfold method with Gaussian basis functions. In general, this matrix unfold method calculates larger temperatures than what generates the input flux, which is the same result as in the Seifert work [120].

APPENDIX B

September 11th 2018 Omega Shot Day SRFs

B.1 Integrated Physics Target - RID 68435



**OMEGA Shot
Request Form**

Facility Status
Campaign/Problems
XOPS Beamlines
Help

Go To RID# This RID# 68435
 Last Modified: 08-Dec-2020 16:37:45
 General > Drivers > Target > Beams > TIM > Fixed > Neutronics

Driver (Help)

Driver	<p>UV Fiducial: <input checked="" type="radio"/> OFF <input type="radio"/> ON</p> <p><i>Note: IR/Green Fiducials are supplied on all shots.</i></p>
<input type="radio"/> OFF <input checked="" type="radio"/> SSD <input type="radio"/> PHX <input type="radio"/> MPD	<p>SSD Driver: Primary driver for OMEGA. May be shot with or without bandwidth.</p> <p>*Pulse Shape -or- Pulse Shape request # <input type="text" value="SG10v001"/> <input type="text" value="v"/> Pulse Delay <input type="text" value="0"/> <input type="text" value="hs"/> <input type="checkbox"/> SSD Sync Modulation: <input type="text" value="ON"/> <input type="text" value="v"/> <input type="text" value="X"/> = <input type="text" value="Max"/> <input type="text" value="Y"/> = <input type="text" value="Max"/></p>
<input checked="" type="radio"/> OFF <input type="radio"/> LEG1 <input type="radio"/> LEG2 <input type="radio"/> LEG3	<p>Backlighter Driver: May feed any one leg of OMEGA System.</p> <p>*Pulse Shape -or- Pulse Shape request # <input type="text" value="v"/> <input type="text" value="v"/> Pulse Delay <input type="text" value=""/> <input type="text" value="hs"/></p>
	<p>Special Instructions:</p> <div style="border: 1px solid gray; height: 40px;"></div>

* Queryable fields: [Wild cards: (_) matches any one character, (%) matches 0 or more characters]

Campaign Editor

Drivers Editor

Beam Editor

Target Editor

SRE Auditor

Update

Copy ...

Reports

Station Reports

Clear

Query

Beam Groups Summary.

30 beam(s) are configured.

Edit Ref:	Beams	Group Name	Energy	Pointing	Focusing	Beam Delay	DPP	DPR	3w Half-Waveplate	Polarization Rotation	Termination	Report Group
1	13-15,22,24-26,28,42,45,46,51,53,55-58,65,66	Capsule Backlighter	450 J/Beam (UV)	10004 / 37.41 / 164.52	800 um (spot size)	1	none	No			Target	F
2	34,43	Au_foil4	450 J/Beam (UV)	1538 / 95.74 / 244.46	0.00 mm (lens position)	3	SG5	No			Target	D
3	36,38	Au_foil3	450 J/Beam (UV)	1538 / 95.74 / 244.46	0.00 mm (lens position)	2	SG5	No			Target	C
4	41,60	Au_foil1	450 J/Beam (UV)	1538 / 95.73 / 244.46	0.00 mm (lens position)	0.00	SG5	No			Target	A
5	48,63	Au_foil5	450 J/Beam (UV)	1538 / 95.74 / 244.46	0.00 mm (lens position)	4	SG5	No			Target	E
6	49,52	Au_foil2	450 J/Beam (UV)	1538 / 95.74 / 244.46	0.00 mm (lens position)	1	SG5	No			Target	B
7	64	Capsule Backlighter	450 J/Beam (UV)	10004 / 37.41 / 164.52	400 um (spot size)	1	none	No			Target	F



Target Information (Help)

<p>Target ID: G 0004 Name or Enter Select from List</p> <p>Type/Description: Gas Cell Outside Diameter: 22000 um Shape: <input type="checkbox"/> Cylindrical <input checked="" type="checkbox"/> Spherical Positioner: TIM-Based Alignment Only: <input type="checkbox"/> (Check = Yes) Record Target Pressure?: <input type="checkbox"/> No <input type="checkbox"/> Tall Cell <input checked="" type="checkbox"/> Transducer Contains Materials Z > 36: <input checked="" type="checkbox"/> Yes <input type="checkbox"/> No This includes hohlraums, foils, shields, pinholes, grids, etc. If "Yes" describe the Z > 36 target components here: Hazardous Materials: (64 max chars) Special Instructions: (64 max chars) Soft Rough Pumping: Target Alignment Procedure: Operations use. PI need not complete. Cryo Pump Off? Target Detection</p>	<p>Target 1 Description G 0004 Name or Enter Select from List Gas Cell 22000 um Cylindrical <input type="checkbox"/> Spherical <input checked="" type="checkbox"/> TIM-Based <input type="checkbox"/> (Check = Yes) No <input type="checkbox"/> Tall Cell <input checked="" type="checkbox"/> Transducer Yes <input checked="" type="radio"/> No <input type="radio"/></p> <p>Target 2 Description NLUJF-1Q19-05-02 Ch[8-4] Spherical <input type="checkbox"/> TIM-Port H2 <input type="checkbox"/> (Check = Yes) No <input type="checkbox"/> Tall Cell <input type="checkbox"/> Transducer Yes <input type="radio"/> No <input checked="" type="radio"/></p> <p>Target 3 Description um Gas TIM <input type="checkbox"/> (Check = Yes) No <input type="checkbox"/> Tall Cell <input type="checkbox"/> Transducer Yes <input type="radio"/> No <input type="radio"/></p> <p>Target 4 Description um Gas TIM <input type="checkbox"/> (Check = Yes) No <input type="checkbox"/> Tall Cell <input type="checkbox"/> Transducer Yes <input type="radio"/> No <input type="radio"/></p>
--	---



TIM Configuration (Help) XRFCSwap DiagnosticSwap

Setup pages are not needed for Empty TSSAC

Diagnostic description	Other diagnostic	Priority	Port	Opposing port
TIM 1 Rowland(Yaakobi) XR Spectrometer 1 (XRS)	<input type="text"/>	Primary	P3	P10
TIM 2 XR Framing Camera 1 (XRFC)	<input type="text"/>	Primary	H3	H18
TIM 3 Rowland(Yaakobi) XR Spectrometer 2 (XRS)	<input type="text"/>	Primary	H18	H3
TIM 4 TIM Target Positioner 4 (TTP)	<input type="text"/>	Primary	P6	P7
TIM 5 XR Framing Camera 3 (XRFC)	<input type="text"/>	Primary	H14	H7
TIM 6 XR Framing Camera 5 (XRFC)	<input type="text"/>	Secondary	P7	P6

Campaign Editor Drivers Editor Beam Editor Target Editor SRF Auditor

Update Copy ... Reports Station Reports



Go To RID# This RID#: 68435
Last Modified: 01-Mar-2021 00:06:52
General > Drivers > Beams > TIM > Fixed > Neutronics

Facility Status
Comments/Problems
XRDs Beaminics
Help

Rowland(Yaakobi) XR Spectrometer 1 (XRS) / TIM 1 EEA Operating Procedures Users Guide

Internal Settings

Crystal Type	ADP
Description	
Crystal Surface	flat
Crystal Length	12 cm
Crystal Width	1 cm
Crystal Position	2
Crystal Tilt	+
Blast Shield Thickness (Be)	10 mils
Filter Material	None
Filter Thickness	mils
Slit Width	3000 μ m
Pinhole Diameter	μ m
LOS Shield	None (Standard)

External Settings

Shift to Target		"
Energy Range	2720 to 3500	ev
Detector Type	BAS MS	
Scan Time		Min.
Sensitivity		μ m
Pixel Size		μ m
Film-cassettes Be thickness	1 mil	

Steering

Make selections in one row only

<input type="radio"/> Target Chamber Center
<input type="radio"/> Same as P ₀ Probe Beam
<input checked="" type="radio"/> Radius 10000 μ m Theta 37.41 Phi 164.52
<input type="radio"/> Distance μ m toward Port

Comments/Requirements

10 μ m Saran/EPVC (C1) filter covering half of the entrance slit. Rotate crystal 4 degrees to the TIM axis.



Go To RID# This RID#: 68435
Last Modified: 01-Mar-2021 00:07:20

Facility Status
Comments/Problems
XOPS
Beamlines
Help

General > Drivers > Beams > TIM > Fixed > Neutronics

XR Framing Camera 1 (XRFC) / TIM 2 ERF [Operating Procedures](#)

Optics

		Make selections in one column only	
Nosecone Type	<input type="radio"/> LLE	<input checked="" type="radio"/> LLNL	<input type="radio"/> LANL
Magnification	4X-16	15um	
Pinhole Size			
Blast Shield			
Frame Type	Straight		
Stand-off Distance	cm	38.1	cm
Roll Angle	Degrees		Degrees
Pinhole Substrate			
Rear Filter	1 mil Be		
SXR Rear Filter			

Interstrip Timing

MCP	4-strip	F1
MCP Module		Requested delay (0-6.55 ns by .05)
Strip#		
1	0	
2		
3	4	
4	6	

Internal Settings

Strip	Bias (Volts)
1	200
2	200
3	200
4	200
PFM Type	50

Misc

Acquisition start time (relative to T=0)	1	ns
Detector	SVCDD3	
CCD Image Size	2048	H x 2048
Monitor Atten.	21	dB
Trigger Atten.	10	dB

Steering

Make selections in one row only			
<input type="radio"/> Target Chamber Center			
<input type="radio"/> Same as P9 Probe Beam			
<input checked="" type="radio"/> Radius	10000	um	Phi 164.52
<input type="radio"/> Distance		um	toward Port

Comments/Requirements



Rowland(Yaakobi) XR Spectrometer 2 (XRS) / TIM 3 EAF Operating Procedures Users Guide

Internal Settings		External Settings	
Crystal Type	ADP	Shift to Target	"
Description		Energy Range	2720 to 3500 eV
Crystal Surface	flat	Detector Type	BAS MS
Crystal Length	12 cm	Scan Time	Min.
Crystal Width	1 cm	Sensitivity	
Crystal Position	2	Pixel Size	μ m
Crystal Tilt	+	Film-cassette Be thickness	1 mil
Blast Shield Thickness (Be)	10 mils		
Filter Material	None		
Filter Thickness	mils		
Slit Width	8000 μ m		
Pinhole Diameter	μ m		
LOS Shield	None (Standard)		

Steering
Make selections in one row only

<input checked="" type="radio"/> Target Chamber Center
<input type="radio"/> Same as P9 Probe Beam
<input type="radio"/> Radius <input type="text"/> μ m
<input type="radio"/> Distance <input type="text"/> μ m toward Port
<input type="radio"/> Theta <input type="text"/> Phi

Comments/Requirements
10 micron Sazan/PVDC (Cl) filter over half of the slit width. Rotate crystal 4 degrees to the Tilt axis.



TIM Target Positioner 4 (TTP) / TIM 4 ERF Operating Procedures Users Guide
PI Section

Target Type: Gas Filled

Target Reference Location

Make selections in one row only

<input type="radio"/>	Target Chamber Center
<input type="radio"/>	Same as P9 Probe Beam
<input checked="" type="radio"/>	Radius: 1538 <input type="text"/> um Theta: 95.74 <input type="text"/> Phi: 244.46 <input type="text"/>
<input type="radio"/>	Distance: <input type="text"/> um toward Port <input type="text"/>

Comments/Requirements

This is the location of the beams on the Au foil. The stalk is located 8.149 mm from this point opposite the foil normal.

XR Framing Camera 3 (XRFC) / TIM 5 [ECAF](#) [Operating Procedures](#)

Optics

		Make selections in one column only	
Nosecone Type	<input type="radio"/> LLE	<input checked="" type="radio"/> LLNL	<input type="radio"/> LANL
Magnification		SXR-3X	
Pinhole Size		15um	
Blast Shield			
Frame Type		Straight	
Stand-off Distance		55.6	cm
Roll Angle			Degrees
Pinhole Substrate			
Rear Filter			
		SXR Rear Filter	
		see comments	

Interstrip Timing

MCP	4-strip	
MCP Module	S4	
Strip#	Requested delay (0-6.35 ns by .05)	
1	0	
2	1	
3	2	
4	3	

Internal Settings

Strip	Bias (Volts)
1	200
2	200
3	200
4	200
PFM Type	200

Misc

Acquisition start time (relative to T-0)	1	ns
Detector	SYCCD2	
CCD Image Size	2048	H x 2048
Monitor Atten.	40	dB
Trigger Atten.	10	dB

Steering

Make selections in one row only			
<input type="radio"/>	Target Chamber Center		
<input type="radio"/>	Same as P9 Probe Beam		
<input checked="" type="radio"/>	Radius	1538	um
<input type="radio"/>	Distance		um toward Port
		Theta	95.74
		Phi	244.46

Comments/Requirements

Input Channel: 25um PH 3 degree Al
 mirror: 5um Polyene-N filter, Center
 Channel: 10um PH 0.001" Be filter
 Output Channel: 25um PH 3degree Al
 mirror: 1um V filter

Optics

Nosecone Type	<input type="radio"/> LLE	Make selections in one column only	
Magnification	<input type="text" value=""/>	<input checked="" type="radio"/> LLNL	<input type="radio"/> LANL
Pinhole Size	<input type="text" value=""/>	SXR 3X	<input type="text" value=""/>
Blast Shield	<input type="text" value=""/>	15um	<input type="text" value=""/>
Frame Type	<input type="text" value=""/>	Straight	<input type="text" value=""/>
Stand-off Distance	<input type="text" value=""/> cm	55.6	<input type="text" value=""/> cm
Roll Angle	<input type="text" value=""/> Degrees		<input type="text" value=""/> Degrees
Pinhole Substrate	<input type="text" value=""/>		<input type="text" value=""/>
Rear Filter	<input type="text" value=""/>	SXR Rear Filter	
		see comments	

Interstrip Timing

MCP	4-strip
MCP Module	S2
Strip#	Requested delay (0-12.7 ns by .10)
1	0
2	.3
3	.6
4	.9

Internal Settings

Strip	Bias (Volts)
1	0
2	0
3	0
4	0
PFM Type	200

Misc

Acquisition start time (relative to P0)	1	ns
Detector	SVCCD4	
CCD Image Size	2048	H x 2048 W
Monitor Atten.	41	dB
Trigger Atten.	10	dB

Steering

Make selections in one row only

<input type="radio"/> Target Chamber Center		
<input type="radio"/> Same as P9 Probe Beam		
<input checked="" type="radio"/> Radius	267	um
<input type="radio"/> Distance		um toward Port
		Phi 244.46

Comments/Requirements

Input Channel: 25um PH 3 degree A1
 mirror 5um Parylene-N filter Center
 Channel: 10um PH 0.001" Be filter
 Output Channel: 25um PH 3degree A1
 mirror 5um V filter

Dante I (DANTE) / FIXED H161 [EAF](#) [Operating Procedures](#)

Dante configuration must be approved by the Instrument Specialist a minimum of four weeks in advance of the campaign.

Source Info

Source Type	Disk	
Source Size	1500	um
Source Axis/Position	Radius (mm)	Theta Phi
Expected Brightness Temperature	100	eV
Signal Start Time	0	ns
Other Sources Present (Explain in Comments)	Yes >	

Channels Requested (Select up to 10)

<input checked="" type="checkbox"/> Channel 1 (50-70 eV)	<input type="checkbox"/> Channel 10 (1600-1800 eV)
<input checked="" type="checkbox"/> Channel 2 (150-180 eV)	<input checked="" type="checkbox"/> Channel 11 (2000-5000 eV)
<input checked="" type="checkbox"/> Channel 3 (250-280 eV)	<input type="checkbox"/> Channel 12 (1800-2500 eV)
<input checked="" type="checkbox"/> Channel 4 (450-520 eV)	<input type="checkbox"/> Channel 13 (2540-3300 eV)
<input checked="" type="checkbox"/> Channel 5 (750-820 eV)	<input type="checkbox"/> Channel 14 (3170-4800 eV)
<input checked="" type="checkbox"/> Channel 6 (900-980 eV)	<input type="checkbox"/> Channel 15 (4300-6300 eV)
<input checked="" type="checkbox"/> Channel 7 (980-1050 eV)	<input type="checkbox"/> Channel 16 (5300-7000 eV)
<input checked="" type="checkbox"/> Channel 8 (1200-1300 eV)	<input type="checkbox"/> Channel 17 (7300-9500 eV)
<input checked="" type="checkbox"/> Channel 9 (1300-1500 eV)	<input type="checkbox"/> Channel 18 (10000-20000 eV)

Comments/Requirements

A capsule backlighter will be driven in addition to the Au foil at a pulse rate of 1000 pulses per second. The backlighter will be 10 mm from the target towards the target.



OMEGA Shot Request Form

Go To RID# This RID#: 68435
Last Modified: 01-Mar-2021 00:13:17

[Facility Status](#)
[Comments/Problems](#)
[XOPS](#)
[Beamlines](#)
[Help](#)

[General](#) > [Drivers](#) > [Target](#) > [Beams](#) > [TIM](#) > [Fixed](#) > [Neutronics](#)

Hard XR Detector 1-4 (HXRD) / FIXED H10 [EAF](#) [Operating Procedures](#)

Filtering

Channel	Filter
HXRD1	3 mm Al
HXRD2	20 mm Al
HXRD3	20 mm Al + 3.25 mm Cu
HXRD4	20 mm Al + 6.3 mm Cu


Special Instructions

[Campaign Editor](#) [Drivers Editor](#) [Beam Editor](#) [Target Editor](#) [SRE Auditor](#)

Visible Camera 2 (CAMERA)	Ride Along ▾	P2A	58.3	54	
Visible Camera 3 (CAMERA)	Ride Along ▾	H8D	72.56	156.13	
XR Pinhole Camera H12 (XRPHC)	Ride Along ▾	H12C	108.89	54	Set up
XR Pinhole Camera H13 (XRPHC)	Ride Along ▾	H13C	92.74	342	Set up
XR Pinhole Camera H4 (XRPHC)	Ride Along ▾	H4A	29.52	234	Set up
XR Pinhole Camera H8 (XRPHC)	Ride Along ▾	H8C	79.3	153.78	Set up
XR Pinhole Camera P2 (XRPHC)	Ride Along ▾	P2C	67.68	54	Set up

[Campaign Editor](#)
 [Drivers Editor](#)
 [Beam Editor](#)
 [Target Editor](#)
 [SRF Auditor](#)

B.2 Au Foil Characterization Target - RID 68712



**OMEGA Shot
Request Form**

Facility Status
Comments/Problems
XOPS Beamlines
Help

Go To RID# This RID#: 68712 Shot Number: 91026
 Last Modified: 11-Sep-2018 16:54:18

General > Drivers > Target > Beams > TIM > Fixed > Neutronics

Driver (Help)

Shot Number: 91026

Driver	<p>UV Fiducial: <input checked="" type="radio"/> OFF <input type="radio"/> ON</p> <p><i>Note: IR/Green Fiducials are supplied on all shots.</i></p> <p>SSD Driver: Primary driver for OMEGA. May be shot with or without bandwidth.</p> <p>*Pulse Shape -or- Pulse Shape request # <input type="text" value="SG10v001"/> <input type="text" value="v"/></p> <p>Pulse Delay <input type="text" value="0"/> ns <input type="checkbox"/> SSD Sync</p> <p>Modulation: <input type="text" value="ON"/> <input type="text" value="X"/> = Max <input type="text" value="Y"/> = Max</p> <p>Backlighter Driver: May feed any one leg of OMEGA System.</p> <p>*Pulse Shape -or- Pulse Shape request # <input type="text" value="v"/> <input type="text" value="v"/></p> <p>Pulse Delay <input type="text" value=""/> ns</p>
	<p>Special Instructions: <input style="width: 100%;" type="text"/></p>

* Queryable fields: Wild cards: (_) matches any one character, (%) matches 0 or more characters

Campaign Editor Drivers Editor Beam Editor Target Editor SRE Auditor

Copy ... Reports Station Reports Clear Query

Shot Number: 91026

Beam Groups Summary

10 beam(s) are configured.

Edit Ref:	Beams	Group Name	Energy	Pointing	Focusing	Beam Delay	DPP	DPR	^{3w} Half-Waveplate	Polarization Rotation	Termination	Report Group
1	34.43	Au_foil4	450 J/Beam (UV)	1538 / 95.74 / 244.46	0.00 mm (lens position)	3	SG5	No			Target	D
2	36.38	Au_foil3	450 J/Beam (UV)	1538 / 95.74 / 244.46	0.00 mm (lens position)	2	SG5	No			Target	C
3	41.60	Au_foil1	450 J/Beam (UV)	1538 / 95.73 / 244.46	0.00 mm (lens position)	0.00	SG5	No			Target	A
4	48.63	Au_foil5	450 J/Beam (UV)	1538 / 95.74 / 244.46	0.00 mm (lens position)	4	SG5	No			Target	E
5	49.52	Au_foil2	450 J/Beam (UV)	1538 / 95.74 / 244.46	0.00 mm (lens position)	1	SG5	No			Target	B

Target Information (Help)

<p>Target 1 Description</p> <p>F-0001 Enter</p> <p>Name or []</p> <p>Select from List</p> <p>Type/Description: Au foil and cone</p> <p>Outside Diameter: 22000 [] um Get TIS Info</p> <p>Shape: Cylindrical [] Gas []</p> <p>Positioner: Tritium TIM [4]</p> <p>Alignment Only [] (Check = Yes)</p> <p>Record Target Pressure? [] (Check = Yes)</p> <p>Contains [] No [] Tall Cell [] Transducer [] Yes [] No</p> <p>Materials Z > 36</p> <p>This includes nobiraums, foils, shields, pinholes, grids, etc. If "Yes" describe the Z > 36 target components here:</p> <p>Hazardous Materials: (64 max chars)</p> <p>Special Instructions: (64 max chars)</p> <p>Soft Rough Pumping: [] Sec. [] (Check = Yes) [] Sec.</p> <p>Target Alignment Procedure: Operations use: P1 need not complete.</p> <p>Cryo Pump Off? [] Standard [] X Axis [] Y Axis [] Both Axes [] Disabled</p> <p>Target Detection [] Cryo Setups for Target 1 [] After "Update", Select this to modify the Shroud Pull and Sub-cooling.</p>	<p>Target 2 Description</p> <p>[] Enter</p> <p>Name or []</p> <p>Select from List</p> <p>Type/Description: []</p> <p>Outside Diameter: [] um</p> <p>Shape: [] Gas []</p> <p>Positioner: [] TIM []</p> <p>Alignment Only [] (Check = Yes)</p> <p>Record Target Pressure? [] (Check = Yes)</p> <p>Contains [] No [] Tall Cell [] Transducer [] Yes [] No</p> <p>Materials Z > 36</p> <p>This includes nobiraums, foils, shields, pinholes, grids, etc. If "Yes" describe the Z > 36 target components here:</p> <p>Hazardous Materials: (64 max chars)</p> <p>Special Instructions: (64 max chars)</p> <p>Soft Rough Pumping: [] Sec. [] (Check = Yes) [] Sec.</p> <p>Target Alignment Procedure: Operations use: P1 need not complete.</p> <p>Cryo Pump Off? [] Standard [] X Axis [] Y Axis [] Both Axes [] Disabled</p> <p>Target Detection [] Cryo Setups for Target 1 [] After "Update", Select this to modify the Shroud Pull and Sub-cooling.</p>	<p>Target 3 Description</p> <p>[] Enter</p> <p>Name or []</p> <p>Select from List</p> <p>Type/Description: []</p> <p>Outside Diameter: [] um</p> <p>Shape: [] Gas []</p> <p>Positioner: [] TIM []</p> <p>Alignment Only [] (Check = Yes)</p> <p>Record Target Pressure? [] (Check = Yes)</p> <p>Contains [] No [] Tall Cell [] Transducer [] Yes [] No</p> <p>Materials Z > 36</p> <p>This includes nobiraums, foils, shields, pinholes, grids, etc. If "Yes" describe the Z > 36 target components here:</p> <p>Hazardous Materials: (64 max chars)</p> <p>Special Instructions: (64 max chars)</p> <p>Soft Rough Pumping: [] Sec. [] (Check = Yes) [] Sec.</p> <p>Target Alignment Procedure: Operations use: P1 need not complete.</p> <p>Cryo Pump Off? [] Standard [] X Axis [] Y Axis [] Both Axes [] Disabled</p> <p>Target Detection [] Cryo Setups for Target 1 [] After "Update", Select this to modify the Shroud Pull and Sub-cooling.</p>	<p>Target 4 Description</p> <p>[] Enter</p> <p>Name or []</p> <p>Select from List</p> <p>Type/Description: []</p> <p>Outside Diameter: [] um</p> <p>Shape: [] Gas []</p> <p>Positioner: [] TIM []</p> <p>Alignment Only [] (Check = Yes)</p> <p>Record Target Pressure? [] (Check = Yes)</p> <p>Contains [] No [] Tall Cell [] Transducer [] Yes [] No</p> <p>Materials Z > 36</p> <p>This includes nobiraums, foils, shields, pinholes, grids, etc. If "Yes" describe the Z > 36 target components here:</p> <p>Hazardous Materials: (64 max chars)</p> <p>Special Instructions: (64 max chars)</p> <p>Soft Rough Pumping: [] Sec. [] (Check = Yes) [] Sec.</p> <p>Target Alignment Procedure: Operations use: P1 need not complete.</p> <p>Cryo Pump Off? [] Standard [] X Axis [] Y Axis [] Both Axes [] Disabled</p> <p>Target Detection [] Cryo Setups for Target 1 [] After "Update", Select this to modify the Shroud Pull and Sub-cooling.</p>
---	--	--	--



TIM Configuration (Help) [XRFC.Swap](#) [Diagnostic.Swap](#)

Setup pages are not needed for Empty, TSSAC

Diagnostic description	Other diagnostic	Priority	Port	Opposing port
TIM 1 <input type="text"/>	<input type="text"/>	<input type="text"/>	P3	P10
TIM 2 <input type="text"/> XR Framing Camera 1 (XRFC)	<input type="text"/>	Primary	H3	H18
TIM 3 <input type="text"/>	<input type="text"/>	<input type="text"/>	H18	H3
TIM 4 <input type="text"/> TIM Target Positioner 4 (TTP)	<input type="text"/>	Primary	P6	P7
TIM 5 <input type="text"/> XR Framing Camera 3 (XRFC)	<input type="text"/>	Primary	H14	H7
TIM 6 <input type="text"/> XR Framing Camera 5 (XRFC)	<input type="text"/>	Secondary	P7	P6

Shot Number: 91026

OMEGA Shot
Request Form



Go To RID# This RID#: 68712 Shot Number: 91026
Last Modified: 11-Sep-2018 16:54:18

[Facility Status](#)
[Comments/Problems](#)
[XOPS](#) [Beamlines](#)
[Help](#)

[General](#) > [Drivers](#) > [Target](#) > [Beams](#) > [TIM](#) > [Eksel](#) > [Neutronics](#)

XR Framing Camera 1 (XRFC) / TIM 2 EAF [Operating Procedures](#)

Optics

Make selections in one column only	
Nosecone Type	<input type="radio"/> LLE <input checked="" type="radio"/> LLNL <input type="radio"/> LANL
Magnification	4X-16 <input type="text"/>
Pinhole Size	15um <input type="text"/>
Blast Shield	<input type="text"/>
Frame Type	Straight <input type="text"/>
Stand-off Distance	<input type="text"/> cm
Roll Angle	<input type="text"/> Degrees
Pinhole Substrate	<input type="text"/>
Rear Filter	1 mil Be <input type="text"/>
SXR Rear Filter	

Interstrip Timing

MCP	4-strip
MCP Module	F1 <input type="text"/>
Strip#	Requested delay (0-6.55 ns by .05)
1	0 <input type="text"/>
2	.5 <input type="text"/>
3	1 <input type="text"/>
4	2 <input type="text"/>

Internal Settings

Strip	Bias (Volts)
1	200 <input type="text"/>
2	200 <input type="text"/>
3	200 <input type="text"/>
4	200 <input type="text"/>
PFM Type	50 <input type="text"/> ps

Misc

Acquisition start time (relative to T=0)	7 <input type="text"/> ns
Detector	SVCDD3
CCD Image Size	2048 <input type="text"/> H x 2048 <input type="text"/> W
Monitor Atten.	21 <input type="text"/> dB
Trigger Atten.	10 <input type="text"/> dB

Steering

Make selections in one row only	
<input type="radio"/> Target Chamber Center	
<input type="radio"/> Same as P9 Probe Beam	
<input checked="" type="radio"/> Radius	10000 <input type="text"/> um
<input type="radio"/> Distance	<input type="text"/> um toward Port <input type="text"/>
<input type="radio"/> Phi	164.52 <input type="text"/>

Comments/Requirements



TIM Target Positioner 4 (TTP) / TIM 4 EEAF [Operating Procedures](#) [Users Guide](#)

PI Section

Target Type: Ambient

Target Reference Location

Make selections in one row only

<input checked="" type="radio"/> Target Chamber Center
<input type="radio"/> Same as P9 Probe Beam
<input type="radio"/> Radius <input type="text"/> um <input type="text"/> Theta <input type="text"/> Phi
<input type="radio"/> Distance <input type="text"/> um toward Port <input type="text"/>

Comments/Requirements

Shot Number: 91026

Optics

Nosecone Type	<input type="radio"/> LLE	Make selections in one column only		<input type="radio"/> LANL
Magnification	<input type="radio"/> LLNL	SXR 3X		
Pinhole Size	15um			
Bias Shield	Straight			
Frame Type	55.6	cm		
Stand-off Distance				
Roll Angle			Degrees	
Pinhole Substrate				
Rear Filter				
SXR Rear Filter see comments				

Interstrip Timing

MCP	4-strip
MCP Module	S4
Strip#	Requested delay (0-6.35 ns by .05)
1	0
2	1
3	2
4	3

Internal Settings

Strip	Bias (Volts)
1	200
2	200
3	200
4	200
PFM Type	200

Misc

Acquisition start time (relative to T-0)	1	µs	
Detector	SYCCD2		
CCD Image Size	2048	H x 2048	W
Monitor Atten.	40	dB	
Trigger Atten.	10	dB	

Steering

Make selections in one row only

<input type="radio"/> Target Chamber Center						
<input type="radio"/> Same as P9 Probe Beam						
<input checked="" type="radio"/> Radius	1538	um	Theta	95.74	Phi	244.46
<input type="radio"/> Distance		um	toward Port			

Comments/Requirements

Input Channel: 25um PH 3 degree AI
 Mirror: 25um PH 3 degree AI
 Output Channel: 25um PH 3 degree AI
 mirror lum V filter

XR Framing Camera 5 (XRFC) / TIM 6 EAF Operating Procedures

Optics

		Make selections in one column only	
Nosecone Type	<input type="radio"/> LLE	<input checked="" type="radio"/> LLNL	<input type="radio"/> LANL
Magnification		SXR 3X	
Pinhole Size		15um	
Bias Shield		Straight	
Frame Type		55.6	
Stand-off Distance		cm	cm
Roll Angle		Degrees	Degrees
Pinhole Substrate			
Rear Filter			
		SXR Rear Filter	
		see comments	

Interstrip Timing

MCP	4-strip
MCP Module	S2
Strip#	Requested delay (0-12.7 ns by .10)
1	0
2	1
3	2
4	3

Internal Settings

Strip	Bias (Volts)
1	0
2	0
3	0
4	0
PFM Type	1000

Misc

Acquisition start time (relative to T=0)	0	hs
Detector	SVCCD4	
CCD Image Size	2048	H x 2048 W
Monitor Atten.	41	dB
Trigger Atten.	10	dB

Steering

Make selections in one row only		
<input type="radio"/> Target Chamber Center		
<input type="radio"/> Same as P9 Probe Beam		
<input checked="" type="radio"/> Radius	267	um
<input type="radio"/> Distance		um toward Port
	Theta	95.74
	Phi	244.46

Comments/Requirements

Input Channel: 25um PH 3 degree Al
 mirror 5um Polyene-N filter Center
 Channel: 10um PH 0.001" Be filter
 Output Channel: 25um PH 3degree Al
 mirror 1um V filter

Dante I (DANTE) / FIXED H161 [EJAF](#) [Operating Procedures](#)

Dante configuration must be approved by the Instrument Specialist a minimum of four weeks in advance of the campaign.

Source Info

Source Type	Disk	
Source Size	1500	um
Source Axis/Position	Radius (mm)	Theta
	1.5	95.74
Expected Brightness Temperature	100	eV
	0	ns
Other Sources Present (Explain in Comments)	No	

Channels Requested (Select up to 10)

- Channel 1 (50-70 eV) Channel 10 (1600-1800 eV)
- Channel 2 (150-180 eV) Channel 11 (2000-5000 eV)
- Channel 3 (250-280 eV) Channel 12 (1800-2500 eV)
- Channel 4 (450-520 eV) Channel 13 (2540-3300 eV)
- Channel 5 (750-820 eV) Channel 14 (3170-4800 eV)
- Channel 6 (900-980 eV) Channel 15 (4300-6300 eV)
- Channel 7 (980-1050 eV) Channel 16 (5300-7000 eV)
- Channel 8 (1200-1300 eV) Channel 17 (7300-9500 eV)
- Channel 9 (1300-1500 eV) Channel 18 (10000-20000 eV)

Comments/Requirements

OMEGA Shot
Request Form



Go To RID# This RID#: 68712 Shot Number: 91026

Last Modified: 11-Sep-2018 16:54:18

[General](#) > [Drivers](#) > [Target](#) > [Beams](#) > [TIM](#) > [Fixed](#) > [Neutronics](#)

[Facility Status](#)
[Comments/Problems](#)
[XOPS](#) [Beamlines](#)
[Help](#)

Hard XR Detector 1-4 (HXRD) / FIXED H10 EAX Operating Procedures

Filtering

Channel	Filter
HXRD1	3 mm Al
HXRD2	20 mm Al
HXRD3	20 mm Al + 3.25 mm Cu
HXRD4	20 mm Al + 6.3 mm Cu

Special Instructions

Shot Number: 91026


[Campaign Editor](#) [Drivers Editor](#) [Beam Editor](#) [Target Editor](#) [SRF Auditor](#)

[Copy ...](#) [Reports](#) [Station Reports](#)

Visible Camera 2 (CAMERA)	Ride Along	P2A			
Visible Camera 3 (CAMERA)	Ride Along	H8D			
XR Pinhole Camera H12 (XRPHC)	Ride Along	H12C	108.89	54	Set up
XR Pinhole Camera H13 (XRPHC)	Ride Along	H13C	92.74	342	Set up
XR Pinhole Camera H4 (XRPHC)	Ride Along	H4A	29.52	234	Set up
XR Pinhole Camera H8 (XRPHC)	Ride Along	H8C	79.3	153.78	Set up
XR Pinhole Camera P2 (XRPHC)	Ride Along	P2C	68.43	54	Set up

B.3 Capsule Characterization Shot - RID 69902

OMEGA Shot
Request Form



[Facility Status](#)
[Comments/Problems](#)
[XOPS](#) [Beamlines](#)
[Help](#)

Go To RID# This RID#: 69902 Shot Number: 91030
 Last Modified: 11-Sep-2018 19:46:58
[General](#) > [Drivers](#) > [Target](#) > [Beams](#) > [TIM](#) > [Fixed](#) > [Neutronics](#)

Driver [\(Help\)](#)

<p>Driver</p> <p><input type="radio"/> OFF <input checked="" type="radio"/> SSD <input type="radio"/> PHX <input type="radio"/> MPD</p>	<p>UV Fiducial: <input checked="" type="radio"/> OFF <input type="radio"/> ON</p> <p><i>Note: IR/Green Fiducials are supplied on all shots.</i></p> <p>SSD Driver: Primary driver for OMEGA. May be shot with or without bandwidth.</p> <p>*Pulse Shape <input type="text" value="SG10v001"/> <input type="text" value=""/></p> <p>-or- Pulse Shape request # <input type="text" value=""/></p> <p>Pulse Delay <input type="text" value="0"/> ns <input type="checkbox"/> SSD Sync</p> <p>Modulation: <input type="text" value="ON"/> <input type="text" value="X = [Max]"/> <input type="text" value="Y = [Max]"/></p> <p>Backlighter Driver: May feed any one leg of OMEGA System.</p> <p>*Pulse Shape <input type="text" value=""/></p> <p>-or- Pulse Shape request # <input type="text" value=""/></p> <p>Pulse Delay <input type="text" value=""/> ns</p>
<p>Special Instructions: <input style="width: 100%;" type="text"/></p>	

* Queryable fields: [Wild cards: (_) matches any one character; (%) matches 0 or more characters]

Beam Groups Summary

20 beam(s) are configured.

Edit Ref:	Beams	Group Name	Energy	Pointing	Focusing	Beam Delay	DPP	DPR	3w Half-Waveplate	Polarization Rotation	Termination	Report Group
1	13-15.22.24- 26.28.42.45.46.51.53.55-58.65.66	Capsule Backlighter	450 J/Beam (UV)	10004 / 37.41 / 164.52	800 um (spot size)	0.00	none	No			Target	A
2	64	Capsule Backlighter	450 J/Beam (UV)	10004 / 37.41 / 164.52	400 um (spot size)	0.00	none	No			Target	A

Target Information (Help)

<p>Target ID: NLUF-1Q19-05-20 Enter</p> <p>Type/Description: Ch[8-4] Select from List</p> <p>Outside Diameter: 861.8 um <input type="text"/> Get TIS Info</p> <p>Shape: Spherical <input checked="" type="checkbox"/> Gas <input type="checkbox"/> Tritium <input type="checkbox"/></p> <p>Positioner: TIM <input type="checkbox"/> TPS2-Port H2 <input type="checkbox"/></p> <p>Alignment Only <input type="checkbox"/> (Check = Yes)</p> <p>Record Target Pressure? <input checked="" type="radio"/> No <input type="radio"/> Tail Cell <input type="radio"/> Transducer <input type="radio"/> Yes <input checked="" type="radio"/> No</p> <p>Contains Materials Z > 36 This includes hohlraums, foils, shields, pinholes, grids, etc. If "Yes" describe the Z > 36 target components here:</p> <p>Hazardous Materials: (64 max chars)</p> <p>Special Instructions: (64 max chars)</p> <p>Soft Rough Pumping:</p> <p>Target Alignment Procedure: Operations use: PI need not complete.</p> <p>Cryo Pump Off?</p> <p>Target Detection</p>	<p>Target 2 Description</p> <p><input type="text"/></p> <p><input type="text"/> um <input type="text"/> Gas <input type="text"/> TIM <input type="text"/></p> <p><input type="checkbox"/> (Check = Yes)</p> <p><input checked="" type="radio"/> No <input type="radio"/> Tail Cell <input type="radio"/> Transducer <input type="radio"/> Yes <input checked="" type="radio"/> No</p> <p><input type="text"/> mg Be <input type="text"/> mg U</p> <p><input type="checkbox"/> (Check = Yes) <input type="text"/> Sec.</p> <p>[TPS_Sphere_IonFront_09-18]</p> <p><input type="checkbox"/> Standard <input type="radio"/> X Axis <input type="radio"/> Y Axis <input type="radio"/> Both Axes <input type="radio"/> Disabled</p> <p><input type="checkbox"/> Cryo Setups for Target 1 After "Update", Select this to modify the Shroud Pull and Sub-cooling.</p>	<p>Target 3 Description</p> <p><input type="text"/></p> <p><input type="text"/> um <input type="text"/> Gas <input type="text"/> TIM <input type="text"/></p> <p><input type="checkbox"/> (Check = Yes)</p> <p><input checked="" type="radio"/> No <input type="radio"/> Tail Cell <input type="radio"/> Transducer <input type="radio"/> Yes <input checked="" type="radio"/> No</p> <p><input type="text"/> mg Be <input type="text"/> mg U</p> <p><input type="checkbox"/> (Check = Yes) <input type="text"/> Sec.</p>	<p>Target 4 Description</p> <p><input type="text"/></p> <p><input type="text"/> um <input type="text"/> Gas <input type="text"/> TIM <input type="text"/></p> <p><input type="checkbox"/> (Check = Yes)</p> <p><input checked="" type="radio"/> No <input type="radio"/> Tail Cell <input type="radio"/> Transducer <input type="radio"/> Yes <input checked="" type="radio"/> No</p> <p><input type="text"/> mg Be <input type="text"/> mg U</p> <p><input type="checkbox"/> (Check = Yes) <input type="text"/> Sec.</p>
--	---	--	--



Go To RID# This RID#: 69902 Shot Number: 91030
 Last Modified: 11-Sep-2018 19:46:58
[General](#) > [Drivers](#) > [Target](#) > [Beams](#) > [TIM](#) > [Fixed](#) > [Neutronics](#)

[Facility Status](#)
[Comments/Problems](#)
[XPCS](#) [Beamlines](#)
[Help](#)

TIM Configuration ([Help](#)) [XRFC Swap](#) [Diagnostic Swap](#)

Setup pages are not needed for Empty, TSSAC

	Diagnostic description	Other diagnostic	Priority	Port	Opposing port
TIM 1	[Rowland(Yaakobi) XR Spectrometer 1 (XRS)]	<input type="text"/>	Primary	P3	P10
TIM 2	[XR Framing Camera 1 (XRFC)]	<input type="text"/>	Primary	H3	H18
TIM 3	[Rowland(Yaakobi) XR Spectrometer 2 (XRS)]	<input type="text"/>	Primary	H18	H3
TIM 4	<input type="text"/>	<input type="text"/>	<input type="text"/>	P6	P7
TIM 5	<input type="text"/>	<input type="text"/>	<input type="text"/>	H14	H7
TIM 6	<input type="text"/>	<input type="text"/>	<input type="text"/>	P7	P6

OMEGA Shot
Request Form



Go To RID# This RID#: 69902 Shot Number: 91030
 Last Modified: 11-Sep-2018 19:46:58
[General](#) > [Drivers](#) > [Target](#) > [Beams](#) > [TIM](#) > [Fixed](#) > [Neutronics](#)

[Facility Status](#)
[Current Problems](#)
[XOPS](#) [Beamlines](#)
[Help](#)

Rowland(Yaakobi) XR Spectrometer 1 (XRS) / TIM 1 EAF [Operating Procedures](#) [Users Guide](#)

Internal Settings

Crystal Type	ADP
Description	
Crystal Surface	flat
Crystal Length	12 cm
Crystal Width	1 cm
Crystal Position	2
Crystal Tilt	+
Blast Shield Thickness (Be)	10 mils
Filter Material	None
Filter Thickness	mils
Slit Width	3000 μ m
Pinhole Diameter	μ m
LOS Shield	None (Standard)

External Settings

Shift to Target	<input type="checkbox"/>	"
Energy Range	2720 to 3500	ev
Detector Type	BAS MS	
Scan Time		Min.
Sensitivity		
Pixel Size		μ m
Film-cassette Be thickness	1 mil	

Steering

Make selections in one row only

<input type="checkbox"/> Target Chamber Center
<input type="checkbox"/> Same as P9 Probe Beam
<input checked="" type="checkbox"/> Radius 10000 μ m
Theta 37.41
Phi 164.52
<input type="checkbox"/> Distance μ m toward Port

Comments/Requirements

10 μ m Saran/PVDC (Cl) filter covering half of the entrance slit. Rotate crystal 4 degrees to the TIM axis.

XR Framing Camera 1 (XRFC) / TIM 2 EAX Operating Procedures

Optics

		Make selections in one column only	
Nosecone Type	<input type="radio"/> LLE	<input checked="" type="radio"/> LLNL	<input type="radio"/> LANL
Magnification	4X-16		
Pinhole Size	15um		
Blast Shield			
Frame Type	Straight		
Stand-off Distance	cm		
Roll Angle	Degrees		
Pinhole Substrate			
Rear Filter	1 mil Be		
SXR Rear Filter			

Interstrip Timing

MCP	4-strip
MCP Module	F1
Strip#	Requested delay (0-6.35 ns by .05)
1	0
2	1.25
3	1.5
4	1.75

Internal Settings

Strip	Bias (Volts)
1	350
2	350
3	350
4	350
PFM Type	50

Misc

Acquisition start time (relative to T=0)	0	ps
Detector	SV/GCD3	
CCD Image Size	2048	H x 2048
Monitor Atten.	21	dB
Trigger Atten.	10	dB

Steering

Make selections in one row only		
<input type="radio"/> Target Chamber Center		
<input type="radio"/> Same as P9 Probe Beam		
<input checked="" type="radio"/> Radius	10000	um
<input type="radio"/> Distance		um toward Port
		Phi 164.52

Comments/Requirements

OMEGA Shot
Request Form



Go To RID# This RID#: 69902 Shot Number: 91030
 Last Modified: 11-Sep-2018 19:46:58
[General](#) > [Drivers](#) > [Target](#) > [Beams](#) > [TIM](#) > [Fixed](#) > [Neutronics](#)

[Facility Status](#)
[Comments/Problems](#)
[XOPS](#) [Beamlines](#)
[Help](#)

Rowland(Yaakobi) XR Spectrometer 2 (XRS) / TIM 3 EAF Operating Procedures Users Guide

Internal Settings

Crystal Type	ADP
Description	
Crystal Surface	flat
Crystal Length	12 cm
Crystal Width	1 cm
Crystal Position	2
Crystal Tilt	+
Blast Shield Thickness (Be)	10 mils
Filter Material	None
Filter Thickness	mils
Slit Width	8000 μ m
Pinhole Diameter	μ m
LOS Shield	None (Standard)

External Settings

Shift to Target			"
Energy Range	2720	to 3500	ev
Detector Type	BAS MS		
Scan Time			Min.
Sensitivity			
Pixel Size			μ m
Film-cassette Be thickness	1 mil		

Steering

Make selections in one row only

<input checked="" type="radio"/> Target Chamber Center	
<input type="radio"/> Same as P9 Probe Beam	
<input type="radio"/> Radius	um
<input type="radio"/> Distance	um toward Port

Comments/Requirements

10 micron Saran/FVDC (C1) filter over half of the slit width. Rotate crystal 4 degrees to the TIM axis.

Dante 1 (DANTE) / FIXED H161 [EAF](#) [Operating Procedures](#)

Dante configuration must be approved by the Instrument Specialist a minimum of four weeks in advance of the campaign.

Source Info

Source Type	Sphere	<input type="text"/>
Source Size	100	um
Source Axis/Position	Radius (mm)	Theta
	10	37.38
		162
Expected Brightness Temperature	1500	eV
Signal Start Time	0	ns
Other Sources Present (Explain in Comments)	No	

Channels Requested (Select up to 10)

<input checked="" type="checkbox"/> Channel 1 (50-70 eV)	<input type="checkbox"/> Channel 10 (1600-1800 eV)
<input checked="" type="checkbox"/> Channel 2 (150-180 eV)	<input checked="" type="checkbox"/> Channel 11 (2000-5000 eV)
<input checked="" type="checkbox"/> Channel 3 (250-280 eV)	<input type="checkbox"/> Channel 12 (1800-2500 eV)
<input checked="" type="checkbox"/> Channel 4 (450-520 eV)	<input type="checkbox"/> Channel 13 (2540-3300 eV)
<input checked="" type="checkbox"/> Channel 5 (750-820 eV)	<input type="checkbox"/> Channel 14 (3170-4800 eV)
<input checked="" type="checkbox"/> Channel 6 (900-980 eV)	<input type="checkbox"/> Channel 15 (4300-6300 eV)
<input checked="" type="checkbox"/> Channel 7 (980-1050 eV)	<input type="checkbox"/> Channel 16 (5300-7000 eV)
<input checked="" type="checkbox"/> Channel 8 (1200-1300 eV)	<input type="checkbox"/> Channel 17 (7300-9500 eV)
<input checked="" type="checkbox"/> Channel 9 (1300-1500 eV)	<input type="checkbox"/> Channel 18 (10000-20000 eV)

Comments/Requirements

OMEGA Shot
Request Form



Go To RID# This RID#: 69902 Shot Number: 91030

Last Modified: 11-Sep-2018 19:46:58

[General](#) > [Drivers](#) > [Target](#) > [Beams](#) > [JIM](#) > [Fixed](#) > [Neutronics](#)

[Facility Status](#)
[Comments/Problems](#)
[XOPS](#) [Beamlines](#)
[Help](#)

Hard XR Detector 1-4 (HXRD) / FIXED H10 EAEF Operating Procedures

Filtering

Channel	Filter
HXRD1	3 mm Al
HXRD2	20 mm Al
HXRD3	20 mm Al + 3.25 mm Cu
HXRD4	20 mm Al + 6.3 mm Cu

Special Instructions

AWO Fashion Display Budget (11.17)									
									Set up
Visible Camera 2 (CAMERA)	Ride Along	P2A							
Visible Camera 3 (CAMERA)	Ride Along	H8D							
XR Pinhole Camera H12 (XRPHC)	Ride Along	H12C	108.89	54					Set up
XR Pinhole Camera H13 (XRPHC)	Ride Along	H13C	92.74	342					Set up
XR Pinhole Camera H4 (XRPHC)	Ride Along	H4A	29.52	234					Set up
XR Pinhole Camera H8 (XRPHC)	Ride Along	H8C	79.3	153.78					Set up
XR Pinhole Camera P2 (XRPHC)	Ride Along	P2C	68.43	54					Set up

APPENDIX C

July 17th 2019 NIF Shot Day

C.1 High Drive Shot N190717-001

Diagnostic	Timing	Filtering	DIM
MACS	17.3 ns and 18.3 ns 230 ps PFM	125 μm Polyimide Filter and 50 μm Aluminized Polyimide	DIM 90-78
SOP	-0.5 ns; 45 ns sweep	2.0 ND	DIM 90-315
VISAR A	2 ns; 31 ns sweep	1.0 ND	DIM 90-315
VISAR B	12 ns; 21 ns sweep	1.0 ND	DIM 90-315

Table C.1: The diagnostic configuration from the high drive shot during the July 2019 NIF shot day.

C.2 Low Drive Shot N190717-002

Diagnostic	Timing	Filtering	DIM
MACS	33.7 ns and 35.4 ns 230 ps PFM	125 μm Polyimide Filter and 50 μm Aluminized Polyimide	DIM 90-78
SOP	10 ns; 45 ns sweep	1.6 ND	DIM 90-315
VISAR A	25 ns; 31 ns sweep	0.0 ND	DIM 90-315
VISAR B	35 ns; 21 ns sweep	0.0 ND	DIM 90-315

Table C.2: The diagnostic configuration for the low drive shot during the July 2019 NIF shot day.

APPENDIX D

February 10th 2020 NIF Shot Day

D.1 High Drive Shot N200210-001

Diagnostic	Timing	Filtering	DIM
MACS	18.3 ns and 20.5 ns 230 ps PFM	125 μm Polyimide Filter and 50 μm Aluminized Polyimide	DIM 90-78
SOP	-0.5 ns; 45 ns sweep	2.0 ND	DIM 90-315
VISAR A	2 ns; 31 ns sweep	0.0 ND	DIM 90-315
VISAR B	12 ns; 21 ns sweep	0.0 ND	DIM 90-315

Table D.1: The diagnostic configuration for the first high drive shot during the February NIF shot day.

D.2 High Drive Shot N200210-002

Diagnostic	Timing	Filtering	DIM
MACS	18.9 ns and 19.5 ns 230 ps PFM	125 μm Polyimide Filter and 50 μm Aluminized Polyimide	DIM 90-78
SOP	-0.5 ns; 45 ns sweep	2.0 ND	DIM 90-315
VISAR A	2 ns; 31 ns sweep	0.0 ND	DIM 90-315
VISAR B	12 ns; 21 ns sweep	0.0 ND	DIM 90-315

Table D.2: The diagnostic configuration for the second high drive shot during the February NIF shot day.

D.3 Low Drive Shot N200211-001

Diagnostic	Timing	Filtering	DIM
MACS	33.7 ns and 35.4 ns 230 ps PFM	125 μm Polyimide Filter and 50 μm Aluminized Polyimide	DIM 90-78
SOP	10 ns; 45 ns sweep	1.6 ND	DIM 90-315
VISAR A	25 ns; 31 ns sweep	0.0 ND	DIM 90-315
VISAR B	35 ns; 21 ns sweep	0.0 ND	DIM 90-315

Table D.3: The diagnostic configuration for the low drive shot during the February NIF shot day.

BIBLIOGRAPHY

BIBLIOGRAPHY

- [1] R. Drake, *High-Energy-Density Physics: Foundation of Inertial Fusion and Experimental Astrophysics*. Graduate Texts in Physics, Springer International Publishing, 2018.
- [2] B. E. Robertson, R. S. Ellis, J. S. Dunlop, R. J. McLure, and D. P. Stark, “Early star-forming galaxies and the reionization of the universe,” *Nature*, vol. 468, no. 7320, pp. 49–55, 2010.
- [3] O. A. Hurricane and J. H. Hammer, “Bent marshak waves,” *Physics of Plasmas*, vol. 13, no. 11, p. 113303, 2006.
- [4] R. G. McClarren, R. P. Drake, J. E. Morel, and J. P. Holloway, “Theory of radiative shocks in the mixed, optically thick-thin case,” *Physics of Plasmas*, vol. 17, no. 9, p. 093301, 2010.
- [5] J. S. Davis, Y. Frank, E. Raicher, M. Fraenkel, P. A. Keiter, S. R. Klein, R. P. Drake, and D. Shvarts, “Measurements of laser generated soft x-ray emission from irradiated gold foils,” *Review of Scientific Instruments*, vol. 87, no. 11, p. 11D609, 2016.
- [6] J. S. Davis, R. P. Drake, M. Fraenkel, Y. Frank, P. A. Keiter, S. R. Klein, E. Raicher, D. Shvarts, and M. R. Trantham, “Soft x-ray emission from laser-irradiated gold foils,” *Physics of Plasmas*, vol. 25, no. 7, p. 073304, 2018.
- [7] J. F. Hansen, S. G. Glendinning, R. F. Heeter, and S. J. E. Brockington, “Dynamic hohlraums as x-ray sources in high-energy density science,” *Review of Scientific Instruments*, vol. 79, no. 1, p. 013504, 2008.
- [8] “<https://pls.llnl.gov/research-and-development/high-energy-density-science/research-areas>,” 2020.
- [9] C. C. Kuranz, H. S. Park, C. M. Huntington, A. R. Miles, B. A. Remington, T. Plewa, M. R. Trantham, H. F. Robey, D. Shvarts, A. Shimony, K. Raman, S. MacLaren, W. C. Wan, F. W. Doss, J. Kline, K. A. Flippo, G. Malamud, T. A. Handy, S. Prsbrey, C. M. Krauland, S. R. Klein, E. C. Harding, R. Wallace, M. J. Grosskopf, D. C. Marion, D. Kalantar, E. Giraldez, and R. P. Drake, “How high energy fluxes may affect rayleigh–taylor instability growth in young supernova remnants,” *Nature Communications*, vol. 9, no. 1, p. 1564, 2018.

- [10] J. E. Bailey, T. Nagayama, G. P. Loisel, G. A. Rochau, C. Blancard, J. Colgan, P. Cosse, G. Faussurier, C. J. Fontes, F. Gilleron, I. Golovkin, S. B. Hansen, C. A. Iglesias, D. P. Kilcrease, J. J. MacFarlane, R. C. Mancini, S. N. Nahar, C. Orban, J. C. Pain, A. K. Pradhan, M. Sherrill, and B. G. Wilson, “A higher-than-predicted measurement of iron opacity at solar interior temperatures,” *Nature*, vol. 517, pp. 56 EP –, 12 2014.
- [11] R. F. Heeter, J. E. Bailey, R. S. Craxton, B. G. DeVolder, E. S. Dodd, E. M. Garcia, E. J. Huffman, C. A. Iglesias, J. A. King, J. L. Kline, and et al., “Conceptual design of initial opacity experiments on the national ignition facility,” *Journal of Plasma Physics*, vol. 83, no. 1, p. 595830103, 2017.
- [12] M. Millot, F. Coppari, J. R. Rygg, A. Correa Barrios, S. Hamel, D. C. Swift, and J. H. Eggert, “Nanosecond x-ray diffraction of shock-compressed superionic water ice,” *Nature*, vol. 569, no. 7755, pp. 251–255, 2019.
- [13] Y. Ping, F. Coppari, D. G. Hicks, B. Yaakobi, D. E. Fratanduono, S. Hamel, J. H. Eggert, J. R. Rygg, R. F. Smith, D. C. Swift, D. G. Braun, T. R. Boehly, and G. W. Collins, “Solid iron compressed up to 560 gpa,” *Phys. Rev. Lett.*, vol. 111, p. 065501, Aug 2013.
- [14] P. Tzeferacos, A. Rigby, A. Bott, A. R. Bell, R. Bingham, A. Casner, F. Cattaneo, E. M. Churazov, J. Emig, N. Flocke, F. Fiuza, C. B. Forest, J. Foster, C. Graziani, J. Katz, M. Koenig, C.-K. Li, J. Meinecke, R. Petrasso, H.-S. Park, B. A. Remington, J. S. Ross, D. Ryu, D. Ryutov, K. Weide, T. G. White, B. Reville, F. Miniati, A. A. Schekochihin, D. H. Froula, G. Gregori, and D. Q. Lamb, “Numerical modeling of laser-driven experiments aiming to demonstrate magnetic field amplification via turbulent dynamo,” *Physics of Plasmas*, vol. 24, no. 4, p. 041404, 2017.
- [15] R. S. Craxton, K. S. Anderson, T. R. Boehly, V. N. Goncharov, D. R. Harding, J. P. Knauer, R. L. McCrory, P. W. McKenty, D. D. Meyerhofer, J. F. Myatt, A. J. Schmitt, J. D. Sethian, R. W. Short, S. Skupsky, W. Theobald, W. L. Kruer, K. Tanaka, R. Betti, T. J. B. Collins, J. A. Delettrez, S. X. Hu, J. A. Marozas, A. V. Maximov, D. T. Michel, P. B. Radha, S. P. Regan, T. C. Sangster, W. Seka, A. A. Solodov, J. M. Soures, C. Stoeckl, and J. D. Zuegel, “Direct-drive inertial confinement fusion: A review,” *Physics of Plasmas*, vol. 22, no. 11, p. 110501, 2015.
- [16] M. E. Cuneo, M. C. Herrmann, D. B. Sinars, S. A. Slutz, W. A. Stygar, R. A. Vesey, A. B. Sefkow, G. A. Rochau, G. A. Chandler, J. E. Bailey, J. L. Porter, R. D. McBride, D. C. Rovang, M. G. Mazarakis, E. P. Yu, D. C. Lamppa, K. J. Peterson, C. Nakhleh, S. B. Hansen, A. J. Lopez, M. E. Savage, C. A. Jennings, M. R. Martin, R. W. Lemke, B. W. Atherton, I. C. Smith, P. K. Rambo, M. Jones, M. R. Lopez, P. J. Christenson, M. A. Sweeney, B. Jones, L. A. McPherson, E. Harding, M. R. Gomez, P. F. Knapp, T. J. Awe, R. J. Leeper, C. L. Ruiz, G. W. Cooper, K. D. Hahn, J. McKenney, A. C. Owen, G. R. McKee,

- G. T. Leifeste, D. J. Ampleford, E. M. Waisman, A. Harvey-Thompson, R. J. Kaye, M. H. Hess, S. E. Rosenthal, and M. K. Matzen, “Magnetically driven implosions for inertial confinement fusion at sandia national laboratories,” *IEEE Transactions on Plasma Science*, vol. 40, no. 12, pp. 3222–3245, 2012.
- [17] G. A. Rochau, J. E. Bailey, G. A. Chandler, G. Cooper, G. S. Dunham, P. W. Lake, R. J. Leeper, R. W. Lemke, T. A. Mehlhorn, A. Nikroo, K. J. Peterson, C. L. Ruiz, D. G. Schroen, S. A. Slutz, D. Steinman, W. A. Stygar, and W. Varnum, “High performance capsule implosions driven by the z-pinch dynamic hohlraum,” *Plasma Physics and Controlled Fusion*, vol. 49, pp. B591–B600, nov 2007.
- [18] J. Lindl, “Development of the indirect-drive approach to inertial confinement fusion and the target physics basis for ignition and gain,” *Physics of Plasmas*, vol. 2, no. 11, pp. 3933–4024, 1995.
- [19] M. E. Cuneo, D. B. Sinars, E. M. Waisman, D. E. Bliss, W. A. Stygar, R. A. Vesey, R. W. Lemke, I. C. Smith, P. K. Rambo, J. L. Porter, G. A. Chandler, T. J. Nash, M. G. Mazarakis, R. G. Adams, E. P. Yu, K. W. Struve, T. A. Mehlhorn, S. V. Lebedev, J. P. Chittenden, and C. A. Jennings, “Compact single and nested tungsten-wire-array dynamics at 14–19ma and applications to inertial confinement fusion,” *Physics of Plasmas*, vol. 13, no. 5, p. 056318, 2006.
- [20] A. L. Kritcher, D. C. Swift, T. Döppner, B. Bachmann, L. X. Benedict, G. W. Collins, J. L. DuBois, F. Elsner, G. Fontaine, J. A. Gaffney, S. Hamel, A. Lazicki, W. R. Johnson, N. Kostinski, D. Kraus, M. J. MacDonald, B. Maddox, M. E. Martin, P. Neumayer, A. Nikroo, J. Nilsen, B. A. Remington, D. Saumon, P. A. Sterne, W. Sweet, A. A. Correa, H. D. Whitley, R. W. Falcone, and S. H. Glenzer, “A measurement of the equation of state of carbon envelopes of white dwarfs,” *Nature*, vol. 584, no. 7819, pp. 51–54, 2020.
- [21] D. B. Hayes, C. A. Hall, J. R. Asay, and M. D. Knudson, “Measurement of the compression isentrope for 6061-t6 aluminum to 185gpa and 46% volumetric strain using pulsed magnetic loading,” *Journal of Applied Physics*, vol. 96, no. 10, pp. 5520–5527, 2004.
- [22] D. B. Schaeffer, W. Fox, R. K. Follett, G. Fiksel, C. K. Li, J. Matteucci, A. Bhattacherjee, and K. Germaschewski, “Direct observations of particle dynamics in magnetized collisionless shock precursors in laser-produced plasmas,” *Phys. Rev. Lett.*, vol. 122, p. 245001, Jun 2019.
- [23] S. Jiang, A. E. Lazicki, S. B. Hansen, P. A. Sterne, P. Grabowski, R. Shepherd, H. A. Scott, R. F. Smith, J. H. Eggert, and Y. Ping, “Measurements of pressure-induced $k\beta$ line shifts in ramp compressed cobalt up to 8 mbar,” *Phys. Rev. E*, vol. 101, p. 023204, Feb 2020.

- [24] G. A. Rochau, J. E. Bailey, R. E. Falcon, G. P. Loisel, T. Nagayama, R. C. Mancini, I. Hall, D. E. Winget, M. H. Montgomery, and D. A. Liedahl, “Zapp: The z astrophysical plasma properties collaboration,” *Physics of Plasmas*, vol. 21, no. 5, p. 056308, 2014.
- [25] H. N. Kornblum, R. L. Kauffman, and J. A. Smith, “Measurement of 0.1–3-keV x rays from laser plasmas,” *Review of Scientific Instruments*, vol. 57, no. 8, pp. 2179–2181, 1986.
- [26] M. Bennett, S. Lebedev, G. Hall, L. Suttle, G. Burdiak, F. Suzuki-Vidal, J. Hare, G. Swadling, S. Patankar, M. Bocchi, J. Chittenden, R. Smith, A. Frank, E. Blackman, R. Drake, and A. Ciardi, “Formation of radiatively cooled, supersonically rotating, plasma flows in z-pinch experiments: Towards the development of an experimental platform to study accretion disk physics in the laboratory,” *High Energy Density Physics*, vol. 17, pp. 63–67, 2015. 10th International Conference on High Energy Density Laboratory Astrophysics.
- [27] C. A. Back, J. D. Bauer, O. L. Landen, R. E. Turner, B. F. Lasinski, J. H. Hammer, M. D. Rosen, L. J. Suter, and W. H. Hsing, “Detailed measurements of a diffusive supersonic wave in a radiatively heated foam,” *Phys. Rev. Lett.*, vol. 84, pp. 274–277, Jan 2000.
- [28] C. A. Back, J. D. Bauer, J. H. Hammer, B. F. Lasinski, R. E. Turner, P. W. Rambo, O. L. Landen, L. J. Suter, M. D. Rosen, and W. W. Hsing, “Diffusive, supersonic x-ray transport in radiatively heated foam cylinders,” *Physics of Plasmas*, vol. 7, no. 5, pp. 2126–2134, 2000.
- [29] J. M. Taccetti, P. A. Keiter, N. Lanier, K. Mussack, K. Belle, and G. R. Magelssen, “A technique for measuring the propagation of a supersonic radiation front in foam via spatially resolved spectral imaging of a tracer layer,” *Review of Scientific Instruments*, vol. 83, no. 2, p. 023506, 2012.
- [30] D. Hoarty, L. Barringer, C. Vickers, O. Willi, and W. Nazarov, “Observation of transonic ionization fronts in low-density foam targets,” *Phys. Rev. Lett.*, vol. 82, pp. 3070–3073, Apr 1999.
- [31] T. Afshar-rad, M. Desselberger, M. Dunne, J. Edwards, J. M. Foster, D. Hoarty, M. W. Jones, S. J. Rose, P. A. Rosen, R. Taylor, and O. Willi, “Supersonic propagation of an ionization front in low density foam targets driven by thermal radiation,” *Phys. Rev. Lett.*, vol. 73, pp. 74–77, Jul 1994.
- [32] P. A. Keiter, G. A. Kyrala, R. G. Watt, G. C. Idzorek, R. R. Peterson, B. Wood, P. Adams, R. E. Chrien, D. Peterson, and M. Wood-Schultz, *Preliminary Results from an Astrophysically Relevant Radiation Transfer Experiment*, pp. 163–170. Dordrecht: Springer Netherlands, 2005.

- [33] G. P. Loisel, J. E. Bailey, D. A. Liedahl, C. J. Fontes, T. R. Kallman, T. Nagayama, S. B. Hansen, G. A. Rochau, R. C. Mancini, and R. W. Lee, “Benchmark experiment for photoionized plasma emission from accretion-powered x-ray sources,” *Phys. Rev. Lett.*, vol. 119, p. 075001, Aug 2017.
- [34] R. C. Mancini, T. E. Lockard, D. C. Mayes, I. M. Hall, G. P. Loisel, J. E. Bailey, G. A. Rochau, J. Abdallah, I. E. Golovkin, and D. Liedahl, “X-ray heating and electron temperature of laboratory photoionized plasmas,” *Phys. Rev. E*, vol. 101, p. 051201, May 2020.
- [35] Y. Zel’dovich and Y. Raizer, *Physics of Shock Waves and High-Temperature Hydrodynamic Phenomena*. Dover Books on Physics, Dover Publications, 2002.
- [36] D. Mihalas and B. Weibel-Mihalas, *Foundations of Radiation Hydrodynamics*. Dover Books on Physics, Dover Publications, 1999.
- [37] R. E. Marshak, “Effect of radiation on shock wave behavior,” *The Physics of Fluids*, vol. 1, no. 1, pp. 24–29, 1958.
- [38] R. A. Chevalier and C. M. Irwin, “X-RAYS FROM SUPERNOVA SHOCKS IN DENSE MASS LOSS,” *The Astrophysical Journal*, vol. 747, p. L17, feb 2012.
- [39] S. Hatchett, J. Buff, and R. McCray, “Transfer of X-rays through a spherically symmetric gas cloud,” *apj*, vol. 206, pp. 847–860, June 1976.
- [40] C. B. Tarter, W. H. Tucker, and E. E. Salpeter, “The Interaction of X-Ray Sources with Optically Thin Environments,” *apj*, vol. 156, p. 943, June 1969.
- [41] C. B. Tarter and E. E. Salpeter, “The Interaction of X-Ray Sources with Optically Thick Environments,” *apj*, vol. 156, p. 953, June 1969.
- [42] C. S. Kochanek, “The physics of flash (supernova) spectroscopy,” *Monthly Notices of the Royal Astronomical Society*, vol. 483, pp. 3762–3772, 12 2018.
- [43] V. Morozova, A. L. Piro, and S. Valenti, “Measuring the progenitor masses and dense circumstellar material of type II supernovae,” *The Astrophysical Journal*, vol. 858, p. 15, apr 2018.
- [44] M. Fraser, “Supernovae and transients with circumstellar interaction,” *Royal Society Open Science*, vol. 7, no. 7, p. 200467, 2020.
- [45] O. Yaron, D. A. Perley, A. Gal-Yam, J. H. Groh, A. Horesh, E. O. Ofek, S. R. Kulkarni, J. Sollerman, C. Fransson, A. Rubin, P. Szabo, N. Sapir, F. Taddia, S. B. Cenko, S. Valenti, I. Arcavi, D. A. Howell, M. M. Kasliwal, P. M. Vreeswijk, D. Khazov, O. D. Fox, Y. Cao, O. Gnat, P. L. Kelly, P. E. Nugent, A. V. Filippenko, R. R. Laher, P. R. Wozniak, W. H. Lee, U. D. Rebbapragada, K. Maguire, M. Sullivan, and M. T. Soumagnac, “Confined dense circumstellar material surrounding a regular type ii supernova,” *Nature Physics*, vol. 13, no. 5, pp. 510–517, 2017.

- [46] Leloudas, G., Hsiao, E. Y., Johansson, J., Maeda, K., Moriya, T. J., Nordin, J., Petrushevskaya, T., Silverman, J. M., Sollerman, J., Stritzinger, M. D., Taddia, F., and Xu, D., “Supernova spectra below strong circumstellar interaction,” *A&A*, vol. 574, p. A61, 2015.
- [47] M. Nicholl, P. K. Blanchard, E. Berger, R. Chornock, R. Margutti, S. Gomez, R. Lunnan, A. A. Miller, W.-f. Fong, G. Terreran, A. Vigna-Gómez, K. Bhrombhakdi, A. Bieryla, P. Challis, R. R. Laher, F. J. Masci, and K. Paterson, “An extremely energetic supernova from a very massive star in a dense medium,” *Nature Astronomy*, vol. 4, no. 9, pp. 893–899, 2020.
- [48] E. Chatzopoulos, J. C. Wheeler, J. Vinko, R. Quimby, E. L. Robinson, A. A. Miller, R. J. Foley, D. A. Perley, F. Yuan, C. Akerlof, and J. S. Bloom, “SN 2008am: A SUPER-LUMINOUS TYPE II_n SUPERNOVA,” *The Astrophysical Journal*, vol. 729, p. 143, feb 2011.
- [49] C. L. Fryer, S. E. Woosley, and A. Heger, “Pair-instability supernovae, gravity waves, and gamma-ray transients,” *The Astrophysical Journal*, vol. 550, pp. 372–382, mar 2001.
- [50] V. Bromm, P. S. Coppi, and R. B. Larson, “The formation of the first stars. i. the primordial star-forming cloud,” *The Astrophysical Journal*, vol. 564, pp. 23–51, jan 2002.
- [51] A. K. Inoue, Y. Tamura, H. Matsuo, K. Mawatari, I. Shimizu, T. Shibuya, K. Ota, N. Yoshida, E. Zackrisson, N. Kashikawa, K. Kohno, H. Umehata, B. Hatsukade, M. Iye, Y. Matsuda, T. Okamoto, and Y. Yamaguchi, “Detection of an oxygen emission line from a high-redshift galaxy in the reionization epoch,” *Science*, vol. 352, no. 6293, pp. 1559–1562, 2016.
- [52] K. Mawatari, A. K. Inoue, T. Hashimoto, J. Silverman, M. Kajisawa, S. Yamanaka, T. Yamada, I. Davidzon, P. Capak, L. Lin, B.-C. Hsieh, Y. Taniguchi, M. Tanaka, Y. Ono, Y. Harikane, Y. Sugahara, S. Fujimoto, and T. Nagao, “Balmer break galaxy candidates at z 6: A potential view on the star formation activity at $z \approx 14$,” *The Astrophysical Journal*, vol. 889, p. 137, feb 2020.
- [53] Schaerer, D. and de Barros, S., “On the physical properties of z -8 galaxies,” *A&A*, vol. 515, p. A73, 2010.
- [54] Schaerer, D. and de Barros, S., “The impact of nebular emission on the ages of z 6 galaxies,” *A&A*, vol. 502, no. 2, pp. 423–426, 2009.
- [55] de Barros, S., Schaerer, D., and Stark, D. P., “Properties of z 3-6 lyman break galaxies - ii. impact of nebular emission at high redshift,” *A&A*, vol. 563, p. A81, 2014.
- [56] B. Strömgren, “The Physical State of Interstellar Hydrogen.,” *The Astrophysical Journal*, vol. 89, p. 526, May 1939.

- [57] F. D. Kahn, “The acceleration of interstellar clouds,” *Bulletin of the Astronomical Institutes of the Netherlands*, vol. 12, p. 187, Nov 1954.
- [58] F. A. Goldsworthy, “On the propagation and structure of ionization fronts,” *Rev. Mod. Phys.*, vol. 30, pp. 1062–1068, Jul 1958.
- [59] F. A. Goldsworthy and M. J. Lighthill, “Ionization fronts in interstellar gas and the expansion of hii regions,” *Philosophical Transactions of the Royal Society of London. Series A, Mathematical and Physical Sciences*, vol. 253, no. 1028, pp. 277–300, 1961.
- [60] W. I. Axford and M. J. Lighthill, “Ionization front in interstellar gas: The structure of ionization fronts,” *Philosophical Transactions of the Royal Society of London. Series A, Mathematical and Physical Sciences*, vol. 253, no. 1029, pp. 301–333, 1961.
- [61] R. P. Drake, G. Hazak, P. A. Keiter, J. S. Davis, C. R. Patterson, A. Frank, E. G. Blackman, and M. Busquet, “DESIGN OF LABORATORY EXPERIMENTS TO STUDY PHOTOIONIZATION FRONTS DRIVEN BY THERMAL SOURCES,” *The Astrophysical Journal*, vol. 833, p. 249, dec 2016.
- [62] W. J. Gray, P. A. Keiter, H. Lefevre, C. R. Patterson, J. S. Davis, B. van Der Holst, K. G. Powell, and R. P. Drake, “Laboratory photoionization fronts in nitrogen gas: A numerical feasibility and parameter study,” *The Astrophysical Journal*, vol. 858, p. 22, apr 2018.
- [63] W. J. Gray, P. A. Keiter, H. Lefevre, C. R. Patterson, J. S. Davis, K. G. Powell, C. C. Kuranz, and R. P. Drake, “Atomic modeling of photoionization fronts in nitrogen gas,” *Physics of Plasmas*, vol. 26, no. 5, p. 052901, 2019.
- [64] B. van der Holst, G. Tóth, I. V. Sokolov, K. G. Powell, J. P. Holloway, E. S. Myra, Q. Stout, M. L. Adams, J. E. Morel, S. Karni, B. Fryxell, and R. P. Drake, “Crash: A block-adaptive-mesh code for radiative shock hydrodynamics—implementation and verification,” *The Astrophysical Journal Supplement Series*, vol. 194, no. 2, p. 23, 2011.
- [65] J. MacFarlane, I. Golovkin, and P. Woodruff, “Helios-cr – a 1-d radiation-magnetohydrodynamics code with inline atomic kinetics modeling,” *Journal of Quantitative Spectroscopy and Radiative Transfer*, vol. 99, no. 1, pp. 381 – 397, 2006. Radiative Properties of Hot Dense Matter.
- [66] P. Keiter, M. Gunderson, J. Foster, P. Rosen, A. Comley, M. Taylor, and T. Perry, “Radiation transport in inhomogeneous media,” *Physics of Plasmas*, vol. 15, no. 5, p. 056901, 2008.
- [67] S. Bouquet, R. Teyssier, and J. P. Chieze, “Analytical study and structure of a stationary radiative shock,” *The Astrophysical Journal Supplement Series*, vol. 127, pp. 245–252, apr 2000.

- [68] R. P. Drake, “Energy balance and structural regimes of radiative shocks in optically thick media,” *IEEE Transactions on Plasma Science*, vol. 35, pp. 171–180, April 2007.
- [69] R. P. Drake and A. B. Reighard, “Context and theory for planar radiative shock experiments in xenon,” *AIP Conference Proceedings*, vol. 845, no. 1, pp. 1417–1420, 2006.
- [70] R. P. Drake, “Theory of radiative shocks in optically thick media,” *Physics of Plasmas*, vol. 14, no. 4, p. 043301, 2007.
- [71] M. Koenig, T. Vinci, A. Benuzzi-Mounaix, S. Lepape, N. Ozaki, S. Bouquet, L. Boireau, S. Leygnac, C. Michaut, C. Stehle, J. P. Chièze, D. Batani, T. Hall, K. Tanaka, and M. Yoshida, “Radiative shock experiments at luli,” *Astrophysics and Space Science*, vol. 298, no. 1, pp. 69–74, 2005.
- [72] C. Michaut, T. Vinci, L. Boireau, M. Koenig, S. Bouquet, A. Benuzzi-Mounaix, N. Osaki, G. Herpe, E. Falize, B. Loupias, and S. Atzeni, “Theoretical and experimental studies of radiative shocks,” *Astrophysics and Space Science*, vol. 307, no. 1, pp. 159–164, 2007.
- [73] P. Mabey, T. Michel, B. Albertazzi, E. Falize, N. Charpentier, and M. Koenig, “Calculating the temperature of strongly radiative shocks,” *Physics of Plasmas*, vol. 27, no. 8, p. 083302, 2020.
- [74] P. A. Keiter, R. P. Drake, T. S. Perry, H. F. Robey, B. A. Remington, C. A. Iglesias, R. J. Wallace, and J. Knauer, “Observation of a hydrodynamically driven, radiative-precursor shock,” *Phys. Rev. Lett.*, vol. 89, p. 165003, Sep 2002.
- [75] S. Bouquet, C. Stéhlé, M. Koenig, J.-P. Chièze, A. Benuzzi-Mounaix, D. Batani, S. Leygnac, X. Fleury, H. Merdji, C. Michaut, F. Thais, N. Grandjouan, T. Hall, E. Henry, V. Malka, and J.-P. J. Lafon, “Observation of laser driven supercritical radiative shock precursors,” *Phys. Rev. Lett.*, vol. 92, p. 225001, Jun 2004.
- [76] A. B. Reighard and R. P. Drake, “The formation of a cooling layer in a partially optically thick shock,” *Astrophysics and Space Science*, vol. 307, no. 1, pp. 121–125, 2007.
- [77] A. J. Visco, R. P. Drake, S. H. Glenzer, T. Döppner, G. Gregori, D. H. Froula, and M. J. Grosskopf, “Measurement of radiative shock properties by x-ray thomson scattering,” *Phys. Rev. Lett.*, vol. 108, p. 145001, Apr 2012.
- [78] R. Drake, F. Doss, R. McClarren, M. Adams, N. Amato, D. Bingham, C. Chou, C. DiStefano, K. Fidkowski, B. Fryxell, T. Gombosi, M. Grosskopf, J. Holloway, B. van der Holst, C. Huntington, S. Karni, C. Krauland, C. Kuranz, E. Larsen, B. van Leer, B. Mallick, D. Marion, W. Martin, J. Morel, E. Myra, V. Nair, K. Powell, L. Rauchwerger, P. Roe, E. Rutter, I. Sokolov, Q. Stout, B. Torralva,

- G. Toth, K. Thornton, and A. Visco, “Radiative effects in radiative shocks in shock tubes,” *High Energy Density Physics*, vol. 7, no. 3, pp. 130–140, 2011.
- [79] C. C. Kuranz, R. P. Drake, C. M. Krauland, D. C. Marion, M. J. Grosskopf, E. Rutter, B. Torralva, J. P. Holloway, D. Bingham, J. Goh, T. R. Boehly, and A. T. Sorce, “Initial conditions of radiative shock experiments,” *Physics of Plasmas*, vol. 20, no. 5, p. 056321, 2013.
- [80] R. P. Drake, F. W. Doss, B. Fryxell, M. J. Grosskopf, J. P. Holloway, B. van der Holst, C. Huntington, C. C. Kuranz, E. S. Myra, V. N. Nair, K. G. Powell, I. V. Sokolov, Q. F. Stout, G. Toth, A. J. Visco, M. L. Adams, J. E. Morel, B. Mallick, and D. Bingham, “Using high power lasers to create radiative shock waves,” in *2009 Conference on Lasers Electro Optics The Pacific Rim Conference on Lasers and Electro-Optics*, pp. 1–2, Aug 2009.
- [81] A. B. Reighard, R. P. Drake, K. K. Dannenberg, D. J. Kremer, M. Grosskopf, E. C. Harding, D. R. Leibbrandt, S. G. Glendinning, T. S. Perry, B. A. Remington, J. Greenough, J. Knauer, T. Boehly, S. Bouquet, L. Boireau, M. Koenig, and T. Vinci, “Observation of collapsing radiative shocks in laboratory experiments,” *Physics of Plasmas*, vol. 13, no. 8, p. 082901, 2006.
- [82] A. B. Reighard, R. P. Drake, J. E. Mucino, J. P. Knauer, and M. Busquet, “Planar radiative shock experiments and their comparison to simulations,” *Physics of Plasmas*, vol. 14, no. 5, p. 056504, 2007.
- [83] F. W. Doss, R. P. Drake, and C. C. Kuranz, “Statistical inference in the presence of an inclination effect in laboratory radiative shock experiments,” *Astrophysics and Space Science*, vol. 336, no. 1, pp. 219–224, 2011.
- [84] F. W. Doss, H. F. Robey, R. P. Drake, and C. C. Kuranz, “Wall shocks in high-energy-density shock tube experiments,” *Physics of Plasmas*, vol. 16, no. 11, p. 112705, 2009.
- [85] F. W. Doss, R. P. Drake, and E. S. Myra, “Oblique radiative shocks, including their interactions with nonradiative polytropic shocks,” *Physics of Plasmas*, vol. 18, no. 5, p. 056901, 2011.
- [86] F. Doss, R. Drake, and C. Kuranz, “Repeatability in radiative shock tube experiments,” *High Energy Density Physics*, vol. 6, no. 2, pp. 157–161, 2010. ICHED 2009 - 2nd International Conference on High Energy Density Physics.
- [87] C. Kuranz, R. Drake, C. Huntington, C. Krauland, C. Di Stefano, M. Trantham, M. Grosskopf, S. Klein, and D. Marion, “Early-time evolution of a radiative shock,” *High Energy Density Physics*, vol. 9, no. 2, pp. 315–318, 2013.
- [88] C. M. Krauland, R. P. Drake, C. C. Kuranz, B. Loupiau, T. Plewa, C. M. Huntington, D. N. Kaczala, S. Klein, R. Sweeney, R. P. Young, E. Falize, B. Villette, and P. A. Keiter, “REVERSE RADIATIVE SHOCK LASER EXPERIMENTS

RELEVANT TO ACCRETING STREAM-DISK IMPACT IN INTERACTING BINARIES,” *The Astrophysical Journal*, vol. 762, p. L2, dec 2012.

- [89] C. M. Krauland, R. P. Drake, C. C. Kuranz, R. Sweeney, M. Grosskopf, S. Klein, R. Gillespie, P. A. Keiter, B. Loupiau, and E. Falize, “Radiative reverse shock laser experiments relevant to accretion processes in cataclysmic variables,” *Physics of Plasmas*, vol. 20, no. 5, p. 056502, 2013.
- [90] M. Koenig, T. Michel, R. Yurchak, C. Michaut, B. Albertazzi, S. Laffite, E. Falize, L. Van Box Som, Y. Sakawa, T. Sano, Y. Hara, T. Morita, Y. Kuramitsu, P. Barroso, A. Pelka, G. Gregori, R. Kodama, N. Ozaki, D. Lamb, and P. Tzeferacos, “Interaction of a highly radiative shock with a solid obstacle,” *Physics of Plasmas*, vol. 24, no. 8, p. 082707, 2017.
- [91] M. Busquet, E. Audit, M. González, C. Stehlé, F. Thais, O. Acef, D. Bauduin, P. Barroso, B. Rus, M. Kozlova, J. Polan, and T. Mocek, “Effect of lateral radiative losses on radiative shock propagation,” *High Energy Density Physics*, vol. 3, no. 1, pp. 8–11, 2007. Radiative Properties of Hot Dense Matter.
- [92] D. Hoarty, A. Iwase, C. Meyer, J. Edwards, and O. Willi, “Characterization of laser driven shocks in low density foam targets,” *Phys. Rev. Lett.*, vol. 78, pp. 3322–3325, Apr 1997.
- [93] F. Suzuki-Vidal, T. Clayson, C. Stehlé, G. F. Swadling, J. M. Foster, J. Skidmore, P. Graham, G. C. Burdiak, S. V. Lebedev, U. Chaulagain, R. L. Singh, E. T. Gumbrell, S. Patankar, C. Spindloe, J. Larour, M. Kozlova, R. Rodriguez, J. M. Gil, G. Espinosa, P. Velarde, and C. Danson, “Counterpropagating radiative shock experiments on the orion laser,” *Phys. Rev. Lett.*, vol. 119, p. 055001, Aug 2017.
- [94] J. E. Cross, G. Gregori, J. M. Foster, P. Graham, J. M. Bonnet-Bidaud, C. Busschaert, N. Charpentier, C. N. Danson, H. W. Doyle, R. P. Drake, J. Fyrth, E. T. Gumbrell, M. Koenig, C. Krauland, C. C. Kuranz, B. Loupiau, C. Michaut, M. Mouchet, S. Patankar, J. Skidmore, C. Spindloe, E. R. Tubman, N. Woolsey, R. Yurchak, and É. Falize, “Laboratory analogue of a supersonic accretion column in a binary star system,” *Nature Communications*, vol. 7, no. 1, p. ncomms11899, 2016.
- [95] C. M. Huntington, A. Shimony, M. Trantham, C. C. Kuranz, D. Shvarts, C. A. Di Stefano, F. W. Doss, R. P. Drake, K. A. Flippo, D. H. Kalantar, S. R. Klein, J. L. Kline, S. A. MacLaren, G. Malamud, A. R. Miles, S. T. Prisbrey, K. S. Raman, B. A. Remington, H. F. Robey, W. C. Wan, and H.-S. Park, “Ablative stabilization of rayleigh-taylor instabilities resulting from a laser-driven radiative shock,” *Physics of Plasmas*, vol. 25, no. 5, p. 052118, 2018.
- [96] G. A. Rochau, J. E. Bailey, Y. Maron, G. A. Chandler, G. S. Dunham, D. V. Fisher, V. I. Fisher, R. W. Lemke, J. J. MacFarlane, K. J. Peterson, D. G.

- Schroen, S. A. Slutz, and E. Stambulchik, “Radiating shock measurements in the z -pinch dynamic hohlraum,” *Phys. Rev. Lett.*, vol. 100, p. 125004, Mar 2008.
- [97] S. X. Coffing, A. A. Angulo, M. R. Trantham, Y. Birnboim, C. C. Kuranz, R. P. Drake, and G. Malamud, “Design and Scaling of an Omega-EP Experiment to Study Cold Streams Feeding Early Galaxies,” *apjs*, vol. 245, p. 27, Dec. 2019.
- [98] H. J. LeFevre, K. Ma, P. X. Belancourt, M. J. MacDonald, T. Döppner, C. M. Huntington, E. Johnsen, P. A. Keiter, and C. C. Kuranz, “A platform for x-ray thomson scattering measurements of radiation hydrodynamics experiments on the nif,” *Review of Scientific Instruments*, vol. 89, no. 10, p. 10F105, 2018.
- [99] L. LANDAU and E. LIFSHITZ, “Chapter ix - shock waves,” in *Fluid Mechanics (Second Edition)* (L. LANDAU and E. LIFSHITZ, eds.), pp. 313 – 360, Pergamon, second edition ed., 1987.
- [100] S. Chandrasekhar, *Radiative Transfer*. Dover Books on Intermediate and Advanced Mathematics, Dover Publications, 1960.
- [101] J. MacFarlane, I. Golovkin, P. Woodruff, D. Welch, B. Oliver, T. Mehlhorn, and R. Campbell, “Simulation of the ionization dynamics of aluminum irradiated by intense short-pulse lasers,” *Inertial Fusion Sciences and Applications 2003*, pp. 457–460, 01 2004.
- [102] H.-K. Chung, M. Chen, W. Morgan, Y. Ralchenko, and R. Lee, “Flychk: Generalized population kinetics and spectral model for rapid spectroscopic analysis for all elements,” *High Energy Density Physics*, vol. 1, 06 2005.
- [103] D. Salzmann, *Atomic Physics in Hot Plasmas*. International series of monographs on physics, Oxford University Press, 1998.
- [104] D. A. Verner and G. J. Ferland, “Atomic Data for Astrophysics. I. Radiative Recombination Rates for H-like, He-like, Li-like, and Na-like Ions over a Broad Range of Temperature,” *apjs*, vol. 103, p. 467, Apr. 1996.
- [105] W. Lotz, “Electron-Impact Ionization Cross-Sections and Ionization Rate Coefficients for Atoms and Ions,” *apjs*, vol. 14, p. 207, May 1967.
- [106] D. A. Verner and D. G. Yakovlev, “Analytic FITS for partial photoionization cross sections,” *aaps*, vol. 109, pp. 125–133, Jan. 1995.
- [107] D. A. Verner, G. J. Ferland, K. T. Korista, and D. G. Yakovlev, “Atomic Data for Astrophysics. II. New Analytic FITS for Photoionization Cross Sections of Atoms and Ions,” *apj*, vol. 465, p. 487, July 1996.
- [108] T. R. Boehly, R. S. Craxton, T. H. Hinterman, J. H. Kelly, T. J. Kessler, S. A. Kumpan, S. A. Letzring, R. L. McCrory, S. F. B. Morse, W. Seka, S. Skupsky, J. M. Soures, and C. P. Verdon, “The upgrade to the omega laser system,” *Review of Scientific Instruments*, vol. 66, no. 1, pp. 508–510, 1995.

- [109] H. R. Griem, *Principles of Plasma Spectroscopy*. Cambridge Monographs on Plasma Physics, Cambridge University Press, 1997.
- [110] D. E. Desenne, J. M. Bruneau, S. Gary, J.-P. Le Breton, M. Louis-Jacquet, C. Chenais-Popovics, and J.-C. J. Gauthier, “Time- and space-resolved k- and l-shell absorption spectroscopy in an expanding laser-produced plasma,” *Proceedings of SPIE*, vol. 2015, 1994.
- [111] J. Bruneau, C. Chenais-Popovics, D. Desenne, J.-C. Gauthier, J.-P. Geindre, M. Klapisch, J.-P. Le Breton, M. Louis-Jacquet, D. Naccache, and J.-P. Perrine, “Time-resolved l-shell absorption spectroscopy: A direct measurement of density and temperature in a germanium laser-produced plasma,” *Phys. Rev. Lett.*, vol. 65, pp. 1435–1438, Sep 1990.
- [112] J. Bruneau, A. Decoster, D. Desenne, H. Dumont, J.-P. Le Breton, M. Boivineau, J.-P. Perrine, S. Bayle, M. Louis-Jacquet, J.-P. Geindre, C. Chenais-Popovics, and J.-C. Gauthier, “Time-resolved study of hot dense germanium by l-shell absorption spectroscopy,” *Phys. Rev. A*, vol. 44, pp. R832–R835, Jul 1991.
- [113] A. Krygier, F. Coppari, G. E. Kemp, D. B. Thorn, R. S. Craxton, J. H. Eggert, E. M. Garcia, J. M. McNaney, H.-S. Park, Y. Ping, B. A. Remington, and M. B. Schneider, “Developing a high-flux, high-energy continuum backlighter for extended x-ray absorption fine structure measurements at the national ignition facility,” *Review of Scientific Instruments*, vol. 89, no. 10, p. 10F114, 2018.
- [114] F. Coppari, D. B. Thorn, G. E. Kemp, R. S. Craxton, E. M. Garcia, Y. Ping, J. H. Eggert, and M. B. Schneider, “X-ray source development for exafs measurements on the national ignition facility,” *Review of Scientific Instruments*, vol. 88, no. 8, p. 083907, 2017.
- [115] J. A. Cobble, T. E. Tierney, and J. Abdallah, “Kilovolt radiation from a laser-produced plasma,” *Journal of Applied Physics*, vol. 102, no. 2, p. 023303, 2007.
- [116] Y. Lin, T. J. Kessler, and G. N. Lawrence, “Distributed phase plates for super-gaussian focal-plane irradiance profiles,” *Opt. Lett.*, vol. 20, pp. 764–766, Apr 1995.
- [117] S. G. Gales and C. D. Bentley, “Image plates as x-ray detectors in plasma physics experiments,” *Review of Scientific Instruments*, vol. 75, no. 10, pp. 4001–4003, 2004.
- [118] B. R. Maddox, H. S. Park, B. A. Remington, N. Izumi, S. Chen, C. Chen, G. Kimminau, Z. Ali, M. J. Haugh, and Q. Ma, “High-energy x-ray backlighter spectrum measurements using calibrated image plates,” *Review of Scientific Instruments*, vol. 82, no. 2, p. 023111, 2011.

- [119] A. L. Meadowcroft, C. D. Bentley, and E. N. Stott, “Evaluation of the sensitivity and fading characteristics of an image plate system for x-ray diagnostics,” *Review of Scientific Instruments*, vol. 79, no. 11, p. 113102, 2008.
- [120] A. Seifter and G. A. Kyrala, “Different methods of reconstructing spectra from filtered x-ray diode measurements,” *Review of Scientific Instruments*, vol. 79, no. 10, p. 10F323, 2008.
- [121] Y. Ehrlich, S. Cohen, Y. Frank, A. Malka, G. Hurvitz, I. Levy, J. Davis, P. A. Keiter, R. P. Drake, D. Shvarts, M. Fraenkel, and Z. Shpilman, “Enhanced accuracy of x-ray spectra reconstruction from filtered diode array measurements by adding a time integrated spectrometer,” *Review of Scientific Instruments*, vol. 88, no. 4, p. 043507, 2017.
- [122] J. MacFarlane, “Visrad—a 3-d view factor code and design tool for high-energy density physics experiments,” *Journal of Quantitative Spectroscopy and Radiative Transfer*, vol. 81, no. 1, pp. 287 – 300, 2003. Radiative Properties of Hot Dense Matter.
- [123] B. Yaakobi, F. J. Marshall, T. R. Boehly, R. P. J. Town, and D. D. Meyerhofer, “Extended x-ray absorption fine-structure experiments with a laser- imploded target as a radiation source,” *J. Opt. Soc. Am. B*, vol. 20, pp. 238–245, Jan 2003.
- [124] P. A. Keiter and R. P. Drake, “Spectral measurements of asymmetrically irradiated capsule backlighters,” *Review of Scientific Instruments*, vol. 87, no. 11, p. 11E338, 2016.
- [125] Y. Ping, D. G. Hicks, B. Yaakobi, F. Coppari, J. Eggert, and G. W. Collins, “A platform for x-ray absorption fine structure study of dynamically compressed materials above 1 mbar,” *Review of Scientific Instruments*, vol. 84, no. 12, p. 123105, 2013.
- [126] “X-ray server url: <https://x-server.gmca.aps.anl.gov>,” 2020.
- [127] S. A. Stepanov, “X-ray server: an online resource for simulations of x-ray diffraction and scattering,” in *Advances in Computational Methods for X-Ray and Neutron Optics* (M. S. del Rio, ed.), vol. 5536, pp. 16 – 26, International Society for Optics and Photonics, SPIE, 2004.
- [128] L. B. Lucy, “An iterative technique for the rectification of observed distributions,” *The Astrophysical Journal*, vol. 79, p. 745, June 1974.
- [129] D. S. C. Biggs and M. Andrews, “Acceleration of iterative image restoration algorithms,” *Appl. Opt.*, vol. 36, pp. 1766–1775, Mar 1997.
- [130] Y. P. Opachich, R. F. Heeter, M. A. Barrios, E. M. Garcia, R. S. Craxton, J. A. King, D. A. Liedahl, P. W. McKenty, M. B. Schneider, M. J. May, R. Zhang,

- P. W. Ross, J. L. Kline, A. S. Moore, J. L. Weaver, K. A. Flippo, and T. S. Perry, “Capsule implosions for continuum x-ray backlighting of opacity samples at the national ignition facility,” *Physics of Plasmas*, vol. 24, no. 6, p. 063301, 2017.
- [131] D. A. Liedahl, “X-ray photoionized plasmas in space and in the laboratory,” *Astrophysics and Space Science*, vol. 336, no. 1, pp. 251–256, 2011.
- [132] R. P. Drake, “How to see a black hole,” *Nature Physics*, vol. 5, no. 11, pp. 786–787, 2009.
- [133] J. MacFarlane, I. Golovkin, P. Wang, P. Woodruff, and N. Pereyra, “Spect3d – a multi-dimensional collisional-radiative code for generating diagnostic signatures based on hydrodynamics and pic simulation output,” *High Energy Density Physics*, vol. 3, no. 1, pp. 181 – 190, 2007. Radiative Properties of Hot Dense Matter.
- [134] G. H. Miller, E. I. Moses, and C. R. Wuest, “The national ignition facility: enabling fusion ignition for the 21st century,” *Nuclear Fusion*, vol. 44, no. 12, p. S228, 2004.
- [135] E. I. Moses, R. N. Boyd, B. A. Remington, C. J. Keane, and R. Al-Ayat, “The national ignition facility: ushering in a new age for high energy density science,” *Physics of Plasmas*, vol. 16, no. 4, p. 041006, 2009.
- [136] S. H. Glenzer and R. Redmer, “X-ray thomson scattering in high energy density plasmas,” *Rev. Mod. Phys.*, vol. 81, pp. 1625–1663, Dec 2009.
- [137] T. Döppner, A. L. Kritcher, D. Kraus, S. H. Glenzer, B. L. Bachmann, D. Chapman, G. W. Collins, R. W. Falcone, J. Hawreliak, O. L. Landen, H. J. Lee, S. L. Pape, T. Ma, P. Neumayer, R. Redmer, and D. C. Swift, “X-ray thomson scattering as a temperature probe for gbar shock experiments,” *Journal of Physics: Conference Series*, vol. 500, no. 19, p. 192019, 2014.
- [138] G. Gregori, S. H. Glenzer, F. J. Rogers, S. M. Pollaine, O. L. Landen, C. Blancard, G. Faussurier, P. Renaudin, S. Kuhlbrodt, and R. Redmer, “Electronic structure measurements of dense plasmas,” *Physics of Plasmas*, vol. 11, no. 5, pp. 2754–2762, 2004.
- [139] D. Kraus, T. Döppner, A. L. Kritcher, A. Yi, K. Boehm, B. Bachmann, L. Divol, L. B. Fletcher, S. H. Glenzer, O. L. Landen, N. Masters, A. M. Saunders, C. Weber, R. W. Falcone, and P. Neumayer, “Platform for spectrally resolved x-ray scattering from imploding capsules at the national ignition facility,” *Journal of Physics: Conference Series*, vol. 717, no. 1, p. 012067, 2016.
- [140] D. Kraus, D. A. Chapman, A. L. Kritcher, R. A. Baggott, B. Bachmann, G. W. Collins, S. H. Glenzer, J. A. Hawreliak, D. H. Kalantar, O. L. Landen, T. Ma, S. Le Pape, J. Nilsen, D. C. Swift, P. Neumayer, R. W. Falcone, D. O. Gericke,

- and T. Döppner, “X-ray scattering measurements on imploding ch spheres at the national ignition facility,” *Phys. Rev. E*, vol. 94, p. 011202, Jul 2016.
- [141] M. Barrios, K. Fournier, S. Regan, O. Landen, M. May, Y. Opachich, K. Widmann, D. Bradley, and G. Collins, “Backlighter development at the national ignition facility (nif): Zinc to zirconium,” *High Energy Density Physics*, vol. 9, no. 3, pp. 626–634, 2013.
- [142] M. A. Barrios, S. P. Regan, K. B. Fournier, R. Epstein, R. Smith, A. Lazicki, R. Rygg, D. E. Fratanduono, J. Eggert, H.-S. Park, C. Huntington, D. K. Bradley, O. L. Landen, and G. W. Collins, “X-ray area backlighter development at the national ignition facility (invited),” *Review of Scientific Instruments*, vol. 85, no. 11, p. 11D502, 2014.
- [143] T. Döppner, A. L. Kritcher, P. Neumayer, D. Kraus, B. Bachmann, S. Burns, R. W. Falcone, S. H. Glenzer, J. Hawreliak, A. House, O. L. Landen, S. LePape, T. Ma, A. Pak, and D. Swift, “Qualification of a high-efficiency, gated spectrometer for x-ray thomson scattering on the national ignition facility,” *Review of Scientific Instruments*, vol. 85, no. 11, p. 11D617, 2014.
- [144] T. Döppner, D. Kraus, P. Neumayer, B. Bachmann, J. Emig, R. W. Falcone, L. B. Fletcher, M. Hardy, D. H. Kalantar, A. L. Kritcher, O. L. Landen, T. Ma, A. M. Saunders, and R. D. Wood, “Improving a high-efficiency, gated spectrometer for x-ray thomson scattering experiments at the national ignition facility,” *Review of Scientific Instruments*, vol. 87, no. 11, p. 11E515, 2016.
- [145] J. A. Oertel, R. Aragonéz, T. Archuleta, C. Barnes, L. Casper, V. Fatherley, T. Heinrichs, R. King, D. Landers, F. Lopez, P. Sanchez, G. Sandoval, L. Schrank, P. Walsh, P. Bell, M. Brown, R. Costa, J. Holder, S. Montelongo, and N. Pederson, “Gated x-ray detector for the national ignition facility,” *Review of Scientific Instruments*, vol. 77, no. 10, p. 10E308, 2006.
- [146] M. B. Schneider, J. P. Holder, D. L. James, H. C. Bruns, J. R. Celeste, S. Compton, R. L. Costa, A. D. Ellis, J. A. Emig, D. Hargrove, D. H. Kalantar, B. J. MacGowan, G. D. Power, C. Sorce, V. Rekow, K. Widmann, B. K. Young, P. E. Young, O. F. Garcia, J. McKenney, M. Haugh, F. Goldin, L. P. MacNeil, and K. Cone, “Time-resolved soft x-ray imaging diagnostic for use at the nif and omega lasers,” *Review of Scientific Instruments*, vol. 77, no. 10, p. 10E321, 2006.
- [147] K. S. Budil, T. S. Perry, P. M. Bell, J. D. Hares, P. L. Miller, T. A. Peyser, R. Wallace, H. Louis, and D. E. Smith, “The flexible x-ray imager,” *Review of Scientific Instruments*, vol. 67, no. 2, pp. 485–488, 1996.
- [148] P. M. Celliers, D. K. Bradley, G. W. Collins, D. G. Hicks, T. R. Boehly, and W. J. Armstrong, “Line-imaging velocimeter for shock diagnostics at the omega laser facility,” *Review of Scientific Instruments*, vol. 75, no. 11, pp. 4916–4929, 2004.

- [149] J. E. Miller, T. R. Boehly, A. Melchior, D. D. Meyerhofer, P. M. Celliers, J. H. Eggert, D. G. Hicks, C. M. Sorce, J. A. Oertel, and P. M. Emmel, “Streaked optical pyrometer system for laser-driven shock-wave experiments on omega,” *Review of Scientific Instruments*, vol. 78, no. 3, p. 034903, 2007.
- [150] M. May, M. Schneider, S. Hansen, H.-K. Chung, D. Hinkel, H. Baldis, and C. Constantin, “X-ray spectral measurements and collisional-radiative modeling of hot, gold plasmas at the omega laser,” *High Energy Density Physics*, vol. 4, no. 3, pp. 78–87, 2008.